ONE- AND TWO-COLOR LASER SPECTROSCOPY WITH PHOTOACOUSTIC AND MULTIPHOTON IONIZATION DETECTION

Thesis by

David Jerry Moll

In Partial Fulfillment of the Requirements
for the Degree of
Doctor of Philosophy

California Institute of Technology
Pasadena, California

1983
(Submitted February 16, 1983)

ACKNOWLEDGMENTS

The studies reported in this thesis required the assistance of many people. I am happy to acknowledge their help. I am especially indebted to my research advisor Professor Aron Kuppermann. He provided a scientific atmosphere which stimulated my creativity while still requiring thoroughness and attention to detail. He provided the moral support of a true friend in several times of crisis. I thank him from the bottom of my heart.

Ron Rianda and Garth Parker both deserve my thanks for their help in performing the experiments described in this thesis. Ron was responsible for most of the electronics hardware and software used in data collection. Garth provided a great deal of assistance during the past year in collecting data and interpreting results. I wish him success as he inherits the resources of room 013 and begins his own experiments.

The experiments described in Paper I involved collaboration with Joe Perry and Professor Ahmed Zewail. I thank them for their contributions to that work.

I would like to thank my friends, Jerry Winniczek, charlie Loerting, and Jack Kaye for the humor, excitement and practical jokes they added to subbasement life. Charlie and Jerry accompanied me on numerous expeditions throughout the southwestern U.S. Jack was always willing to discuss scientific as well as nonscientific problems.

Both Professor J. L. Beauchamp and Professor K. C. Janda took an interest in my work. It was partially through their efforts, I am sure, that I was able to obtain permanent employment.

The chemistry department instrument and electronics shops played an important role in the construction and maintenance of the equipment used in my experiments. I want to thank Bill Schulke, Tony Stark, Guy Duremberg, Ray Garcia, and Delmer Dill of the instrument shop, and Tom Dunn of the electronics shop. In particular, Tom provided a long-term loan of some equipment that was essential for the completion of the two-color experiments.

I am indebted to Heidi Tanciar and Adria McMillan for their assistance in dealing with Caltech's bureaucracy. I also must thank Kathy Lewis as well as Heidi for their excellent typing of this thesis manuscript.

I am grateful to the Department of Energy, Eastman Kodak Company, the Shell Companies Foundation, and the Caltech Chemistry Department for financial support during my graduate student career.

Finally, I am especially thankful to my parents, my wife Sharon, and her parents for their support and encouragement during my stay at Caltech.

Abstract

The techniques of pulsed photoacoustic spectroscopy and multiphoton ionization spectroscopy have been used to study several types of weak optical transitions in the ultraviolet or visible spectral regions for gas phase molecules. Both one- and two-color experiments have been performed. The one-color experiments involved the study of high vibrational overtones and spin-forbidden transitions. The two-color experiments demonstrated the application of photoacoustic detection of stimulated emission pumping for populating high vibration levels of the ground electronic state. Two-color experiments were also used to study excited state absorption processes in aniline.

Pulsed laser photoacoustic spectra of CD_3H in the region of the Δv_{CH} = 5, 6, and 7 CH stretch overtones were obtained. These overtones and nearby combination bands displayed sharp rotational structure, indicating a minimum excited state population relaxation time of 5×10^{-12} sec. A combination sum analysis was used to generate excited state rotational constants B'. These constants reflect the geometries of the excited states, and therefore provide a sensitive probe of the mixing between various zero order excited states.

Photoacoustic detection was used to monitor a stimulated emission pumping process in p-difluorobenzene. Using the

$\tilde{A}^1B_{2u}$ 5' state as an intermediate state, several vibrational levels of the ground electronic state were populated. The photoacoustic technique is an attractive alternative to other techniques because of its sensitivity, simplicity, and its ability to differentiate between stimulated emission pumping and excited state absorption.

Time-resolved excited state absorption studies were performed on aniline using the multiphoton ionization and photoacoustic detection techniques. Signals from both of these techniques were measured as a function of the time delay between two laser pulses of different wavelength. The first pulse excited the S_1 0-0 transition. The second pulse excited either S_1 or a triplet state produced by intersystem crossing, depending on the time delay between pulses. Both ionization and dissociation processes were observed. By varying the conditions of excitation, it appears that a given amount of energy can be selectively channeled into either ionization or dissociation pathways. These results were explained using a simple Franck Condon factor model.

The application of pulsed laser photoacoustic spectroscopy to the study of weak absorptions in the visible and ultraviolet spectral regions was investigated. Photoacoustic spectra of triplet states in CS_2, SO_2, biacetyl, and thiophosgene were obtained. An attempt to detect the $\tilde{a}^3B_{1u}$ state in benzene, produced instead a two-photon spectrum of several Rydberg states. It was discovered that the sensitivity of

the pulsed photoacoustic technique for extremely weak absorptions is limited by the increased probability of multiphoton absorption when high intensities are used.

Finally, in two appendices, the detection of the $\tilde{a}^3A_2$ state in CS_2 by the multiphoton ionization technique is presented. The CS_2 study demonstrates the utility of the multiphoton ionization technique for detecting spin-forbidden transitions at high resulution and with great sensitivity.

Table of Contents

Page

Acknowledgments. ii

Abstract iv

Introduction 1

Paper I: High Overtone Photoacoustic Spectroscopy of Some Methyl-Containing Molecules. I. Rotational Analysis. 12

Paper II: Photoacoustic Detection of Stimulated Emission Pumping in p-Difluorobenzene 71

Paper III: Two-Color Time-Resolved Photoacoustic and Multiphoton Ionization Spectroscopy of Aniline. 103

Paper IV: Detection of Weak Absorptions in the Visible and Ultraviolet by Pulsed Laser Photoacoustic Spectroscopy 147

Appendix A: A Description of Laser Systems and Related Electronics 186

1. Introduction. 187

2. Laser Systems 187

2.1 MY34 Nd:YAG Laser. 187

2.2 DL18 Dye Laser 189

2.3 UV400 N_2 Laser and DL200 Dye Laser 192

3. Crystal Phasematching Angle Control 193

4. Electronics for Two-Laser Experiments 197

Appendix B: The Design of Photoacoustic Cells for Pulsed Laser Excitation 207

1. Introduction. 208

2. Photoacoustic Cell Design 208

2.1 PAC1 208

Table of Contents (continued)

Page

2.2 PAC2 209

2.3 PAC3 211

2.4 PAC4 212

2.5 PAC5 214

3. Conclusions 214

Appendix C: Wavelength Conversion by Stimulated Raman Scattering 217

Appendix D: Detection of the $^3A_2$ State of CS_2 by Multiphoton Ionization 228

Proposition I: A Direct Measurement of the Internal Conversion Rate in the S_3 State of Naphthalene Using Picosecond Two-Color Time-Resolved Multiphoton Ionization Spectroscopy 241

Proposition II: Collisional Relaxation of Rovibrational Levels of Formaldehyde Prepared by Stimulated Emission Pumping . .251

Proposition III: An Experimental Investigation of the Mechanism of Plasma Formation during Metal Processing with High Power Ultraviolet Lasers 260

Proposition IV: H_2O Vapor Detection in the Chemical Oxygen Iodine Laser by a New Dye Laser Intracavity Absorption Technique 273

Proposition V: A Radio-Chemical Tracer Study of the Tungsten Regenerative Cycle in Incandescent Lamps Containing $CBrF_3$ 283

Introduction

The experimental work described in this thesis is concerned primarily with the detection of weak optical absorptions in the gas phase. The optical transitions studied in the course of this research were weak for one of the following reasons. (1) The absorption involved a multi-quantum vibrational transition in the ground electronic state. (2) The transition resulted from stimulating emission out of a sparsely populated electronic state back to the ground electronic state. (3) The transition involved an excited state absorption process from an electronic state with a small population. (4) The absorption resulted from a spin-forbidden transition between states of different spin multiplicities.

The results presented in papers I-IV are spectroscopic studies of transitions from each of the above four categories, respectively. They were obtained using the photoacoustic spectroscopy (PAS) or multiphoton ionization (MPI) detection techniques. These techniques will be described briefly in the next two sections.

Photoacoustic Spectroscopy

The photoacoustic effect was first described in detail by Alexander Graham Bell in 1881.[1] Recently, due to the widespread availability of lasers, it has been used extensively in studies of gases, as well as liquids and solids. Excellent reviews of this technique can be found in books

published by Pao[2] and Rosencwaig.[3]

In a typical gas phase photoacoustic experiment, an intensity-modulated light beam is directed into a chamber containing the gas sample to be studied. If the sample absorbs some of the incident light, the molecules excited by the absorption process may undergo collisional deactivation. Eventually, some of the initially absorbed energy appears as translational energy of the molecules and is detected by a microphone as a periodic pressure increase. Recording the microphone signal as the wavelength of the incident light is scanned produces a photoacoustic spectrum.

In the PAS experiments described in this thesis, a tunable pulsed dye laser was used as the excitation source. Molecules excited by a <10 nsec pulse from this laser typically undergo collisional relaxation in a few μsec. A local pressure increase appears in the region of the laser beam. This pressure increase propagates radially outward as a cylindrical pressure wave. It is detected when it strikes a microphone mounted in the wall of the photoacoustic cell. A pulsed laser photoacoustic spectrum is generated by monitoring the amplitude of this pressure wave as a function of excitation wavelength.

The PAS technique has been used widely in the study of weak absorptions arising from high vibrational overtone transitions,[4,5] detection of atmospheric pollutants,[6,7] and

and excited state absorption.[8,9] We have used the pulsed PAS technique to investigate both high vibrational overtones and spin-forbidden transitions. Paper I presents the results if a pulsed PAS study of high vibrational overtones of CD_3H. The resolved rotational structure in these spectra permitted rotational analysis which generated the excited state rotational constants B'. Since these constants reflect the geometry of the excited state, they provide a sensitive probe of the mixing between various zero order vibrational states. Paper IV presents a discussion of the applicability of the pulsed PAS technique for studying extremely weak spin-forbidden transitions to triplet states. Several examples of triplet state spectra obtained using the pulsed PAS tehcnique are given to illustrate the advantages and disadvantages of that technique.

A second, completely different class of PAS experiments focuses on the dynamics of excited states in molecules. Since the PAS technique is sensitive to the nonradiative decay of excited molecules, it provides a unique tool for studying excited state dynamics. The wide variety of problems studied in the past includes investigation of vibrational relaxation rates,[10] thermochemical effects following dissociation,[11] electronic relaxation kinetic effects,[12] and radiationless transitions.[11,13] All of these studies used a CW laser PAS technique in which the change of phase angle of

the PAS signal with respect to the intensity modulation was monitored. This method permits time-resolution studies in the 100 μsec timescale or slower. We have developed a new gas phase two-color time-resolved pulsed PAS technique which permits a new class of dynamics experiments to be performed with nanosecond or faster time resolution. Briefly, the output beams of two pulsed dye lasers are overlapped inside a photoacoustic cell in a collinear counterpropagating configuration. The time delay Δt between the output pulses of the two lasers can be adjusted with nanosecond precision. The first pulse can excite an electronic state of the sample molecules, which can fluoresce or nonradiatively transfer to another state through internal conversion or intersystem crossing. Depending on the value of Δt chosen, the second pulse will find molecules in the ground state, the state initially excited by the first pulse, or some other state populated by a radiationless process. If the molecules are in an excited state, the second pulse may be absorbed in an excited state absorption process, or stimulate emission out of the excited state down to a lower state in the molecule. Since the PAS technique responds to the total amount of energy deposited in the sample, the excited state absorption or stimulated emission processes produce larger or smaller PAS signals, respectively. Varying the wavelengths of the laser pulses, or changing Δt, while monitoring the PAS signal allows

a new and versatile technique for studying excited state dynamics.

Paper II describes the use of the two-color time-resolved PAS technique to populate high vibration levels of the ground electronic state of p-difluorobenzene using stimulated emission pumping. The increase or decrease in the photoacoustic signal provides a simple method for determining whether stimulated emission or excited state absorption has occurred.

Paper III presents a study of excited state absorption in aniline performed using the two-color time-resolved PAS technique and a MPI technique. Absorption from both S_1 and a vibrationally excited triplet state produced by intersystem crossing to states lying above the adiabatic ionization potential was studied. It was discovered that a given amount of excitation energy can be selectively channeled into either ionization or dissociation, depending on the way in which the energy is deposited in aniline.

Multiphoton Ionization Spectroscopy

When very intense photon fields interact with a molecule multiphoton absorption processes become highly probably. Under these conditions, the molecule may be excited above the ionization potential and subsequently ionize. In typical MPI experiments, an intense UV or visible laser pulse is

focused into a gaseous sample, producing an ionization current which is measured as a function of wavelength. When integral multiples of the photon energy are resonant with states in the sample, an increase in ionization current occurs.

MPI spectroscopy has primarily been applied to the study of two-photon excited states in molecules such as benzene,[14,15] 1,3-butadiene,[16] hexatriene,[17] etc. Recent MPI experiments have detected the masses of fragments produced and/or the kinetic energy of released electrons in molecules such as NO,[18,19] I_2,[18,20] H_2S,[21] NH_3,[22] benzene,[18,20,23,24] acetaldehyde,[25] aniline,[26] azulene,[27] naphthalene[27] and organometallics.[28]

Paper III presents a study of aniline which used the MPI technique to complement the results obtained with the two-color time-resolved photoacoustic technique. In the MPI experiments, the wavelengths of the two-laser pulses and Δt were also varied, but an ion current was detected instead of a photoacoustic signal. The combination of both MPI and PAS detection in these experiments provided a powerful method for probing excited state dynamics above the ionization potential.

Appendix D contains a paper which describes the use of a MPI technique to detect spin-forbidden transitions in CS_2.[29] The $\tilde{a}^3A_2$ state of CS_2 was detected using a one-photon spin-forbidden transition as a rate limiting initial step. Subsequent absorption of additional photons through the triplet

manifold ionized the molecule. Therefore, by measuring the ionization current as a function of laser wavelength, the spectrum of the $^3A_2$ state was generated. This technique promises to allow measurement of spin-forbidden transitions with great sensitivity and high resolution.

A description of the laser systems and related electronics used in the PAS and MPI experiments is contained in Appendix A. Appendix B contains a description of the photoacoustic cells used in these experiments and summarizes the important criteria for optimizing cells for pulsed laser excitation. Appendix C contains a discussion of wavelength conversion by stimulated Raman scattering (SRS), and a description of a high pressure cell for SRS in H_2.

References

1. A. G. Bell, Philos. Mag. 11, 510 (1881).
2. Y.-H. Pao, edit. Optoacoustic Spectroscopy and Detection (Academic Press, New York, 1979).
3. A. Rosencwaig, Photoacoustics and Photoacoustic Spectroscopy (Wiley, New York, 1980).
4. K. V. Reddy, D. F. Heller and M. J. Berry, J. Chem. Phys. 76, 2814 (1982).
5. K. K. Lehmann, G. J. Scherer and W. Klemperer, J. Chem. Phys. 76, 6441 (1982).
6. L. B. Kreuzer and C. K. N. Patel, Science 173, 45 (1971).
7. C. K. N. Patel, E. G. Burkhardt and C. A. Lambert, Science 184, 1173 (1974).
8. V. P. Zharov, V. S. Letokhov and E. A. Ryabov, Appl. 12, 15 (1977).
9. C. K. N. Patel, R. J. Kerl and E. G. Burkhardt, Phys. Rev. Lett. 38, 1204 (1977).
10. T. L. Cottrell, I. M. Macfarlane, A. W. Read and A. H. Young, Trans. Faraday Soc. 62, 2655 (1966).
11. W. R. Harshbarger and M. B. Robin, Acc. Chem. Res. 6, 329 (1973).
12. W. R. Harshbarger and M. B. Robin, Chem. Phys. Lett. 21, 462 (1973).
13. T. F. Hunter and M. G. Stock, Chem. Phys. Lett. 22, 368 (1973); J. Chem. Soc. Faraday Trans. II 70, 1028 (1974).

14. P. M. Johnson, J. Chem. Phys. 62, 4562 (1975).

15. P. M. Johnson, J. Chem. Phys. 64, 4143 (1976).

16. P. M. Johnson, J. Chem. Phys. 64, 4638 (1976).

17. D. H. Parker, S. J. Sheng and M. A. El-Sayed, J. Chem. Phys. 65, 5534 (1976).

18. L. Zandee and R. B. Bernstein, J. Chem. Phys. 71, 1359 (1979).

19. J. C. Miller and R. N. Compton, J. Chem. Phys. 75, 22 (1981).

20. J. C. Miller and R. N. Compton, J. Chem. Phys. 75, 2020 (1981).

21. J. C. Miller, R. N. Compton, T. E. Carney and T. Baer, J. Chem. Phys. 76, 5648 (1982).

22. J. H. Glownia, S. J. Riley, S. D. Colson, J. C. Miller and R. N. Compton, J. Chem. Phys. 77, 68 (1982).

23. U. Boesl, H. J. Neusser and E. W. Schlag, Chem. Phys. 55, 193 (1981).

24. J. T. Meek, R. K. Jones and J. P. Reilly, J. Chem. Phys. 73, 3503 (1980).

25. G. J. Fisanick, T. S. Eichelberger IV, B. A. Heath and M. B. Robin, J. Chem. Phys. 72, 5571 (1980).

26. T. G. Dietz, M. A. Duncan, M. G. Liverman and R. E. Smalley, Chem. Phys. Lett. 70, 246 (1980).

27. D. M. Lubman, R. Naaman and R. N. Zare, J. Chem. Phys. 72, 3034 (1980).

28. G. J. Fisanick, A. Gedanken, T. S. Eichelberger IV, N. A. Kuebler and M. B. Robin, J. Chem. Phys. 75, 5215 (1981).

29. R. Rianda, D. J. Moll and A. Kuppermann, Chem. Phys. Lett. 73, 469 (1980).

Paper I: High Overtone Photoacoustic Spectroscopy of Some Methyl-Containing Molecules. I. Rotational Analysis.

High Overtone Photoacoustic Spectroscopy of Some Methyl-Containing Molecules. I. Rotational Analysis[a)]

D. J. Moll,[b)] J. W. Perry, A. Kuppermann, and A. H. Zewail
Arthur Amos Noyes Laboratory of Chemical Physics,[c)]
California Institute of Technology, Pasadena, CA 91125, USA

(Received

Pulsed laser photoacoustic spectra of CD_3H in the region of the CH stretch overtones Δv_{CH} = 5,6, and 7 are presented. These overtones and nearby combination bands display sharp rotational structure, indicating a minimum excited state population relaxation time of 5×10^{-12} sec. A combination sum analysis is used to generate excited state rotational constants B'. These constants reflect the geometry of the excited state, and therefore provide a sensitive probe of the mixing between various zero order excited states. The nature and extent of this mixing are discussed, and a model for a statistical rotational constant is presented.

---

a) Research supported in part by the U. S. Department of Energy (Contract No. DE-AS03-765F00767, Project Agreement No. DE-AT03-76ER72004). Report Code CALT-76764-

b) Work performed in partial fulfillment of the requirements for the Ph. D. degree in Chemistry at the California Institute of Technology.

c) Contribution No.

I. INTRODUCTION

Recent spectroscopic studies of highly excited vibrational states of polyatomic molecules have yielded important information about them.[1-13] Many of these studies have attempted to elucidate (1) the nature of such states populated by a single photon absorption, and (2) the dynamics of the intramolecular vibrational energy redistribution which follows their excitation.

In most spectroscopic studies of high vibrational states of polyatomic saturated hydrocarbon gases at room temperature, the predominate features appearing in the spectra have been attributed to CH or CD stretch overtones. These features are typically broad (50-150 cm^{-1} wide), nearly Lorentzian in shape, and the intensity of the absorption bands decreases as the vibrational quantum number of the overtone increases. The pure overtone bands are sometimes closely associated with weaker nearby combination bands. This broadness and near-Lorentzian shape have been attributed to homogeneous lifetime broadening on the 50-100 femtosecond timescale.[7] Similar studies of low temperature crystals of naphthalene[11,12] and durene[13] have also yielded Lorentzian lineshapes but with widths as narrow as 25 cm^{-1}. Even this broadening severely limits the amount of useful information which can be obtained by spectroscopic means. In addition to the band line shape characteristics, the only other parameters usually obtained in these experiments are the absolute absorption strength

and the transition energy.

In this paper (I) and the following one (paper II[14]) we present spectroscopic results for several high vibrational states of CD_3H, and discuss their implications for the nature and dynamics of these states. This molecule has a CH stretch-type oscillation whose frequency is substantially different from any of the molecule's other fundamental frequencies. This fact, coupled with the relatively small moments of inertia of the CD_3H symmetric top and the low density of vibrational states results in high vibrational states having features which are sufficiently isolated and sufficiently resolved to give much more detailed information about these states than is usually possible for larger and more complex molecules.

In this paper we present an interpretation of the rotational features associated with the $v = 5, 6$ and 7 vibrational overtones of the totally symmetric CH stretching mode ($\nu_1 = 2992\ cm^{-1}$) of CD_3H and several nearby combination bands. In paper (II) we present an interpretation of the vibrational characteristics of the same vibrational overtone bands of CD_3H, and present overtone spectra of several similar molecules.

2. Background

CD_3H is an oblate ($I_z > I_x = I_y$) symmetric top molecule belonging to the C_{3v} point group. Many of the degeneracies present in the CH_4 spherical top rotational spectrum are removed in CD_3H. In particular, parallel transition between levels of A_1 symmetry in C_{3v} molecules are not influential by first-order Coriolis effects, unlike perpendicular bands.[15] Therefore, it should be possible to obtain unique reliable values for rotational constants for these bands. Such excited state rotational constants reflect the overall geometry of these states and provide a sensitive indication of the mixing present between various nearly degenerate excited vibrational levels.

The vibrational absorption spectrum of CD_3H was first measured by Benedict, et al.[16] Rotational studies of the v=1 and v=2 levels of the ν_1 totally symmetric CH stretch modes were carried out by Rea and Thompson,[17] and Wiggins, et al.[18] respectively. The v=3 and v=4 levels were studied by Bovey.[15] The highest resolution study of CD_3H was carried out by Jennings and Blass[19] on the ν_2 fundamental which is a parallel type band corresponding to the CD_3 symmetric stretching mode centered at 2143 cm^{-1}. We believe that the ground state parameters of Jennings and Blass are the most accurate ones to date. A listing of known vibrational and rotational constants is given in table 1. Gray and Robiette[26] have recently

determined the quadratic and cubic potential constants of methane by fitting spectroscopic data from six isotopic methanes including CD_3H.

In this paper we present the pulsed laser photoacoustic spectra of the v = 5,6 and 7 vibrational overtones of the ν_1 totally symmetric C-H stretching mode of CD_3H, as well as nearby combination bands involving one less quantum of CH stretch and the two quanta of the degenerate CH bending motion of E symmetry. Five of the bands exhibit distinct rotational structures which permit a combination sum rotational analysis from which the vibrational transition energies and the excited state rotational constants B' are obtained. The values of B' reflect the overall geometry of the excited state. Since each vibrational state has its own specific geometry and rotational constant, the interaction of different vibrational states produces deviations from the expected rotational constants. In the case of CD_3H these deviations are substantial and indicate significant mixing of vibrational states.

3. Experimental

The spectra presented in this paper were obtained using a pulsed laser photoacoustic spectrometer. A detailed description of this apparatus will be given elsewhere,[27] but some of its characteristics as well as the sample preparation and data handling are summarized below.

3.1 Sample Preparation

The CD_3H sample used in these experiments was obtained from Stohler Isotope Chemicals, and was used without further purification. The isotopic purity of the CD_3H was specified as 99% D. The photoacoustic cell was evacuated to 1×10^{-6} torr for at least 12 hours before filling with CD_3H. The photoacoustic spectra in the region of the v=5 and 6 CH stretch overtones were obtained using a CD_3H pressure of 370 torr, while the reduced transition intensity of the v=7 spectrum required a sample pressure of 1385 torr. The spectra did not change over a period of several days. They showed sharp rotational structure, which is absent in the corresponding CH_4, CDH_3 and CD_2H_2 spectra (see paper II). We conclude that this sharp structure cannot be attributed to isotopic impurities, small leaks, or outgassing of the photoacoustic cell.

3.2 Laser System

The laser system consisted of a Molectron[28] MY-34 pulsed Nd:YAG laser and a Molectron DL-18 dye laser. The second and third harmonics of the amplified Nd:YAG output were used to

pump dye solutions of Exciton oxazine 725, rhodamine 640, or coumarin 540A in methanol or ethanol. The oxazine 725 oscillator output was amplified once by a transversely pumped dye amplifier. The rhodamine 640 oscillator output was amplified by a longitudinally pumped dye amplifier. The coumarin 540A oscillator output was amplified by two consecutive transversely pumped dye amplifiers.

Individual pulse energies were monitored by measuring the light reflected off two consecutive thin quartz flat beamsplitters with a Laser Precision RKP-335 pyroelectric detector. Laser pulse energies varied as a function of wavelength within the range between 2 and 15 mJ/pulse. Dye laser FWHM pulse widths were reported by the manufacturer to be about 4×10^{-9} seconds. The pulse repetition rate was 10 Hz.

Absolute wavelength calibration was carried out using an iron-neon hollow cathode discharge lamp dispersed by a 0.5 meter Ebert-type monochrometer. The absolute accuracy of the wavelengths reported in this paper is ±0.5 Å while the accuracy of the wavelength differences important for determining rotational constants is ±0.2 Å. The bandwidth of the laser was ~0.5 cm^{-1}.

3.3 Photoacoustic Cell

The photoacoustic cell used in this study was similar to that of West, et al.[29] Its design reflected the important criteria that (1) the microphone detector was positioned as close as possible to the laser beam to maximize the amplitude

of the outward moving cylindrical pressure wave, and (2), scattered light striking the walls of the cell near the microphone was minimized to reduce the background signal produced by local heating of the cell walls.

The cell was constructed using $^{3}/_{8}$" brass Swagelock fittings. A Knowles Electronics[30] BT1759 miniature electret microphone with built-in FET preamp was attached with epoxy resin to the side of a brass $^{3}/_{8}$" Swagelock tee having an inner diameter of $^{9}/_{32}$ inches such that it was about 6 mm from the cell axis. Carefully cleaned quartz windows were mounted 6 cm away from the microphone and aligned so that both windows were exactly perpendicular to the laser beam.

The photoacoustic signal from the miniature electret microphone following the laser excitation pulse has characteristics similar to those described by Chin, et al.[31] An initial peak associated with the cylindrical pressure wave reached the microphone approximately 65 μsec after the laser pulse, followed by a complicated sequence of additional pulses and ringing due to scattered light phenomenon. The delay between the laser pulse and the initial photoacoustic signal varies linearly with the distance of the microphone to the axis of the laser beam and is determined by the speed of sound in the gas. The spectrum is generated by monitoring the amplitude of the first peak as a function of laser wavelength. This amplitude is a linear function of the energy per laser pulse.

Due to the high intensity associated with pulsed laser beams

care was taken to minimize nonlinear optical effect. The dye laser beam diameter was nominally 8 mm and an aperture allowed only the central 5 mm of the beam to enter the cell. With this configuration a linear dependence of the photoacoustic signal with pulse energy from 300 torr of neopentane at 633 nm was observed. However, when a contracting telescope was used to reduce the beam diameter to approximately 2 mm the baseline of the neopentane spectrum shifted upwards and became irreproducible. The linear dependence of signal on pulse energy obtained without the telescope and the absence of low lying electronic states in CD_3H appropriate for inducing resonance enhanced multiphoton electronic excitation or stimulated Raman processes in this system permits us to conclude that non-linear effects in the measured overtone spectra were unimportant. An additional confirmation of this conclusion is given by the similarity between our pulsed photoacoustic spectrum of CH_4 in the region near 619 nm shown in paper(II)and the long path absorption spectrum of Giver[32] and the cw photoacoustic spectrum of Stella, et al.[33]

The effect of sample pressure on the photoacoustic spectra was also investigated, Spectra of neopentane in the region near the v=0→6 CH stretching mode were taken at 102, 300, and 760 torr, the only observed effect being an increase in photoacoustic signal with increasing pressure, without any change in the shape of these spectra. Previous measurements of pressure broadening in the $2\nu_1$ band, the $3\nu_3$ band, and a line at

6190 Å all gave pressure broadening coefficients of approximately 0.087 cm^{-1}/atm.[34-36] If CD_3H has similar pressure broadening coefficients the maximum expected pressure broadening in our experiments would be less than 0.2 cm^{-1}, well within the bandwidth of our laser.

3.4 Data Handling

Electronic signals from the Knowles Electronics BT1759 electret microphone were limited to a frequency range of 300 to 10^4 Hz by an electronic filter and amplified by a factor of about 3×10^4. The peak of the first pressure wave was integrated by a differential gated integrator system with an integration window of 15 μsec. Signals from the pyroelectric joulemeter were processed in a similar manner by a second integrator system.

A microcomputer system controlled the dye laser grating scan and digitized and stored the signals from both integrators every 0.1 Å. Each CD_3H spectrum was scanned several times. The spectra were then laser-intensity-normalized and averaged. The CD_3H 0→5,6, and 7 CH stretch experimental spectra of Figures 1 to 3 respectively represent averages of 24, 36, and 120 laser shots for each 0.1 Å. Effective integration time constants and scan rates for the 0→5 and 6 spectra were adjusted so that the effective resolution was limited to ~0.5 cm^{-1} by the laser bandwidth. The 0→7 transition resolution was limited by the time constant used to ~0.7 cm^{-1}.

The CD_3H photoacoustic spectra corresponding to the $v= 0 \rightarrow 6$ and 7 stretch overtones absorptions displayed large backgrounds which were approximately wave-length independent. We feel that the signal produced by light scattering inside the cell accounts for most of the constant background since the position of the axis of the photoacoustic cell with respect to the laser beam and the cleanliness of the quartz windows greatly affected the magnitude of the background. Due to the uncertainty in the relative contributions of scattered light signals versus a real background absorption we have chosen for purposes of presentation to subtract off 90% of the apparent background in the $v= 0 \rightarrow 6$ and 7 spectra of figures 2 and 3. The $v= 0 \rightarrow 5$ experimental spectrum of figure 1a was left unchanged.

3.5 Approximate Absorption Cross Sections

Approximate absorption cross sections for the various assigned vibrational transitions are listed in table II. The values given correspond to the peak of the central Q branch. These cross sections were estimated by considering the absolute photoacoustic signals, laser energy/pulse, and sample pressures, after calibrating our spectrum of CH_4 shown in fig. 1 with the CH_4 absolute absorption cross sections of Giver[32] obtained for the some transition by a long path absorption method. The some deactivation efficiencies were assumed in CH_4 and CD_3H for the purpose of this estimation.

The absolute photoacoustic signal exhibits a strong dependence on the positions of the cell with respect to the laser beam, increasing as the microphone moves closer to that beam. When light actually strikes the cell walls, a dramatic increase in signal occurs. For each spectrum measured an attempt was made to maximize the true absorption signal and minimize the scattered light signal. The resulting absolute calibration is therefore only approximate. The relative intensities of different vibrational states and their implications are discussed in paper II[14].

A search was also made for state $|8_1\rangle$ in the region 487.7 nm to 476.7 nm, but without success. Signal to noise considerations in that spectral region indicate that state $|8_2\rangle$ or any other nearby combination bands must be at least a factor of 20 less intense than transitions to the $|7_1\rangle$ or $|6_1,2_5\rangle$ states.

4. Rotational Analysis

4.1 Assignment

Figures 1a, 2, and 3 show pulsed photoacoustic spectra of CD_3H in the region of the v=0→5,6, and 7 overtones of the totally symmetric CH stretching mode. Each spectrum displays two major vibrational bands, each containing a clearly resolved P and R branch and a sharp central Q branch characteristic of a symmetric top parallel type transition.[37a] The overlap between the two bands becomes stronger for higher overtones, making the v=7 spectrum congested enough that one Q branch is almost obscured by the other vibrational band's P branch.

The vibrational assignment is discussed in detail in Paper II,[14] however,a summary of the results is presented below to enable labeling of the spectral features. Various models for vibrational excitation have been used to describe the motion in the excited state, such as the local mode model or the normal coordinate approach. For clarity the CD_3H states are labeled with a notation describing the fundamental vibrations in accordance to ref. 26, but we are not implying the nature of the excited states by using this notation. Spectroscopic studies such as this one combined with theoretical models[38,39] should significantly advance our understanding of these states.

The features as assigned in Paper II centered at approx-

imately 724.5 nm, 616.1 nm, and 541.2 nm correspond to the $v = 0 \rightarrow 5, 6$, and 7 transitions respectively of the totally symmetric ν_1 CH stretch mode, henceforth designated as $|5_1\rangle$, $|6_1\rangle$, and $|7_1\rangle$. The features centered near 731.5 nm, 618.8 nm, and 539.4 nm correspond to transitions from the ground vibrational state to an excited combination band consisting of two quanta of the degenerate e CH bending ν_5 mode and 4,5, or 6 quanta respectively of the totally symmetric ν_1 CH stretch mode. We will designate these states by $|4_1, 2_5\rangle$ $|5_1, 2_5\rangle$, and $|6_1, 2_5\rangle$. An additional feature near 544.7 nm is tentatively assigned as a combination band involving 6 quanta in the ν_1 mode, one quantum in the ν_5 mode and one quantum in the ν_6 degenerate CD_3 bending mode, denoted by $|6_1, 1_5, 1_6\rangle$.

The rotational energy levels of an oblate symmetric top molecule in a specific vibrational level are given by

$$F(J,K) = BJ(J+1) + (C-B)K^2 - D_J J^2(J+1)^2 - D_{JK}(J+1)K^2 - D_K K^4 \qquad (1)$$

where B, C, D_J, D_{JK}, and D_K are the usual rotational constants.[37b] For a parallel band $\Delta K = 0$ and $\Delta J = 0, \pm 1$ except that $\Delta J = 0$ is forbidden if $K=0$. Using these selection rules the wave numbers of the P, Q, and R branches are given respectively by

$$P(J,K) = [\nu_0 - (B'+B'')J + (B'-B''-D_J'+D_J'')J^2 + 2(D_J'+D_J'')J^3 - (D_J'-D_J'')J^4] + [(C'-C'') - (B'-B'') - D_{JK}'J(J-1) + D_{JK}''J(J+1)]K^2 - (D_K'-D_K'')K^4 \quad (2a)$$

$$Q(J,K) = (B'-B'')J(J+1) + (C'-C''-B'+B'')K^2 - (D_J'-D_J'')J^2(J+1)^2 - (D_{JK}'-D_{JK''})J(J+1)K^2 - (D_K'-D_K'')K^4 \quad (2b)$$

$$R(J,K) = [\nu_0 + 2B' - 4D_J' + (3B'-B''-12D_J')J + (B'-B''-13D_J' + D_J'')J^2 - (6D_J'-2D_J'')J^3 - (D_J'-D_J'')J^4] + [(C'-C'') - (B'-B'') - D_{JK}'(J+1)(J+2) + D_{JK}''J(J+1)]K^2 - (D_K'-D_K'')K^4 \quad (2c)$$

where the prime and double prime refer to excited and ground vibrational states respectively.

A computer program utilizing Eqs. (2a) through (2c) and the appropriate Boltzmann factors, degeneracies, matrix elements, and spin statistics[37c] was written to generate symmetric top rotational spectra. The excellent signal to noise ratio in the spectrum of fig. 1a suggested using a least squares routine to adjust parameters in the spectral generation program to reproduce the experimentally observed spectrum. This was attempted using the CHD_3 ground state parameters of Jennings

and Blass[19] and a FWHM linewidth of 0.5 cm^{-1}. Excited state parameters were adjusted from the v=4 data of Bovey[15] until an approximate fit was observed. The least squares routine was then allowed to make final adjustments on the excited state parameters.

Values for B' and ν_0 for the spectrum of figure 1a converged easily. These values along with constants generated by the combination sum approach of section 4.3 are given in Table VIII. The results of the two methods agree within the corresponding error limits. Other excited state parameters did not satisfactorily converge because experimental resolution prevented observation of individual K components, the presence of noise, and the possibility of excited state perturbations. Figure 1b shows a typical spectrum generated by the least squares routine corresponding to the region near the $|5_1$ and $|4_1,2_5\rangle$ states of CD_3H. It should be noted that the rates of the intensities of these two bands was one of the adjustable parameters in this fitting routine.

Similar least squares fits were attempted for the spectra in figures 2 and 3. The increased noise and large constant background (see section 3.4) limited the accuracy of these fits and a combination sum approach yielded more reliable results (see section 4.3). The synthesized spectra were used, however, to assign the individual J transitions in the congested regions of overlapping rotational features.

The resolution of the laser system (0.5 cm^{-1}) prevented

the observation of single K components of specific J rotational transitions, although shading of individual J lines is observed at high values of J. Comparison of synthesized spectra at our experimental resolution with actual positions of the K=0 lines indicated that the maximum of each J transition occurred at the position of the K=0 line. Tables 3-7 contain the position of the peaks of the various J transitions, as determined from the digitized and averaged data. These positions correspond roughly to the positions of the K=0 transitions.

4.2 Ground State Combination Differences

Ground vibrational state rotational constants can be accurately determined even in the presence of excited state perturbations using the technique of ground state combination differences.[25,40] The combination difference $\Delta F''(J,K) = R(J-1) - P(J+1,K)$ involves transitions having the same upper state. From equation (1)

$$\begin{aligned}\Delta F''(J,K) &= F(J+1,K) - F(J-1,K) \\ &= (4B''-6D_J''-4D_{JK}''K^2)(J+\tfrac{1}{2}) - 8D_J''(J+\tfrac{1}{2})^3 \end{aligned} \tag{5}$$

our photoacoustic spectra yield only approximate positions of the K=0 lines and D_J'' is much smaller than B". Therefore a plot of $[R(J-1) - P(J+1)]/(J+\tfrac{1}{2})$ vs. $(J+\tfrac{1}{2})^2$ should yield a line with slope $8D_J''$ and intercept 4B". B" was determined from spectra of the $|5_1\rangle$, $|6_1\rangle$, $|4_1,2_5\rangle$, $|5_1,2_5\rangle$, and $|6_1,2_5\rangle$ states of CD_3H. The average value of B" obtained in this way was

$3.29 \pm 0.03\ cm^{-1}$. The relatively large standard deviation is a result of the low resolution which prevents observation of individual K lines. Our value of B" is consistent with the accurate value of $3.279053\ cm^{-1}$ of Jennings and Blass.[19]

4.3 Excited State Combination Sums

The rotational constants of the upper vibrational state can be obtained by the combination sum R(J-1,K) + P(J,K).[15,37d] From equation (2) and (4)

$$R(J-1,K) + P(J,K) = 2\nu_0 + 2[(C'-B') - (C''-B'')]K^2 - 2(D_K'-D_K'')K^4 + 2[(B'-B'') - (D_{JK}'-D_{JK}'')K^2] - 2(D_J'-D_J'')J^2(J^2+1) \quad (6)$$

for K=0 eq . (5) reduces to

$$R(J-1,0) + P(J,0) = 2\nu_0 + 2(B'-B'')J^2 - 2(D_J'-D_J'')J^2(J+1) \quad (7)$$

Figures 4-6 show plots of the combination sums R(J-1,0) + P(J,0) vs. J^2 for the states $|5_1\rangle$, $|6_1\rangle$, $|4_1\rangle$, $|\bar{5}_1,2_5\rangle$, and $|6_1,2_5\rangle$. The lack of curvature indicates that the coefficient $2(D_J'-D_J'')$ is much smaller than 2(B'-B"), which agrees with values obtained for $|3_1\rangle$ and $|4_1\rangle$ by Bovey.[15] Least squares fits of our data were used to generate the values of ν_0 and B' shown in table 8. The value of B" used was the accurate value $3.279053\ cm^{-1}$ of Jennings and Blass.[19] Error limits were determined from standard deviation of the slope and intercept.

No strong perturbations are apparent in the spectra

shown in figures 1 or 2, but this is almost certainly due to the low resolution and congestion in our spectra. Small perturbations in the $|3_1\rangle$ and $|4_1\rangle$ states of CD_3H were observed by Bovey.[15] The increased density of vibrational states at the energies of these spectra makes the presence of perturbations likely.

A rotational analysis of the $|7_1\rangle$ state and the feature near 544.7 nm was not attempted. The low signal to noise and congestion found in the spectrum of figure 3 made this impossible. An approximate value of B' for the $|6_1,2_5\rangle$ state is listed in table VIII, but is subject to some question. Intensity and position perturbations for the P(9), P(10), R(7), R(10), R(11), and R(12) transitions to the $|6_1,2_5\rangle$ state, The extreme congestion between the $|7_1\rangle$ and $|6_1,2_5\rangle$ states and the low signal to noise ratio makes the assignment of the individual J transitions in $|6_1,2_5\rangle$ difficult. The slope of the combination sum line shown in figure 10 definitely is positive, however, indicating that B' for $|6_1,2_5\rangle$ is larger than B".

4.4 Rotational Temperature

The individual J transition intensities in figure 2a and 3 are consistent with those generated by the computer program described in section 4.1 if Boltzmann statistics at room temperature are used. The fact that the gas temperature remains at room temperature during the experiment is consistent with the small absorption coefficient (see section 5.2) of the transitions observed here.

5. Discussion

CD_3H displays a CH stretch type oscillation whose frequency is substantially different from any of its other fundamental oscillation frequencies. The small number of vibrational modes, small interaction between modes, and small moments of inertia have allowed a detailed analysis of the rotational features of several high vibrational states. Unlike benzene where even the v=2 and 3 levels of the CH stretch mode are too broad and congested for rotational analysis,[1] CHD_3 possesses a full range of vibrational overtones of the CH stretch mode plus nearby combination bands which exhibit sharp rotational structure. The excited state rotational constant B' is easy to obtain and is an extremely sensitive indicator of geometry changes in the excited state caused by interaction of both observed and unobserved vibrational states with the state being studied. Therefore the rotational analysis provides a sensitive probe of the nature of highly excited vibrational states and the dynamics of intramolecular vibrational energy redistribution following excitation of these states.

5.1 Lifetimes

The low density of vibrational states present in CD_3H and the large difference in frequency between the CH stretch mode and other modes of the molecule leads to the prediction that energy deposited into the CH stretch mode by single photon

absorption is likely to remain localized for a relatively long period of time. This indeed seems to be the case. The R(2), R(3) and R(4) rotational lines of the $|5_1\rangle$ state have FWHM linewidths of 1.0 cm^{-1}. The same set of rotational lines for state $|6_1\rangle$ have FWHM linewidths of 1.3 cm^{-1}. These linewidths correspond to minimum population decay times of 5×10^{-12} and 4×10^{-12} seconds respectively.[41-43] These lifetimes represent only minimum lifetime because (1) we are approaching the limit of our laser resolution and (2) we are not observing a single rotational line, but rather a small group of unresolved K lines.

Stella, et al.[33] observed an unassigned rotational line in CH_4 at 6457.19 Å in the vicinity of the v=6 CH stretch overtone with a linewidth less than or equal to their experimental resolution of 0.03 Å, corresponding to a minimum population lifetime of $\sim70\times10^{-12}$ sec. If the lifetime of CH stretch-type mode in CD_3H is greater than or equal to that of similar modes in CH_4, the energy deposited into a mode of predominately CH stretch character in CD_3H by single photon absorption may remain localized in such modes for time scales comparable to the average time between collisions for pressures $\geq$1000 torr. Therefore, CH stretch type modes in CD_3H or other similar small molecules may be good candidates for studying the effects of selective high vibrational excitation on bimolecular reaction rates. Of course, the state specific reactive process must in addition be able to compete with deactivation processes

for such studies to be possible.

These studies also suggest higher resolution experiments to investigate the linewidth of the R(0) line in states $|4_1\rangle$, $|5_1\rangle$, $|6_1\rangle$, and $|7_1\rangle$ to determine the dependence of the linewidth of a single isolated K line on vibrational state.

5.2 Discussion of Rotational Constants

Three attempts to explain the CD_3H rotational constants obtained in this work are presented in the following three subsections. Only the third is able to qualitatively explain the observed data.

In trying to explain the CD_3H rotational constants, we considered in succession interpretations based on a) non-interacting vibrational states, b) two interacting vibrational states, and c) three or more interacting vibrational states. Although only the last was able to explain the data, information derived from the preceding two approaches was used in it. We will therefore describe all three.

a) Non-interacting state model.

Figure 7 shows the know rotational constants from this work and previous work for vibrational states of CD_3H of the form $|v_1\rangle$ and $|v_1, 2_5\rangle$. The rotational constant B' corresponds to the moment of inertia along an axis perpendicular to the C_{3v} symmetry axis. For transitions to states $|v_1\rangle$ with v_1 between 0 and 4, B'_v is a linear function of v_1 in agreement with the

standard expression [37a]

$$B_{[v_i]} = B_e - \sum_i \alpha_i^B \left(v_i + \frac{d_i}{2}\right). \tag{8}$$

$B_{[v_i]}$ is the rotational constant for the state designated by the set of vibrational quantum numbers $[v_i]$, B_e is the equilibrium rotational constant, the sum is over all vibrational modes, d_i is the degeneracy of the ith vibrational mode, and the α_i^B are small constants. The experimental value of α_1^B is 0.0160 cm^{-1}.[15] Non-interacting states of the form $|v_1\rangle$ should fall on this line.

B_{5_1} exhibits a slight positive deviation from this line and B_{6_1} is shifted substantially above the $\alpha_i^B = 0.160$ cm^{-1} line. One explanation for this behavior is the presence of additional terms in equation (8) of the form

$$-\sum_{i \geq j} \beta_{ij}^B \left(v_i + \frac{d_i}{2}\right)\left(v_j + \frac{d_i}{2}\right) \tag{9}$$

As the molecule approaches dissociation, however, vibrational coordinates lengthen rapidly and the $B_{[v_1]}$ curve should bend downward implying that β_{ij}^B should be positive. The points for B_{5_1} and B_{6_1} are above the straight line, implying that $\beta_{ij}^B < 0$. In addition, the size of the deviation for B_{6_1} cannot be accounted for by a small higher order correction. We conclude that the non-interacting states model does not explain the observed rotational constants.

b) Two interacting states.

A more plausible cause is the Fermi resonance between different zero order vibrational states. Figures 1 and 2 each show two states of the form $|v_1\rangle$ and $|(v-1)_1, 2_5\rangle$. As these states get closer together (figure 2) their intensities become comparable, a direct result of Fermi resonance between the two states. (The details of this Fermi resonance are discussed in paper II.) For two interacting vibrational levels with zero order rotational constants B_n^o and B_i^o which interact with Fermi mixing coefficients a and b the new rotational constants are given by[37e,44]

$$B_n = a^2 B_n^o + b^2 B_i^o$$

$$B_i = b^2 B_n^o + a^2 B_i^o \qquad (10)$$

where $a^2 + b^2 = 1$ (11)

The two new constants B_n and B_i are therefore intermediate between the zero order constants B_n^o and B_i^o. The size of the shift from the zero order rotational constants to the new rotational constants reflects the amount of interaction between the vibrational levels.

In CD_3H the CH bond is perpendicular to the axis corresponding to the B' constant. This explains why the anharmonicity of the CH stretch mode is so effective in increasing the moment of inertia I_B and therefore in decreasing B'. On the other hand, an increase in the CH bending mode (v_5) vibration quantum num-

ber decreases the average distance between the H atom and the B axis, causing B' to increase. These qualitative considerations suggest that mixing in CH bend character from combination bands of the form $|(v-1)_1, 2_5\rangle$ with pure CH stretch overtones of the form $|v_1\rangle$ effectively increases B'_{v_1} from its zero order α_i^B line, in agreement with our observation. The decrease in rotational constant between the $|4_1, 2_5\rangle$ and $|5_1, 2_5\rangle$ states also agrees qualitatively with the 2-level Fermi mixing model, where the $|5_1, 2_5\rangle$ state interacts strongly with the $|6_1\rangle$ one.

This simple two-level Fermi mixing model, however, does not quantitatively account for the rotational constants of the combination band states of the form $|v_1, 2_5\rangle$. Allen and Plyler[24] have partially resolved the rotational structure of the A_1 component of the state $|2_5\rangle$. They report a value for B'-B" of about 0.01 cm^{-1}. Using the Jennings and Blass[19] value for B" we obtain $B'_{2_5} = 3.289\ cm^{-1}$ for that state. This value agrees closely with the result $B'_{2_5} = 3.28831\ cm^{-1}$ predicted from Dupre-Maquaire, et al's[23] measurement of $\alpha_5^B = -4.627 \times 10^{-3}\ cm^{-1}$ and Jennings and Blass's[19] value of $B" = 3.279053\ cm^{-1}$. The rotational constant $B_{v_1, 2_5}$, in going from $B_{0_1, 2_5}$ to $B_{4_1, 2_5}$ or $B_{5_1, 2_5}$ should only change by the α_i^B term in equation (8). The dashed line in figure 8 indicates this behavior which parallels the α_i^B line of the states $|v_1\rangle$.

The rotational constants $B_{4_1, 2_5}$, $B_{5_1, 2_5}$, and B_6 fall above this dashed line. If B_{2_5} is correct and only a two-level

Fermi interaction occurred, all values for B_{v_1} and $B_{v_1,2_5}$ should have fallen on the dashed line or between it and the solid line, at least until higher order corrections like Eq. (9) become important.

It immediately follows from Eqs. (10) and (11) that

$$B_n + B_i = B_n^o + B_i^o \tag{12}$$

Eq. (12) is the so-called "sum rule". Using this rule, our values for B_n and B_i, and the α_i^B line, values for $B_{4_1,2_5}^o$ and $B_{5_1,2_5}^o$, can be obtained. These zero order values, $B_{4_1,2_5}^o$ and $B_{5_1,2_5}^o$, and Allen and Phyler's value for B_{2_5} do not fit an equation of the form of Eq. (8), further illustrating the inadequacy of the two level Fermi resonance model for rotational constants to explain the data.

c) Three or more interacting states.

To obtain states with rotational constants above the dashed line of figure 7 it is necessary to mix in states with high rotational constant character. These additional states, which we have not observed, must consist of a few states from the bath of background states. Figure 8 depicts three classes of zero order states which we feel must interact to produce the states observed spectroscopically. The optical states are those states which couple optically to the ground state. This coupling may be strong or weak, but it provides the optical transition probability necessary for optical spectroscopy. The $|v_1\rangle$ states fall into this category. The strong

coupling states are those which would not be seen optically unless they couple strongly to the optical states, borrowing enough optically allowed character to actually show up directly in optical spectra. The $|v_1, 2_5\rangle$ states fall into this category. The weak coupling states are those background states which do not produce spectroscopic features of their own. A small number of these states, however, may couple weakly to both the optical and the strong coupling states. This coupling produces small changes in the spectroscopic parameters of the observed states. Each weak coupling state which couples results in only small changes in these parameters, but the presence of several such states could amplify this effect to produce substantial deviations from the expected zero order values.

The rotational constant B' of CD_3H is highly sensitive to the contributions of the weak coupling states. The two level Fermi resonance model involving states of the form $|v_1\rangle$ and $|(v_1-1)_1, 2_5\rangle$ does not adequately account for the observed rotational constants. Added contributions of weak coupling states must be invoked to explain qualitatively the observed rotational features.

The information in Table 1 is useful in indicating which types of states from the weak coupling states category are likely candidates for introducing higher rotational constant character into the observed spectra. In CD_3H, as energy is

added into either the ν_1, ν_2 or ν_4 mode, the corresponding B rotational constants decrease. In contrast, the one for ν_5 increases with increasing excitation energy ($\alpha_5^B > 0$). The behavior for ν_3 and ν_6 is not known. As a result, vibrational states in the region of our spectra which contain substantial amounts of ν_5 character are likely candidates for couplings which result in an increase of B.

The rotational constant for state $|6_1, 2_5\rangle$ has large error limits but seems to also fall substantially above the dashed line in figure 7. This again implies a need for coupling to states of higher rotational constants, such as several weak coupling states or possibly the state appearing at 544.7 nm.

The rotational features of the spectra presented in this work have been explained qualitatively by introducing coupling between 3 or more zero order vibrational states. An interesting question is: what is the expected behavior of the rotational constants for the higher energy vibrational overtones not yet observed? For small excitation energies the rovibrational states of small molecules can be accurately described by simple quantum mechanical models. Each vibrational level has a characteristic rotational constant which is inversely proportional to the moment of inertia of that particular state. At high energies, however, the increased density of states, increased coupling between states, and

finite linewidths of individual rovibrational levels produces a behavior which although accurately described by quantum mechanics, is hard to elicit theoretically bacause the corresponding Schrödinger equation is difficult to solve. Under these conditions, however, it is expected that the internal motion of the molecule will approach a classical mechanical behavior. Concurrently, the molecule's motion is no longer limited to specific vibrational modes because of the rapid scrambling of energy between them. In such a high energy classical and statistical limit, the energy and angular momentum are the only easily discernible good constants of the motion. The classical analog of the quantum mechanical rotational constant can be defined in this limit as a statistical rotational constant[45] which is proportional to a time average of the reciprocal of the moment of inertia, averaged over the molecular motions.

In our CD_3H spectra the rotational constants for different vibrational levels are significantly different from each other, reflecting the dominant contributions of various zero-order states. This behavior is characteristic of the quantum nature of the system. As the classical statistical limit is approached at higher energies, however, the increased scrambling of energy could cause the spectroscopic rotational constants to converge to a statistical rotational constant which becomes independent of the way in which the energy is initially deposited in the molecule and is a function only

of the energy itself.

One approach for calculating the statistical rotational constant is to use a classical mechanical model for the rovibrational motions of the molecular motions of the molecular nuclei, and calculate $\langle B_{class\ E} \rangle$ by calculating the average of the quantity

$$\frac{\hbar}{4\pi c}\left(\sum_i m_i q_i^2(t)\right)^{-1}$$

over a trajectory corresponding to total internal energy E, where t is time, m_i is the mass of the ith atom, and q_i its distance from the moment of inertia axis being considered. In the statistical limit, this average should become independent of the trajectory's initial conditions.

Given a potential energy function V describing the interaction between the atoms, the implementation of a classical trajectory calculation for a molecule of the complexity of CD_3H is feasible and relatively straightforward.[46] Numerical studies of this type may be appropriate at the present time. Comparison of calculated statistical rotational constants and observed spectroscopic rotational constants for vibrational overtones at higher energies may provide a sensitive method for detecting the onset of statistical behavior in CD_3H or other molecules.

6. Conclusions

The exact description of highly excited vibrational states in polyatomic molecules has been a subject of considerable interest. By carefully selecting CD_3H, a small molecule with high symmetry, symmetric top rotational structure, small moments of inertia, and low density of vibrational states we have been able to easily obtain pulsed laser photoacoustic spectra of several high vibrational overtones and combination bands which exhibit sharp rotational structure. The analysis of this rotational structure leads to the following conclusions.

1) For CD_3H (and presumably other small molecules with resolvable rotational structure) simple rotational analyses of high vibrational overtone spectra provide sensitive methods for obtaining information about the types of zero order vibrational modes which contribute to the actual states excited.
2) The observed high vibrational overtones of the totally symmetric CH stretch in CD_3H contain significant contributions from other types of modes, including degenerate CH bend motions.
3) It is necessary to invoke coupling with background vibrational overtones and combination bands in CD_3H.

4) A simple classical trajectory model for a statistical rotational constant was proposed. Comparisons between calculated statistical rotational constants and spectroscopic rotational constants obtained from future studies of higher vibrational overtones may provide a sensitive method for detecting the approach to statistical behavior in CD_3H or other molecules.

The wealth of information about high vibrational states in CD_3H obtained form this low resolution study suggests that the application of higher resolution techniques to CD_3H and other similar small molecules may provide a detailed quantitative description of the exact nature of their high vibrational states.

Acknowledgements

We gratefully thank Professor K. Janda and Professor R. Marcus for useful discussion, Dr. J. J. Barrett for help with the design of the photoacoustic cell, and Professor J. L. Beauchamp for supplying the CD_3H sample.

TABLE I. CD_3H Spectroscopic Parameters from Previous Studies.[a]

Parameter	Ground State Parameters Value (cm^{-1})
B''[b]	3.279053(61)
C''[c]	2.6297(3)
D_J''[b]	$5.010(19)\times10^{-5}$
D_{JK}''[b]	$-4.030(69)\times10^{-5}$
D_K''[c]	$1.8(3)\times10^{-5}$
H_J''[b,d]	$1.020(59)\times10^{-8}$
H_{JK}''[b,d]	$-3.80(15)\times10^{-8}$
H_{KJ}''[b,d]	$5.15(40)\times10^{-8}$

State[e]	Excited State Parameters ν	$B'-B''$	$C'-C''$	$D_J'-D_J''$	$D_{JK}'-D_{JK}''$	$D_K'-D_K''$
$\|1_3\rangle$[c]	1002.					
$\|1_6\rangle$[c]	1035.					
$\|1_4,-1_6\rangle$[f]	1237.					
$\|1_5\rangle$[g]	1292.4992(8)	$4.641(11)\times10^{-3}$	$2.0628(12)\times10^{-2}$	$-1.29(3)\times10^{-6}$	$-2.52(8)\times10^{-6}$	$3.50(6)\times10^{-6}$
$\|2_3\rangle$[c]	1988.87(3)					

TABLE I. (Continued)

	Excited State Parameters					
State[e]	$\bar{\nu}$	$B'-B''$	$C'-C''$	$D_J'-D_J''$	$D_{JK}'-D_{JK}''$	$D_K'-D_K''$
$\|1_2\rangle$[b]	2142.5776	$-1.7549(19)\times10^{-2}$	$-2.22(3)\times10^{-2}$	$9.03(43)\times10^{-7}$	$7.576(54)\times10^{-6}$	$-1.0045(64)\times10^{-5}$
$\|1_4\rangle$[c]	2250.88(10)	-0.059(5)	-0.023(5)	$2.3(2)\times10^{-5}$	$7.1(5)\times10^{-5}$	$-11.0(3)\times10^{-5}$
$\|1_5,1_6\rangle$[f]	2332.					
$\|2_5\rangle$ (A)[h]	2564.6	0.01				
$\|2_5\rangle$ (E)[h]	2592.64	0.007	0.0449	$-5.0(8)\times10^{-5}$	$-3.\times10^{-5}$	
$\|1_1\rangle$[i]	2992.33	-0.0179				
$\|1_3,2_6\rangle$[f]	3051.					
$\|1_2,1_6\rangle$[f]	3181.					
$\|1_4,1_6\rangle$[f]	3283.					
$\|1_3,1_5,1_6\rangle$[f]	3315.					
	3327.					
$\|1_2,1_5\rangle$[f]	3456.					
$\|1_1,1_2\rangle$[j]	5135.04 (or 5134.84)					
$\|2_1\rangle$[k]	5865.02	-.0381	-0.0181			
$\|3_1\rangle$[l]	8623.31	-.0499		$-1.\times10^{-5}$		
$\|4_1\rangle$[l]	11266.94	-.0641	-0.0350	$6.\times10^{-6}$	$5.\times10^{-6}$	

TABLE I. (Continued)

[a]Numbers in parentheses are the estimated errors in the last digit of the parameter values. Some correspond to 95% confidence limits and others are standard deviations. Please see the references indicated for details.

[b]Ref. 19.

[c]Ref. 20.

[d]These constants correspond to small higher order corrections to the energy expression of eq. 1. They are defined in ref. 21.

[e]The notation is described in the text, section 4.1.

[f]Ref. 22.

[g]Ref. 23.

[h]Ref. 24.

[i]Ref. 17.

[j]Ref. 25.

[k]Ref. 18.

[l]Ref. 15.

TABLE II. Estimated Absorption Cross Sections for CD_3H[a]

Vibrational Band[b]	Photon Energy (cm^{-1})[c]	Absorption Cross Section (cm^2)
$\|5_1\rangle$	13799	$(3\pm1)\times10^{-24}$
$\|6_1\rangle$	16228	$(3\pm1)\times10^{-24}$
$\|7_1\rangle$	18473	$(7\pm3)\times10^{-27}$
$\|4_1,2_5\rangle$	13668	$(1\pm0.5)\times10^{-24}$
$\|5_1,2_5\rangle$	16157	$(3\pm1)\times10^{-25}$
$\|6_1,2_5\rangle$	18534	$(1\pm0.5)\times10^{-26}$
$\|6_1,1_5,1_6\rangle$	18353	$(3\pm1)\times10^{-27}$

[a]See section 5.2 for a description of the estimation method.

[b]Assignment is from ref. 14. The notation is discussed in the text, section 4.1.

[c]The photon energy of the cross section measurement is expressed in vacuum wavenumbers, and corresponds to the peak of the Q-branch of the specified vibrational band.

[d]Tentative assignment.

TABLE III. Observed Wavenumbers ($\bar{\nu}_{vac}$) for the $|4_1, 2_5\rangle$ State.[a]

J	P(J) (cm^{-1})	R(J) (cm^{-1})
0	...	...
1	13661.8[b]	13680.3
2	13665.5	13687.6
3	13648.2	13693.6
4	13641.9	13699.7
5	13635.7	13706.0
6	13628.6	13713.5[b]
7	13621.8[b]	13719.1
8	13614.8	13725.1
9	13608.2	13731.1
10	13601.0	13737.3
11	13593.8	13742.9
12	13587.0	13748.7
13	13580.1	13755.0
14	13573.3	13759.5[b]
15	...	13766.6[b]

[a]The reported values are accurate to ±0.6 cm^{-1}, and the differences are accurate to ±0.4 cm^{-1}.

[b]These points were not included in the combination sum analysis bacause of incomplete data or uncertainty in the position of the band.

TABLE IV. Observed Wavenumbers ($\bar{\nu}_{vac}$) for the $|S_1\rangle$ State.[a]

J	P(J) (cm^{-1})	R(J) (cm^{-1})
0	...	13807.4[b]
1	...	13813.9
2	13787.6	13819.9
3	13780.6	13825.8
4	13773.6	12831.7
5	13766.6	13837.2
6	13759.5	13842.9
7	13752.3	13848.1
8	13744.8	13853.2
9	13737.3	13858.2
10	13729.8	13863.0
11	13721.5	13867.8
12	13713.5	13872.5
13	13705.3	13876.5
14	13696.7	13881.0
15	13688.1	13885.0
16	13679.4	13889.2[b]
17	...	13892.8[b]
18	...	13896.5[b]
19	13651.4[b]	...

[a]The reported values are accurate to ± 0.6 cm^{-1}, and the differences are accurate to ± 0.4 cm^{-1}.

[b]These points were not included in the combination sum analysis because of incomplete data or uncertainty in the position of the band.

TABLE V. Observed Wavenumbers ($\bar{\nu}_{vac}$) for the $|5_1, 2_5\rangle$ State.[a]

J	P(J) (cm^{-1})	R(J) (cm^{-1})
0	...	...
1	16150.9[b]	16169.4
2	16143.0	16174.9[b]
3	16136.3[b]	16182.0
4	16129.5	16189.0
5	16122.7	16194.5
6	16116.0	16200.8
7	16109.0	16206.9
8	16102.2	16212.9
9	16094.9	16217.4
10	16088.2	...
11	16079.9[b]	...
12	16072.7[b]	16234.5[b]
13	16067.8[b]	16239.3[b]

[a]The reported values are accurate to ±0.8 cm^{-1}, and the differences are accurate to ±0.5 cm^{-1}.

[b]These points were not included in the combination sum analysis of incomplete data or uncertainty in the position of the band.

TABLE VI. Observed Wavenumbers ($\bar{\nu}_{vac}$) for the $|6_1\rangle$ State.[a]

J	P(J) (cm^{-1})	R(J) (cm^{-1})
0	...	16236.6[b]
1	...	16243.0[b]
2	16216.3[b]	16249.3
3	16209.8	16255.4
4	16202.9	16261.7
5	16195.9	16267.8
6	16189.0	16273.6
7	16182.0	16279.2
8	16174.9	16284.8
9	16167.8	16290.3
10	16160.0	16295.4
11	16152.7	16301.0
12	16145.1	16306.3
13	16137.0	16311.6
14	16129.5	16316.7
15	16121.7	16321.2
16	16113.9	16327.8
17	16104.0	...
18	16099.4[b]	...
19	16092.1[b]	...
20	16084.6[b]	...

[a]The reported values are accurate to ±0.08 cm^{-1}, and the differences are accurate to ±0.05 cm^{-1}.

[b]These points were not included in the combination sum analysis because of incomplete data or uncertainty in the position of the band.

TABLE VII. Observed Wavenumbers ($\bar{\nu}_{vac}$) for the $|6_1, 2_5\rangle$ State.[a]

J	P(J) (cm^{-1})	R(J) (cm^{-1})
0	...	...
1	18524.9[b]	18545.1
2	18518.8	18552.3
3	18512.0	18558.8
4	18505.5	18566.0
5	18499.4	18572.5
6	18492.9	18579.1
7	18486.8	18586.3[c]
8	18481.0[b]	18592.1[b]
9	18473.5[c]	18598.3[c]
10	18468.7[c]	18606.6[c]
11	...	18611.1[c]
12	...	18618.0[c]

[a]The reported values are accurate to ±1 cm^{-1}, and the differences are accurate to ±0.7 cm^{-1}.

[b]These points were not used in the combination sum analysis because of incomplete data or uncertainty in the position of the band.

[c]These points were not used in the combination sum analysis because they appeared to be strongly perturbed.

TABLE VIII. CD_3H Spectroscopic Constants from Present Study[a]

Assignment[b]	$\bar{\nu}_0$ (cm^{-1})[c,d]	B' (cm^{-1})[e,d]
$\|4_1, 2_5\rangle$	13668.1(1)	3.258(1)
	13667.8(9)[f]	3.26(2)[f]
$\|5_1\rangle$	13801.1(1)	3.2060(9)
	13801.0(2)[f]	3.203(3)[f]
$\|5_1, 2_5\rangle$	16156.4(2)	3.247(3)
$\|6_1\rangle$	16230.07(9)	3.202(6)
$\|6_1, 1_5, 1_6\rangle$[g]	18353.0(5)[h]	...
$\|7_1\rangle$	18473.0(5)[h]	...
$\|6_1, 2_5\rangle$	18531.9(2)	3.301(7)

[a]Obtained by combination sum analysis unless otherwise stated. (See footnote f.)

[b]Assignment is from ref. 14. The notation is discussed in the text, section 4.1.

[c]Vibrational frequencies in vacuum wavenumbers.

[d]Values in parenthesis are the uncertainties in the last digit, equal to 2 standard deviation units.

[e]B' is the rotational constant in vacuum wavenumbers.

[f]Values obtained from least squares fitting of the experimental spectrum.

[g]Assignment is tentative.

[h]Insufficient structure was available for a rotational analysis to be performed, The value given corresponds to the position of the peak of the central Q-branch.

REFERENCES

1. K. V. Reddy, D. F. Heller, and M. J. Berry, J. Chem. Phys. 76, 2814 (1982).
2. G. A. West, R. P. Mariella, Jr., J. A. Pete, W. B. Hammond, and D. F. Heller, J. Chem. Phys. 75, 2006 (1981).
3. B. R. Henry and W. R. A. Greenlay, J. Chem. Phys. 72, 5516 (1980).
4. H. L. Fang and R. L. Swofford, J. Chem. Phys. 73, 2607 (1980).
5. M. S. Burberry and A. C. Albrecht, J. Chem. Phys. 71, 4631 (1979).
6. R. G. Bray and M. J. Berry. J. Chem Phys. 71, 4909 (1979).
7. (a) D. F. Heller and S. Mukamel, in Picosecond Phenomena, edit. by C. V. Shank, E. P. Ippeu and S. L. Shapiro, (Springer, New York, 1978), p. 51. (b) J. Chem. Phys. 70, 463 (1979).
8. K. V. Reddy and M. J. Berry, Faraday Disc. Chem. Soc. 67, 188 (1979).
9. W. R. A. Greenlay and B. R. Henry, J. Chem. Phys. 69, 82 (1978).
10. B. R. Henry, Accounts of Chem. Res. 19, 207 (1977).
11. J. W. Perry and A. H. Zewail, J. Chem. Phys. 70, 582, (1979).
12. J. W. Perry and A. H. Zewail, Chem. Phys. Lett. 65, 31 (1979).
13. J. W. Perry and A. H. Zewail, J. Phys. Chem. 85, 934 (1981).

14. J. W. Perry, D. J. Moll, A. H. Zewail, and A. Kuppermann, forthcoming.

15. L. F. H. Bovey, J. Chem. Phys. 21, 830 (1953).

16. W. S. Benedict, K. Morikawa, R. B. Barnes, and H. S. Taylor, J. Chem. Phys. 5, 1 (1937).

17. D. G. Rea and H. W. Thompson, Trans. Faraday Soc. 52, 1304 (1956).

18. T. A. Wiggins, E. R. Shull, J. M. Bennett, and D. H. Rank, J. Chem. Phys. 21, 1940 (195).

19. D. E. Jennings and W. E. Blass, J. Molecular Spect. 55, 445 (1975).

20. H. W. Kattenberg and S. Brodersen, J. Mol. Spect. 59, 126 (1976).

21. T. L. Barnett and T. H. Edwards, J. Molecular Spect. 20, 347 (1966).

22. J. K. Wilmshurst and H. J. Bernstein, Can. J. Chem. 35, 226 (1957).

23. J. Dupre-Maquaire, J. Dupre, and G. Tarrago, J. Mol. Spect. 90, 63 (1981).

24. H. C. Allen, Jr. E. K. Plyer, J. Res. Nat Bur. Stand. Sect. A, 63A, 145 (1959).

25. W. F. Blass and T. H. Edwards, J. Molecular Spectrosc. 24, 16 (1967).

26. D. L. Gray and A. G. Robiette, Molecular Physics 37, 1901 (1979).

27. D. J. Moll and A. Kuppermann, forthcoming.

28. Molectron Corporation, 177 North Wolfe Rd., Sunnyvale, California 94086.

29. G. A. West, D. R. Siebert, and J. J. Barrett, J. Appl. Phys. 51, 2823 (1980).

30. Knowles Electronics, Inc., 3100 N. Mannheim Rd., Franklin Park, Illinois 60131.

31. S. L. Chin, D. K. Evans, R. D. McAlpine, and W. N. Selander, Appl. Optics 2, 65 (1982).

32. L. P. Giver, J. Quant. Spectrosc. Radiat. Transfer, 19, 311 (1978).

33. G. Stella, J. Gelfand, and W. H. Smith, Chem. Phys. Lett. 39. 146 (1970).

34. J. Gelfand and W. Hermina, Chem. Phys. Lett. 65, 201 (1979).

35. L. Darton and J. S. Margolis, J. Quant. Spectrosc. Radiat. Transfer 13, 969 (1973).

36. J. S. Margolis, J. Quant. Spectrosc. Radiat. Transfer 11, 69 (1971).

37. G. Herzberg, Molecular Spectra and Molecular Structure II, Infrared and Raman Spectra of Polyatomic Molecules (D. Van Nostrand Co., Inc., New York, 1945). (a) p. 400; (b) p. 26; (c) p. 421; (d) P. 391; (e) P. 378.

38. L. Halonen and M. S. Child, Molecular Physics 11, 1 (1982).

39. R. J. Hayward and B. R. Henry, J. Molecular Spectrosc. 50, 58 (1974).

40. W. E. Blass and T. H. Edwards, J. Molecular Spectrosc. 24, 116 (1967).

41. Von V. Weisskopf and E. Wigner, Z. Phys. 63, 54 (1930).

42. F. Bloch, Phys. Rev. 70, 460 (1946).

43. I. I. Rabi, N. F. Ramsey, and J. Schwinger, Rev. Mod. Phys. 26, 167 (1954).

44. A. Ade and D. M. Dennison, Phys. Rev. 43, 716 (1933).

45. The idea of a classical statistical rotational constant emanated from a discussion between some of the authors and R. A. Marcus, whose contribution is hereby acknowledged.

46. J. D. Mc Donald and R. A. Marcus, J. Chem. Phys. 65, 2180 (1976).

Figure Captions

FIG. 1. Spectrum of CD_3H in the region near the $\Delta v=5$ CH-stretching overtone. (a) Pulsed laser photoacoustic spectrum of a 370 torr sample at a temperature of ~25° C; it is an average of two scans, each at 12 laser pulses for 0.01 nm wavelength interval. The signal intensities in this and all other experimental spectra presented in this paper were corrected for the variation of the incident laser light intensity with wavelength. (b) Theoretical fit to the experimental spectrum (see Section 4.1). The lower abscissa gives the air wavelength and the upper abcissa the vacuum wavenumber. The ordinates are in arbitrary units and have been normalized to unity at the top of the $|5_1\rangle$ Q branch. They represent signal intensity above the actual experimental baseline without a background subtraction. The symbols P(J), Q, and R(J) correspond to rotational transitions of $\Delta J=-1,0$, and +1 respectively where J is the rotational quantum number of the ground state. The symbols $|v_i,v_j\rangle$ represent the quantum numbers of the upper state, as described in section 4.1.

FIG. 2. Pulsed laser photoacoustic spectrum of CD_3H in the region near the $\Delta v=6$ CH-stretching overtone. The spectrum shown used a sample pressure of 370 torr at ~25° C and is an average of 3 scans, each at 12 laser pulses per 0.01 nm wavelength interval. The lower abscissa gives the air wavelength, and the upper abscissa the vacuum wavenumber. The ordinate origin corresponds the approximately 90% of the observed sig-

nal at the right hand side of the spectrum. This baseline correction is due to the background signal from scattered light in the photoacoustic cell (see Section 3.4).

FIG. 3. Pulsed laser photoacoustic spectrum of CD_3H in the region near the $\Delta v=7$ CH-stretching overtone. The spectrum shown used a sample pressure of 1385 torr at ≈25° C and is an average of 4 scans, each at 30 laser pulses per 0.01 nm wavelength interval. Theabscissae and the corrections for background and normalization of the ordinate are as described in the caption of Figure 2. The symbols P(J), Q, and R(J) and $|v_i,v_j\rangle$ are as described in the caption of Figure 1.

FIG. 4. Combination sum P(J) + R(J-1) plot for CD_3H vibrations states present in the spectrum of Figure 1. Combination sums for $|5_1\rangle$ are indicated by the open triangle symbols and correspond to the ordinate scale on the left. Combination sums for $|4_1,2_5\rangle$ are indicated by the open circle symbols and correspond to the ordinate scale on the right. All ordinate values are in vacuum wavenumbers. The lines represent least square fits to the data.

FIG. 5. Combination sum P(J) + R(J-1) plot for CD_3H vibrational states present in the spectrum of Figure 2. Combination sums for $|6_1$ are indicated by the open triangle symbols and correspond to the ordinate scale on the left. Combination

sums for $|5_1,2_5\rangle$ are indicated by the open circle symbols and correspond to the ordinate scale on the right. All ordinate values are in vacuum wavenumbers. The lines represent least squares fits to the data.

FIG. 6. Combination sum P(J) + (J-1) plot for CD_3H state $|6_1,2_5\rangle$. The points shown by open triangles were used in the least squares fitting of the line for the combination sum analysis. The points shown by open circles correspond to strongly perturbed features in the spectrum of Figure 3 and were not used in the combination sum analysis. The ordinate scale is in vacuum wavenumbers.

FIG. 7. CD_3H rotational constants B' vs. CH stretch quantum numbers. The open triangle symbols correspond to previous studies (see Table I). The full circle symbols correspond to our data. The error bars represent ±2 standard deviations obtained from the least squares fits of the combination sum analysis. The open square symbols correspond to zero order rotational constants for a model involving 2 interacting vibrational states of the form $|v_1\rangle$ and $|(v-1)_1,2_5\rangle$. The solid line is the result of a least square fit to the points $|0\rangle$, $|1_1\rangle$, $|2_1\rangle$, $|3_1\rangle$, and $|4_1\rangle$ and represents the effects of the CH-stretch quantum number on the rotational constant B' for noninteracting vibrational states. The dashed line is a similar line obtained for states of the form $|v_1,2_5\rangle$. The values for B' are in vacuum wavenumbers.

FIG 8. Three classes of zero order states for CD_3H vibrational overtones. The optical states are the source of the optical transition strength in their immediate spectral region. The strong coupling states are the direct source of only a small amount of optical transition strength, and produce spectral features because of intensity borrowing from the optical states. The weak coupling states produce no spectroscopic features of their own, but interact enough with the other classes of states to change the latter's spectroscopic features.

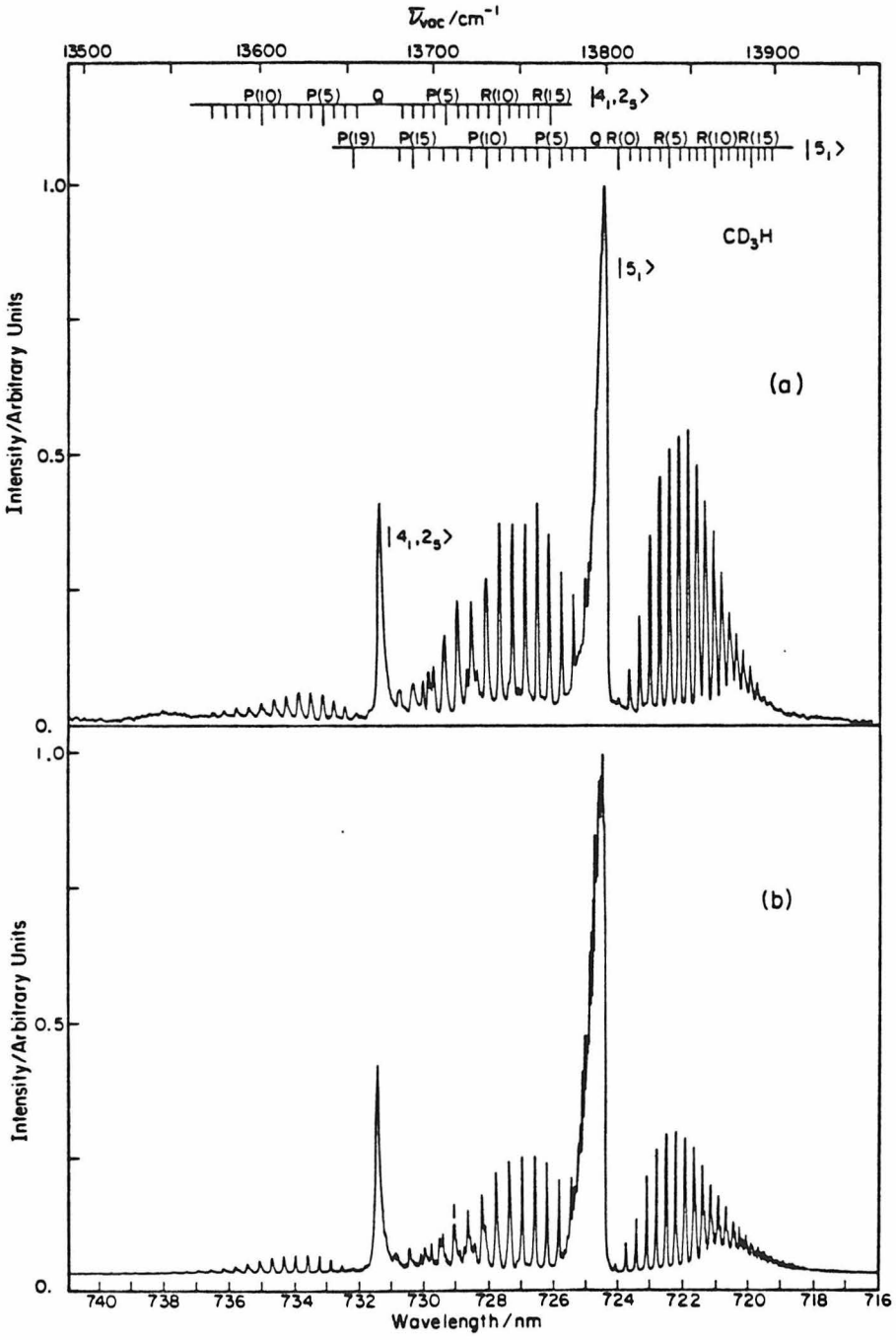
$\bar{\nu}_{vac}$ /cm^{-1}
13500
13600
13700
13800
13900
P(10) P(5) Q P(5) R(10) R(15) |4$_1$,2$_3$>
P(19) P(15) P(10) P(5) Q R(0) R(5) R(10)R(15) |5$_1$>
CD$_3$H
|5$_1$>
(a)
|4$_1$,2$_3$>
Intensity/Arbitrary Units
1.0
0.5
0.
(b)
740
738
736
734
732
730
728
726
724
722
720
718
716
Wavelength/nm

Figure 1

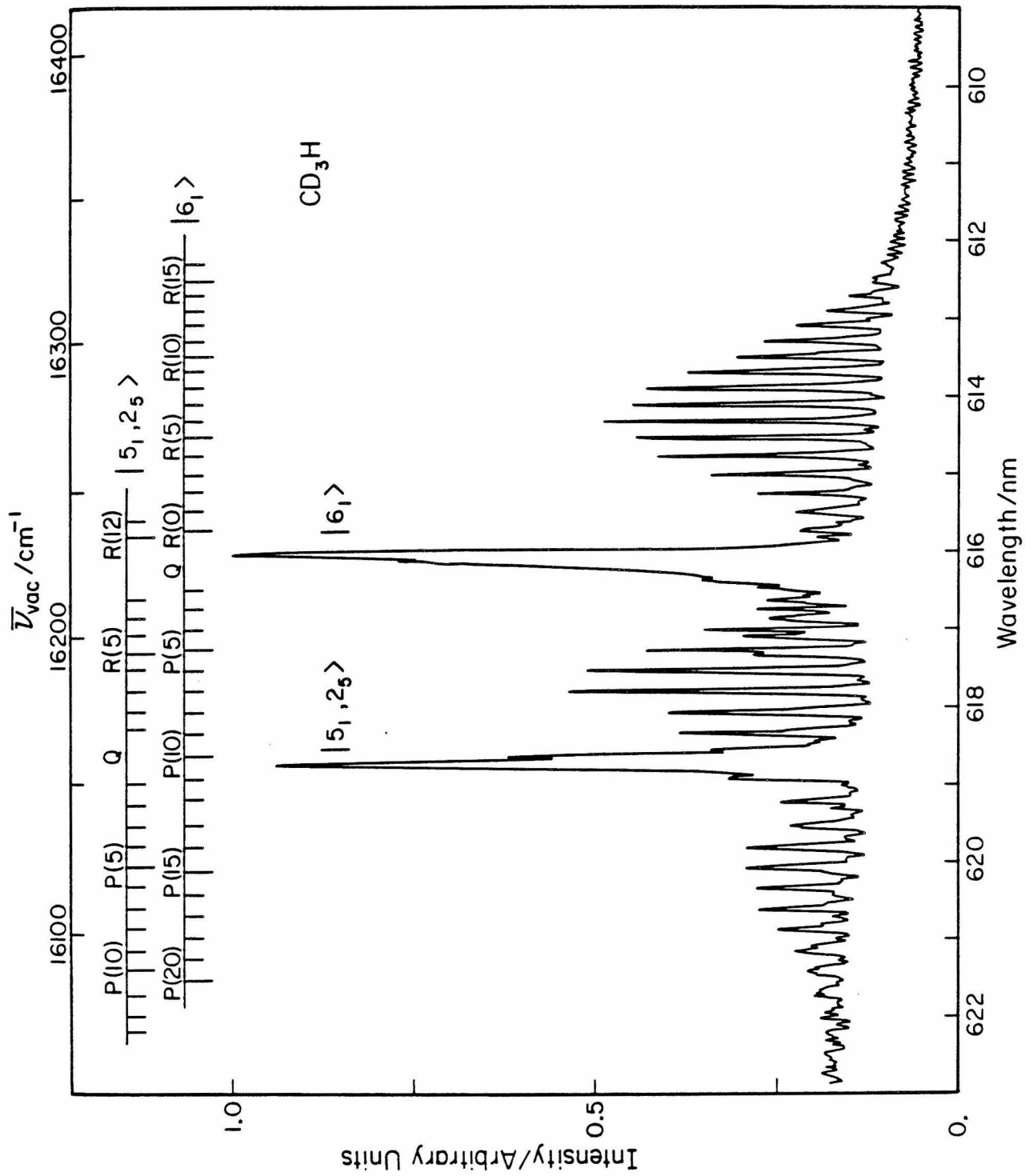
$\bar{\nu}_{vac}$ /cm^{-1}
16100
16200
16300
16400
P(10)
P(20)
P(5)
P(15)
Q
P(10)
R(5)
P(5)
R(12)
Q R(0)
R(10)
R(5)
R(15)
$|5_1, 2_5\rangle$
$|6_1\rangle$
CD_3H
$|5_1, 2_5\rangle$
$|6_1\rangle$
1.0
0.5
0.
Intensity/Arbitrary Units
622
620
618
616
614
612
610
Wavelength/nm

Figure 2

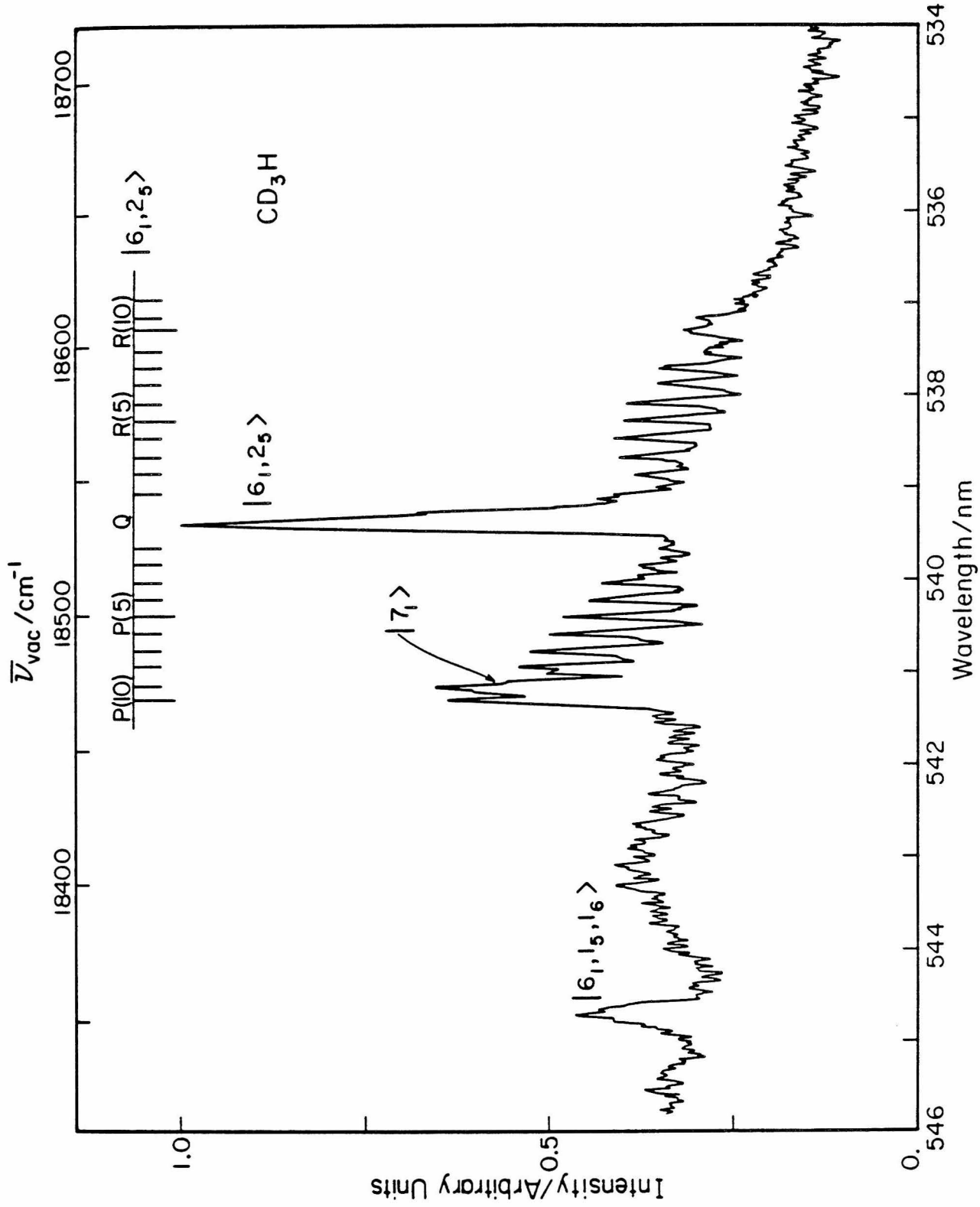
$\bar{\nu}_{vac}$ /cm^{-1}
18700
18600
18500
18400
P(10)
P(5)
Q
R(5)
R(10)
$|6_1,2_5\rangle$
CD_3H
$|6_1,2_5\rangle$
$|7_1\rangle$
$|6_1,1_5,1_6\rangle$
546
544
542
540
538
536
534
Wavelength/nm
1.0
0.5
0.
Intensity/Arbitrary Units

Figure 3

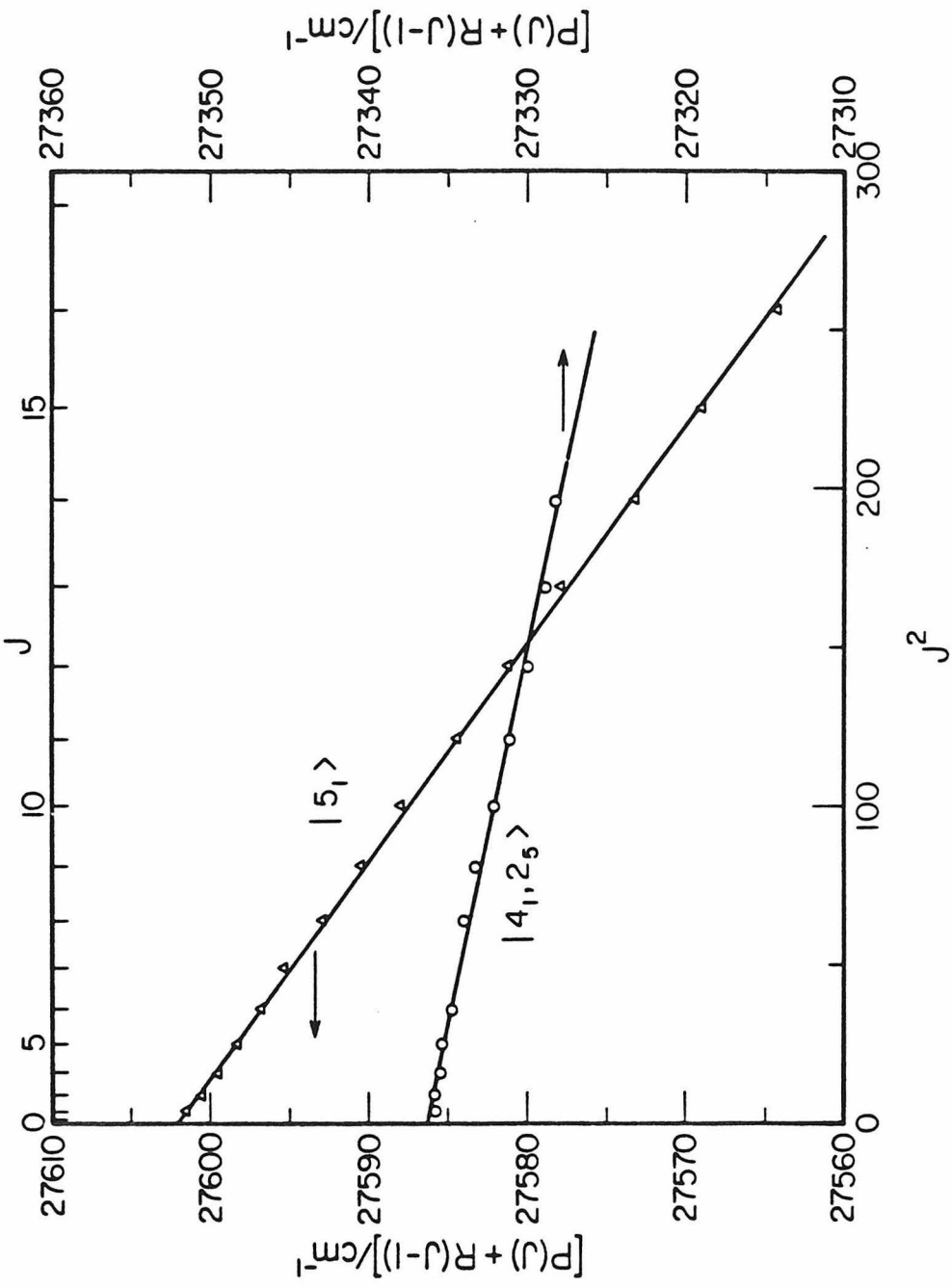
[P(J) + R(J-1)]/cm⁻¹
27610
27600
27590
27580
27570
27560
0
5
10
15
J
0
100
200
300
J²
[P(J) + R(J-1)]/cm⁻¹
27360
27350
27340
27330
27320
27310
|5₁⟩
|4₁,2₅⟩

Figure 4

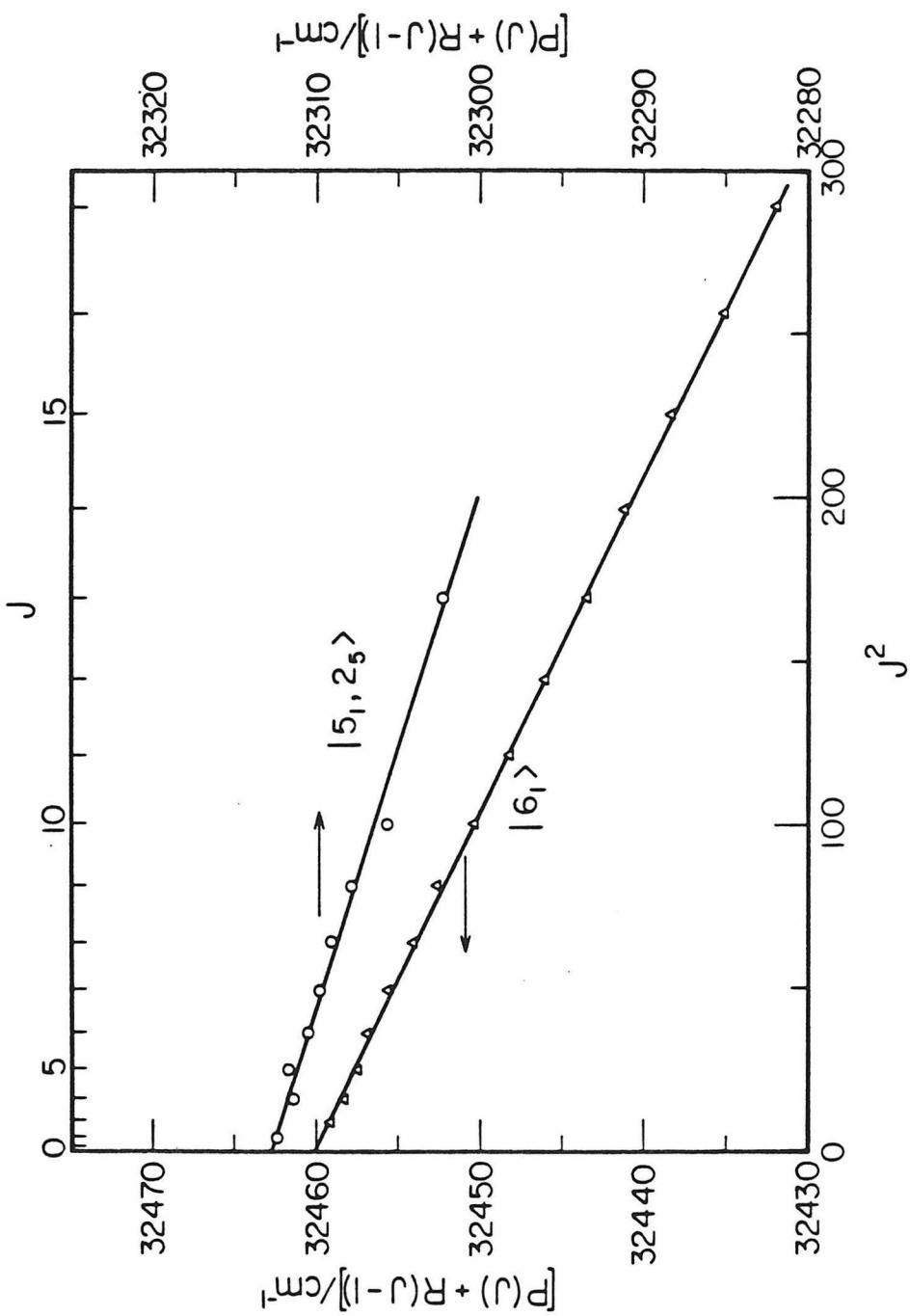
[P(J) + R(J-1)]/cm⁻¹
32470
32460
32450
32440
32430
0
5
10
15
J
0
100
200
300
J²
32320
32310
32300
32290
32280
[P(J) + R(J-1)]/cm⁻¹
|5₁, 2₅⟩
|6₁⟩

Figure 5

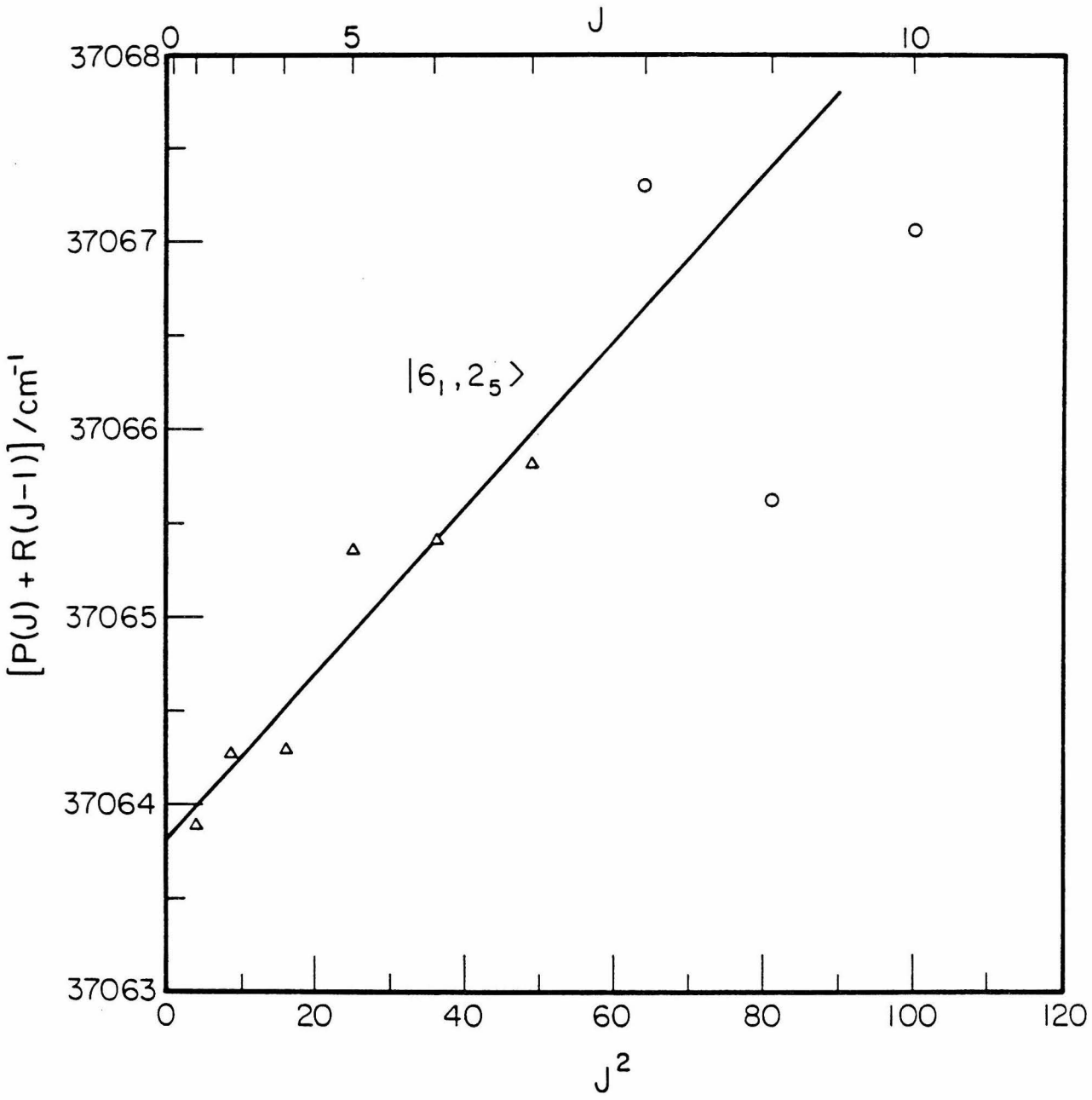
J
0
5
10
37068
37067
37066
37065
37064
37063
[P(J) + R(J-1)] /cm⁻¹
|6₁, 2₅>
0
20
40
60
80
100
120
J²

Figure 6

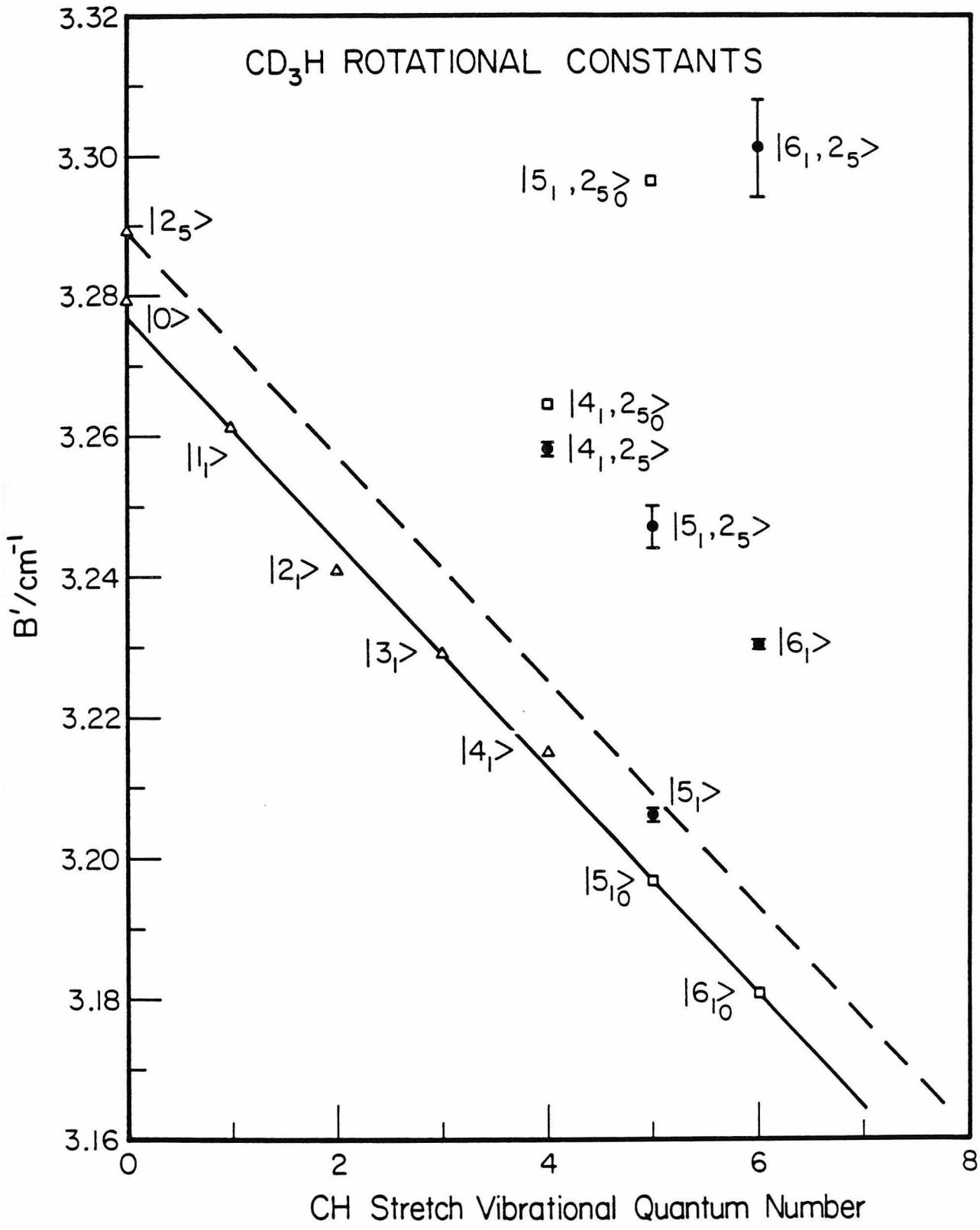
CD3H ROTATIONAL CONSTANTS
B'/cm-1
CH Stretch Vibrational Quantum Number
3.32
3.30
3.28
3.26
3.24
3.22
3.20
3.18
3.16
0
2
4
6
8
|2₅>
|0>
|1₁>
|2₁>
|3₁>
|4₁>
|5₁>
|5₁,2₅>₀
|6₁,2₅>
|4₁,2₅>₀
|4₁,2₅>
|5₁,2₅>
|6₁>
|5₁>₀
|6₁>₀

Figure 7

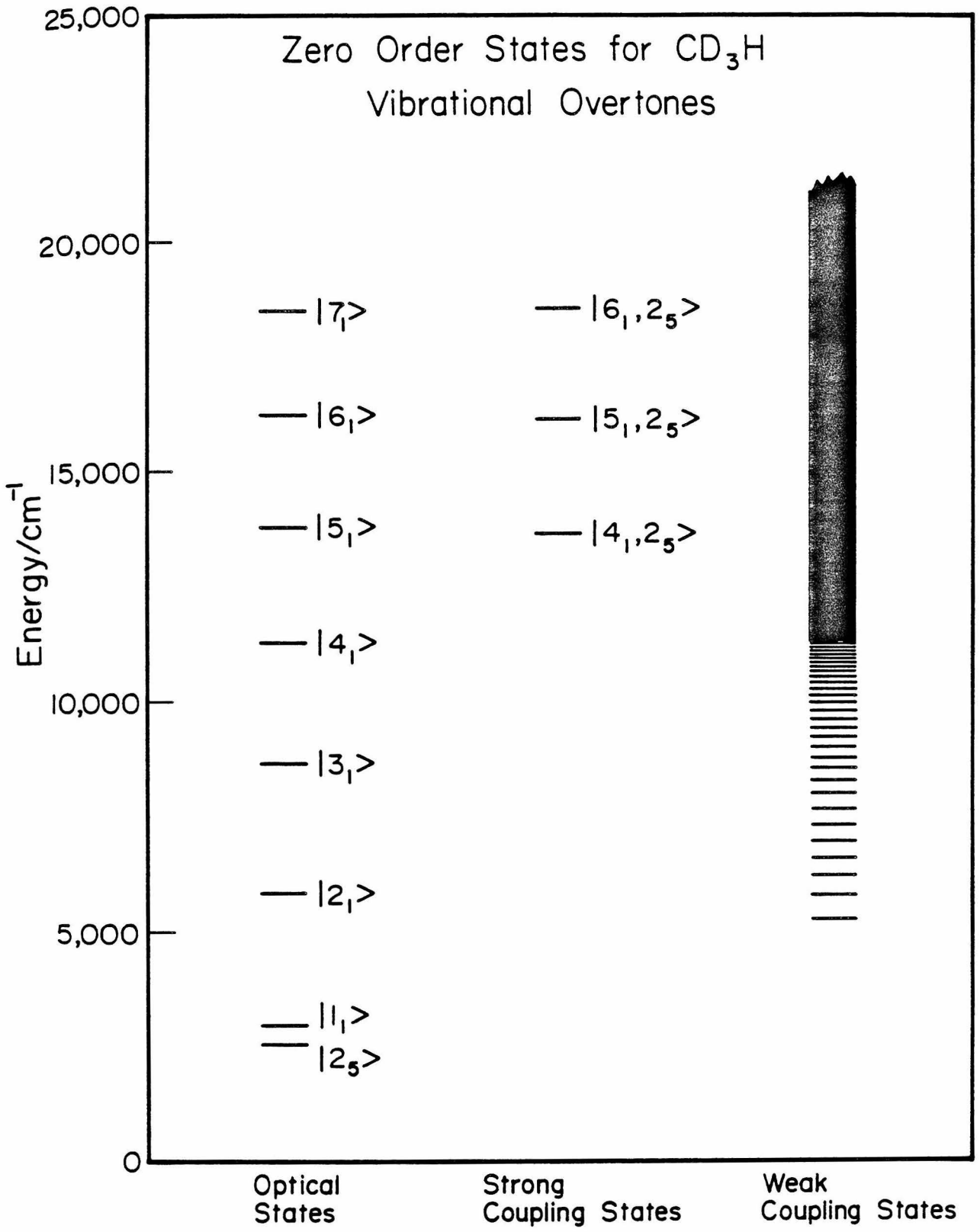
Zero Order States for CD_3H
Vibrational Overtones
25,000
20,000
15,000
10,000
5,000
0
Energy/cm^{-1}
$|7_1>$
$|6_1>$
$|5_1>$
$|4_1>$
$|3_1>$
$|2_1>$
$|1_1>$
$|2_5>$
$|6_1,2_5>$
$|5_1,2_5>$
$|4_1,2_5>$
Optical States
Strong Coupling States
Weak Coupling States

Figure 8

Paper II: Photoacoustic Detection of Stimulated Emission Pumping in p-Difluorobenzene.

Photoacoustic Detection of Stimulated Emission Pumping in p-Difluorobenzene.[a]

D. J. Moll[b], G. R. Parker, Jr. and A. Kuppermann
Arthur Amos Noyes Laboratory of Chemical Physics,[c]
California Institute of Technology, Pasadena, CA 91125, USA
(Received

Photoacoustic detection has been used to monitor a stimulated emission pumping process in p-difluorobenzene. Using the $\tilde{A}\ ^1B_{2u}\ 5^1$ state as an intermediate state, several vibrational levels of the ground electronic state were populated. The photoacoustic technique is an attractive alternative to other techniques because of its sensitivity, simplicity, and the ability to differentiate between stimulated emission pumping and excited state absorption. An example of excited state absorption in aniline is given.

---

[a] Research supported in part by the U. S. Department of Energy, (Contract No. DE-AS03-765F00767, Project Agreement No. DE-AT-03-76ER72004).

[b] Work performed in partial fulfillment of the requirements for the Ph. D. degree in Chemistry at the California Institute of Technology.

[c] Contribution No.

I. INTRODUCTION

Stimulated emission pumping (SEP) has recently been demonstrated as a powerful technique for selectively preparing large numbers of molecules in specific highly excited rovibrational states in the ground electronic state for diatomic or small polyatomic molecules.[1-4] The SEP process produces this selective population transfer in two sequential steps. First a PUMP laser excites molecules from an initial level 1 in the ground electronic state to level 2 in an excited electronic state. A second laser, the DUMP, then stimulates emission out of this excited state to a lower energy state, level 3, resulting in an overall transfer of population from level 1 to level 3. SEP therefore provides an alternate route for exciting molecules to level 3 that may be much more efficient in some cases than direct excitation from level 1 to level 3.

SEP is especially attractive for producing large populations in specific high vibrational states of the ground electronic state because it often allows the substitution of favorable Franck-Condon factors and easily obtainable tunable visible or UV laser for weak $|\Delta v| > 1$ vibrational transitions and difficult to obtain tunable IR lasers. In formaldehyde, for example, it was estimated that greater than 0.02% of the total thermal population within the PUMP beam was transferred to a specific rotational level in the $\nu_4=4$ vibrational state by an SEP process.[3]

This paper describes the use of the photoacoustic effect

for detecting and monitoring the SEP process, and demonstrates its utility in a specific molecule, p-difluorobenzene (p-DFB). By monitoring the total energy remaining in the sample after the PUMP and DUMP pulses using the photoacoustic effect, it is possible to determine if the DUMP pulse stimulated emission out of level 2 or if it excited the molecule from level 2 to a higher energy state.

2. Previous SEP Detection Techniques

Two techniques have previously been used to monitor the SEP process. Kittrel, et al.[1] and Reisner, et al.[3] in their studies of SEP in I_2 and formaldehyde respectively, monitored the change in fluorescence from level 2 (an excited singlet state) as a function of the DUMP pulse wavelength. When the DUMP stimulated emission out of level 2 to level 3, this fluorescence decreased. To minimize the effects of pulse to pulse variations in the PUMP intensity the PUMP beam was split into 2 equal-intensity beams which both passed through the sample cell. The difference in fluorescence intensity produced by the 2 beams was monitored while the DUMP pulse, which passed only through one PUMP beam, was scanned in wavelength. This technique is relatively uncomplicated and employs the high sensitivity of fluorescence detection techniques. One disadvantage of this detection scheme arises from its sensitivity to processes other than the stimulation of emission from the excited electronic state which could also decrease the detected fluorescence. For example, the excited state produced by the PUMP pulse could absorb DUMP photons (instead of stimulating emission), thereby exciting the molecule to higher electronic states which rapidly predissociate or autoionize. This additional excitation process would effectively decrease the observed fluorescence. For the case of I_2 and formaldehyde, the spectroscopic evidence clearly supports the almost exclusive occurrence of SEP . However, attempts to observe SEP processes involving the $\tilde{A}\,^1B_2$ state

of aniline (see section 6) strongly indicate the presence of up-pumping by the "DUMP" pulse to auto-ionizing or pre-dissociative states which competes effectively with stimulating emission back to the ground electronic state.[5] Therefore, without a prior detailed knowledge of the spectroscopy of the molecule to be investigated and a careful investigation of possible other fluorescence-decreasing processes, the fluorescence detection technique could give misleading results.

A second method of monitoring the SEP process was employed by Lawrence and Knight[2,4]. They demonstrated SEP as an effective method of populating vibrational levels of the ground electronic state in a medium-sized polyatomic molecule, p-DFB,[2] and used the SEP process as a preparative method to produce specific vibrational states whose lifetimes were measured.[4] In these experiments the standard PUMP and DUMP pulses were followed by a third pulse, the PROBE pulse, which excited molecules prepared by SEP up to specific states whose fluorescence is detected. The PROBE pulse is effective in producing fluorescence only if the correct vibrational level has been prepared. This technique offers the advantage of specific detection of the level prepared by SEP, rather than assuming that a decrease in fluorescence corresponds to the preparation of a specific vibrational state. The possibility of partial absorption of the DUMP pulse and further excitation is not eliminated, but by monitoring the population of the targeted final vibrational state, the extent of the

stimulated emission process is directly observed. The major disadvantage of this technique is the complexity of obtaining and overlapping 3 different laser pulses, both temporally and spatially. In addition, the spectroscopy of the molecule being studied must be known sufficiently to allow selection of an appropriate wavelength for the PROBE laser.

The photoacoustic method for detection of SEP presented in the present paper does not specifically detect the population of the targeted vibrational state. Instead it monitors the excess energy remaining in the sample after both the PUMP and DUMP pulses. The PUMP pulse alone excites the molecule up to an excited electronic state which relaxes radiatively and nonradiatively. The nonradiative pathway, eventually leads, through collisions, to an increase in translational energy of the molecules which is detected as a pressure increase by a simple microphone. When the DUMP pulse stimulates emission out of the excited electronic state, the fraction of energy following the nonradiative pathway decreases, less energy appears as translational energy, and a smaller signal is detected from the microphone. If, on the other hand, the DUMP pulse is absorbed, more energy is deposited in the system and it is likely that the amount of energy following the nonradiative pathway will increase. This leads to an increase in the microphone signal. Therefore, by monitoring the increase or decrease in photoacoustic signal when the DUMP pulse immediately follows the PUMP pulse, compared to

the PUMP pulse alone, it is possible to differentiate between excited state absorption and stimulated emission. The extent of the effect can be estimated if the relative quantum yields for nonradiative processes from the excited states are known. The ability to differentiate between absorption and stimulated emission provides a distinct advantage over the simple fluorescence detection method. The simplicity of the photoacoustic detection method compated to monitoring fluorescence due to a third PROBE pulse makes it an attractive alternative to detecting molecules in the targeted vibrational state directly.

4. Experimental

The two-color time-resolved photoacoustic measurement involved in monitoring SEP described here is a new application of photoacoustic spectroscopy. This same technique is directly applicable to gas phase excited state absorption measurements with nanosecond or faster resolution.[5] (We are aware of only one other nanosecond timescale photoacoustic spectroscopy measurement, and this involved a solid phase sample.[6])

4.1 Lasers and Optics

The experimental arrangement is depicted in figure 1. It consisted of 2 counter-propagating collinear beams from frequency doubled dye lasers which passed through a photoacoustic cell containing p-DFB. The PUMP pulse was supplied by dye laser #1, a Molectron[7] DL200 dye laser pumped by a Molectron UV400 laser. The dye laser output was frequency doubled in a KDP crystal, collimated with a 25 cm focal length lens, and directed into the photoacoustic cell. Using Coumarin 485 dye in ethanol, typical UV pulse energies at the photoacoustic cell entrance were $\sim 15 \times 10^{-6}$ joules. The DUMP pulse was supplied by dye laser #2, a Molectron DL18 dye laser with an oscillator and single longitudinally pumped amplifier, pumped by a Molectron MY34 Nd:YAG laser. The output of dye laser #2 was also doubled in a KDP crystal and directed into the opposite end of the photoacoustic cell. A beam contracting telescope was used to match the beam

diameter of the doubled output of dye laser #2 to the ~1 mm diameter of the dye laser #1's output. Using R6G dye in ethanol, typical UV pulse energies before the photoacoustic cell were between 2 and 10 millijoules. UV outputs from either dye laser were monitored off beamsplitters with a Laser Precision[8] pyroelectric joulemeter, model RkP-335, and readout unit, model Rk-3230. The analog output from the readout unit was processed by a differential gated integrator system described later.

Initial experiments indicated that the two dye lasers were interacting with each other due to the collinear counter-propagating beam arrangement. This was eliminated by using Corning 7-54 UV pass filters to block the visible output after each doubling crystal, and Corning 0160 glass before each doubling crystal to keep the UV produced by one laser from entering the other.

Wavelength scans of either dye laser were achieved using micro-computer controlled stepping motors to drive the gratings. The phasematching angle for the doubling crystal of dye laser 1 was adjusted manually during wavelength scans. The crystal for dye laser 2 was controlled by the micro-computer using a pre-determined 5th order polynomial in wavelength. Wavelengths were calibrated using a uranium/neon hollow cathode lamp and the optogalvanic effect.[9] UV output linewidths were ≤ 1 cm^{-1}.

4.2 Timing and Wavelength Scanning

The timing between laser pulses was controlled by a

series of three delay generators. Triggered by the Nd:YAG laser flashlamp sync signal, the first delay generator produced a ~160 μsec delay which then triggered two other delay generators which triggered the Nd:YAG Q-switch and N laser thyratron. Long-term jitter between pulses, as monitored with a Hewlett Packard 5082-4220 PIN photodiode (-18 volt reverse bias, τ_{rise} <1 nsec), was less than ±2 nsec, with short term (10 sec) jitter of ±1 nsec. Pulsewidths of the doubled output of each dye laser were ≤5 nsec.

For experiments where the DUMP wavelength was scanned, the PUMP laser was operated at 20 Hz and the DUMP laser was fired only on alternating PUMP pulses. A differential gated integrator measured the difference in amplitude of the two photoacoustic signals from PUMP alone, and PUMP with DUMP. The integrator output along with pulse energy of the DUMP laser were digitized and stored on floppy disk.

4.3 Photoacoustic Cell

Photoacoustic spectroscopy and the design of photoacoustic cells has been recently reviewed.[10,11] The photoacoustic cell used in this study was similar to that of West, et al.,[12] and modified slightly from our earlier studies.[13] The 18 cm long by .9 cm diameter cell was constructed of stainless steel and aluminum. Quartz windows were held in place at each end using Viton o-rings. Since extreme sensitivity was not essential in working with the strong absorptions in p-DFB, the cell was designed to eliminate signals arising from scattered light striking the microphone or cell

walls. Since most light scattering occurs at the windows, this was minimized by a series of apertures both inside and outside the cell. The microphone, Knowles Electronics[14] BT1759, was located 6 cm away from the PUMP entrance window to minimize absorption of the PUMP pulse before it reached the vicinity of the microphone. The microphone was positioned over a 3/16" diameter hole in the cell wall and held in place with epoxy resin.

4.4 Sample Preparation

P-DFB, 98% purity from Aldrich, was subjected to several liquid N_2 freeze-pump-thaw cycles and then vacuum distilled on a vacuum line operated at 5×10^{-7} torr pressure, before filling the photoacoustic cell. Sample pressures ranged from 0.020 to 0.060 torr as measured by a Baratron (10 torr head). At the lower sample pressures helium was sometimes added to increase the photoacoustic signal through enhanced collisional deactivation. This had no effect on the % change in signal resulting from the SEP process.

5. Stimulated Emission Pumping in p-Difluorobenzene

We chose p-DFB to demonstrate the effectiveness of photoacoustic detection for monitoring SEP because of its extensively studied absorption and emission spectra and to allow comparison with previous SEP studies in the same molecule.[2,4]

5.1 Background

Infrared and Raman,[15] and 2-photon[16] studies have determined the ground state vibrational frequencies of p-DFB. The $S_1(^1B_{2u})$ excited state vibrational frequencies have been determined from absorption studies.[16-20] Single vibronic level fluorescence from 19 absorption bands has been studied.[21] Low pressure lifetimes and fluorescence quantum yields from single vibronic levels of S_1 have been measured.[22-24] Several notations have been used in labeling the ground state vibrations of p-DFB. We have used the standard Mulliken convention[25] in this paper, which is also used in ref. 21. Transitions between vibronic levels in the ground electronic state and the first excited singlet ($^1B_{2u}$) are denoted by N_i^j, where N is the number of the mode involved and i and j are the number of quanta in mode N in the ground and excited electronic states, respectively.

Figure 2 shows a photoacoustic spectrum of p-DFB produced by scanning the PUMP laser (no DUMP present). Assignments of the stronger transitions are given in table 1. In addition to the strong 0-0 band at 265.54 nm, the p-DFB spectrum predominantly consists of progressions in ν_5 and ν_3, plus sequences associated with members of these progressions.[21] The 6_0^1

band is the strongest observed absorption involving quantum changes in modes other than ν_5 and ν_3.[21] Single vibronic level fluorescence studies have identified the transition labeled k in figure 2 as involving excitation from the ground vibration state to an excited state Fermi resonance between states 5^1 and 6^2,[21] with 5^1 contributing most of the transition intensity.

5.2 Results

Figure 3 shows a photoacoustic SEP spectrum of p-DFB produced by exciting the strong transition to the 5^1 and 6^2 resonant levels at 37659 cm^{-1} with the PUMP laser and scanning the DUMP laser from 286 nm to 284 nm. The figure shows three scans taken with different delay times between the PUMP and DUMP pulses. When the DUMP pulse occurs 20 nsec before or 38 nsec after the PUMP pulse, no change in photoacoustic signal is observed. When the DUMP pulse follows the PUMP pulse by 4 nsec, the signal decreases by up to 10% at certain wavelengths, indicating that a SEP process is occurring at those wavelengths. The appearance of SEP only when DUMP immediately follows PUMP is consistent with the fluorescence lifetime of 10 nsec observed for the 5^1 level of S_1.[22-24] Photoacoustic signal decreases as large as 15% have been observed. The per cent change depends critically on the spatial overlap of the two beams. No excited state absorption is observed for p-DFB for the DUMP wavelengths used.

The SEP transitions observed in the 4 nsec spectrum of

figure 3 are easily assigned by considering the p-DFB single vibronic level fluorescence spectra and ground state fundamentals given in ref. 21. In absorption and emission, the Frank Condon factors allow large changes in vibrational quantum numbers of only modes ν_3 and ν_5.[21]

Quantum number changes for ν_6 are limited to ±1. Changes in quantum numbers in other modes produce transitions which are weaker by an order of magnitude. Table 2 lists the possible ground electronic state vibrational levels which, according to Franck-Condon arguments, are expected to be most intense in fluorescence from the 5^1 or 6^2 levels populated by the PUMP laser. Each expected fluorescence transition is detected as a decrease in photoacoustic signal caused by SEP, although some transitions appear only as unresolved shoulders on the rotational envelopes of stronger transitions. The agreement between predicted and observed transition energies for the $3_1 5_1 6_1$ and 5_3 levels is within expectations, considering the ±5 cm^{-1} accuracy of the fluorescence data[21] and the difference in excitation bandwidth (28 cm^{-1} for fluorescence vs. $\leq$ 1 cm^{-1} for SEP).[26] The relative SEP intensities agree well with the resolved fluorescence spectrum intensities after exciting the 5^1 level.[21]

Figure 4 shows a time resolved photoacoustic spectrum of p-DFB obtained by varying the relative time between the PUMP and and DUMP pulses, while fixing their respective photon energies at 37659 cm^{-1} and 35108 cm^{-1}. This excited the 5^1 and 6^2 levels of S_1 and stimulates emission down to the $3_1 5_1 6_1$ level

of the ground electronic state. The time dependence of the SEP effect detected as a decrease in photoacoustic signal correlates with the 10 nsec fluorescence lifetime[22-24] of the 5^1 level of S_1 mentioned previously, if the laser pulse widths are taken into account.

The wavelength and time dependence of the p-DFB SEP signal detected by the photoacoustic effect provide strong confirmation of the accuracy and utility of this new technique for monitoring SEP.

6. Photoacoustic Detection of Excited State Absorption In Aniline

In this section the ability to detect excited state absorption, in contrast to stimulated emission, will be demonstrated briefly by presenting data on aniline.

Figure 5 shows a time-resolved photoacoustic spectrum of aniline obtained in a similar manner to that of the p-DFB spectrum of figure 4. In this case a 0.378 torr sample of aniline was used and the PUMP and DUMP photon energies were 34032 cm^{-1} and 18797 cm^{-1}, respectively. The PUMP pulse energy was 5.4 μJ, and the DUMP pulse energy was 6.5 mJ. Under these conditions the PUMP excited the 0-0 transition from S_0 to the S_1 state,[27-28] DUMP excited no transitions from the ground state and cannot stimulate emission from S_1,[32] and DUMP possibly may excite aniline from S_1 up to S_n, a state observed in vacuum UV absorption studies.[30-32] (DUMP is not the correct terminology for a pulse which promotes excited state absorption. Its use is retained here for comparison with SEP results.)

In the spectrum of figure 5 a large <u>increase</u> in photoacoustic signal of up to 70% is observed when the DUMP pulse follows PUMP by 0 to 20 nsec. When DUMP is delayed longer than 20 nsec, the signal decreases to a level that is still 20% higher than when DUMP precedes PUMP. The fluorescence lifetime of the vibrationless level of S_1 is approximately 8 nsec,[33-35] and therefore the large increase from 0 to 20 nsec delay results from excitation of the singlet state by the

DUMP pulse. The longer apparent lifetime and increased signal before 0 are a result of the width of the PUMP and DUMP pulses. The increase in signal for delays longer than 20 nsec most likely results from absorption from a long-lived triplet state produced by intersystem crossing.[36] The excited state absorption effects in aniline are presented in detail in ref. 5.

7. Conclusions

The results presented on p-DFB clearly demonstrate the sensitivity of the photoacoustic technique for monitoring SEP processes. The actual population transfer produced in these experiments was small due to the low pulse energy of the PUMP pulse. Increasing the PUMP pulse energy should only enhance the results reported here because of the increased signal to noise ratio.

Tha ability to detect excited state absorption, as demonstrated by the aniline study, and to distinguish that effect from SEP by simply monitoring the direction of change in the photoacoustic signal, makes this technique an attractive alternative to the fluorescence detection method. The simplicity of photoacoustic detection compared with the PROBE laser-induced-fluorescence technique should also be emphasized.

The two-color time-resolved photoacoustic spectroscopy technique demonstated here is a powerful tool for excited state spectroscopy. The results on p-DFB and aniline demonstrates its ability to determine single vibronic level lifetimes, detect gas phase excited state absorption from both singlet and triplet states, and also monitor SEP processes. By using amplified picosecond laser, the temporal resolution could easily be extended to the picosecond regime.

TABLE I. Observed Vibronic Transitions in the p-DFB $S_1(^1B_{2u})$ Photoacoustic Spectrum

Designation in Fig. 2	Vibronic Band Assignment[a]	Transition Energy (cm^{-1})[a]
a	8_1^1	36594
b	30_3^3	36726
c	17_1^1	36740
d	30_2^2	36764
e	27_1^1	36797
f	30_1^1	36802
g	0_0^0	36840
h	6_0^1	37248
i	$5_0^1 30_2^2$	37583
j	$5_0^1 30_1^1$	37621
k	$5_0^1(6_0^2)$[b]	37659

[a]From ref. 20 and 21.

[b]Fermi resonance mixes the 5^1 and 6^2 vibrational levels. The transition probability is predominantly derived from the 5^1 level.

TABLE II. p-DFB Vibrational Levels Populated by Stimulated Emission Pumping

Vibrational Band	Vibrational Energy (cm^{-1})	Predicted DUMP Transition Energies (cm^{-1})	Observed DUMP Transition Energies (cm^{-1})
3_2	2515[b]	35144	d
$3_1 5_1 6_1$	2565[b]	35094	35108
5_3	2595[b]	35064	35073
$3_1 6_3$	2604[c]	35055	d
$5_2 6_2$	2615[c]	35044	d

[a]Using a PUMP photon energy of 37659 cm^{-1}.

[b]Determined from 0-0 fluorescence data of ref. 21

[c]Determined from ground electronic state vibrational frequencies of ref. 21. Anharmonicity was not included.

[d]Transition is present, but as a broad unresolved feature.

REFERENCES

1. C. Kittrell, E. Abramson, J. L. Kinsey, S. A. McDonald, D. E. Reisner, R. W. Field, and D. H. Katayama, J. Chem. Phys. 75, 2056 (1981).

2. W. D. Lawrence and A. E. W. Knight, J. Chem. Phys. 76, 5637 (1982).

3. D. E. Reisner, P. H. Vaccaro, C. Kittrell, R. W. Field, J. L.Kinsey, and H. -L. Dai, J. Chem. Phys. 77, 573 (1982).

4. W. D. Lawrence and A. E. W. Knight, J. Chem. Phys. 77, 570 (1982).

5. D. J. Moll, G. R. Parker, Jr. and A. Kuppermann,"Two-Color Time-Resolved Photoacoustic and Multiphoton Ionization Spectroscopy of Aniline", to be published.

6. M. G. Rockley and J. Paul Devlin, Appl Phys. Lett. 31, 24 (1977).

7. Molectron Corporation, 177 N. Wolfe Road, Sunnyvale, California 94086, USA.

8. Laser Precision Corp., 1231 Hart Street, Utica, New York 13502, USA.

9. R. A. Keller, R. Engleman, Jr. and B. A. Palmer, Appl. Optics 19, 836 (1980).

10. "Optoacoustic Spectroscopy and Detection", Yoh-Han Pao, edit. (Academic Press, New York, New York, 1977).

11. A. Rosenwaig, "Photoacoustics and Photoacoustic Spectroscopy", (John Wiley and Sons, New York 1980).

12. G. A. West, D. R. Seibert, and J. J. Barrett, J. Appl. Phys. 51, 2823 (1980).

13. D. J. Moll, J. W. Perry, A. Kuppermann, and A. H. Zewail, "High Overtone Photoacoustic Spectroscopy of Some Methyl-Containing Molecules. I. Rotational Analysis", to be published.

14. Knowles Electronics, Inc., 3100 N. Mannheim Rd., Franklin Park, Illinois 60131, USA.

15. J. H. S. Green, Spectrochem. Acta A 26, 1503 (1970).

16. M. J. Robey and E. W. Schlag, Chem. Phys. 30, 9 (1978).

17. C. D. Cooper, J. Chem. Phys. 22, 503 (1954).

18. S. N. Thakur and N. L Singh, Indian J. Pure Appl. Phys. 7, 765 (1969).

19. Y. Udagawa, M. Ito, and S. Nagakura, J. Mol. Spectrosc. 36, 541 (1970).

20. T. Cvitas and M. J. Hollas, Mol. Phys. 18, 793 (1970).

21. R. A. Coveleskie and C. S. Paramenter, J. Mol. Spectrosc. 86, 86 (1981).

22. C. Guttman and S. A. Rice, J. Chem. Phys. 61, 661 (1974).

23. L. J. Volk and E. K. C. Lee, J. Chem. Phys. 67, 236 (1977).

24. D. Phillips, M. G. Rockley, and M. D. Swords, Chem. Phys. 38, 301 (1979).

25. R. S. Mulliken, J. Chem. Phys. 23, 1997 (1955).

26. It appears that the calculated positions of the $3_n^0 5_1^{1,0} 6_1^{0,2}$ sequence shown in fig. 6 of reference 22 are too high by 858 cm^{-1}, the ν_5 fundamental frequency. Also the 0-0 single vibronic level fluorescence of the 5_3^0 transition is displaced 2595 cm^{-1} from 0_0^0 fluorescence, compared to the calculated value of 2574 cm^{-1}, indicating the possibility of perturbations of this level. These two clarifications bring the assignments of ref. 22 and this paper into agreement.

27. N. Ginsberg and F. A. Matsen, J. Chem. Phys. 13, 167 (1945).

28. J. C. D. Brand, D. R. Williams, and T. J. Cook, J. Molecular Spectroscopy 20, 359 (1966).

29. M. Quack and M. Stuckberger, J. Molecular Spectroscopy 43, 87 (1972).

30. K. Kimura, H. Tsubomura, and S. Nagakura, Bull. Chem. Soc. Japan 37, 1336 (1964).

31. K. Kimura and S. Nagokura, Molecular Phys. 9, 177 (1965).

32. K. Fuke and S. Nagakura, J. Molecular Spectrosc. 64, 139 (1977).

33. H. Von Weyssenhoff and F. Kraus, J. Chem. Phys. 54, 2387 (1971).

34. W. R. Wave and A. M. Garcia, J. Chem. Phys. 61, 187 (1974).

35. R. Scheps, D.Florida, and S. A. Rice, J. Chem. Phys. 61, 1730 (1974),

36. K. C. Cadogan and A. C. Albracht, J. Phys. Chem. 73, 1868 (1969).

Figure Captions

Figure 1. Experimental arrangement for photoacoustic detection of stimulated emission. The PUMP beam from dye laser #1 and the DUMP beam from dye laser #2 enter a photoacoustic cell collinearly from opposite directions. The various labels are defined as follows: A - aperture, BS - beamsplitter, C1 and C2 - KDP doubling crystals, D1 - pyroelectric energy probe, D2 - high speed photodiode, F1 and F4 - UV blocking filters, F2 and F3 - UV pass filters, HCL - Uranium/Neon Hollow Cathode Lamp, L1 and L2 - beam contracting telescope, L3 - 25 cm focal length lens, P - prism.

Figure 2. Pulsed photoacoustic spectrum of a portion of the $\tilde{X}^1A_{1g} \rightarrow \tilde{A}^1B_{2u}$ transition in p-difluorobenzene. The sample consisted of 0.022 torr p-difluorobenzene and 3.32 torr helium. The photoacoustic signal has been corrected for the variation of incident laser pulse energy with wavelength. The vibronic bands labeled by the letters a through k are also listed in Table I. Each letter designates the following vibronic transitions: a - 8_1^1, b - 30_3^3, c- 17_1^1, d - 30_2^2, e - 27_1^1, f - 30_1^1, g - 0_0^0, h - 6_0^1, i - $5_0^1 30_2^2$, j $5_0^1 30_1^1$, k - 5_0^1. The symbol N_i^j implies a transition with i quanta of mode N in the lower

level and j quanta of mode N in the upper level. The modes are numbered using the convention of Ref. 25.

Figure 3. Photoacoustic stimulated emission pumping spectrum of a 0.051 torr sample of p-difluorobenzene obtained by pumping the 5_0^1 transition at 37659 cm^{-1} and scanning the DUMP pulse wavelength. The upper and lower abscissae give the photon energy and wavelength of the DUMP pulse. The ordinates give the percent change in photoacoustic signal due to the stimulated emission process. The transition labels refer to transitions induced by the DUMP pulse. They are described in the caption for Fig. 2. (a) The DUMP pulse precedes the PUMP pulse by 20 nsec. (b) The DUMP pulse occurs 4 nsec after the PUMP pulse. (c) The DUMP pulse occurs 38 nsec after the PUMP pulse. In each spectrum the signal shown is the difference in photoacoustic signal produced by PUMP alone and PUMP plus DUMP. The difference signal has been corrected for variations in the DUMP laser pulse energy during the scan.

Figure 4. Time-resolved stimulated emission pumping photoacoustic spectrum of a 0.051 torr sample of p-difluorobenzene. The PUMP pulse excites the 5_0^1 transition at 37659 cm^{-1}. The DUMP pulse stimulates emission out of the 5^1-6^2 resonant levels down to

the $3_1 5_1 6_1$ level. The spectrum was generated by scanning the delay between the PUMP and DUMP pulses. The abscissa gives the time delay between the two pulses, $\Delta t = t_{DUMP} - t_{PUMP}$. The ordinate gives the percent change in photoacoustic signal due to the stimulated emission process. The photoacoustic signal has not been corrected for variations in the PUMP or DUMP pulse energies.

Figure 5. Time-resolved pulsed photoacoustic spectrum of a 0.378 torr sample of aniline. The PUMP photon excited the S_0 to S_1 0-0 transition at 34032 cm^{-1}. The DUMP photon energy was 18797 cm^{-1}. The spectrum was generated by scanning the time delay between the PUMP and DUMP pulses. The abscissa gives the time delay between the two pulses, $\Delta t = t_{DUMP} - t_{PUMP}$. The photoacoustic signal has not been corrected for variations in the PUMP or DUMP pulse energies.

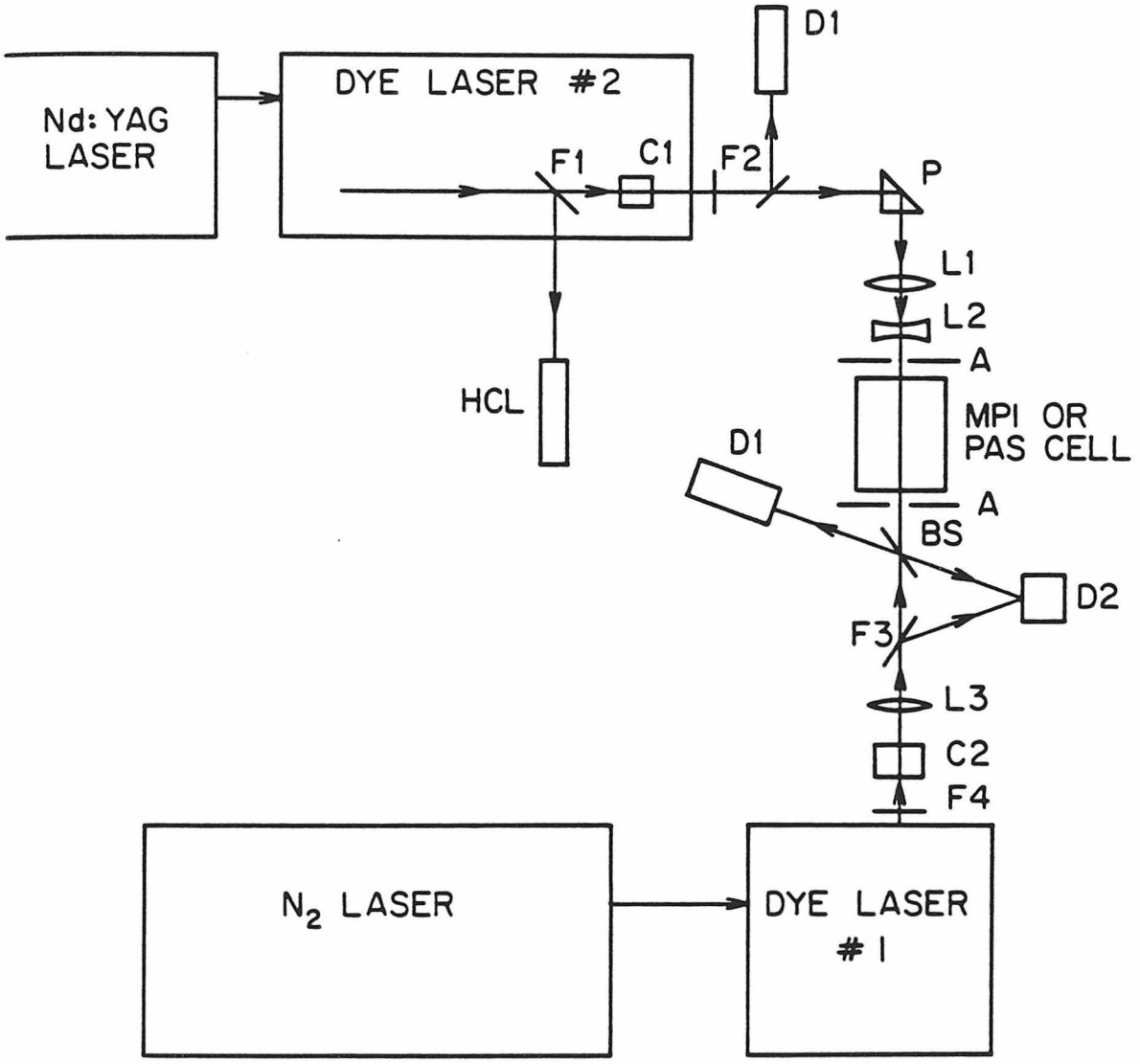
Nd: YAG
LASER
DYE LASER #2
D1
F1
C1
F2
P
L1
L2
A
HCL
MPI OR
PAS CELL
D1
A
BS
D2
F3
L3
C2
F4
N_2 LASER
DYE LASER
#1

Figure 1

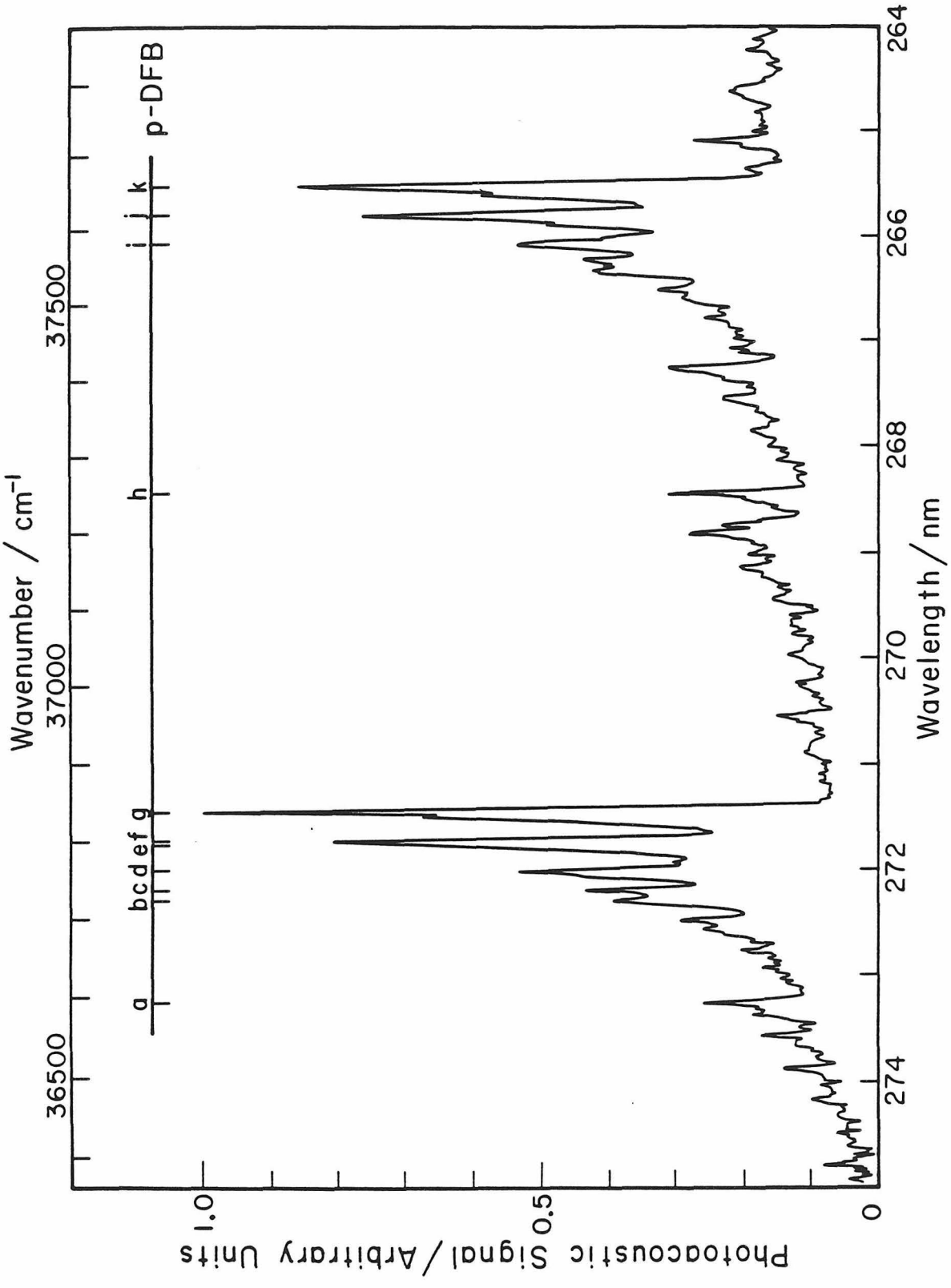
Wavenumber / cm⁻¹
36500
37000
37500
Wavelength / nm
264
266
268
270
272
274
a
b c d e f g
h
i j k
p-DFB
Photoacoustic Signal / Arbitrary Units
0
0.5
1.0

Figure 2

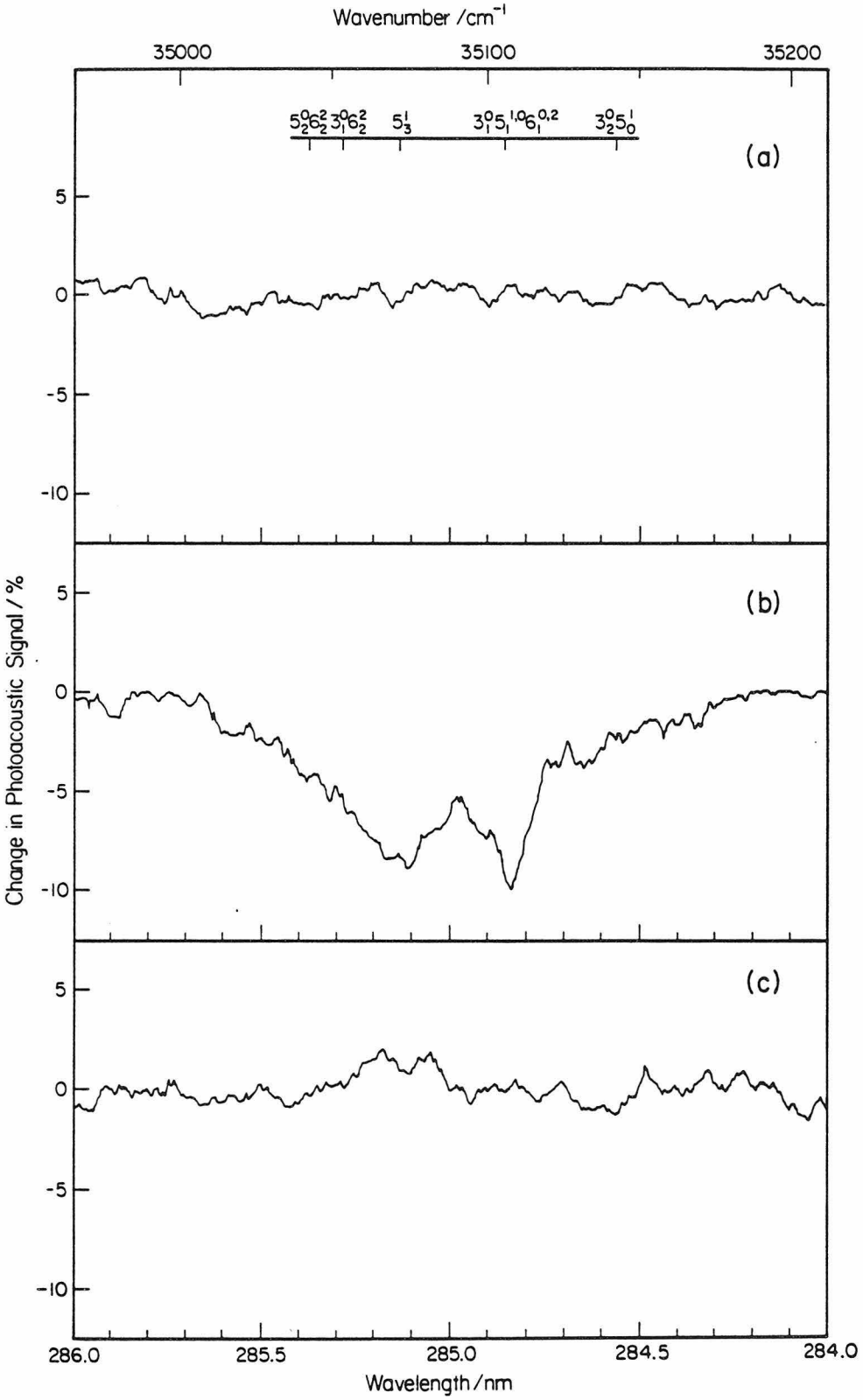
Wavenumber /cm⁻¹
35000
35100
35200
$5_2^0 6_2^2$ $3_1^0 6_2^2$ 5_3^1 $3_1^0 5_1^{1,0} 6_1^{0,2}$ $3_2^0 5_0^1$
(a)
(b)
(c)
5
0
-5
-10
Change in Photoacoustic Signal / %
286.0
285.5
285.0
284.5
284.0
Wavelength / nm

Figure 3

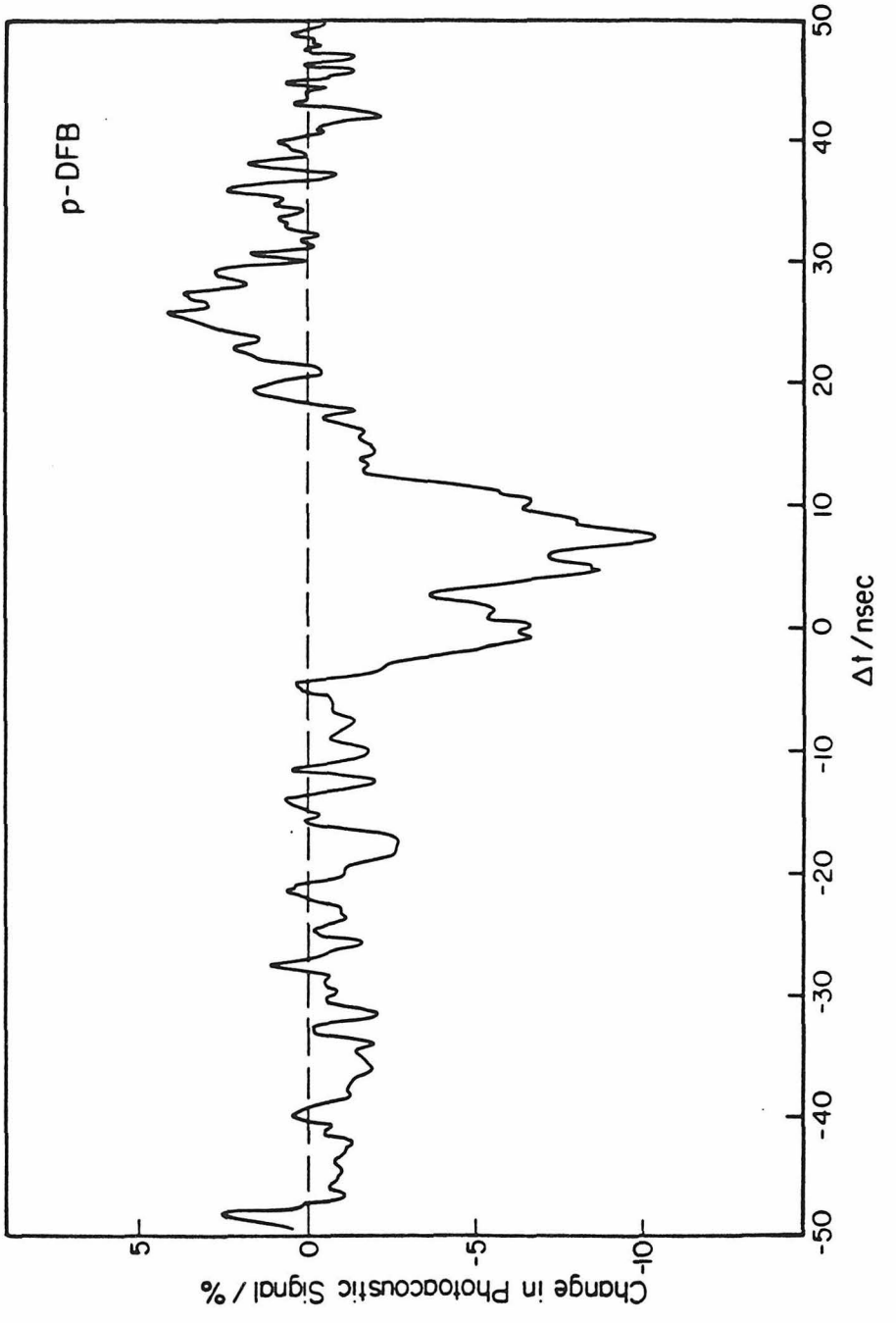
p-DFB
Change in Photoacoustic Signal / %
5
0
-5
-10
-50
-40
-30
-20
-10
0
10
20
30
40
50
Δt / nsec

Figure 4

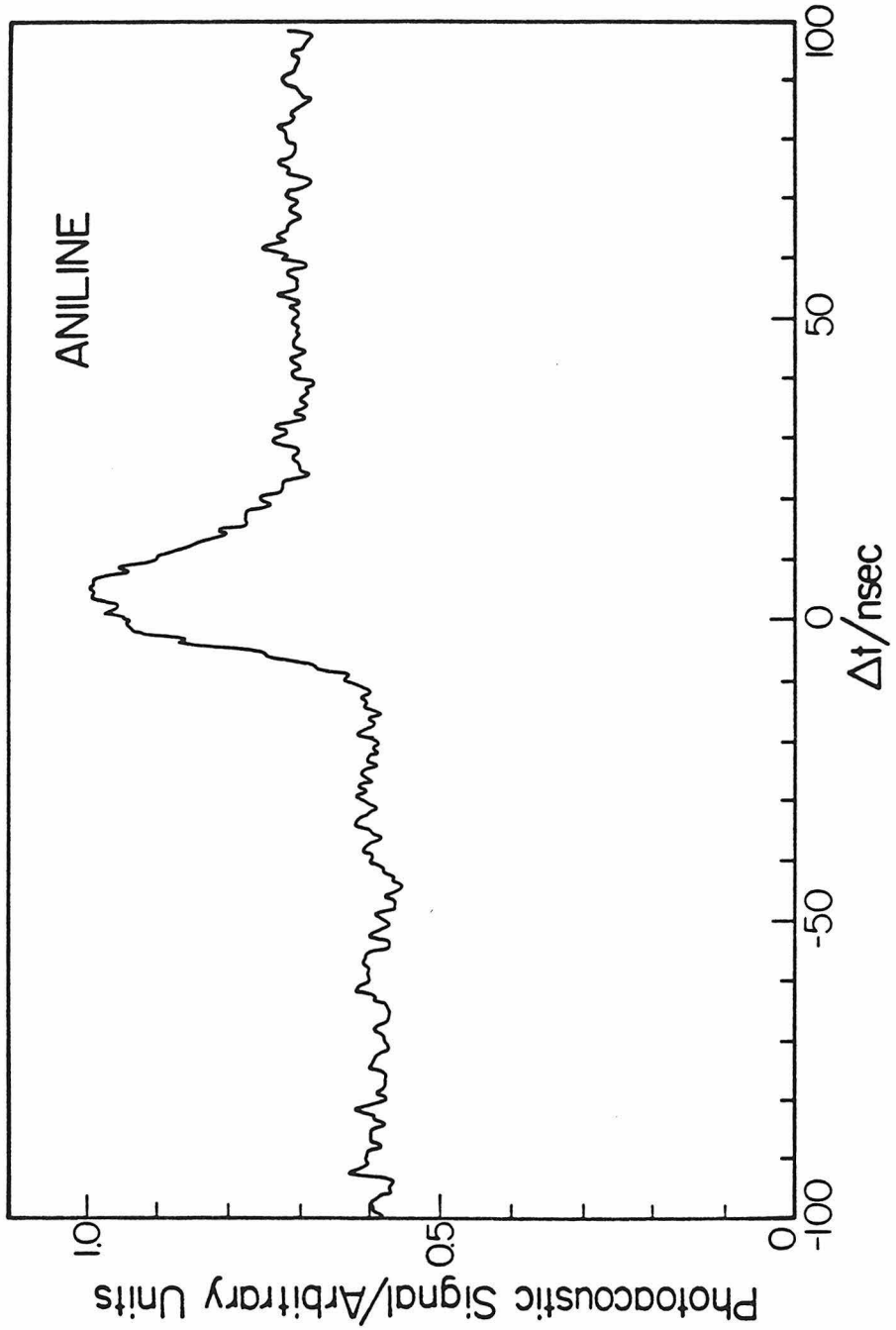
ANILINE
Photoacoustic Signal/Arbitrary Units
1.0
0.5
0
-100
-50
0
50
100
Δt/nsec

Figure 5

Paper III: Two-Color Time-Resolved Photoacoustic and Multiphoton Ionization Spectroscopy of Aniline.

Two-Color Time-Resolved Photoacoustic and Multiphoton Ionization Spectroscopy of Aniline[a)]

D. J. Moll[b)], G. R. Parker, Jr. and A. Kuppermann
Arthur Amos Noyes Laboratory of Chemical Physics[c)]
California Institute of Technology, Pasadena, CA 91125 USA

(Received

The multiphoton ionization and photoacoustic signals from aniline have been detected as a function of time delay between two laser pulses of different wavelength. The first pulse excited the S_1 0-0 transition. The second pulse excited either S_1 or a triplet state produced by intersystem crossing, depending on the delay time between pulses. Both ionization and dissociation processes are observed. By varying the conditions of excitation it appears that a given amount of energy can be selectively channeled almost exclusively into either ionization or dissociation pathways. The results are explained using a simple Franck-Condon factor model.

---

a) Research supported in part by the U. S. Department of Energy, (Contract No. DE-AS03-765F00767, Project Agreement No. DE-AT03-76ER720004).

b) Work performed in partial fulfillment of the requirements for the Ph. D. degree in Chemistry at the California Institute of Technology.

c) Contribution No.

I. INTRODUCTION

In typical multiphoton ionization (MPI) experiments, an intense UV or visible laser pulse is focused into a gaseous sample, producing an ionization current which is measured as a function of wavelength. When integral multiples of the photon energy are resonant with states in the sample an increase in ionization current occurs. Recent MPI experiments have detected the masses of fragments produced and/or the kinetic energy of released electrons in molecules such as NO,[1,2] I_2,[1,3] H_2S,[4] NH_3,[5] benzene,[1,3,6,7] acetaldehyde,[8] aniline,[9] azulene,[10] naphthalene,[10] and organometallics.[11] Three mechanisms have been proposed to explain the observed fragmentation: (1) multiple absorption of photons in neutral valence, Rydberg, and autoionizing states to produce superexcited states which eventually autoionize and dissociate into the observed fragments, (2) initial preparation of the parent ion by multiphoton absorption with subsequent absorption of more photons to dissociative or predissociative ionic states, and (3) dissociation from the neutral manifold before reaching the ionization potential (IP), followed by ionization or further dissociation of the fragments. There is strong evidence, particularly from MPI photoelectron studies, that indicates that most molecules follow mechanism (2) where ionization to the parent ion occurs as soon as sufficient energy to reach the IP of the molecule has been absorbed. Mechanism (1) has only been reported in a few scattered cases, as a minor process in MPI through the $A^2\Sigma^+$ (v=3) state of NO,[2] and in

azulene.[10] Mechanism (3) has been observed in weakly bound organometallic systems.[11]

This paper presents two-color time-resolved photoacoustic and MPI results on aniline which strongly support the presence of mechanism (3) in that molecule for excitation from a state prepared by intersystem crossing. In this specific case, the molecule is excited above the adiabatic IP, but dissociates almost exclusively into neutral fragments rather than ionizing. By varying the conditions of excitation in aniline, a given amount of energy can be channeled almost exclusively into either ionization or dissociation.

Aniline was initially selected for these experiments because of our interest in photoacoustic detection of stimulated emission pumping.[12] After initial excitation to a vibronic level in S_1 we observed only additional excitation to higher excited states, when a second laser pulse was introduced instead of stimulating emission back down to a vibrational level of the ground electronic state. An investigation of the excited state absorption phenomena is reported in this paper.

2. Background

The electronically excited states of aniline have been extensively studied by absorption,[13-20] emission,[21-30] and multiphoton techniques.[31-35] The lowest excited singlet ($^1B_2$) with a 0-0 transition at 34032 cm^{-1} exhibits a sharp single vibronic level absorption spectrum with a broad underlying continuum. Fluorescence lifetime and quantum yield measurements of single vibronic levels indicate a fluorescence lifetime ranging from 5.8 to 9.8 nsec, and a quantum yield for fluorescence ranging from 0.1 to 0.3.[24] The 0-0 level of S_1, which is used in this study, has a fluorescence lifetime and quantum yield of 8.57 nsec and 0.30, respectively.[24]

T_1 phosphorescence with a lifetime of 4.2 seconds has been observed from the low-lying $^3A_1$ state in aniline in solid solution at 77° K after exciting S_1.[28] The ratio of phosphorescence to fluorescence quantum yields was 3.1, and total luminescence quantum yields were estimated at close to one.[28] An additional low-lying T_2 state ($^3B_2$) was postulated to be isoenergetic with S_1 to explain early fluorescence lifetime data,[21] but no direct evidence for the location of that state has appeared. The energy of T_1 was determined from phosphorescence which places that state about 7200 cm^{-1} below S_1.[27]

Extrememly efficient 2-photon ionization has been observed for aniline using S_1 as an intermediate state, made possible by the low IP (62,100 cm^{-1} [36]) and the fully allowed nature of the transitions between S_0 and S_1.[31,32] At inten-

sities below 10 megawatts/cm^2 the parent ion accounted for 100% of the ion signal. When increased to 20 megawatts/cm^2 the parent ion still accounted for 85% of the ion signal.[32]

3. Experimental

The two-color time resolved photoacoustic and MPI experiments reported in this paper involved subjecting a gas phase sample of aniline to two counter-propagating collinear laser pulses with different wavelengths and variable delay Δt between them, adjustable with nanosecond precision. The resulting total ion current was measured as a function of Δt at different wavelengths using a simple parallel plate MPI cell. The energy deposited into the sample which was quickly transformed into translational energy of the gas molecules was detected as a pressure wave by a microphone in a photoacoustic cell. The amplitude of this pressure wave was also measured as a function of Δt at different wavelengths. Specific details of the experiments are discussed in the following sections.

3.1 Optics and Laser Systems

The experimental arrangement is shown in fig. 1. It consisted of 2 counterpropagating collinear beams from frequency doubled dye lasers which passed through either a photoacoustic cell or an MPI cell containing a gas phase sample of aniline. The PUMP pulse used to initially populate the S_1 state was supplied by dye laser #1 (DL1), a Molectron[37] model DL200 dye laser pumped by a Molectron UV400 N_2 laser. The output of DL1 was frequency doubled in a KDP crystal, collimated with a 25 cm focal length quartz lens, and directed into the sample cell. Using rhodamine 6G dye in ethanol,

typical UV pulse energies ranged from 0.5 to 10 μJ at the sample cell entrance. The TRANSFER pulse which transferred population from S_1 to a higher excited state was supplied by dye laser #2 (DL2), a Molectron model DL18 dye laser with an oscillator and single longitudinally pumped amplifier, pumped by a Molectron MY34 Nd:YAG laser. In some experiments the transfer pulse was the 2nd or 4th harmonic of the Nd:YAG laser. The TRANSFER pulse was directed into the opposite end of the sample cell after passing through a beam contracting telescope which matched the beam diameter of the doubled DL2 output to the 1 mm diameter beam of DL1.

PUMP and TRANSFER pulse energies were monitored off beamsplitters with a Laser Precision[38] pyroelectric joulemeter, model RkP-335, and Rk-3230 readout unit. The analog output from the readout unit was processed by a differential gated integrator system described later. Linewidths of all laser outputs were $<1\ cm^{-1}$.

Initial experiments indicated that the 2 lasers were interacting with each other due to the collinear counter-propagating beam arrangement. This was eliminated by using Corning 7-54 UV pass filters to block the visible output after each doubling crystal, and Corning 0160 glass before each doubling crystal to keep the UV produced by one laser from entering the other laser.

3.2 Timing Between Laser Pulses

The accuracy of the time delay $\Delta t = t_{transfer} - t_{pump}$

between the PUMP and TRANSFER pulses and the ability to continuously scan Δt were critical to the performance of these experiments. Three delay generators were used to control the timing between the 2 pulses. The first was triggered by the Nd:YAG flashlamp synchronization output and generated most of the 160 μsec delay before the Q-switch normally fires. After this initial delay, two fast-risetime delay generators (τ_r < 10 nsec)were used to independently trigger the Nd:YAG Q-switch and the N_2 laser thyratron. Long-term jitter in Δt, as monitored with a Hewlett Packard 5082-4220 PIN photodiode (-18 volt reverse bias, τ_r < 1 nsec), was less than ±2 nsec, with short term (10 seconds) jitter of ±1 nsec. Pulsewidths of the doubled output of each dye laser were ≤5 nsec. Nd:YAG 2nd and 4th harmonic pulsewidths were ~10 nsec.

The delay Δt between pulses was continuously scanned using a 1 revolution/hour clock-drive motor to turn the vernier delay knob of one of the delay generators. During the scan, absolute values of Δt were monitored with the photodiode and a 10 nsec risetime oscilloscope. The final data were replotted using a time axis generated by a polynomial fit of the Δt data points to correct for a small nonlinearity in the Δt scan system. The accuracy of the time values shown in the figures is estimated at ±2 nsec.

3.3 Photoacoustic Cell

Photoacoustic spectroscopy has been used in a variety of applications. Excellent reviews of the technique can be

found in ref. 39 and 40. The photoacoustic cell used in these experiments was similar to cells used previously.[41,42] The 18 cm long by .9 cm diameter cell was constructed of stainless steel and aluminum. Quartz windows were held in place at each end using Vitron o-rings. Since extreme sensitivity was not essential in working with the strong absorptions in aniline, the cell was designed to eliminate signals arising from scattering light striking the microphone or cell walls. Since most light scattering occurs at the windows, this was minimized by a series of apertures both inside the cell and out. The microphone, Knowles Electronics model BT 1759,[43] was located 6 cm away from the PUMP entrance window to minimize absorption of the PUMP pulse before it reached the vicinity of the microphone. The microphone was positioned over a 3/16" diameter hole in the cell wall and held in place with epoxy resin.

3.4 MPI Cell

The MPI cell was a simple biased parallel plate-type cell which has been described elsewhere.[44] Briefly, it consists of a stainless steel cell containing two parallel plates 0.75 in. square, separated by 0.75 in. and quartz windows. The plates are biased with 22.5 volts. The charge pulse is detected by a Canberra 2001A charge-sensitive preamplifier with a sensitivity of 10 V/picocoulomb. The slow decay time of the preamplifier (50 μsec) allows total integration of the charge produced by 2 laser pulses for $|\Delta t| < 1$ μsec.

3.5 Signal Processing

Signals from either the photoacoustic cell or the MPI cell were limited to a frequency range of typically 100 to 8×10^4 Hz by an electronic filter and then amplified. The peak of the first pressure wave of the photoacoustic signal or the peak of the MPI signal from the charge sensitive pre-amplifier were integrated by a differential gated integrator system with an integration window of 15 μsec. Signals from the pyro-electric joulemeter were processed in a similar manner by a second integrator system. A microcomputer digitized and stored the signals from both integrators at periodic time intervals approximately equal to the time constant of the gated integrators, as Δt was scanned.

3.6 Sample Preparation

Aniline was obtained from Mallinckrodt and subjected to a minimum of 4 liquid N_2 freeze-pump-thaw cycles and a vacuum distillation on a vacuum line operated at 5×10^{-7} torr before use. Samples were stored in darkness. When filling the MPI or photoacoustic cells, the final pressure was allowed to stabilize for several minutes before closing the cell valve to minimize wall absorption effects.

4. Results

The photoacoustic spectrum of a 0.37 torr sample of aniline in the region of the S_1 0-0 transition is shown in figure 2. Several of the prominent bands, including the 0-0 transition, are labeled according to the assignment of reference 14. This spectrum was obtained by scanning the wavelength of DL1.

The results presented in the following sections were obtained by pumping the 0-0 transition at 34032 cm^{-1} with the PUMP pulse and measuring the photoacoustic and MPI signals as a function of Δt for TRANSFER pulse wavelengths of 532 nm, ~305 nm, and 266 nm. The 0-0 transition was chosen for PUMP to avoid the effects of vibrational energy redistribution within S_1. Preliminary studies where higher vibrational levels of S_1 were pumped gave similar results to those described below.

4.1 532 nm TRANSFER Pulse

Fig. 3a shows the MPI time-resolved spectrum of aniline obtained by exciting the S_1 0-0 transition at 34,032 cm^{-1} with the PUMP pulse, using the Nd:YAG 2nd harmonic at 532 nm as the TRANSFER pulse, and varying Δt. For $|\Delta t| \geq 20$ nsec the MPI signal is due almost entirely to a 2-photon ionization with a one-photon resonance in S_1, induced by the PUMP pulse. The efficiency of this process required reducing the PUMP pulse energy to 0.5 μJ/pulse to avoid saturating the charge sensitive preamplifier, which occurs at ion yields greater than

10^7 ions/pulse. The 2 mJ transfer pulse produced no detectable ions at these sensitivities.

For $|\Delta t| < 5$ nsec, i.e. both pulses overlapped in time, a sharp decrease in ion yield greater than 25% is observed. This effect has been previously observed under beam conditions and attributed to competition between ionization from S_1 induced by a second PUMP photon, or excitation from S_1 to a rapidly predissociating state induced by the 532 nm TRANSFER pulse, as shown in figure 4.[9] The predissociation process is apparently fast enough that the molecule dissociates before another TRANSFER or PUMP photon can be absorbed to ionize the molecule. This mechanism is supported by VUV absorption studies[16,17,19] which show strong absorptions near 52,800 cm^{-1}, the presence of a photodecomposition film on the windows after extended data collection, and the photoacoustic measurements presented next. The N-H bond energy is only 28,000 cm^{-1}, making it the lowest energy dissociation pathway.[45,46]

Figure 3b shows the corresponding photoacoustic time-resolved spectrum. An <u>increase</u> of almost 70% in photoacoustic signal is observed near $\Delta t=0$. In addition, the signal for $\Delta t > 20$ nsec (TRANSFER pulse after PUMP pulse) is about 20% larger than for $\Delta t < -20$ nsec (TRANSFER pulse before PUMP pulse).

The pulsed photoacoustic technique is sensitive to energy deposited in the sample, but only to energy which is rapidly transformed into translation energy on the μsec timescale. Since the photoacoustic signal increased substantially for values of Δt where the ionization signal decreased, the photo-

acoustic detection technique appears to be much more sensitive to the dissociation process than to the ionization process. It is possible that the dissociation process channels a detectable amount of energy directly into translational energy of the fragments. Pressure waves from the vacuum UV photodissociation of O_2 have been predicted theoretically[47] and observed experimentally.[48] Non-dissociative excited states such as S_1 require collisional deactivation before the energy is released, a process which may be less efficient on the μsec timescale for pressures less than 0.5 torr. The ionization process may also be inefficient depending on recombination and electron attachment rates. The time dependence of the actual photoacoustic signal also supports the channeling of excitation energy into kinetic energy of the fragments. For values of Δt in fig. 3b where an increase in photoacoustic signal is seen, the pressure wave appears at the microphone about 2 μsec earlier than for excitation of S_1 alone or for $\Delta t < -20$ nsec. (In aniline at 0.37 torr we normally detect the pressure wave about 65 μsec after the laser pulse. This delay results from both collisional deactivation times and the transit time of the pressure wave from the laser beam to the microphone.). The 70% increase in photoacoustic signal for $\Delta t \simeq 0$ also supports the efficient release of kinetic energy through dissociation. For equal efficiencies of translational energy release the maximum increase in signal possible (every molecule excited by PUMP is also excited by TRANSFER) is 55%, based on photon energies.

To produce a 70% increase, a mechanism like dissociation must be occurring which releases translation energy more efficiently than the collisional deactivation of S_1.

In summary, the experimental evidence for PUMP and TRANSFER (532 nm) producing dissociation is: (1) an increase in photoacoustic signal occurs when a decrease in MPI signal is observed, (2) the pressure wave is detected about 2 μsec earlier, and (3) the signal increase caused by the TRANSFER pulse is larger than predicted by photon energy considerations alone.

From fluorescence and phosphorescence quantum yields and lifetimes it is known that the initially excited 0-0 level of S_1 disappears with a lifetime of 8.5 nsec due to intersystem crossing to a nearly triplet state, which is probably the $^3A_1$ state, and fluorescence.[24,28] The increase in photoacoustic signal near $\Delta t=0$ in fig. 3b is therefore due to excitation to a predissociative state from the 0-0 level of S_1 prepared by the PUMP pulse. For $\Delta t > 20$ nsec, the increase must be caused by triplet-triplet absorption from the state prepared by intersystem crossing from S_1. Triplet-triplet absorption in aniline has been observed from 320 to 600 nm in rigid solution at 77° K.[49] Our gas phase photoacoustic results indicate an absorption at 532 nm from a vibrationally excited triplet state to a predissociative triplet state. Fig. 4 is a diagram showing the processes occurring with the 532 nm TRANSFER pulse.

The differences in widths of the features at $\Delta t=0$ in figure 3a and 3b result from two different processes. In figure 3a, the MPI spectrum, there is competition between the ionization process occurring during the PUMP pulse. In figure 3b, however, the large increase in photoacoustic signal is produced from the S_1 population which has a longer lifetime than the PUMP pulsewidth.

4.2 305 nm TRANSFER Pulse

Figure 5a shows the MPI time-resolved spectrum of aniline obtained under conditions similar to the spectrum of figure 3a, except that now the TRANSFER pulse is near 305 nm. At this wavelength the TRANSFER pulse's photon energy falls just below the S_1 hot bands, but in combination with the 34032 cm^{-1} PUMP pulse, the molecule can be excited to about 4700 cm^{-1} above the adiabatic IP of 62100 cm^{-1}.[36]

In figure 5a the MPI signal shows an 8-fold increase in yield near $\Delta t=0$ which decays exponentially with a time constant of 8.9 ± 0.2 nsec back to the $\Delta t < 0$ signal level. This 8-fold increase is a strong contrast to the decrease observed using the 532 nm TRANSFER pulse. (The periodic oscillations in the decay curve are not reproducible and result from jitter in the PUMP pulse timing.) The figure 5a spectrum is insensitive to pressure over a range of 0.004 to 0.37 torr, and the decay time constant should be close to the 8.5 nsec fluorescence decay constant[24] of S_1 if laser pulsewidths are considered. This implies that after intersystem crossing

from the S_1 0-0 level, the TRANSFER pulse is no longer capable of efficiently ionizing the molecule.

From energy considerations alone there is no reason to expect the large decrease in ion yield for $\Delta t > 10$ nsec, since complete collisional deactivation of the vibrationally excited triplet produced by intersystem crossing is unlikely at 0.004 torr for timescales less than 50 nanoseconds, and there is no inherent reason why ionization from triplet states should be difficult.[44]

Consideration of vibrational effects offers an explanation of the inability to ionize the state produced by intersystem crossing. The initial excitation of S_1 produces a state whose energy is almost 100% electronic energy. The vibrational wavefunction for this state is a zero point energy wavefunction. During intersystem crossing to the $^3A_1$ state, the total energy remains the same, but 7200 cm^{-1} is converted from electronic to vibrational energy. The new vibrational wavefunction corresponds to a highly excited vibrational level with an energy of 7200 cm^{-1}. The probability of direct ionization involves the Franck-Condon factor between the ion and the level of the neutral molecule from which ionization occurred. Therefore for small changes in geometry between S_1, T_1, and the ion, the vertical IP from S_1 is expected to be about 7200cm^{-1} lower than the vertical IP from the state produced by intersystem crossing. Larger changes in geometry may decrease the 7200 cm^{-1} difference, but it is still likely that the 305 nm TRANSFER pulse can only ionize the S_1 state,

and not the vibrationally excited triplet state, by a direct ionization process. Even if Franck-Condon factors make the direct ionization process highly unlikely, there is still the possibility of absorption to a triplet quasidiscrete level above the adiabatic IP that rapidly undergoes an autoionization process. Photoelectron energy analysis following MPI through the $\tilde{B}$ state in ammonia provides an example of vibrational autoionization occurring from quasidiscrete levels.[5] A triplet quasidiscrete level must exist in aniline near 66800 cm^{-1} if the absorption from T_1 is to occur.

Figure 5b shows the time-resolved photoacoustic spectrum corresponding to the conditions of figure 5a. Two features are immediately obvious. First, the sharp increase in MPI signal observed in figure 5a does not appear. This agrees with the result of the previous section that the photoacoustic technique has a low sensitivity to ionization. It also implies that substantial amounts of dissociation are unlikely, in agreement with previous aniline MPI fragmentation studies.[31,32] Second, an inverse exponential increase occurs, starting near $\Delta t=0$, and rising to a 40% increase in signal on a time-scale similar to the decay observed in the figure 5a MPI spectrum. Figure 6 shows a spectrum similar to figure 5b which covers a larger range of Δt. The photoacoustic signal increase for $\Delta t > 0$ is long-lived, lasting at least 10-15 μsec. The observed decay may be an artifact of our photoacoustic detection technique caused because the pressure waves created by the PUMP and TRANSFER pulses no longer arrive at the

microphone within the integration gate, or because of diffusion of the initially excited molecules out of the laser beam region. The decay rate did not change when an electric field of 80 volts/cm was applied, indicating that the increase in photoacoustic signal is not caused by absorption of the TRANSFER pulse by ions resulting from the PUMP pulse.

The photoacoustic results imply that the triplet state produced by intersystem crossing is long-lived (>10 μsec) in the gas phase, and that it does absorb the 305 nm TRANSFER pulse. This absorption must populate a quasidiscrete level above the adiabatic IP which, according to the MPI results, does not ionize. Autoionizing molecular states are expected to have lifetimes[50] shorter than 10^{-13} sec. The only process that could compete effectively with the formation of ions on that timescale would be a fast dissociation process. H_2 photodissociation quantum yields of 10% have been measured both for single photon absorption above the IP,[51] and MPI processes above the IP.[52] The photoacoustic pressure wave reaches the microphone about 2 μsec earlier for $\Delta t > 10$ nsec, as expected for a dissociation process, as discussed in section 4.1. Further support for the dissociation mechanism comes from the photoproduct analysis discussed in section 5.

Figure 7 depicts the processes involved in the 305 nm TRANSFER pulse experiments. It is interesting that a given amount of energy can be deposited into aniline and selectively channeled either into ionization or dissociation channels almost exclusively, depending on the way in which the

energy is put into the molecule. Pumping the molecule up through the singlet manifold channels the energy into ionization. Introducing a delay of >10 nsec in the middle of the excitation process allows an intersystem crossing process to select a new electronic manifold of states and converts some electronic energy into vibrational energy. The additional excitation now is directed into a dissociative channel.

Attempts were made to detect stimulated emission in aniline using the photoacoustic detection technique as was demonstrated in ref. 12. By using the PUMP laser to excite the 0-0 level of S_1 and scanning the TRANSFER laser from 305.5 nm to 300.5 nm with Δt=2-4 nsec, we hoped to stimulate emission using the fluorescence lines observed near 302.5 nm.[26] No decreases in photoacoustic signal were observed. Instead, we detected weak hot band absorption to S_1 and a small wavelength independent increase in photoacoustic signal caused by the excited state absorption from the small triplet population produced at the values of Δt we used.

4.3 266 nm TRANSFER Pulse

Figure 8 shows a time-resolved MPI system obtained by again pumping the 0-0 transition of S_1, but using a TRANSFER pulse at 266 nm, the 4th harmonic of the Nd:YAG laser. Excitation by both the PUMP and TRANSFER pulses brings aniline about 9500 cm^{-1} above its adiabatic IP, enough excess energy to ionize either S_1 or T_1 by a direct ionization process. As expected, for all values of $\Delta t > 0$ an increase in MPI

signal is observed. For Δt near 0 a 100% increase in MPI signal is observed, corresponding to excitation from S_1. For $\Delta t > 25$ nsec, a 15% increase in MPI signal occurs, implying that the triplet is finally being ionized. The signal to noise ratio in the spectrum of figure 8 is low, but the increase in signal for $\Delta t > 25$ nsec was reproducible in the several scans attempted.

One could ask why the 266 nm pulse does not excite molecules which can be ionized by the PUMP pulse for $\Delta t < 0$. Photoacoustic signals produced by the 266 nm pulse alone arrive at the microphone 2-3 μsec earlier than for excitation of the S_1 0-0 transition. 266 nm excites aniline to a state which has an energy about 9,600 cm^{-1} above the N-H bond energy, and the absorption spectrum has become broad and diffuse at that energy.[24] Therefore we tentatively feel that the state excited by 266 nm alone may predissociate with a reasonable quantum yield, decreasing the ion yield from subsequent ionization by the PUMP pulse for $\Delta t < 0$.

The photoacoustic time-resolved spectrum using the 266 nm transfer pulse is almost flat for $-100 < \Delta t < 100$ nsec for conditions similar to those in figure 3b or figure 5b. A slight increase of ~1% may occur for $\Delta t > 0$, but this effect is almost obscured by noise. The 266 nm pulse alone, as mentioned earlier, does produce a pressure wave which arrives at the microphone 2-3 μsec before the pressure wave due to excitation of the S_1 0-0 transition. This may imply dissociation. From energy considerations and the MPI spectrum of

figure 8 we expect molecules excited by both the 266 nm and 305 nm pulses to predominantly ionize. Since the photoacoustic technique is not highly sensitive to ionization in aniline, the increase in signal from excited state absorption is expected to be small.

5. Photoproduct Detection

The two alternative pathways described in section 4.2 lead predominantly to ions or neutral fragments, depending on the excitation scheme employed. We attempted a mass spectrometric product analysis after irradiating under case (A) conditions, which should produce predominantly ions (Δt= 0-5 nsec, TRANSFER pulse λ= 305 nm),or under case (B) conditions which should produce neutral fragments (Δt=100 nsec, TRANSFER pulse λ= 305 nm). In both cases, the PUMP pulse was tuned to the S_1 0-0 transition. Two new matched quartz absorption cells (1 inch diameter × 4 inches long) with teflon stopcocks were filled simultaneously with typically 0.37 torr aniline, and 0.10 torr He for a reference gas. Irradiation times were 45 minutes at 10 Hz repetition rate with pulse energies of about 3 μJ and 500 μJ for PUMP and TRANSFER pulses, respectively. After irradiation, the He/H_2 ratio was measured after liquid N_2 trapping of other photoproducts, and also the entire mass spectrum of the samples was recorded. Preliminary results indicate that more H_2 is produced for case (B) conditions than for case (A). Case (B) conditions also produce a small amount of product with a m/e peak at 114, which is not produced under case (A) conditions. H_2 could be produced by breaking a N-H or C-H bond, followed by the H atom extracting another H atom during a reactive collision. The mass 114 peak is more difficult to explain. Several molecules with the formula $C_6H_{14}N_2$ are known to give strong mass 114 peaks,[53,54] but producing these molecules

from aniline requires breaking the aromatic ring and addition of more H atoms. The results presented here are only preliminary, and we are investigating other more direct ways of monitoring the fragmentation process in aniline.

6. Conclusions

The two-color time-resolved photoacoustic and MPI results presented in this paper give indirect but strong evidence for both ionization and dissociation occurring in aniline for energies slightly above the adiabatic IP. By simply varying the delay time Δt between the PUMP and TRANSFER pulses the energy can be selectively channeled almost exclusively into either ionization or dissociation. This selectivity is believed to occur because conversion of a large amount of electronic energy into vibrational energy takes place during intersystem crossing, and thereby alters the Franck-Condon factors for direct ionization and increases the energy of the vertical IP. The intersystem crossing also transfers the electronic energy into a different manifold of electronic states. The ability to channel a given amount of energy selectively into either ionization or dissociation channels is an exciting possibility for the field of laser selective chemistry.

The decay of ionization signal during intersystem crossing does not seem to be an artifact of aniline alone. Fig. 9 shows preliminary results on benzene obtained by pumping the $\tilde{X}^1A_{1g} \rightarrow \tilde{A}^1B_{2u}\, \nu'_{18}$ -0 transition in benzene,[55] and using a 266 nm TRANSFER pulse. The ionization signal decays exponentially with a time constant of 82 ± 2 nsec, in close agreement to the observed fluorescence lifetime of 79 nsec.[56] Previous two-color MPI experiments on azulene and benzophenone, however, did not detect exponential decays in ionization signal,[10] Since the Franck Condon factor explanation of the

observed MPI signal decays holds for internal conversion as well as intersystem crossing, the two-color time-resolved MPI technique may be a powerful tool for investigating ultrafast internal conversion processes using picosecond lasers.

Additional experiments are needed to completely understand the excited state dynamics in aniline near its IP. Two-color time-resolved MPI studies with photoelectron energy analysis and mass analysis of fragments are logical next steps to increase our understanding.

1) L. Zandee and R. B. Bernstein, J. Chem. Phys. 71, 1359 (1979).

2) J. C. Miller and R. N. Compton, J. Chem. Phys. 75, 22 (1981).

3) J. C. Miller and R. N. Compton, J. Chem. Phys. 75, 2020 (1981).

4) J. C. Miller, R. N. Compton, T. E. Carney, and T. Baer, J. Chem. Phys. 76, 5648 (1982).

5) J. H. Glownia, S. J. Riley, S. D. Colson, J. C. Miller, and R. N. Compton, J. Chem. Phys. 77, 68 (1982).

6) U. Boesl, J. J. Neusser, and E. W. Schlag, Chem. Phys. 55, 193 (1981).

7) J. T. Meek, R. K. Jones, and J. P. Reilly, J. Chem. Phys. 73, 3503 (1980).

8) G. J. Fisanick, T. S. Eichelberger IV, B. A. Heath, and M. B. Robin, J. Chem. Phys. 72, 5571 (1980).

9) T. G. Dietz, M. A. Duncan, M. G. Liverman, and R. E. Smalley, Chem. Phys. Lett. 70, 246 (1980).

10) D. M. Lubman, R. Naaman, and R. N. Zare, J. Chem. Phys. 72, 3034 (1980).

11) G. J. Fisnick, A. Gedanken, T. S. Eichelberger IV, N. A. Kuebler, and M. B. Rovin, J. Chem. Phys. 75, 5215 (1981).

12) D. J. Moll, G. R. Parker, Jr. and A. Kuppermann, "Photoacoustic Detection of Stimulated Emission Pumping in p-Difluorobenzene", to be published.

13) N. Ginsberg and F. A. Matsen, J. Chem. Phys. 13, 167 (1945).

14) J. C. D. Brand, D. R. Williams, and T. J. Cook, J. Molecular Spectrosc. 20, 359 (1966).

15) A. Amirav, U. Even, and J. Jortner, Chem. Phys. Lett. 83, (1981).

16) K. Kimura, J. Tsubomura, and S. Nagadura, Bull. Chem. Soc. Japan 37, 1336 (1964).

17) K. Kimura and S. Nafakura, Molecular Phys. 9, 117, (1965).

18) H. Tsubomura and T. Sakata, Chem. Phys. Lett. 21, 511 (1973).

19) K. Fuke and S. Nagakura, J. Molecular Spectrosc. 64, 139 (1977).

20) N. Mikami, A. Hiraya, I. Fujiwara, and M. Ito, Chem. Phys. Lett. 74, 531 (1980).

21) H. Von Weyssenhoff and F. Kraus, J. Chem. Phys. 54, 2387 (1971).

22) M. Quack and M. Stockburger, J. Molecular Spectrosc. 43, 87 (1972).

23) W. R. Wave and A. M. Garcia, J. Chem. Phys. 61, 187 (1974).

24) R. Scheps, D. Florida, and S. A. Rice, J. Chem. Phys. 61, 1730 (1974).

25) M. Jacon, C. Fardeux, R. Lopes-Delfado, and A. Tramer, Chem. Phys. 24, 145 (1977).

26) D. A. Chernoff and S. A. Rice, J. Chem. Phys. 70, 2511 (1979).

27) G. N. Lewis and M. Kasha, J. Am. Chem. Soc. 66, 2100 (1944).

28) V. L. Ermolaev, Opt. Spectrosc. (USSR) 11, 266 (1961).

29) E. C. Lim and S. K. Chakrabarti, J. Chem. Phys. 47, 4726 (1967).

30) V. I. Stenberg, S. P. Singh, and P. J. Kothari, Spectrosc. Lett. 11, 731 (1978).

31) J. Brophy and C. T. Rettner, Chem. Phys. Lett. 67, 351 (1979).

32) T. G. Deitz, M. A. Duncan, M. G. Liverman, and R. E. Smalley, Chem. Phys. Lett. 70, 246 (1980).

33) L. Goodman and R. P. Rava, J. Chem. Phys. 74, 4826 (1981).

34) D. Proch, D. M. Rider, and R. N. Zare, J. Photochemistry 17, 249 (1981).

35) S. Leutwyler and U. Even, Chem. Phys. Lett. 81, 578 (1981).

36) K. Watanake, T. Nakayama, and J. Mottl, J. Quant. Spectrosc. Radiative Transfer 2, 369 (1962).

37) Molectron Corp., 177 North Wolfe Rd., Sunnyvale, California 94086, USA.

38) Laser Precision Corp. 1231 Hart St., Utica, New York

39) Optoacoustic Spectroscopy and Detection, Yoh-Han Pao, edit. (Academic Press, New York, New York, 1977).

40) A. Rosenwaig, Photoacoustics and Photoacoustic Spectroscopy, (John Wiley and Sons, New York, 1980).

41) G. A. West, D. R. Sievert, and J. J. Barrett, J. Appl. Phys. 51, 2823 (1980).

42) D. J. Moll, J. W. Perry, A. Kuppermann, and A. H. Zewail, "High Overtone Photoacoustic Spectroscopy of Some Methyl-Containing Molecules. I. Rotational Analysis." To be published.

43) Knowles Electronics, Inc., 3100 N. Mannheim Rd., Franklin Prk, Illinois 60131, USA.

44) R. Rianda, D. J. Moll, and A. Kuppermann, Chem. Phys. Lett. 73, 469 (1980).

45) S. W. Benson and H. E. O'Neal, Kinetic Data on Gas Phase Unimolecular Reactions, National Bureau of Standards Washington, DC, NSEDS-NBS 21, 1970.

46) J. A. Kerr, Chem. Rev. 66, 465 (1966).

47) W. Zuzak and B. Ahlborn, Physica 41, 193 (1969).

48) R. C. Cross and R. Ardila, Can. J. Phys. 48, 2640(1970).

49) K. C. Cadogan and A. C. Albrecht, J. Phys. Chem. 73, 1868 (1969).

50) J. W. Rabalais, Principles of Ultraviolet Photoelectron Spectroscopy (Wiley, New York 1977), p. 78.

51) J. E. Mentall and E. P. Gentieu, J. Chem. Phys. 52, 5641 (1970).

52) S. T. Pratt, P. M. Dehmer, and J. L. Dehmer, "Resonant Multiphoton Ionization of H_2 via the $B^1\Sigma_u^+$, v=7, J=2 and 4 levels with Photoelectron Energy Analysis", submitted to J. Chem. Phys.

53) A. Cornu and R. Massot, Compilation of Mass Spectral Data, Vol. 2, 2nd edit. (Heyden and Sons, New York, 1975).

54) S. R. Heller and G. W. A. Milne, EPA/NIH Mass Spectral Data Base, Vol. 1, NSRDS-NBS63 (1978).

55) G. Herzberg, Molecular Spectra and Molecular Structure III. Electronic Spectra and Electronic Structure of Polyatomic Molecules, (Van Nostrand Reinhold Co., New York, 1966), p. 178.

56) K. G. Spears and S. A. Rice, J. Chem. Phys. 55, 5561 (1971).

Figure Captions

Figure 1. Experimental arrangement for two-order time-resolved photoacoustic and multiphoton ionization experiments. The PUMP beam from dye laser #1 and the TRANSFER beam from dye laser #2 enter a photoacoustic spectroscopy (PAS) or multiphoton ionization (MPI) cell collinearly from opposite directions. The various labels are defined as follows: A - aperture, BS - beamsplitter, C1 and C2 - KDP doubling crystals, D1 - pyroelectic energy probe, D2 - high speed photodiode, F1 and F4 - UV blocking filter, F2 and F3 - UV pass filter, HCL - uranium/neon hollow cathode lamp, L1 and L2 - beam contracting telescope, L3 - 25 cm focal length lens, P - prism.

Figure 2. Pulsed photoacoustic spectrum of a portion of the $\tilde{X}^1A_1 \rightarrow \tilde{A}^1B_2$ transition in aniline obtained using a 0.37 torr sample pressure. The photoacoustic signal has been corrected for the variation in incident laser pulse energy with wavelength. Pulse energies ranged from 1 to 10 μJ. The vibronic bands are labeled by the symbol $k^{v'}_{v''}$ which implies a transition from v'' quanta in mode k in the ground electronic state to an excited electronic state with v' quanta in mode k. I represents the NH_2 out-of-plane rocking mode. 6a and 12 represent a_1 symmetry ring modes. 1 represents a ring-stretching mode. The assignment was taken from Ref. 14.

Figure 3. Two-color time-resolved spectra of aniline. The PUMP pulse excites the $S_0 \rightarrow S_1$ 0-0 transition at 34,032 cm^{-1}. The TRANSFER pulse photon energy is 18,797 cm^{-1} (532 nm). The abscissa gives the time delay between pulses, $\Delta t = t_{TRANSFER} - t_{PUMP}$. (a) Multiphoton ionization detection. The sample pressure was 0.010 torr. PUMP and TRANSFER pulse energies were 0.5 μJ and 2.0 mJ, respectively. (b) Photoacoustic detection. The sample pressure was 0.38 torr. PUMP and TRANSFER pulse energies were approximately 5.4 μJ and 6.5 mJ, respectively. Both spectra have not been corrected for fluctuations in pulse energy.

Figure 4. Energy level diagram which shows the excitation processes corresponding to the spectra of Fig. 3. The PUMP and TRANSFER pulses have photon energies of 34,032 cm^{-1} and 18,797 cm^{-1}, respectively.

Figure 5. Two-color time-resolved spectra of aniline. The PUMP pulse excites the $S_0 \rightarrow S_1$ 0-0 transition at 34,032 cm^{-1}. The TRANSFER pulse photon energy is 32,787 cm^{-1} (305 nm). The abscissa gives the time delay between pulses, $\Delta t = t_{TRANSFER} - t_{PUMP}$. (a) Multiphoton ionization detection. The sample pressure was 0.004 torr. PUMP and TRANSFER pulse energies were 0.4 μJ and 13 μJ, respectively. (b) Photoacoustic detection. The sample pressure

was 0.37 torr. PUMP and TRANSFER pulse energies were 5.2 μJ and 300 μJ, respectively. The dashed line gives the expected noise-free signal. Both spectra have not been corrected for fluctuations in pulse energy.

Figure 6. Two-color time-resolved photoacoustic spectrum of aniline. The conditions are similar to those of Fig. 5b except that a wider range of Δt is shown. The dashed line indicates the expected signal if noise is removed. The downward drift for $\Delta t > 5$ μsec is discussed in Section 4.2.

Figure 7. Energy level diagram which shows the excitation processes corresponding to the spectra of Fig. 5a, 5b and 6. The PUMP and TRANSFER pulses have photon energies of 34, 032 cm^{-1} and 32,787 cm^{-1}, respectively. The potential curves and vibrational levels do not correspond to known molecular parameters.

Figure 8. Two-color time-resolved MPI spectrum of 0.004 torr sample of aniline. The 1.2 μJ PUMP pulses excites the $S_0 \rightarrow S_1$ 0-0 transition at 34,032 cm^{-1}. The 6.2 μJ TRANSFER pulses have photon energies of 37590 cm^{-1} (266 nm). The abscissa gives the time delay between pulses, $\Delta t = t_{TRANSFER} - t_{PUMP}$. The spectrum has not been corrected for fluctuations in pulse energies.

Figure 9. Two-color time-resolved MPI spectrum of a 0.021 torr sample of benzene. The 0.6 μJ PUMP pulses excited the $\tilde{X}^1A_{1g} \rightarrow \tilde{A}^1B_{2u}$ ν'_{18}-0 transition at 38607 cm^{-1}. The 1.4 μJ TRANSFER pulses had photon energies of 37590 cm^{-1} (266 nm). The abscissa gives the time delay between pulses, Δt - $t_{TRANSFER}$ - t_{PUMP}. The spectrum has not been corrected for fluctuations in pulse energies.

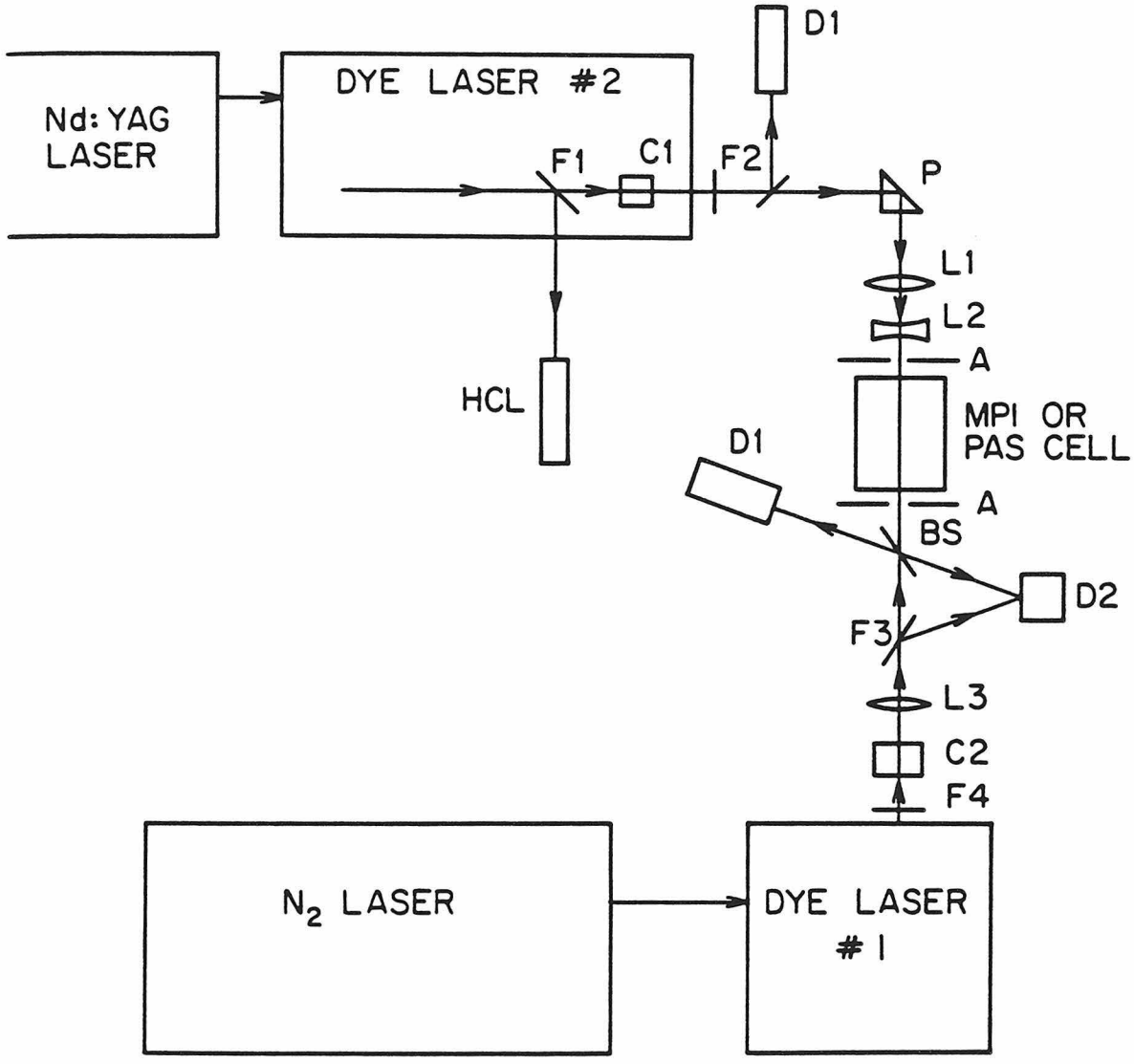
Nd: YAG
LASER
DYE LASER #2
F1
C1
F2
D1
P
L1
L2
A
MPI OR
PAS CELL
A
BS
D2
F3
L3
C2
F4
HCL
D1
N_2 LASER
DYE LASER
#1

Figure 1

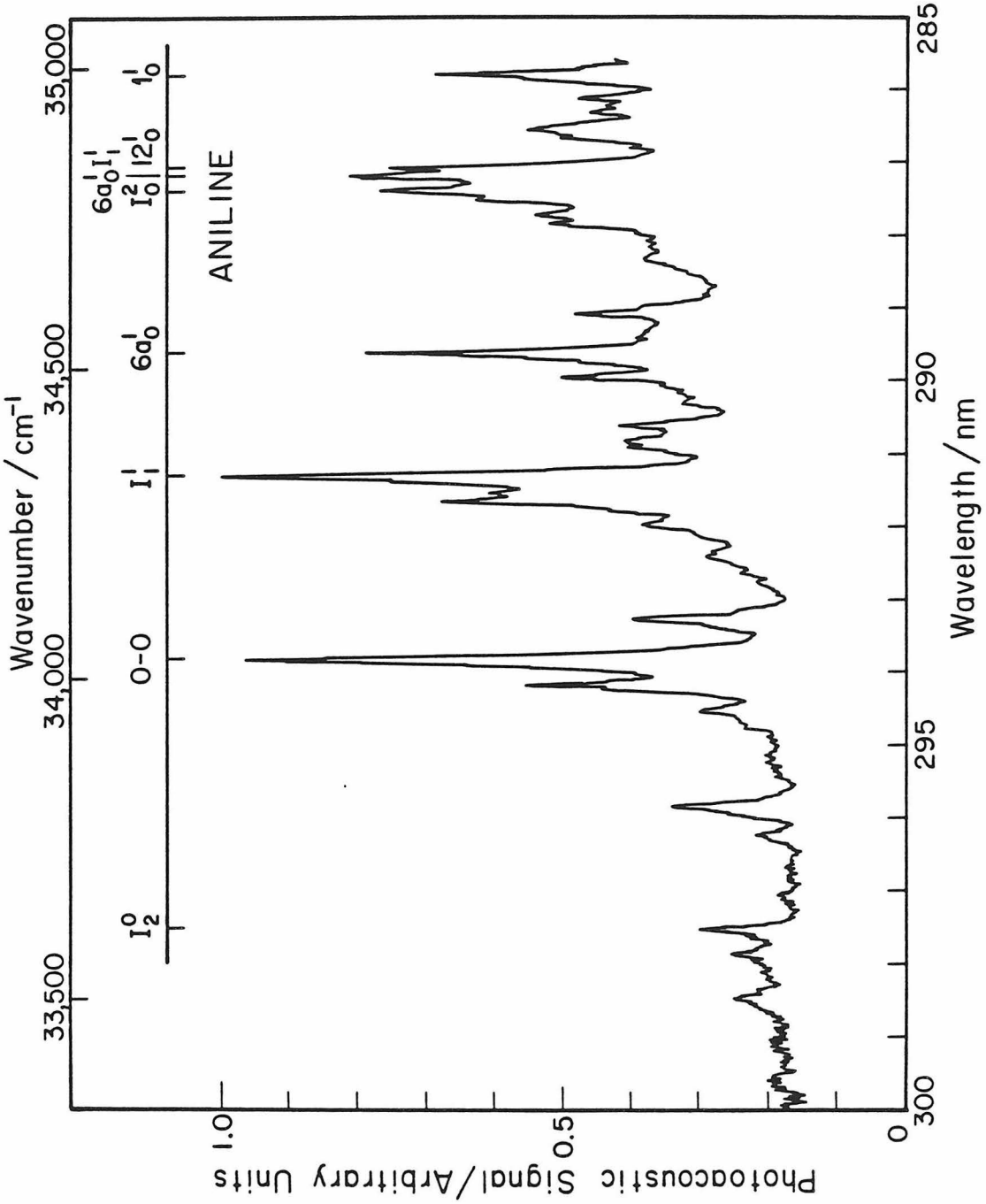
ANILINE
0-0
I_2^0
I_1^1
$6a_0^1$
$6a_0^1I_1^1$
$I_0^2|12_0^1$
1_0^1
Wavenumber / cm^{-1}
33,500
34,000
34,500
35,000
Wavelength / nm
285
290
295
300
Photoacoustic Signal/Arbitrary Units
0
0.5
1.0

Figure 2

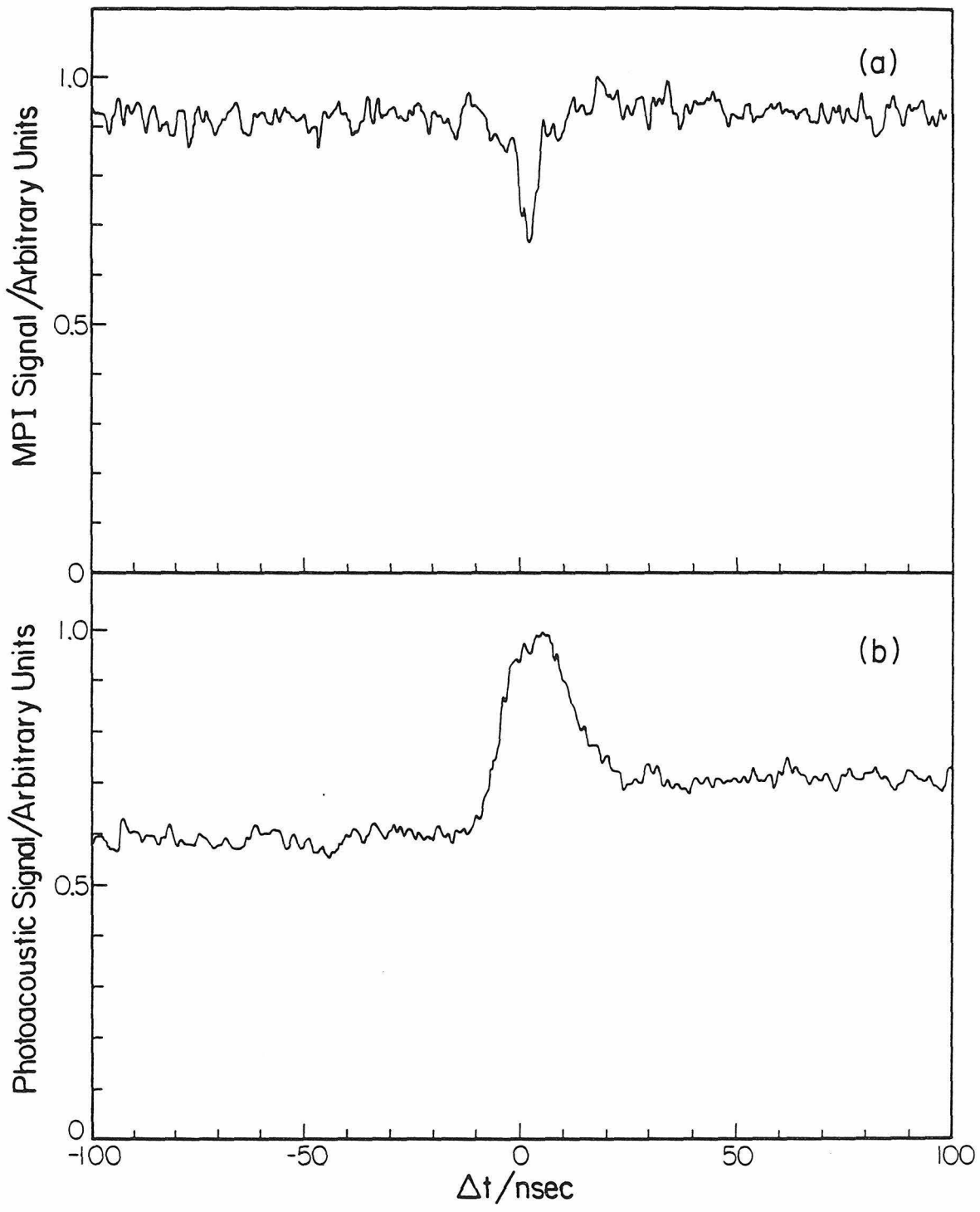
(a)
1.0
0.5
0
MPI Signal /Arbitrary Units
(b)
1.0
0.5
0
Photoacoustic Signal/Arbitrary Units
-100
-50
0
50
100
Δt/nsec

Figure 3

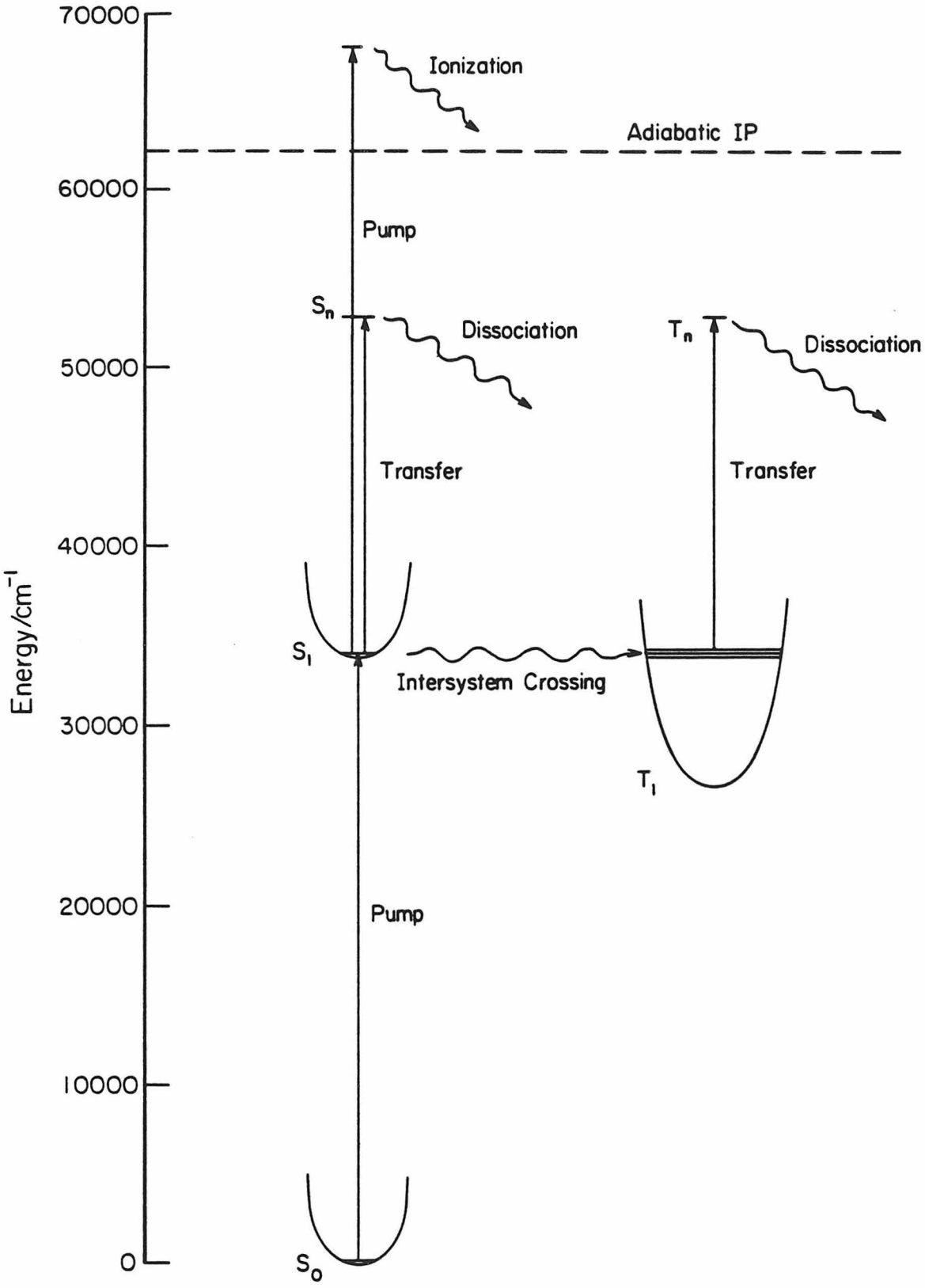
70000
60000
50000
40000
30000
20000
10000
0
Energy/cm⁻¹
Ionization
Adiabatic IP
Pump
Sn
Dissociation
Tn
Dissociation
Transfer
Transfer
S1
Intersystem Crossing
T1
Pump
S0

Figure 4

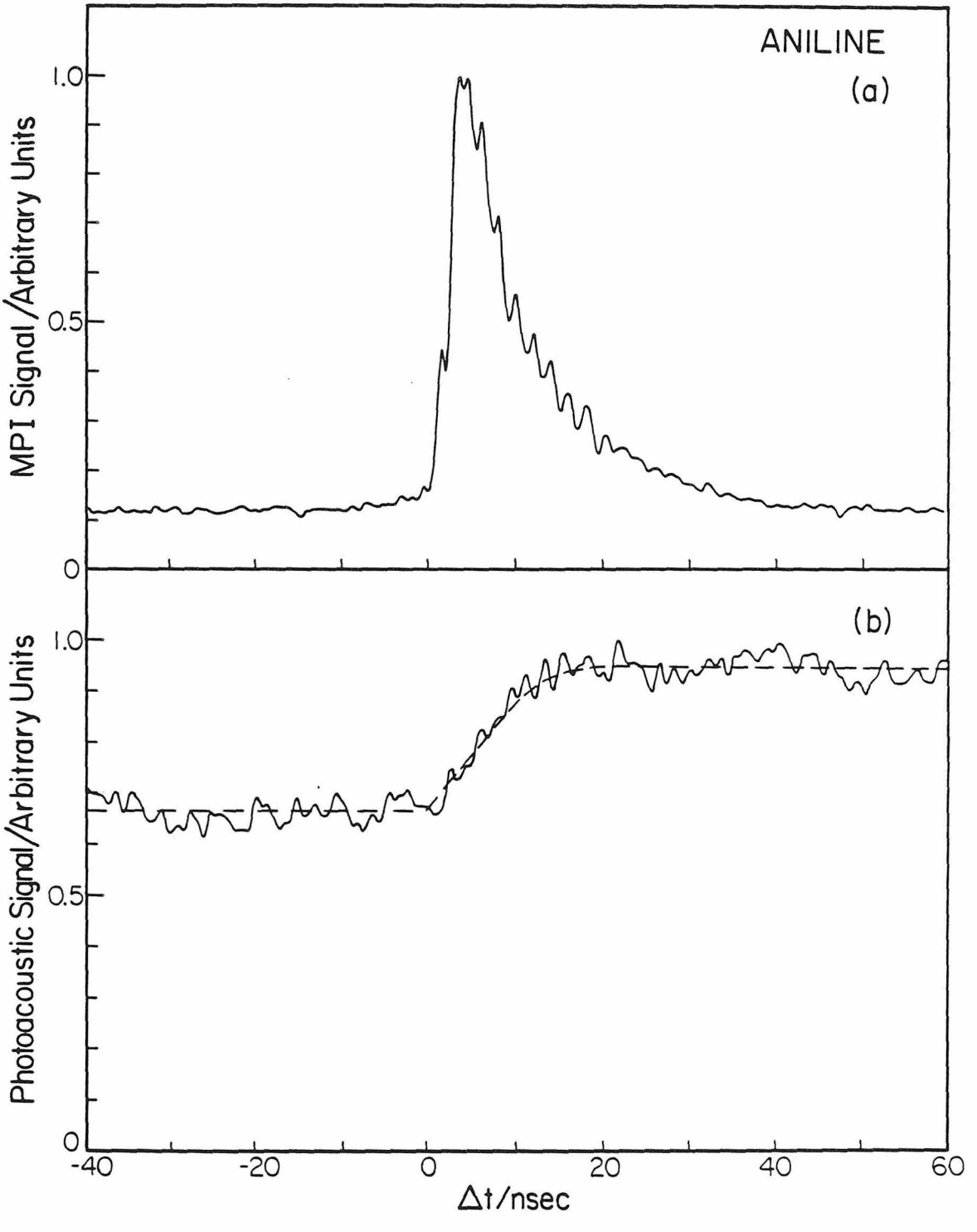
ANILINE
(a)
MPI Signal /Arbitrary Units
1.0
0.5
0
(b)
Photoacoustic Signal/Arbitrary Units
1.0
0.5
0
-40
-20
0
20
40
60
Δt/nsec

Figure 5

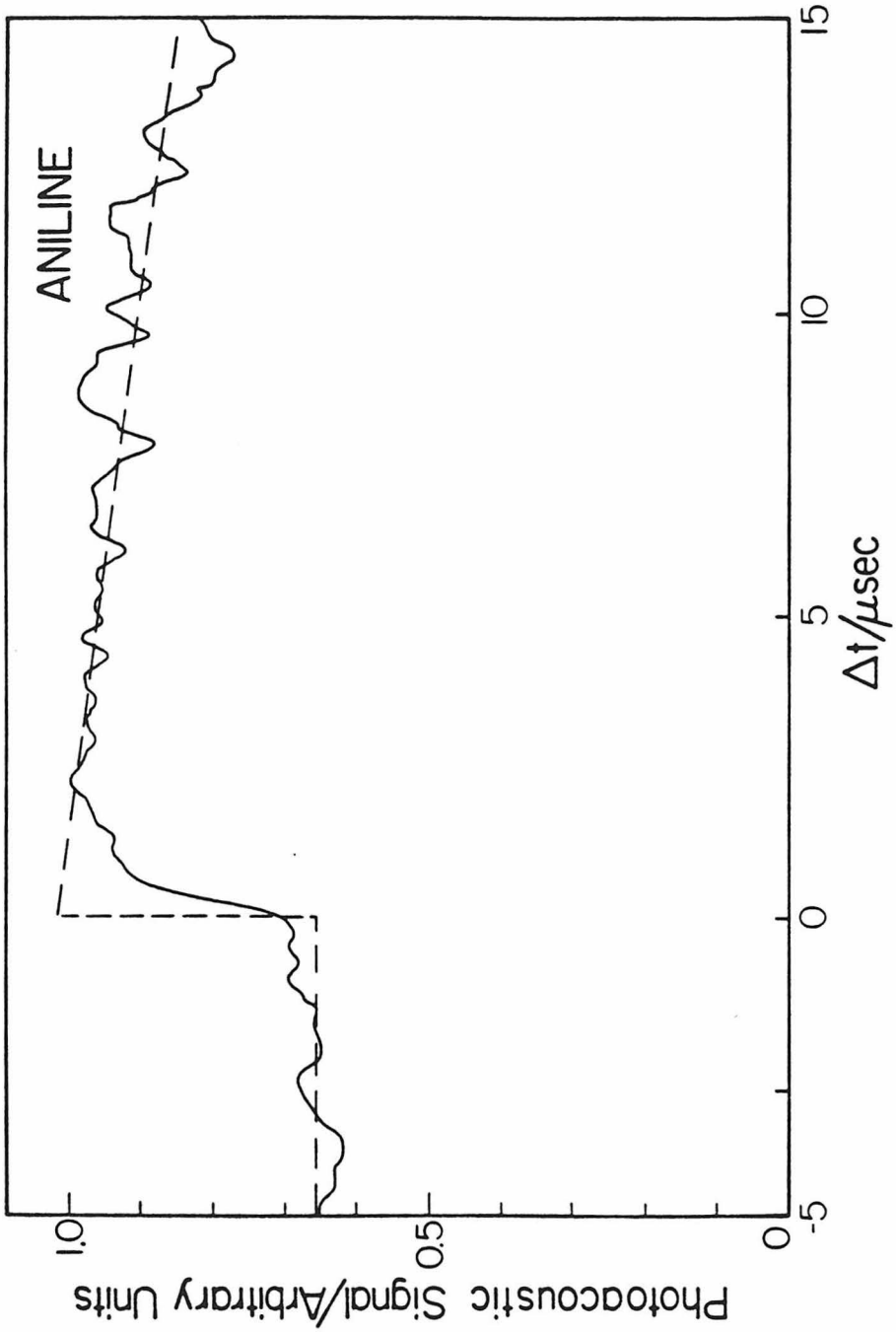
ANILINE
Photoacoustic Signal/Arbitrary Units
0
0.5
1.0
-5
0
5
10
15
Δt/μsec

Figure 6

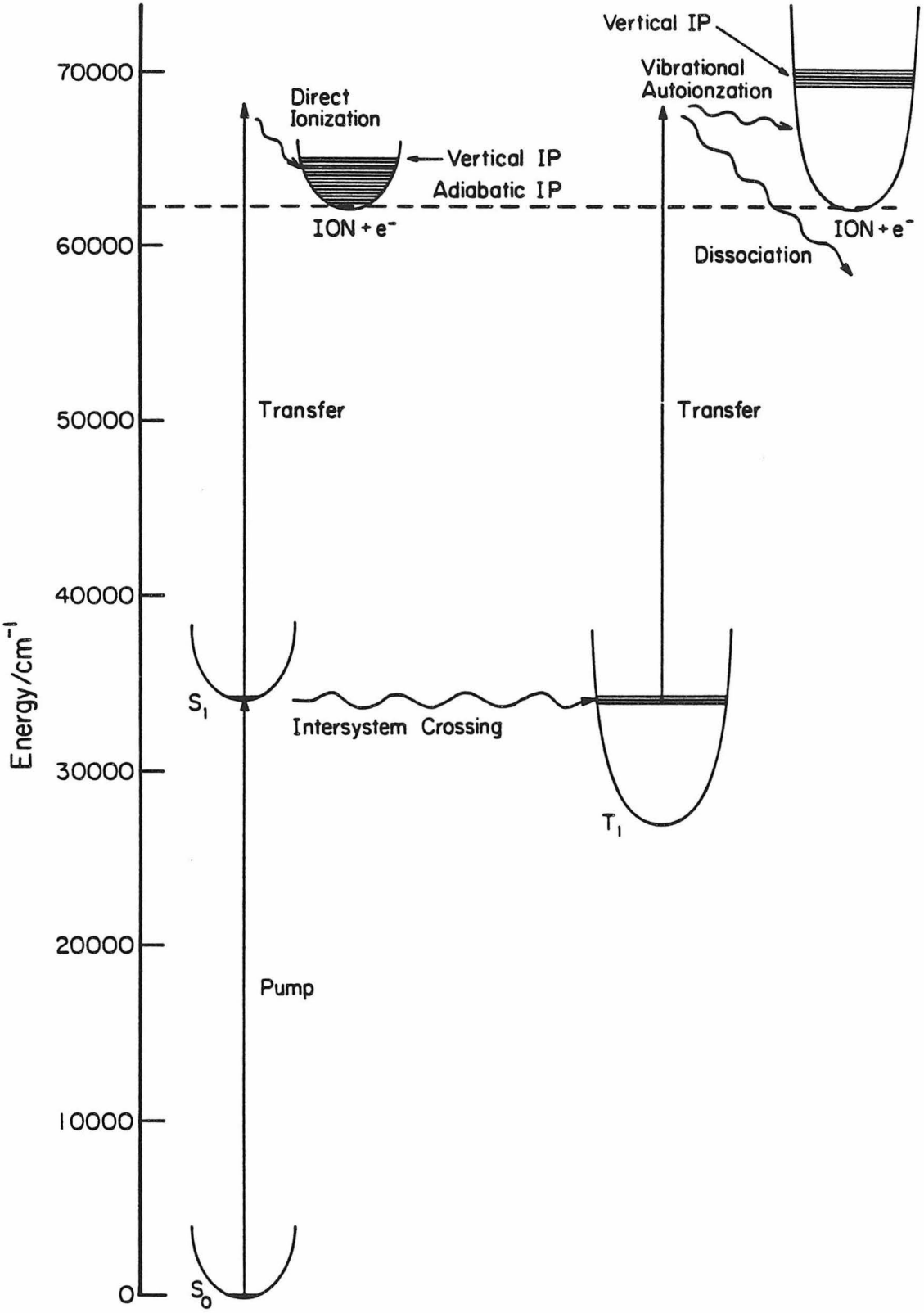
Vertical IP
Vibrational Autoionzation
Direct Ionization
Vertical IP
Adiabatic IP
ION + e⁻
ION + e⁻
Dissociation
Transfer
Transfer
Energy/cm⁻¹
70000
60000
50000
40000
30000
20000
10000
0
S₁
Intersystem Crossing
T₁
Pump
S₀

Figure 7

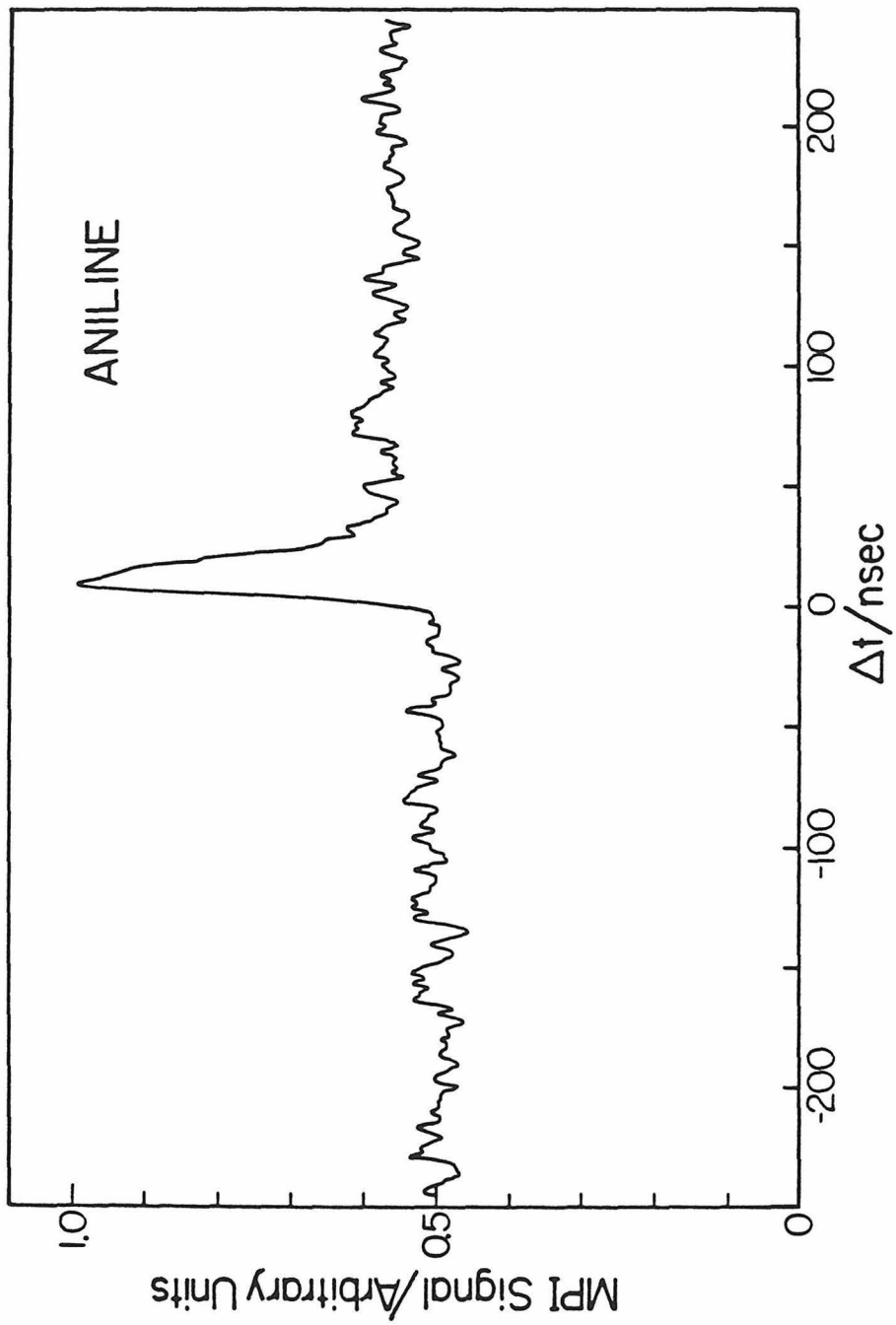
ANILINE
MPI Signal/Arbitrary Units
1.0
0.5
0
-200
-100
0
100
200
Δt/nsec

Figure 8

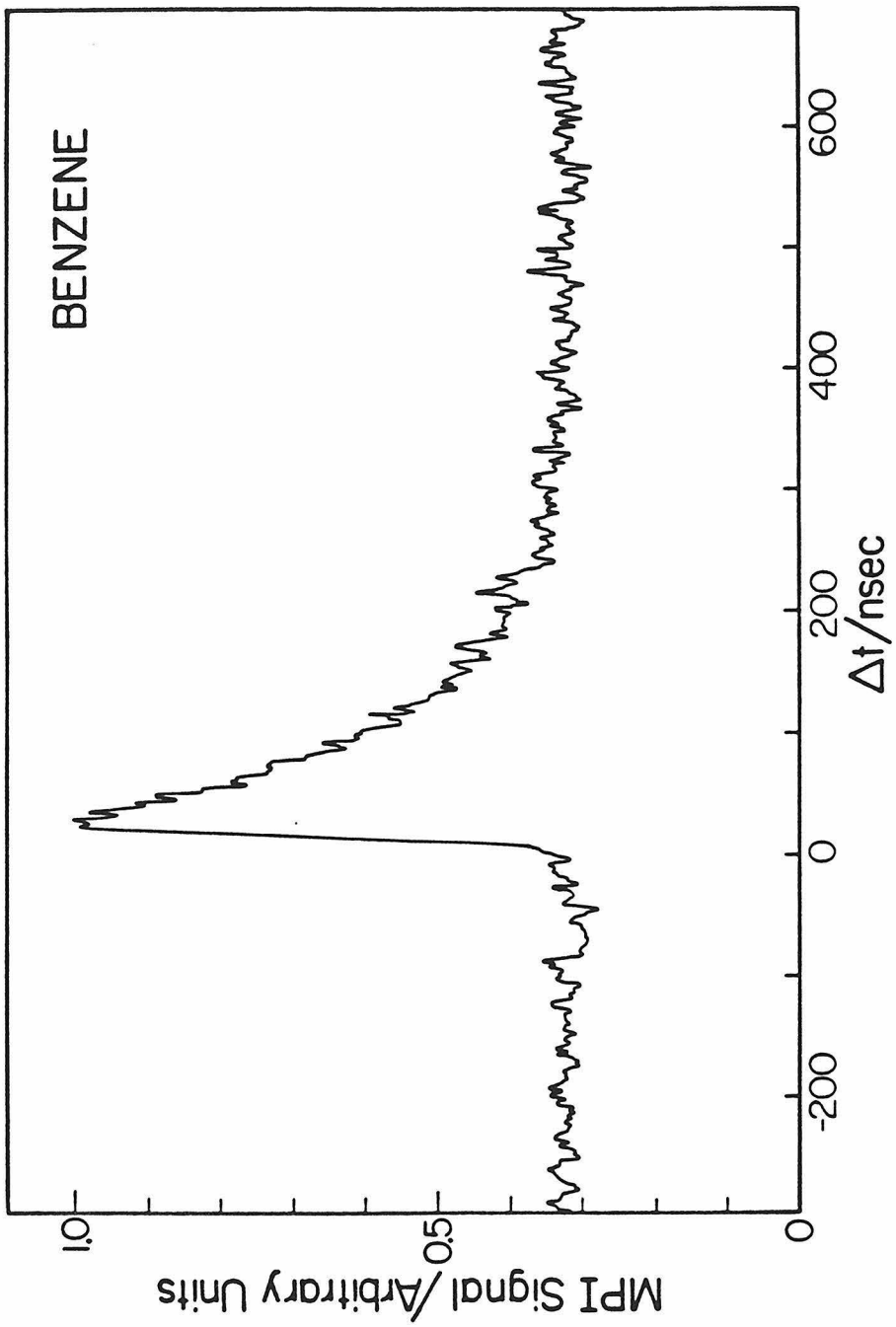
BENZENE
MPI Signal /Arbitrary Units
1.0
0.5
0
-200
0
200
400
600
Δt/nsec

Figure 9

Paper IV: Detection of Weak Absorptions in the Visible and Ultraviolet by Pulsed Laser Photoacoustic Spectroscopy.

Detection of Weak Absorptions in the Visible and Ultraviolet by Pulsed Laser Photoacoustic Spectroscopy

D. J. Moll[†] and A. Kuppermann

The application of pulsed laser photoacoustic spectroscopy to the study of weak absorptions in the visible and ultraviolet spectral regions is discussed. The pulsed technique is compared to more conventional CW laser photoacoustic spectroscopy. Several examples of triplet state spectra are given. The sensitivity of the pulsed technique for extremely weak absorptions is limited by the increased probability of nonlinear effects when high intensities are used.

[†]Work performed in partial fulfillment of the requirements for the PhD degree in Chemistry at the California Institute of Technology.

1. Introduction

A gas phase molecule in an excited state created by absorption of light can lose its energy and return to the ground state in the following ways: (1) It can radiatively deexcite by emitting a photon. (2) The absorbed energy can induce a photochemical reaction such as a rearrangement or bond cleavage process. (3) The molecule can transfer internal energy to another molecule's internal degrees of freedom through inelastic collisions. (4) A collision with another molecule can convert internal energy into translational or kinetic energy of motion between the two molecules. The last process is the basis for most gas phase photoacoustic spectroscopy experiments. In typical experiments of this type, an intensity or wavelength modulated light beam passes through a gaseous sample and is partially absorbed. The amount of absorption is determined by the absorption cross section and concentration of the absorbing species. Some fraction of the deposited energy is converted into kinetic energy through collisional deactivation, resulting in a localized pressure increase which is detected by a nearby microphone as a photoacoustic signal. Processes (1) and (3) can decrease or delay the photoacoustic signal. Process (2) can either contribute to or decrease the photoacoustic signal depending on the nature of the system being studied.[1-3]

Photoacoustic spectroscopy was first reported by Bell in 1881.[4] Recently, due to the widespread availablity of laser sources, it has experienced a widespread utilization for the study of liquids and solids as well as gases.[5-7] Its primary advantages are high sensitivity, simplicity, applicability to solids and liquids as well as gases, and its ability to detect nonradiative decay processes rather than radiative processes.

This paper presents an overview of our work on a particular application of photoacoustic spectroscopy — detection of weak absorptions in the visible and ultraviolet wavelength regions using pulsed laser excitation. The advantages and disadvantages of pulsed excitation will be discussed and illustrated with spectroscopic examples.

2. CW vs. Pulsed Excitation

Many recent photoacoustic studies have used a mechanical chopper to modulate the output of a CW laser in the 10 - 10^4 Hz range. The high average powers of these lasers and the sensitivity of the photoacoustic technique have allowed the measurement of absorption coefficients in the 10^{-10} cm^{-1} range using photoacoustic cells with a length of only 10 cm[8]. The weak absorptions due to forbidden electronic transitions, however, usually require excitation wavelengths in the blue or ultraviolet spectral regions. CW dye lasers have high

average power outputs in the visible, but are subject to very low conversion efficiencies when their output is frequency doubled into the ultraviolet. Pulsed lasers have much higher conversion efficiencies for doubling to produce UV (up to 40%). A variety of nonlinear processes such as frequency doubling, frequency mixing, stimulated Raman shifting, 3rd harmonic generation, and other high order processes are now routinely used with pulsed lasers to produce tunable coherent output at wavelengths as short as 38 nm.[9]

Photoacoustic spectroscopy with pulsed excitation has been used in numerous recent studies.[10-21] Almost all studies to date, however, have not attempted to measure extremely small absorptions in the ultraviolet using tunable pulsed UV laser excitation. We have attempted to investigate spin-forbidden singlet-triplet absorptions using this technique. The sensitivity of this technique, as compared to conventional CW photoacoustic techniques, is influenced by several factors. First, the average power of most tunable pulsed UV lasers is considerably lower than CW visible dye lasers or CO_2 lasers. This immediately decreases the photoacoustic signal because fewer photons are available to be absorbed. Some of this loss can be regained by gating the detection electronics so that only the amplitude of the first pressure wave emitted from the laser beam interaction region is detected. In effect, this concentrates the absorbed energy into an expanding

cylindrical shell which moves out radially from the laser beam rather than distributing it uniformly throughout the cell as in the CW case. Therefore, for a given amount of input energy, the pulsed excitation produces a larger amplitude signal. Gated detection also allows almost total elimination of background signals due to light scattering or absorption at the windows. By simply moving the windows back away from the microphone, the pressure increases from window effects arrive at the microphone later then the pressure wave caused by gas sample absorption. Gated detection, in general, allows a partial regaining of the sensitivity lost because of lower average power in the UV spectral region.

Pulsed photoacoustic spectroscopy differs from the CW case in a second way. When CW excitation is employed with a low chopping frequency (~10 Hz), the excited molecules have a long time period during which they can collisionally relax before the light source is turned back on. Pulsed techniques derive their high sensitivities from pressure wave phenomena. If deexcitation is slow, >10 μsec, a great reduction in sensitivity occurs because the pressure wave is distributed over a large spatial and temporal region, reducing its maximum amplitude. For example, the $O_2\tilde{b}\ ^1\Sigma_g^+$ state near 762.0 nm is known to collisionally deactivate with a time constant of about 3×10^{-3} seconds at 300 torr.[22] CW intracavity photoacoustic spectroscopy detects absorption to this

state with an excellent signal-to-noise ratio.[23] Our attempts to detect this state using pulsed photoacoustic detection failed because the long collisional relaxation time prevented the formation of pressure waves. The CW technique is much more sensitive to absorption in molecules with long collisional deactivation times than the pulsed technique, making the latter a less universal detection method.

A third factor in favor of CW photoacoustic detection arises from the typical cavity design of CW lasers. Because of the high threshold for lasing and the low peak powers (compared to pulsed lasers) most output coupling mirrors for CW lasers transmit only 1 to 10% of the incident light. Output coupling for pulsed lasers can be as high as 96%. This causes the circulating power inside the cavity of a CW laser to be much larger than the actual output power. Placing a photoacoustic cell inside the cavity of a CW laser produces effective incident power levels of 80 watts or higher.[23]

Fourth, pulsed excitation offers significant advantages because of the possibility of performing time-resolved studies using two laser pulses. This technique has been demonstrated in solids[11] and used also in gas phase studies of p-difluorobenzene[24] and aniline.[3]

The high intensities involved in pulsed excitation produce a fifth major difference between pulsed and CW techniques,

nonlinear processes. The signals produced by multiphoton absorption can surpass the expected signals from weak spin-forbidden transitions when high intensities are employed. This effect will be discussed in more detail in Section 4.4.

3. Experimental

Photoacoustic cells for pulsed excitation should be designed in such a way that the amplitude of the detected pressure wave caused by gas absorption is maximized, and the background signals caused by window scattering and window absorption are minimized.

3.1 Photoacoustic Cell

We have tried a number of different cell designs. The most recent model gives high sensitivity, good reproducibility and is inexpensive and simple to construct.[3,24] It consists of a 18 cm long by 0.9 cm inner diameter cell constructed of stainless steel and aluminum. The central portion of the cell is constructed from a 1/2" Swagelok tee and stainless steel tubing. Quartz windows are mounted at each end using Viton o-ring seals. A Knowles Electronics BT1759[25] miniature electret microphone with a nominal sensitivity of 0.01 Volt/Pascal is positioned over a 3/16" diameter hole in the side of the tee and held in place with epoxy resin. To maximize the signal from the pressure wave, the side of the tee was

milled down before mounting the microphone to allow the microphone to be as close as possible to the laser beam. The cell length was chosen to delay the signal caused by scattered light and absorption at the windows, which results from heating of the cell walls or windows, respectively. Scattered light signals are further reduced by placing four apertures inside the cell and an aperture outside the cell at its entrance.

3.2 Electronics

The electret microphone used in these studies has a built-in FET preamplifier which is powered by a 1.5 volt battery. The preamplified signal was typically limited to a frequency range of 10^2 - 10^4 Hz by an electronic filter and amplified. The peak of the first pressure wave was integrated by a differential gated integrator system with an integration window of 15 μsec. Signals from a pyroelectric joulemeter were processed in a similar manner by a second integrator system to provide a normalization signal.

A microcomputer system controlled the dye laser grating scan, doubling crystal phasematching angle, and digitized and stored signals from both integrators every 0.1 Å.

3.3 Laser Systems

The spectra presented in this paper were obtained using two different dye laser systems. A Molectron UV400 N_2 laser

was used to pump a Molectron DL200 dye laser. The dye laser fundamental output down to 360 nm was used. Pulse energies ranged from 1 to 250 μJ/pulse with a ∿6 x 10^{-9} sec pulse-width, a linewidth of about 0.5 cm^{-1}, and a 20 Hz repetition rate.

For weaker absorptions, a more powerful laser system was used, consisting of a Molectron MY34 Nd:YAG laser which pumped a DL18 dye laser. Visible output, obtained from various dyes pumped by the 2nd and 3rd harmonics of the Nd:YAG laser, ranged from 1 t0 50 mJ/pulse with a linewidth of about 0.5 cm^{-1} at a 10 Hz repetition rate. UV output was produced by doubling the dye laser output or by mixing the dye laser output with the 1064 nm Nd:YAG fundamental. During wavelength scans, the KDP crystal phasematching angle was adjusted every 0.1 Å by a microcomputer using a predetermined 5th order polynomial in wavelength. UV outputs ranged from 1 to 10 mJ/pulse.

All spectra were normalized with respect to incident pulse energy to correct for the wavelength dependence of the dye gain curve and output pulse energy fluctuations.

4. Results

This section presents specific examples of spectra obtained using the pulsed laser photoacoustic technique which demonstrate the sensitivity, usefulness and limitations of this method.

4.1 High Vibrational Overtones

Figures 1 and 2 show pulsed laser photoacoustic spectra of some high vibrational overtones in acetylene. Vibrational overtones of acetylene[26] as well as numerous other polyatomic molecules have been studied by the CW photoacoustic technique.

In Fig. 1, the strong band system centered near 15,600 cm^{-1} has been assigned as the v = 5 C-H stretch overtone.[26] Another weaker band can be seen centered at 15,530 cm^{-1}. In all, five vibrational bands have been detected in this region using a high resolution intracavity CW laser photoacoustic technique where the wavelength of the dye laser is modulated slightly instead of the usual intensity modulation technique.[26] The greater sensitivity at visible wavelengths of the CW intracavity technique, compared to the pulsed technique, is demonstrated by this example. This same band system was also studied previous by long path absorption.[27]

Figure 2 shows a pulsed photoacoustic spectrum of the v = 7 CH stretching overtone in acetylene centered at 21,210 nm. This preliminary spectrum, although noisy, still displays the characteristic P and R branches and is the first reported spectrum of this particular state. With additional signal averaging, the individual J lines could easily be resolved, permitting a rotational analysis.

We have also investigated high vibrational overtones of CD_3H in the regions of the v = 5, 6 and 7 levels of the C-H stretch mode using the pulsed photoacoustic spectroscopy technique.[28]

4.2 Spin-Forbidden Transitions with Spinorbit Coupling

In the usual level of approximation, optical transitions between states of different spin multiplicity are not allowed. In all molecules, however, if the level of approximation is increased, this transition becomes possible, but remains weak. Spin orbit coupling, which couples the electron spin and angular momenta, can perturb the zero order states by mixing in character of states with different spin multiplicities.[29] This perturbation becomes larger in nuclei with higher charges, producing transitions of slightly more intensity between levels of different multiplicity than for molecules with light nuclei. Oscillator strength is a convenient criterion for classifying the strengths of electronic transitions since it is proportional to the integral of the absorption coefficient over the entire electronic band.[29] Spin-allowed transitions typically have oscillator strengths falling between 1 and 10^{-4}, depending on symmetry selection rules and dipole transition moments. Spin-forbidden transitions have oscillator strengths falling between 10^{-5} and 10^{-10}, depending on the symmetry requirements for spin-orbit coupling and the presence of heavy nuclei. We have attempted to detect spin-forbidden transitions which lie in the 10^{-5} - 10^{-6} range in molecules which contain oxygen, sulfur or halogen atoms as spin orbit enhancers, and also transitions which are near the 10^{-10} limit in hydrocarbons, using the pulsed photoacoustic technique.

CS_2. The absorption bands in CS_2 from 390 to 330 nm have been studied extensively.[30-38] The vibrational and rotational structure in the absorption spectrum indicates that the spectrum results from transitions between a linear ground state ($^1\Sigma_g^+$) and a bent excited state of B_2 symmetry.[32] Zeeman effects indicate that the observed B_2 state is a component of a $^3A_2$ state with substantial triplet splitting.[33,34] Variable-angle low-energy electron impact spectroscopy also confirms the singlet-triplet nature of the transition.[37]

Figure 3 shows a pulsed photoacoustic spectrum of CS_2 obtained using a maximum energy/pulse of 110 μJ and a sample pressure of 300 torr. Barrow and Dixon[35] have determined that the oscillator strength of the $\tilde{a}^3A_2$ state in CS_2 is about 5×10^{-7}, placing it among the stronger spin-forbidden transitions, as expected from the presence of sulfur atoms which enhance the spin orbit coupling. The spectrum of Fig. 3 has an excellent signal-to-noise ratio, which implies that this technique should be applicable to the study of much weaker transitions.

SO_2. The role of SO_2 in atmospheric chemistry[39] has stimulated considerable interest in its spectroscopy. The lowest energy triplet state absorption in SO_2 ($\tilde{X}^1A_1 \rightarrow \tilde{a}^3B_1$) is centered at 370 nm. This state has been investigated by absorption,[40-42] phosphorescence[43] and laser-induced phosphorescence.[44]

Figure 4 shows a pulsed photoacoustic spectrum of SO_2 which includes well-resolved transitions to the lower vibrational levels of the $^3B_1$ state. Clearly resolved rotational structure is present in the spectrum of the (000)→(110) transition shown in Fig. 5. The rotational perturbation observed by Brand and co-workers[42] and Merer[40] at the K' = 15 level and upward near 368 nm is also present in the photoacoustic spectrum of Fig. 5. This perturbation is believed to arise from an interaction with b_2 vibrational levels of a nearly $^3A_2$ state.

Biacetyl. The interactions between the low-lying singlet and triplet states of biacetyl have received extensive study by a variety of techniques including fluorescence,[45-48] absorption,[49,50] molecular beam techniques[51,52] and CW photoacoustic spectroscopy.[53] Energy transfer into the biacetyl $T_1(^3A_u)$ state from triplet states in other molecules has often been used to study nonradiative processes in these molecules.[53,54] Figure 6 shows a pulsed photoacoustic spectrum of the $T_1(^3A_u)$ state of biacetyl. In contrast to CS_2 and SO_2, the biacetyl triplet spectrum contains broad unresolved features. Vibronic bands appear only as weak peaks superimposed on a broad electronic band

Thiophosgene. The visible absorption system in thiophosgene ($CSCl_2$) consists primarily of two overlapping weak electronic bands. The lowest energy band has been assigned as the $\tilde{X}^1A_1 \rightarrow \tilde{a}^3A_2$ ($n \rightarrow \pi^*$) transition[55-58] which has an

origin at 17492 cm^{-1}. The higher energy band is a symmetry forbidden $\tilde{X}^1A_1 \rightarrow \tilde{A}^1A_2$ ($n \rightarrow \pi^*$) transition[59] with an origin near 18730 cm^{-1}. Thiophosgene belongs to the small class of molecules in which fluorescence has been detected from the second excited singlet state,[60,61] in violation of Kasha's rule that polyatomic molecules emit only from the lowest electronically excited level of a given multiplicity.[62]

A pulsed photoacoustic spectrum of the weak visible absorption system of thiophosgene is shown in Fig. 7. This spectrum is a composite spectrum formed by combining several spectra taken using different laser dyes. The spectral region surrounding the origin of the $\tilde{a}^3A_2$ state is shown in Fig. 8. The wide dynamic range of the pulsed photoacoustic technique is apparent from a comparison of Figs. 7 and 8.

The examples given in this section of pulsed photoacoustic spectroscopy of triplet states demonstrate the usefulness of this technique for studying relatively strong spin-forbidden transitions. Unfortunately, all triplet states given as examples have been studied previously by long pathlength absorption experiments. The photoacoustic studies provide no additional spectroscopic information. They simply demonstrate that the pulsed photoacoustic technique is capable of detecting these transitions. Weaker transitions which fall in the lower range of oscillator strengths for spin-forbidden transitions are not detected easily by this method or the

long pathlength absorption technique. The problems which arise when studying very weak transitions will be discussed in the following sections.

4.3 Overlapping Bands

In most molecules, only low-lying triplet states have been studied spectroscopically. Broad singlet states often mask the weak absorptions arising from triplet states at higher energies.[29] The photoacoustic technique is also not immune to this problem. Figure 9 shows a spectrum of 1,1-dichloroethylene in the region where the lowest triplet state is expected to appear.[63,64] Our pulsed photoacoustic spectroscopy attempt to observe this state in ethylene failed because of nonlinear effects similar to those described for benzene in the next section. We hoped that the chlorine substituents would increase the triplet state transition intensity through enhanced spinorbit coupling. Unfortunately, as shown in Fig. 9, a strong signal is observed which rises rapidly with increasing photon energy. This signal results from the tail of an absorption due to a strong charge transfer band involving the chlorine substituents. The expected triplet state spectrum is obscured by this charge transfer band.

4.4 Nonlinear Effects

At high intensities the probability of nonlinear optical effects such as multiphoton absorption, stimulated Raman

scattering, frequency doubling, etc. increases dramatically with respect to ordinary linear absorption. The major advantage of the pulsed photoacoustic technique is that it allows the use of pulsed lasers with high intensity outputs which permit efficient generation of tunable UV output using nonlinear optical processes. The high intensities required for efficient UV generation and higher sensitivity place an upper limit on the sensitivity of this technique. As intensity increases, the probability of multiphoton absorption increases, and eventually surpasses the probability of absorbing only one photon in an extremely weak spin-forbidden transition. When this happens, the photoacoustic spectrum is produced by states at two, three or four times the photon energy, instead of the one-photon resonance with the triplet state.

Nonlinear absorption predominated when we attempted to study the $\tilde{X}^1A_{1g} \rightarrow \tilde{a}^3B_{1u}$ transition[65] in benzene using the pulsed photoacoustic technique. This extremely weak transition has been observed in liquid [66-71] and gaseous[72,73] benzene from 3000 to 3400 $\mathring{A}$ in the presence of O_2. It has not been observed in the free molecule.

Figure 10 shows a pulsed photoacoustic spectrum in the region 330 to 322 nm. Three broad peaks are present which do not resemble the expected triplet state spectrum. Similar peaks do appear, however, in absorption spectra in the vacuum

UV region at twice the photon energy.[74] Closer examination indicates close agreement between the positions of these states and the Rydberg states identified as $2R'_{020}$, $2R'_{040}$ and $2R''_{000}$ by Wilkinson.[74] In our spectrum, however, the transitions are shifted to higher energy by about 380 cm^{-1}. The strength of the Rydberg transitions in benzene led Wilkinson to assign them as $^1A_{1g} \rightarrow {}^1E_{1u}$ or $^1A_{2u}$ allowed transitions. The presence of inversion symmetry in benzene suggests that vibronic coupling with a u-type vibrational mode is required to see these same states in a two-photon spectrum. The $\nu_{20}(e_{2u})$ mode with a ground electronic state frequency of 398 cm^{-1} may be active in the vibronic coupling, since it also appears in vibrational progressions involving other nearby Rydberg states in benzene.[74] Vibronic coupling with the ν_{20} mode would explain the 380 cm^{-1} shift in energy of the observed states between the one- and two-photon spectra.

Further information of the two-photon nature of the pulsed photoacoustic spectrum of benzene is provided by Fig. 11 which shows a multiphoton ionization (MPI) spectrum[38] of benzene in the same spectral region. MPI spectroscopy is known to be extremely sensitive to resonances with Rydberg states. The transitions present in the photoacoustic spectrum also appear in the MPI spectrum with similar intensities and wavelengths. The MPI signal was roughly proportional to intensity squared.

Similar nonlinear absorption effects appeared in pulsed photoacoustic spectra of 1,3-butadiene and hexatriene when we tried to detect extremely weak spin-forbidden transitions in those molecules.

In the benzene experiments, this incident beam was unfocused with a diameter of ∿5 mm. Expanding the beam diameter would decrease nonlinear absorption. It also appears to substantially decrease the pulsed photoacoustic signal. Apparently, the absorbed energy is distributed over a larger volume. This decreases the maximum amplitude of the detected pressure wave. In benzene we were unable to decrease the two-photon signal enough to allow observation of the triplet state spectrum.

5. Conclusions

The results of our triplet state studies indicate that the pulsed photoacoustic technique is easily able to detect spin-forbidden transitions which have a significant amount of spinorbit coupling. Triplet states in molecules of this type, however, have been studied extensively using long pathlength absorption techniques. Extremely weak spin-forbidden transitions in hydrocarbons are difficult to detect by pulsed photoacoustic methods because of the increased probability of nonlinear absorption to higher states in these molecules. The nonlinear absorption can easily be larger than the absorption due to the one-photon spin-forbidden transition. The development of tunable CW lasers with high power UV outputs

or high power long pulse tunable UV lasers should minimize nonlinear effects. These lasers, when combined with present photoacoustic detection techniques, should provide an effective method for studying extremely weak absorptions in the ultraviolet.

The recently demonstrated two-color time-resolved pulsed photoacoustic technique[24,28] provides a new method of measuring excited state absorption and dynamics. The sensitivity of the pulsed photoacoustic technique should allow these studies to be performed using triplet states with significant amounts of spinorbit coupling as intermediate states.

References

1. W. R. Harshbarger and M. B. Robin, Acc. Chem. Res. 6, 329 (1973).
2. W. R. Harshbarger and M. B. Robin, Chem. Phys. Lett. 21, 462 (1973).
3. D. J. Moll, G. R. Parker, Jr. and A. Kuppermann, "Two-Color Time-Resolved Photoacoustic and Multiphoton Ionization Spectroscopy of Aniline", to be published.
4. A. G. Bell, Philos. Mag. 11, 510 (1981).
5. Y.-H. Pao, edit., Optoacoustic Spectroscopy and Detection (Academic Press, New York, New York, 1979).
6. A. Rosencwaig, Photoacoustics and Photoacoustic Spectroscopy (Wiley, New York, 1980).
7. C. K. N. Patel and A. C. Tam, Rev. of Mod. Phys. 53, 517 (1981).
8. C. K. N. Patel and R. J. Kerl, Appl. Phys. Lett. 30, 578 (1977).
9. J. Reintjes, C.-Y. She and R. C. Eckardt, IEEE J. Quant. Elect. QE-14, 581 (1978).
10. T. F. Deutsch, Opt. Lett. 1, 25 (1977).
11. M. G. Rockley and J. P. Devlin, Appl. Phys. Lett. 31, 24 (1977).
12. J. G. Parker and D. N. Ritke, J. Chem. Phys. 59, 3713 (1973).
13. R. W. Shaw, Appl. Phys. Lett. 35, 253 (1979).

14. J. E. Allen, Jr., W. R. Anderson and D. R. Crosley, Opt. Lett. 1, 118 (1977).

15. T. Aoki and M. Katayama, Jap. J. Appl. Phys. 10, 1303 (1971).

16. P. C. Claspy, C. Ha and Y.-H. Pao, Appl. Opt. 16, 2972 (1977).

17. C. W. Brue, B. Z. Sojka, B. G. Hurd, W. R. Watkins, K. O. White and Z. Derzko, Appl. Opt. 15, 2970

18. G. A. West and J. J. Barrett, Opt. Lett. 4, 395 (1979).

19. D. A. Siebert, G. A. West and J. J. Barrett, Appl. Opt. 19, 53 (1980).

20. G. A. West, D. R. Siebert and J. J. Barrett, J. Appl. Phys. 51, 2823 (1980).

21. S. L. Chin, D. K. Evens, R. D. McAlpine and W. N. Selander, Appl. Opt. 21, 65 (1982).

22. S. A. Lawton, S. E. Novick, H. P. Broida and A. V. Phelps, J. Chem. Phys. 66, 1381 (1977).

23. K. V. Reddy, PhD Thesis, University of Wisconsin-Madison (1977).

24. D. J. Moll, G. R. Parker, Jr. and A. Kuppermann, "Photoacoustic Detection of Stimulated Emission Pumping in p-Difluorobenzene", to be published.

25. Knowles Electronics, Inc., 3100 N. Mannheim Rd., Franklin Park, IL 60131, USA.

26. G. J. Scherer, K. K. Lehmann and W. Klemperer, "The High-Resolution Visible Overtone Spectrum of Acetylene", in press.

27. K. Hedfeld and P. Lueg, Zeitschrift Physik 77, 446 (1932).

28. D. J. Moll, J. W. Perry, A. Kuppermann and A. H. Zewail, "High Overtone Photoacoustic Spectroscopy of Some Methyl-Containing Molecules. I. Rotational Analysis", to be published.

29. S. P. McGlynn, T. Azumi and M. Kinoshita, Molecular Spectroscopy of the Triplet State, (Prentice-Hall, New Jersey, 1969).

30. L. N. Liebermann, Phys. Rev. 60, 496 (1941).

31. A. E. Douglas, Can. J. Phys. 36, 147 (1958).

32. B. Kleman, Can. J. Phys. 41, 2034 (1963).

33. A. E. Douglas and E. R. V. Milton, J. Chem. Phys. 41, 357 (1964).

34. J. T. Hougen, J. Chem. Phys. 41, 363 (1964).

35. T. Barrow and R. N. Dixon, Mol. Phys. 25, 137 (1973).

36. M.-J. Hubin-Franskin and J. E. Collin, J. Electron Spectrosc. 7, 139 (1975).

37. W. M. Flicker, O. A. Mosher and A. Kuppermann, J. Chem. Phys. 69, 3910 (1978).

38. R. Rianda, D. J. Moll and A. Kuppermann, Chem. Phys. Lett. 73, 469 (1980).

39. J. Heicklen, Atmospheric Chemistry (Academic Press, New York, 1976), p. 331.

40. A. J. Merer, Disc. Faraday Soc. 35, 127 (1963).

41. J. C. D. Brand, V. T. Jones and C. Di Lauro, J. Mol. Spectrosc. 40, 616 (1971).

42. J. C. D. Brand, V. T. Jones and C. Di Laruo, J. Mol. Spectrosc. 45, 404 (1973).

43. A. G. Gaydon, Proc. Roy. Society 146A, 901 (1934).

44. F. B. Wampler, R. C. Oldenborg and W. W. Rice, J. Appl. Phys. 50, 6117 (1979).

45. H. Okabe and W. A. Noyes, Jr., J. Amer. Chem. Soc. 79, 801 (1957).

46. R. Van der Werf, D. Zevenhuijzen and J. Kommandeur, Chem. Phys. Lett. 27, 325 (1974).

47. G. M. McClelland and J. T. Yardley, J. Chem. Phys. 58, 4368 (1973).

48. C. S. Parmenter and H. M. Poland, J. Chem. Phys. 51, 1551 (1969).

49. J. W. Sidman and D. S. McClure, J. Amer. Chem. Soc. 77, 6461 (1955).

50. J. W. Sidman and D. S. McClure, J. Amer. Chem. Soc. 77, 6471 (1955).

51. M. Gurnick, J. Chaiken, T. Benson and J. D. McDonald, J. Chem. Phys. 74, 99 (1981).

52. J. Chaiken, M. Gurnick and J. D. McDonald, J. Chem. Phys. 74, 106 (1981).

53. M. B. Robin, J. Luminescence 12/13, 131 (1976).

54. K. Kaya, W. R. Harshbarger and M. B. Robin, J. Chem. Phys. 60, 4231 (1974).

55. L. Burnelle, J. Chem. Phys. 24, 620 (1956).

56. D. C. Moule and C. R. Subramanian, J. Mol. Spectrosc. 48, 336 (1973).

58. W. M. Flicker, O. A. Mosher and A. Kuppermann, Chem. Phys. Lett. 57, 183 (1978).

59. J. C. D. Brand, J. H. Callomon, D. C. Moule, T. Tyrrell and T. H. Goodwin, Trans. Faraday Soc. 61, 2365 (1965).

60. S. Z. Levine, A. R. Knight and R. P. Steer, Chem. Phys. Lett. 29, 73 (1974).

61. D. Phillips and R. P. Steer, J. Chem. Phys. 67, 4780 (1977).

62. M. Kasha, Disc. Faraday Soc. 9, 14 (1950).

63. A. Kuppermann, W. M. Flicker and O. A. Mosher, Chem. Rev. 79, 77 (1979).

64. D. G. Wilden and J. Comer, J. Phys. B: Atom. Molec. Phys. 12, L371 (1979).

65. A. C. Albrecht, J. Chem. Phys. 38, 354 (1963).

66. A. L. Sklar, J. Chem. Phys. 5, 669 (1937).

67. G. N. Lewis and M. Kasha, J. Amer. Chem. Soc. 66, 2100 (1944).

68. A. C. Pitts, J. Chem. Phys. 18, 1416 (1950).

69. D. F. Evans, Nature 178, 534 (1956).

70. D. F. Evans, J. Chem. Soc. 1351 (1957).

71. D. P. Craig, J. M. Hollas and G. W. King, J. Chem. Phys. 29, 974 (1958).

72. D. F. Evans, J. Chem. Soc. 3885 (1957).

73. G. E. Kimball, J. Chem. Phys. 8, 188 (1940).

74. P. G. Wilkinson, Can. J. Phys. 34, 596 (1956).

Figure Captions

Figure 1. Pulsed laser photoacoustic spectrum of acetylene in the region of v = 5 CH stretch overtone. The sample pressure was 760 torr. This spectrum and all subsequent spectra have been corrected for the variation of pulse energy with wavelength.

Figure 2. Pulsed laser photoacoustic spectrum of acetylene in the region of the v = 7 CH stretch overtone. The sample pressure was 1870 torr. Rotational lines are barely visible above the noise. The large constant background is produced by scattered light striking the walls of the photoacoustic cell.

Figure 3. Photoacoustic spectrum of the $\tilde{X}^1\Sigma_g^+ \rightarrow \tilde{a}^3A_2$ transition of CS_2 obtained using a sample pressure of 300 torr. The band assignments at the top are from Kleman[32] where Σ, Π, Δ, ..., correspond to $k' = \ell'' = 0, 1, 2, \ldots$. k is the symmetric top quantum number and ℓ is the quantum number associated with the vibrational angular momentum. The symbol

$$\sum^{1,2}_{3}$$

implies $v_1' = 1$, $v_2' = 2$, $v_2'' = 3$ and $v_3' = v_1'' = v_3'' = 0$. Vibrational modes 1, 2 and 3 correspond to the symmetric stretch, bend and antisymmetric stretch with double prime and single prime corresponding to ground and excited electronic states, respectively.

Figure 4. Pulsed photoacoustic spectrum of a portion of the $\tilde{X}^1A_1 \rightarrow \tilde{a}^3B_1$ transition in SO_2. The sample pressure was 930 torr and laser pulse energies were ∿50 μJ. The vibronic bands are labeled with the symbol (ijk) where i, j and k are the number of quanta in the excited state symmetric stretch, bend and anti-symmetric stretch, respectively.

Figure 5. Pulsed photoacoustic spectrum of the (110) vibronic band of the $SO_2\tilde{X}^1A_1 \rightarrow \tilde{a}^3B_1$ transition which shows partially resolved rotational structure. The sample pressure was 390 torr.

Figure 6. Pulsed photoacoustic spectrum of the $\tilde{X}^1A_g \rightarrow \tilde{a}^3A_u$ transition in biacetyl. The sample pressure was ∿20 torr and pulse energies were about 200 μJ.

Figure 7. Pulsed photoacoustic spectrum of the overlapping $\tilde{a}^3A_2$ and $\tilde{A}^1A_2$ states in thiophosgene. The sample pressure was 100 torr. The spectrum shown is a composite of several spectra taken over different dye ranges. The relative amplitudes of the different spectra were adjusted in the regions of overlap.

Figure 8. Pulsed photoacoustic spectrum of thiophosgene in the spectral region surrounding the origin of the $\tilde{X}^1A_1 \rightarrow \tilde{a}^3A_2$ transition. The origin appears at 17,492 cm^{-1}. The sample pressure was 100 torr.

Figure 9. Pulsed photoacoustic spectrum of 1,1-dichloroethylene in the wavelength region where the lowest triplet state should appear. The observed signal results from the rising edge of a strong charge transfer band. The sample consisted of 200 torr dichloroethylene and 200 torr N_2 to enhance the signal.

Figure 10. Pulsed photoacoustic spectrum of benzene in the spectral region where the $\tilde{X}^1A_{1g} \rightarrow \tilde{a}^3B_{1u}$ transition should occur. The three broad peaks correlate with the $2R'_{020}$, $2R'_{040}$ and $2R''_{000}$ Rydberg states studied by Wilkinson[74] if vibronic coupling with the $\nu_{20}(e_{2u})$ mode is invoked. The appearance of Rydberg state occurs through a two-photon absorption process. The sample pressure was 60 torr.

Figure 11: Multiphoton ionization spectrum of benzene in the same spectral region as Fig. 10. The sample pressure was 10 torr. The Rydberg transitions present in the spectrum of Fig. 10 also appear in this spectrum.

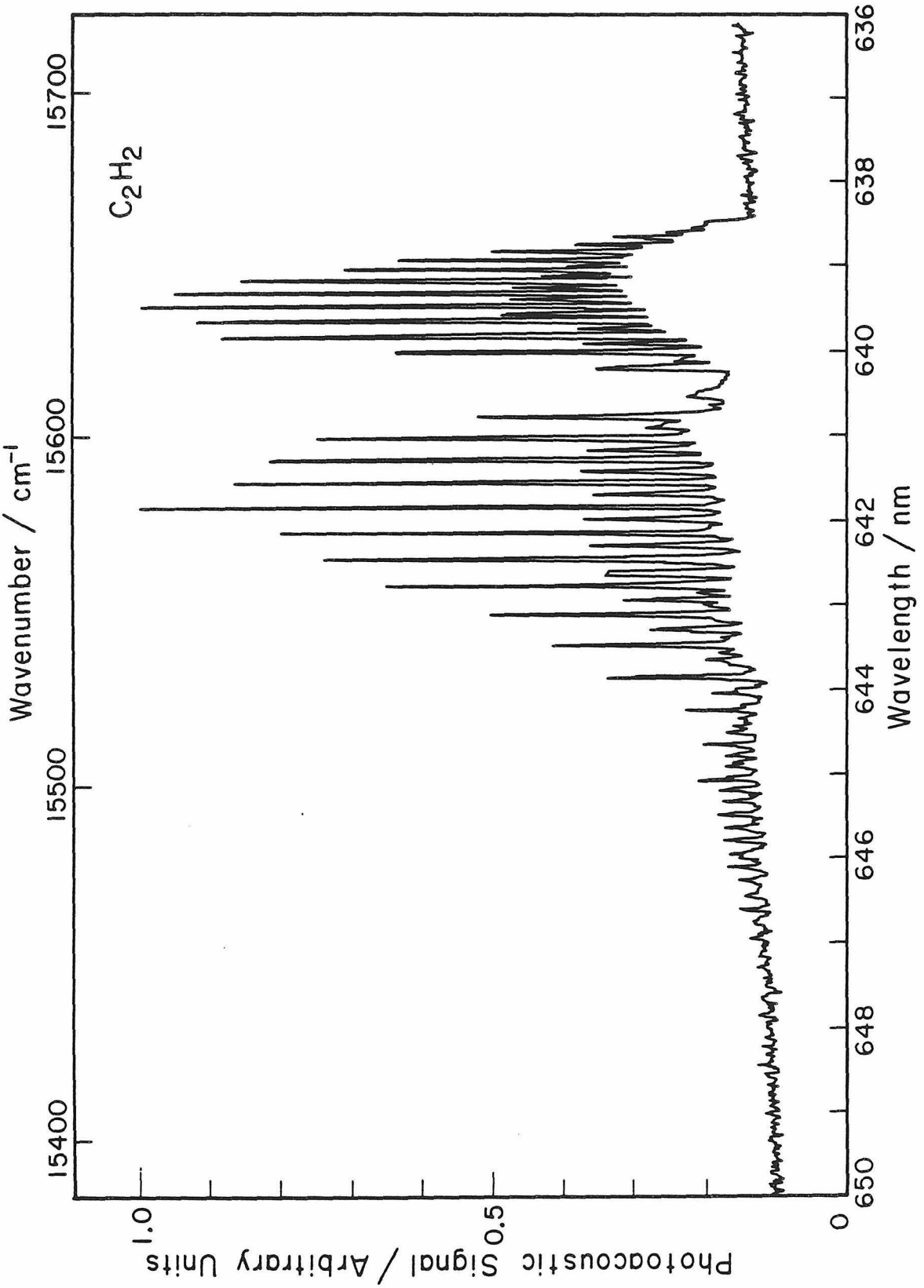
C_2H_2
Wavenumber / cm^{-1}
15400
15500
15600
15700
Wavelength / nm
636
638
640
642
644
646
648
650
Photoacoustic Signal / Arbitrary Units
0
0.5
1.0

Figure 1

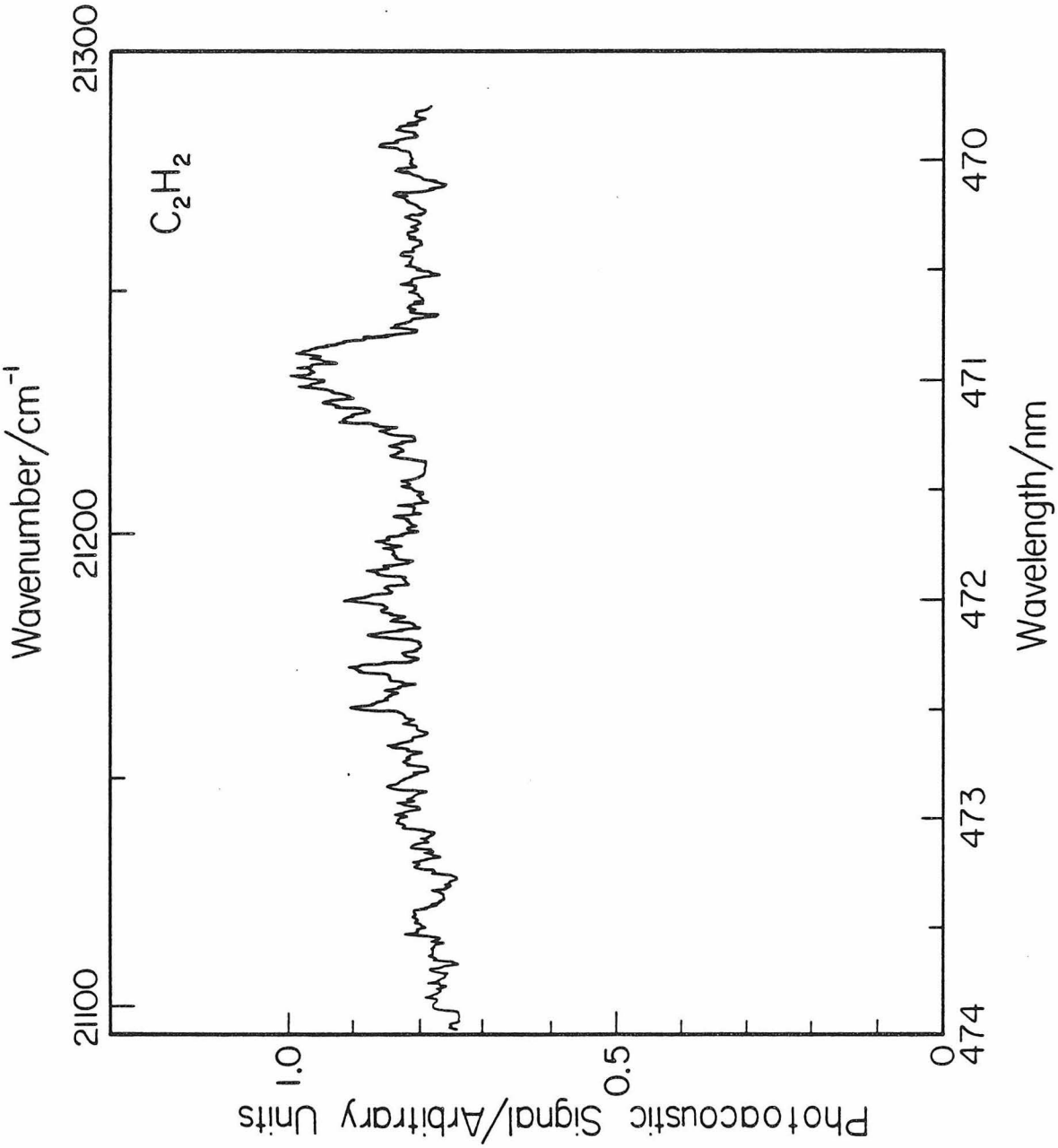
Wavenumber/cm⁻¹
21300
21200
21100
C₂H₂
Photoacoustic Signal/Arbitrary Units
1.0
0.5
0
474
473
472
471
470
Wavelength/nm

Figure 2

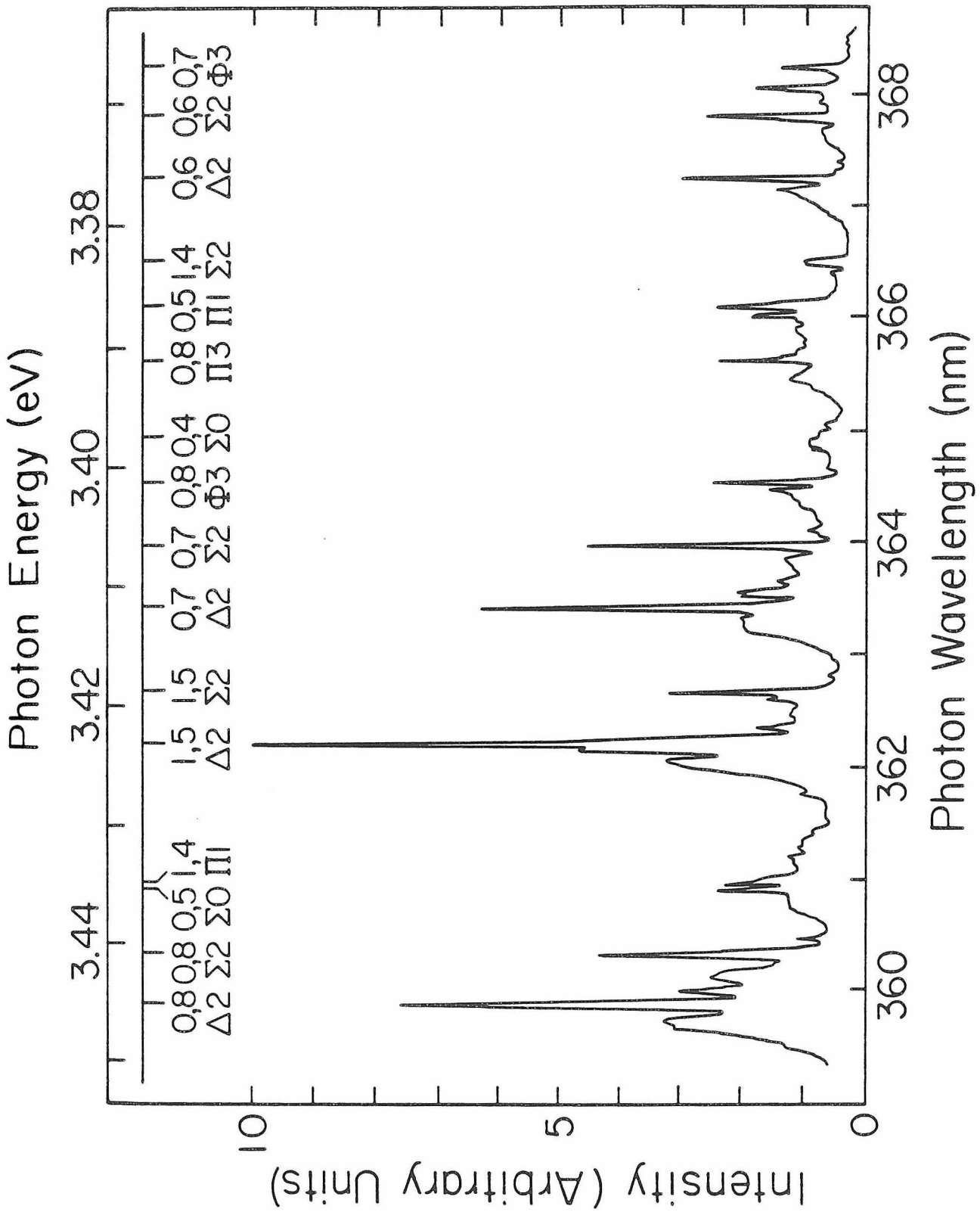
Photon Energy (eV)
3.44
3.42
3.40
3.38
0,8 0,8 0,5 1,4
Δ2 Σ2 Σ0 Π1
1,5 1,5
Δ2 Σ2
0,7 0,7
Δ2 Σ2
0,8 0,4
Φ3 Σ0
0,8 0,5 1,4
Π3 Π1 Σ2
0,6 0,6 0,7
Δ2 Σ2 Φ3
Intensity (Arbitrary Units)
10
5
0
360
362
364
366
368
Photon Wavelength (nm)

Figure 3

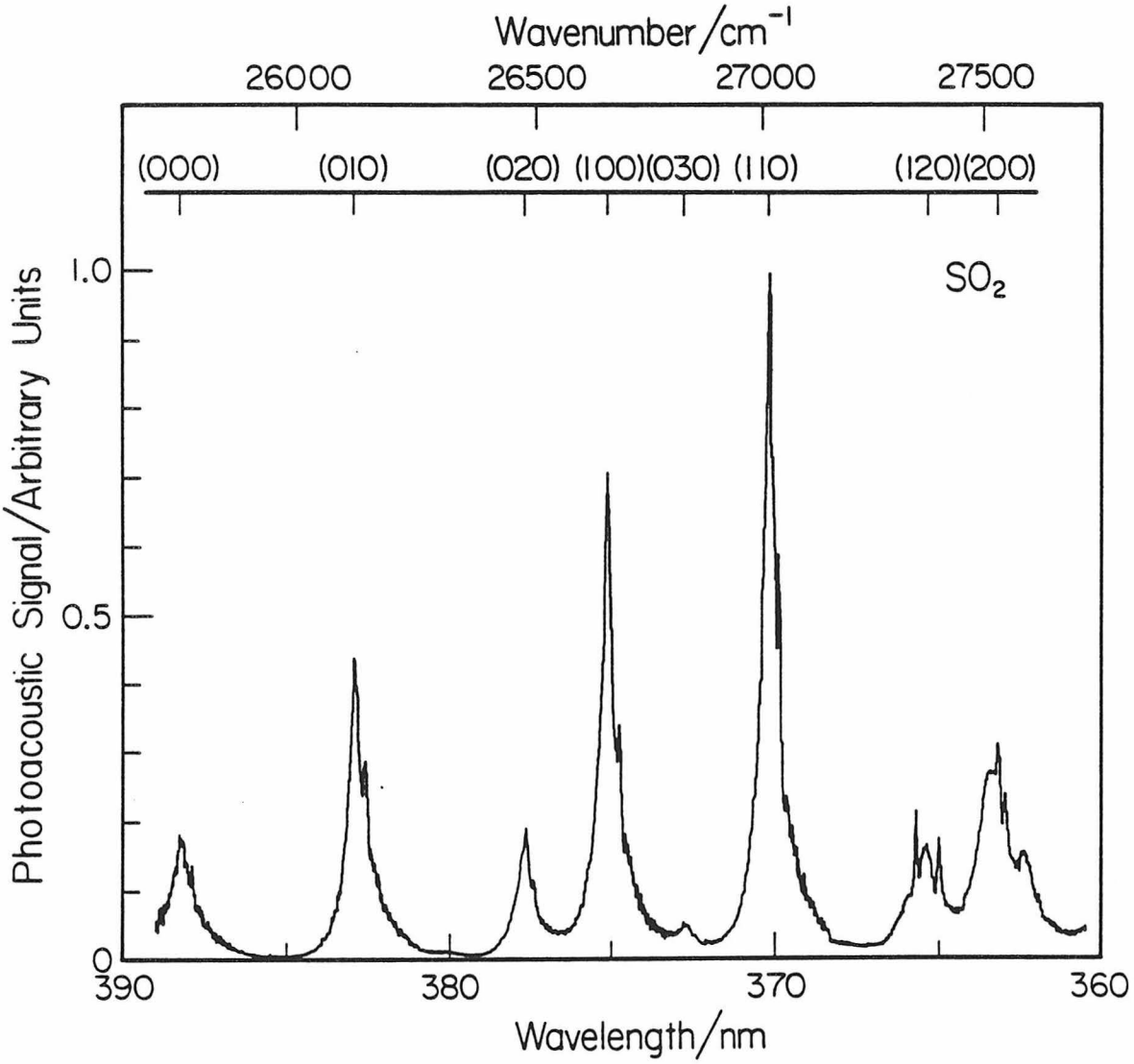
Wavenumber/cm⁻¹
26000
26500
27000
27500
(000)
(010)
(020)
(100)
(030)
(110)
(120)
(200)
SO2
Photoacoustic Signal/Arbitrary Units
1.0
0.5
0
390
380
370
360
Wavelength/nm

Figure 4

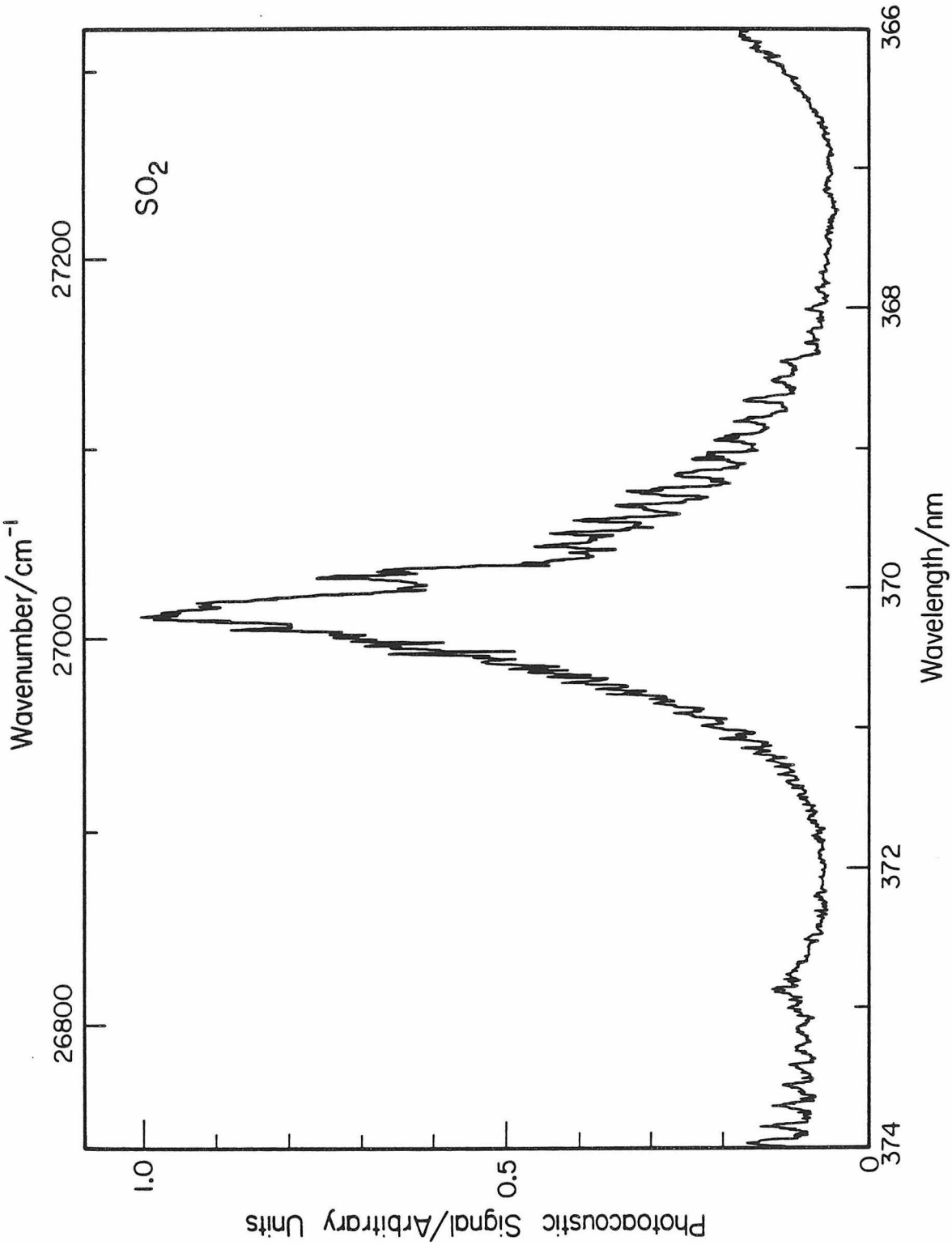
SO_2
Wavenumber/cm^{-1}
26800
27000
27200
Wavelength/nm
366
368
370
372
374
Photoacoustic Signal/Arbitrary Units
0
0.5
1.0

Figure 5

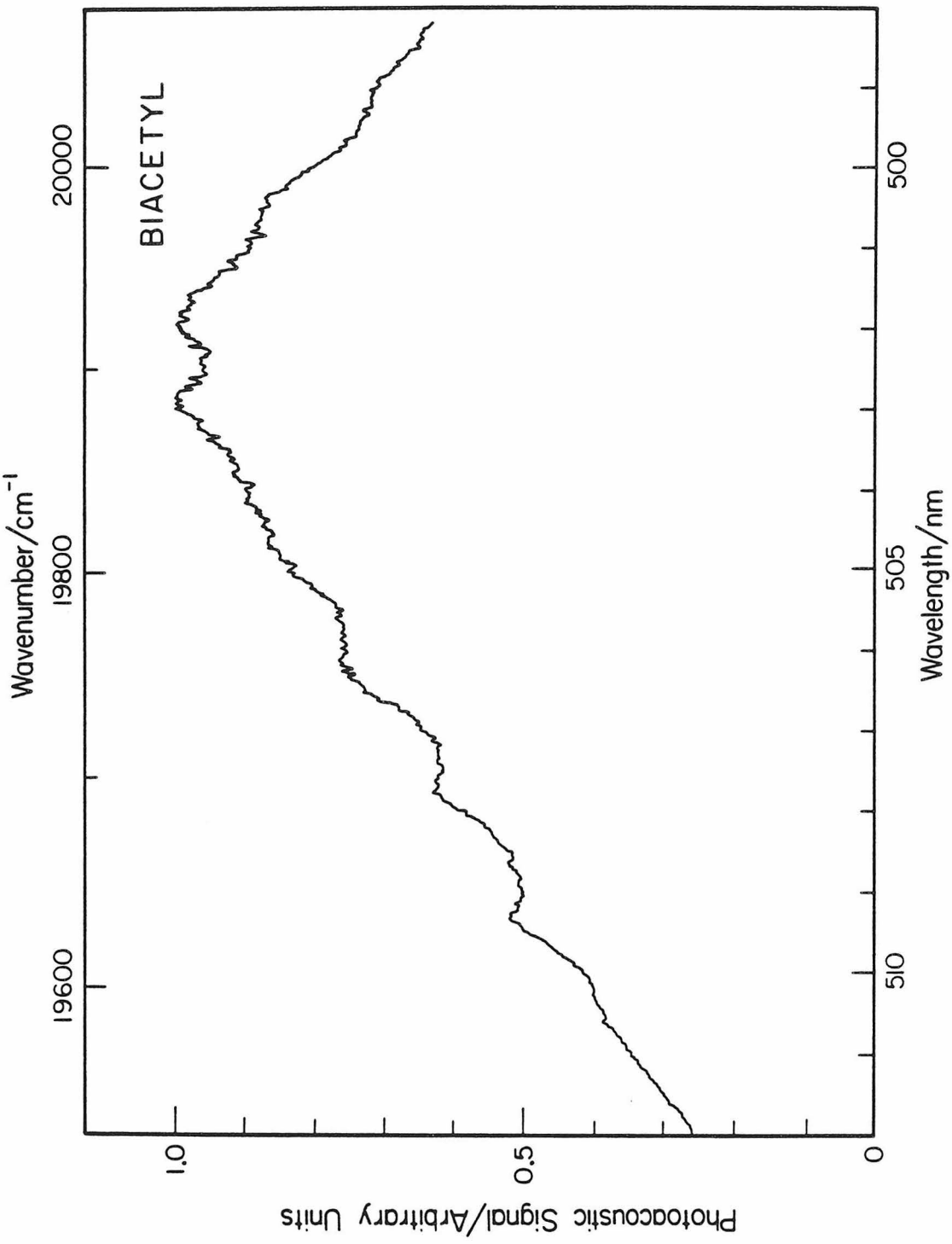
BIACETYL
Wavenumber/cm⁻¹
19600
19800
20000
Wavelength/nm
510
505
500
Photoacoustic Signal/Arbitrary Units
0
0.5
1.0

Figure 6

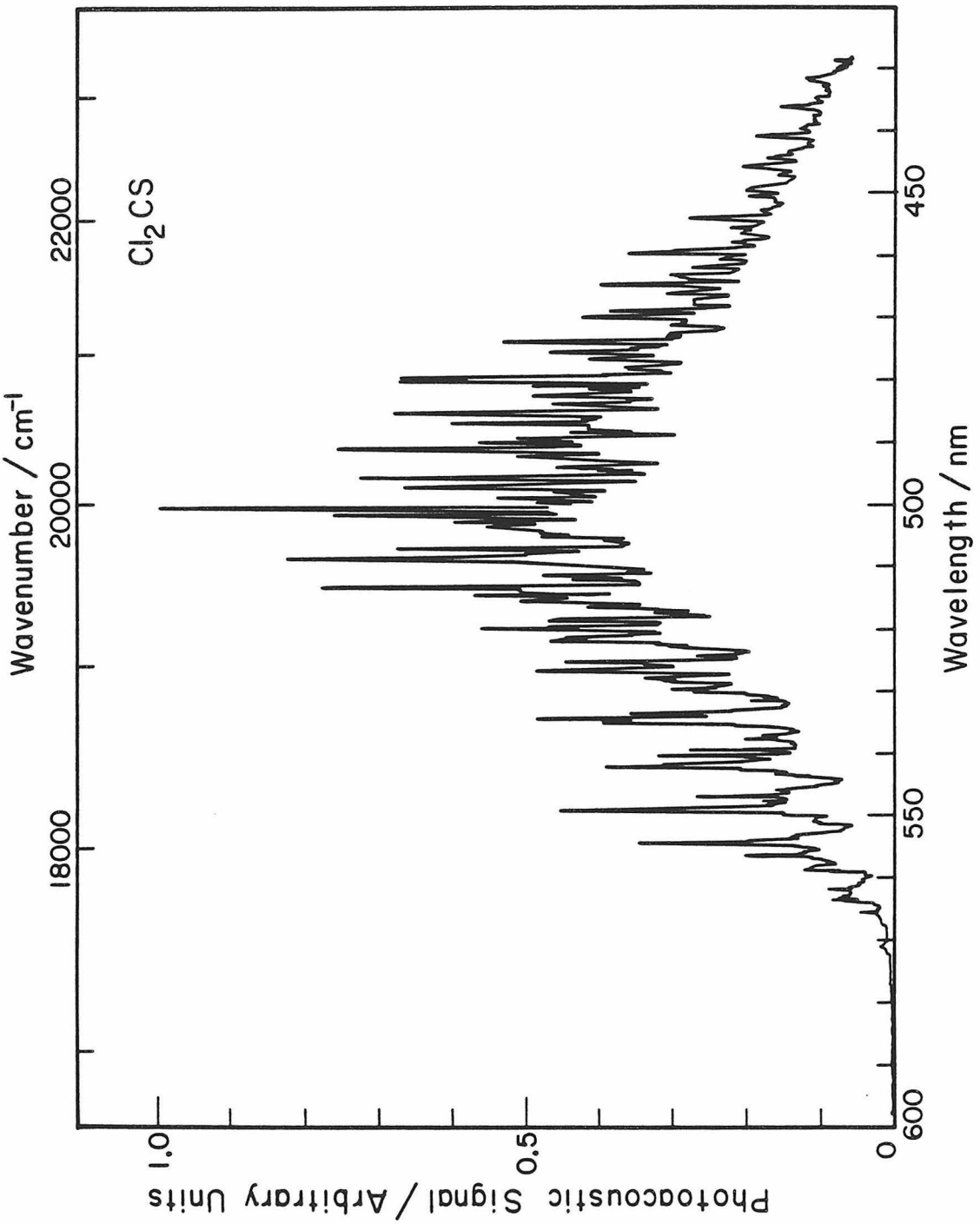
Cl_2CS
Wavenumber / cm^{-1}
18000
20000
22000
Wavelength / nm
450
500
550
600
Photoacoustic Signal / Arbitrary Units
0
0.5
1.0

Figure 7

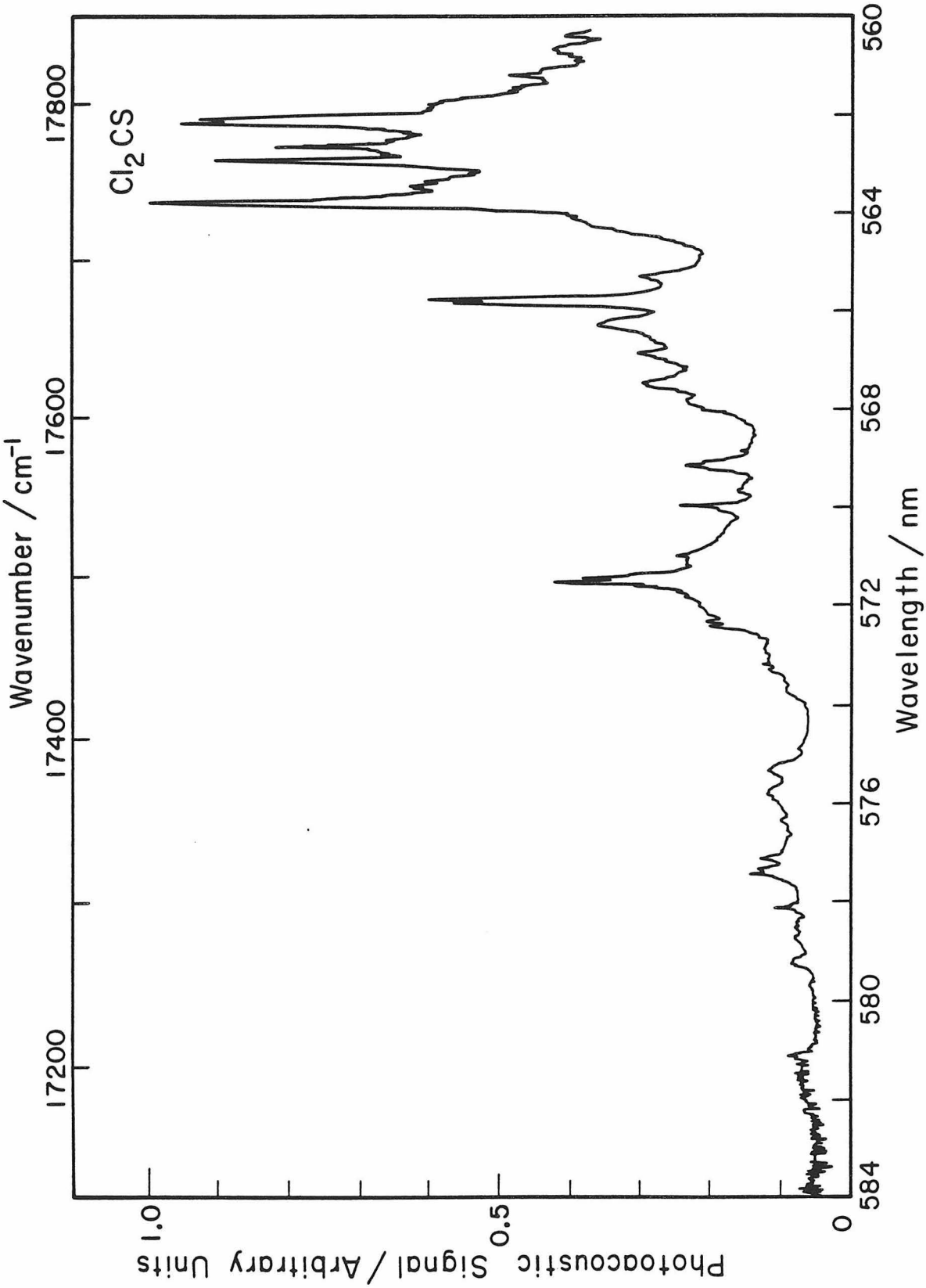
Cl_2CS
Wavenumber / cm^{-1}
17800
17600
17400
17200
Wavelength / nm
560
564
568
572
576
580
584
Photoacoustic Signal / Arbitrary Units
0
0.5
1.0

Figure 8

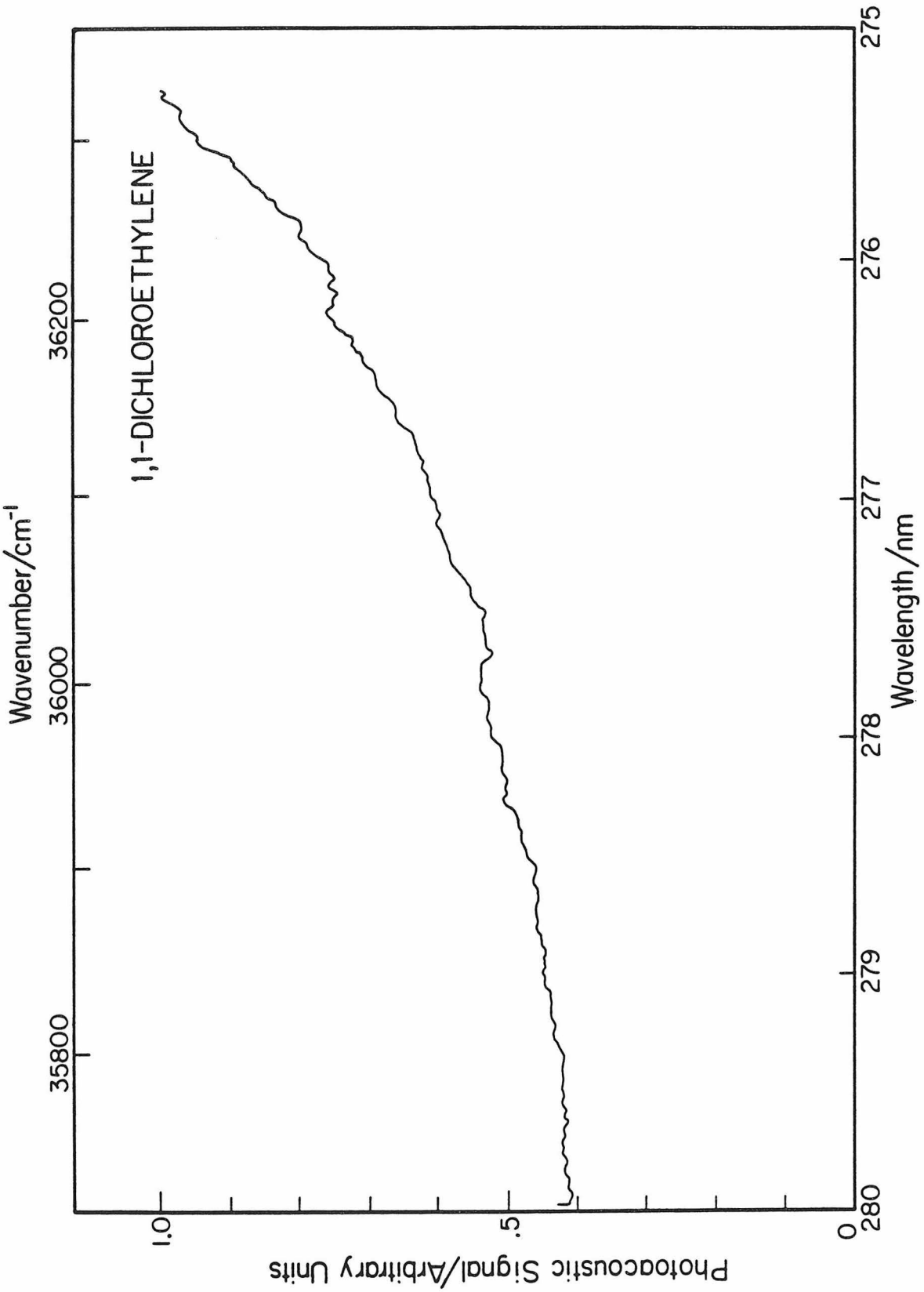
1,1-DICHLOROETHYLENE
Wavenumber/cm⁻¹
35800
36000
36200
Wavelength/nm
275
276
277
278
279
280
Photoacoustic Signal/Arbitrary Units
0
.5
1.0

Figure 9

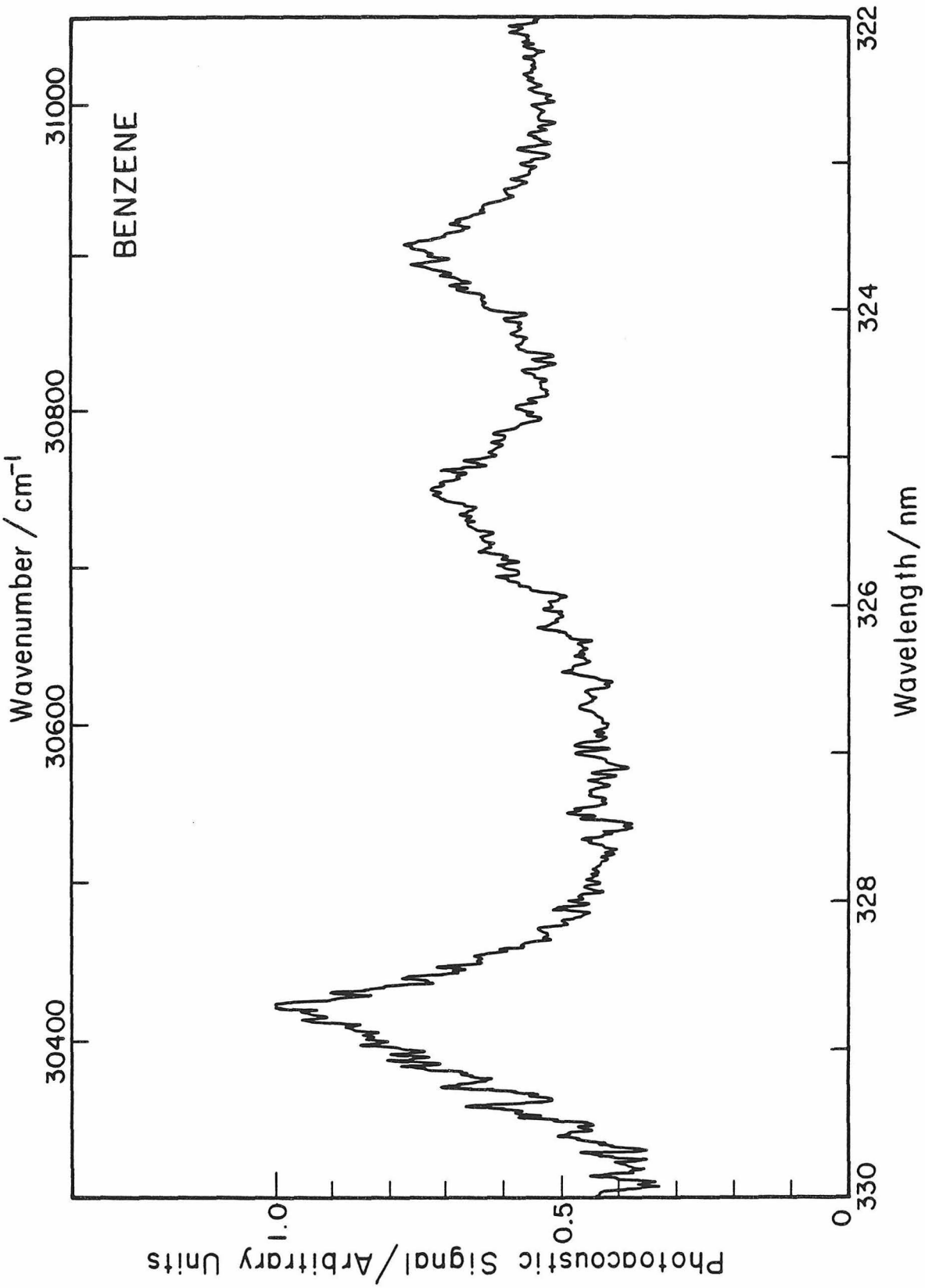
BENZENE
Wavenumber / cm⁻¹
30400
30600
30800
31000
Wavelength / nm
322
324
326
328
330
Photoacoustic Signal / Arbitrary Units
0
0.5
1.0

Figure 10

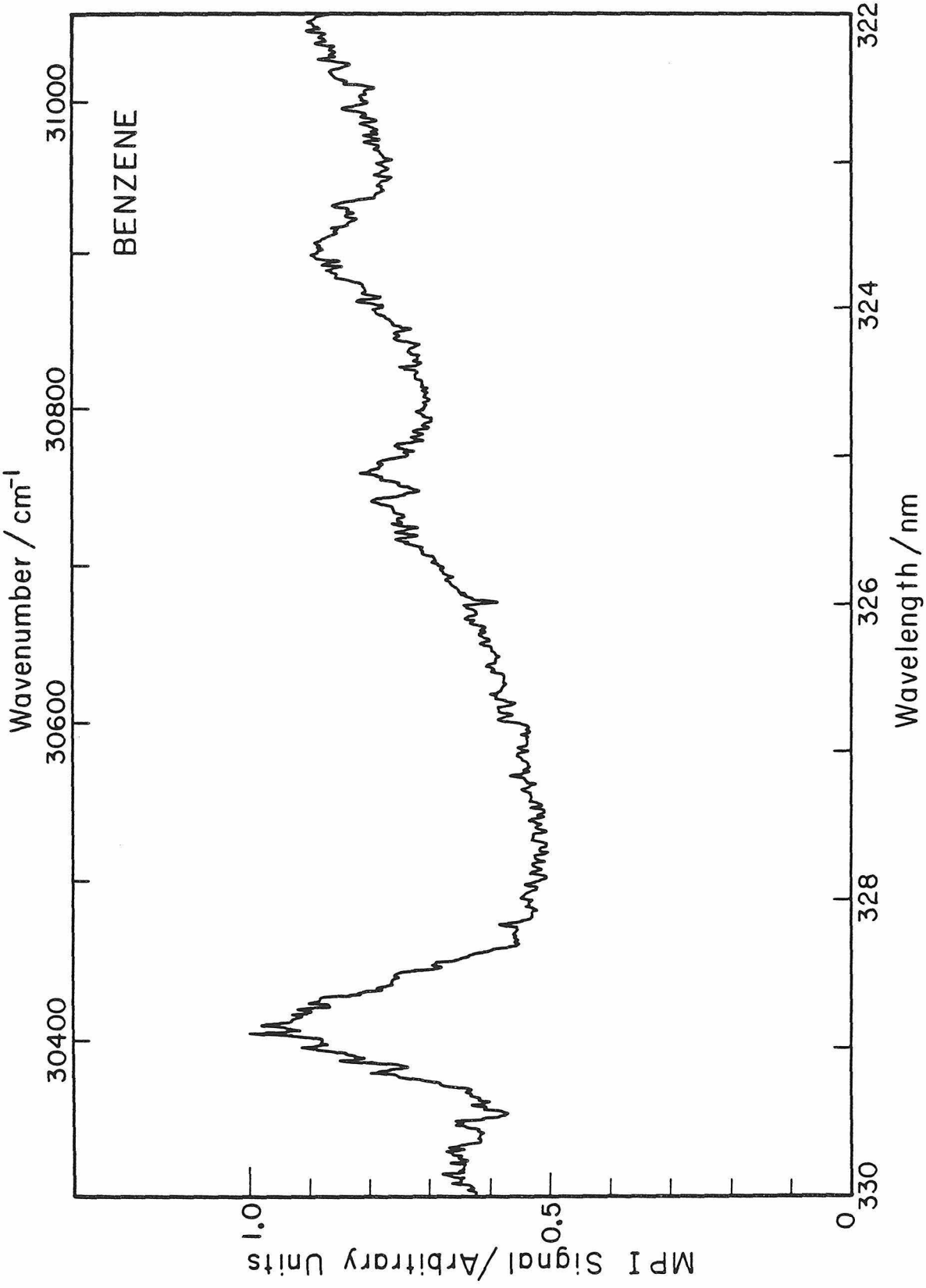
BENZENE
Wavenumber / cm⁻¹
30400
30600
30800
31000
Wavelength / nm
322
324
326
328
330
MPI Signal /Arbitrary Units
0
0.5
1.0

Figure 11

APPENDIX A: A Description of Laser Systems and Related Electronics.

1. Introduction

The lasers used in the experiments described by Papers I-IV in the main body of this thesis consisted of a Molectron MY34 pulsed Nd:YAG laser, a Molectron DL18 dye laser, a Molectron UV400 pulsed N_2 laser, and a Molectron DL200 dye laser. These lasers and their operation are described in detail in the Molectron service and operating manuals supplied with each laser. The specific details of operating each laser will not be covered here. Instead, I will describe briefly the general features of each laser. The crystal scanning drive on the DL18 dye laser was interfaced to the microcomputer used to drive the grating in the DL200 laser and collect data. The microcomputer and the interfacing of the grating scan system were described in the thesis of Ronald Rianda and will not appear here. The details of the crystal scanning circuitry will be described in Section 3.

Papers II and III contain the results of two-color time-resolved experiments. The circuitry involved in triggering the Nd:YAG and N_2 lasers will be described in Section 4.

2. Laser Systems

2.1 MY34 Nd:YAG Laser

Figure 1 shows an optical schematic of the MY34 Nd:YAG laser. The MY34 uses a proprietary cavity design which

combines an unstable resonator with polarization output coupling. The unstable resonator design allows the beam to fill the active volume of the Nd:YAG rod. The polarization extraction produces a low-divergence, near diffraction-limited beam with a near-Gaussian intensity profile. The polarizer in the cavity transmits p-polarized light and reflects s-polarized light. Therefore, light in the cavity traveling to the right in Fig. 1 is p-polarized. When this light returns, after passing through the $\lambda/4$ plate twice and reflecting off M_2, it is s-polarized and gets extracted from the cavity. The Pockels cell is a cylindrical-ring-electrode KD*P Pockels cell which fires approximately 150 μsec after the flashlamp trigger signal.

Light which leaves the oscillator is amplified by a second Nd:YAG rod/flashlamp system and directed into the harmonics box. The Nd:YAG fundamental is doubled using a type II KD*P crystal in a temperature-controlled oven. Another similar crystal mixes the fundamental and second harmonic to produce the third harmonic at 355 nm. A versatile series of dielectric beamsplitters and total reflectors allows any beam to be directed to any output port. The specified output pulse energy for each harmonic is shown below

Wavelength	Pulse Energy
1064 nm	700 mJ
532	225
355	125

In April 1980, when the laser was received, the 532 nm output pulse energy was 360 mJ. The laser fires at a 10 Hz repetition rate with an adjustable pulse length of 15-30 nanoseconds for the fundamental.

2.2 DL18 Dye Laser

The DL18 dye laser is shown schematically in Fig. 2. The second or third harmonic of the MY34 Nd:YAG laser is directed into an oscillator dye cell and one or two additional amplifier dye cells, depending on the operating configuration, using dielectric beam splitters or total reflectors. The oscillator consists of a grating, output coupling mirror, 40X achromatic prism beam expander, half-waveplate, and dye cell. Typically, 10-20% of the pump beam is directed into the oscillator dye cell. The remaining pump beam is directed into one or two amplifier dye cells. The second amplifier, the post amplifier, can be transversely or longitudinally pumped. For longitudinal pumping, the pump beam is decoupled from the dye laser output by pumping in a counter-propagating, slightly off-axis direction, and the oscillator output passes through a 4X beam expander to match beam diameters in the post amplifier. The DL18 dye laser output has a specified linewidth of 0.01 nm at 560 nm and conversion efficiencies of 30% and 20% at 560 nm and 500 nm, respectively. Using different dyes, the fundamental

scanning range is 400-900 nm. Table I contains a list of laser dyes and suggested starting concentrations for the DL18 dye laser.

The wavelength range is extended by using nonlinear frequency doubling and mixing. KPB, KDP and KD*P crystals in temperature-controlled ovens can be mounted in a rotatable mount to allow angle phasematching. The KDP and KD*P crystals (D, E, F and G) use type I phasematching. Pump beams enter the crystals polarized in a vertical plane. The UV output is horizontally polarized. Phasematching is achieved by rotating these crystals about a vertical axis. The KPB crystals (B and C) also use type I phasematching with vertically polarized pump and horizontally polarized output beams. These crystals rotate around a horizontal axis for phasematching.

For frequency doubling, the crystal with the appropriate wavelength range is mounted in the dye laser output beam. When the phasematching angle is correct, the UV output is detected easily from the fluorescence it produces when it strikes a piece of white paper. The residual fundamental beam is eliminated by UV pass/visible blocking filters or the dispersive prism system described in the section on stimulated Raman scattering. During wavelength scans the phasematching angle is adjusted by a micro-computer which also collects data and scans the grating, as described in the next section.

TABLE I. Dye Solution Concentrations for DL18 Dye Laser.[a]

Dye	Solvent	Oscillator[b]	1st Amplifier	Post Amplifier
Stilbene 420	MeOH	8.3×10^{-4}	1.0×10^{-3}	4.5×10^{-4} T[c]
C480	EtOH	5.0×10^{-3}	Not Determined	Not Determined
C500	EtOH	4.5×10^{-3}	3.3×10^{-3}	1.0×10^{-3} T
C540A	EtOH	1.2×10^{-2}	6.0×10^{-3}	4.0×10^{-3} T
R6G	EtOH	3.0×10^{-4}	-[d]	5.0×10^{-5} L
R610	EtOH	5.0×10^{-4}	-	2.3×10^{-4} T
R640	MeOH	1.5×10^{-3}	-	7.0×10^{-5} L
DCM	MeOH	$<10^{-3}$[e]	-	Osc. Conc.÷ 2 T
Crystal Violet	EtOH	$<10^{-2}$	-	Osc. Conc.÷ 6 T
Oxazine 725	MeOH	1.0×10^{-2}	-	Osc. Conc.÷ 6 T

[a]Concentrations given are starting concentrations only. Output wavelength tuning curves can be shifted to longer or shorter wavelengths by increasing or decreasing, respectively, the oscillator dye concentration.

[b]All concentrations in units of molarity (moles of solute/liter of solution).

[c]T implies transverse pumping. L implies longitudinal pumping.

[d]First amplifier not used.

[e]< symbol is used for saturated solutions. Mix up solution at the indicated concentration and allow solute to dissolve as much as possible.

Frequency mixing is similar to frequency doubling, except that a photon from the Nd:YAG pump laser replaces one of the dye lser photons in the nonlinear process. A dichroic beam combiner is used to overlap the dye fundamental with the Nd:YAG fundamental or second or third harmonic. When mixing with the 1064 nm Nd:YAG fundamental, a half-wave plate rotates the 1064 nm beam polarization to vertical to match the vertically polarized dye laser beam.

2.3 UV400 N_2 Laser and DL200 Dye Laser

The two-laser experiments described in Papers II and III, and early photoacoustic spectroscopy studies, used a lower power pulsed dye laser system. The pump laser was a Molectron UV400 N_2 laser which produces 10 nsec 400 kilowatt pulses at 337.1 nm. This laser operates with a 30 kilovolt discharge channel containing N_2. The discharge excites N_2 molecules and creates a population inversion which lases on the $\tilde{C}^3\pi_u \rightarrow \tilde{B}^3\pi_g$ transition.

The N_2 laser was used to pump a Molectron DL200 dye laser which is shown schematically in Fig. 3. The DL200 consists of a single dye cell inside a cavity formed by a grating and output coupling mirror. A beam expanding telescope is used to illuminate more lines on the grating and reduce beam divergence. Using a variety of dyes, this N_2 laser pumped dye laser system produces output in the

range of 360-900 nm and a maximum pulse energy of 300 μJ. An accessory turret containing 5 KDP crystals can be used to frequency double the dye laser output, producing UV down to 260 nm with a maximum pulse energy of 25 μJ.

3. Crystal Phasematching Angle Control

For continuous wavelength scans in the ultraviolet using the DL18 dye laser, both the grating and crystal angle must be scanned simultaneously. The grating scan is controlled by the scan circuitry on the prototype board described in the thesis of Ronald Rianda. The crystal scanning system which I developed is described in this section.

The grating scan in the DL18 incorporates a sine drive which transforms the rotation of a stepping motor shaft into a linear wavelength scan. The prototype board designed by Ronald Rianda generates periodic pulses which drive the stepping motor for the wavelength scan. Every 0.01 nm, the scan circuitry generates an interrupt which tells the microcomputer to collect data and update the wavelength displayed on the terminal. The machine language program which controls the wavelength scan is called STPRS.

The crystal angle is a complicated, nonlinear function of wavelength. We chose to model this function over small wavelength intervals as a polynomial in grating counter units. (Grating counter units equal the wavelength in angstroms

multiplied by the grating order.) This polynomial is determined by a least squares fit of experimentally determined data points of grating counter units and crystal angle. Acceptable wavelength scans can be obtained by taking data points every 25 or 50 grating counter units and using a 5th order polynomial.

Data collection and curvefitting are performed using the BASIC program CRYST. Three options in CRYST are available for data entry: terminal entry where the user types in both grating counter unit and crystal angle, computer-assisted data entry where the computer scans the grating and the user types in crystal angles, and data modification which allows modification of existing data. Immediately after entry, the data are stored in DEBBI single precision floating point format. Grating counters units are stored starting at BE80 and crystal angles starting at BE00. The data are shifted by subtracting off the average to increase the accuracy of the fit. The shifted grating counter unit data are scaled by dividing by 256. A polynomial of order 1 to 5 is determined from a least squares fit to the shifted and scaled data. The resulting coefficients are adjusted for the scaling and shifting, converted to SBC310 highspeed math board floating point format by user subroutine USR4 contained in program SCSU4, and stored starting at memory location BF74. The average of the grating counter unit data XT is stored at BF70.

A modified version of STPRS was written, called LSCAN, which incorporates the crystal scan routines. The crystal angle polynomial is evaluated every 0.01 nm, and the result is sent to the DL222 crystal scan control in the DL18 dye laser. The current grating counter unit PCNTR is shifted by subtracting XT and used as the argument for the polynomial. The polynomial is evaluated in floating point format using Horner's method of expanded parentheses and the SBC310 high-speed math board. The floating point result is converted to 16 bit fixed point integer format. The eight least significant bits are sent to port A of the Intel 8255 parallel port on the prototype board which is memory mapped at 2FE8. 7405 open collector drivers were used to increase the 8255 output to meet the input voltage and current specifications of the Molectron DL222 digital servo open loop control for the crystal drive. A latch signal from port B1 of the 8255 (memory mapped at 2FE9) latches the eight least significant bits into the DL222. The eight most significant bits are sent in a similar manner through port A of the 8255 and latched into the DL222 using a latch signal from port B0.

The Molectron DL222 was originally designed to accept two analog voltages which correspond to the eight least significant bits and the eight most significant bits. An analog to digital converter alternately sampled both voltages and sent the digital data to RCA-CD4042B quad clocked latches.

RCA-CD4063B four-bit magnitude comparators compared the latch data to the current crystal position stored in RCA-CD40193B presetable binary up/down counters, and increased or decreased the crystal angle until the crystal was at the correct angle.

The DL222 was modified to accept digital data directly from the microcomputer. The analog to digital converter chip U15 was replaced with a 16-pin component header having the eight data lines from port A of the 8255 parallel port on pins 2-9. The latch lines from U26A and U26B were cut just before test points 2 and 7. These test points were connected to ports B0 and B1 of the 8255 parallel port for software control of the latching operation.

The crystal scanning system just described permits scanning over entire dye gain curves while maintaining phasematching of the crystal. When slight adjustments are made in the dye laser optics, the output beam direction can change slightly. This change is easily compensated for by using the "CAL" control on the DL222. Using LSCAN, the crystal is positioned at an angle corresponding to the grating counter unit. The DL222 is put in the "CAL" mode, the crystal angle is adjusted for maximum power, and then the DL222 is returned to "OPER" mode. In this way, the same coefficients can be used over periods of several weeks, even though repeated tweaking of the dye laser is required every day.

Problems arise occasionally at high power levels. Large dips occur in the output vs. wavelength curve. This is believed to occur because of local heating of the crystal, which introduces changes in the index of refraction due to temperature increases. This effect is minimized by taking the initial polynomial data under conditions similar to those under which the experiment will be carried out.

Recently, INRAD announced a new autotracking second harmonic generation system, model S-12. This system automatically optimizes the crystal angle for maximum conversion efficiency. A dual element photodiode senses the slight shift in output beam direction when the crystal is not phase-matched, and supplies a correction signal to the crystal angle servo motor. Systems of this type which function automatically are reported to be simple to use and reliable. Eventually the polynomial system should be upgraded to a fully automatic scan system.

4. Electronics for Two-Laser Experiments

Papers II and III presented the results of some two-color time-resolved spectroscopy experiments. These experiments required the synchronization of pulses from two independent lasers with nanosecond precision. The electronics used to trigger the two lasers and collect data were described briefly in the two papers. This section will present a more

in-depth description of the electronics needed to perform those experiments.

The UV400 N_2 laser can be externally triggered with a +5 to +30 volt pulse with a risetime of less than 1 μsec. The laser fires 500-1000 nsec later with a specified jitter of less than 4 nsec. The MY34 Nd:YAG laser triggering is more complicated. The flashlamps must fire about 150 μsec before the Q-switch opens, to allow the maximum deposition of energy into the ND:YAG rods. The rear panel of the laser has trigger inputs and synchronization outputs for both the flashlamps and Q-switch. The output pulse temporal jitter is specified at ±1 nsec when triggered by an electrical pulse with a risetime of <15 nsec.

A schematic of the trigger and data collection electronics is shown in Fig. 4. The Nd:YAG laser internal 10 Hz clock serves as the trigger source. The Nd:YAG flashlamps are fired internally by this clock, and the lamp sync output triggers a Rutherford 87B pulse generator. This pulse generator supplies most of the nominal 150 μsec delay required before the Q-switch opens. Since most pulse generators have jitter in delay time on the order of 0.1%, the initial 150 μsec time period cannot be used to actually trigger the Q-switch. Instead, the initial 150 μsec delay triggers a pair of fast risetime pulse generators which each generate a delay of <200 nsec before triggering the N_2 laser and the

Nd:YAG Q-switch, respectively. This allows the 150 μsec delay to fluctuate on the μsec timescale, but still keeps the timing between the two laser pulses reproducible on the nsec timescale.

In Fig. 4, pulse generators B and C are the fast risetime pair of pulse generators. B is a Hewlett Packard 8005B 20 MHz pulse generator with a risetime $\lesssim$ 10 nsec. C is an E-H International 139B 50 MHz pulse generator with a risetime $\lesssim$ 6 nsec. In practice, the Rutherford pulse generator (A) has an erratic risetime of approximately 1 μsec so the C pulse generator is triggered from the B pulse generator's trigger out terminal. This insures that B and C are locked together independent of the output waveform of A. Long-term jitter between pulses, as monitored with a Hewlett Packard 5082-4220 PIN photodiode (-18 volt reversebias, $\tau_{rise} < 1$ nsec), was less than ±2 nsec, with a short-term (10 sec) jitter of ±1 nsec. Pulsewidths of the doubled output of each dye laser were $\lesssim$5 nsec.

In some experiments where wavelengths were scanned (Paper II), it was necessary to correct signals for fluctuations in laser pulse energy. Since we have only one pyroelectric joulemeter, we designed a detection system which subtracts out the fraction of the total signal due to the N_2 dye laser system in real time. The remaining signal from the Nd:YAG dye laser system is stored along with intensity data from that laser. To accomplish this, we fired the N_2

laser at 20 Hz, twice the Nd:YAG laser repetition rate, by operating pulse generator B in the double pulse mode. The photoacoustic or MPI signals were integrated by a differential gated integrator system which added the signal when both lasers fired and subtracted the signal when only the N_2 laser fired. Pulse generator D, a Molectron model 122 dual gate generator, produced the integration gates for the integrators. Pulses were sent alternately to first the "add" gate input of the integrator and then to the "subtract" gate input by a homebuilt pulse router. The pulse router consisted of a flip-flop, triggered by pulse generator B, which selected which channel of a multiplexer would be active. The pulses from pulse generator D passed through the multiplexer and were directed to either the "add" or "subtract" integrator gate inputs.

The photoacoustic or MPI signals were initially processed by an Ithaco 4302 dual channel 24dB/octave electronic filter. The signal passed through both channels sequentially. The first channel was operated as a low-pass filter with a gain of 1 or 10. The second channel was operated as a high-pass filter, also with a gain of 1 or 10. Further amplification and filtering was performed with a Molectron model 131 amplifier/shaper. The integrator was a Molectron model 112 differential gated integrator.

Nd:YAG laser pulse energies were measured with a Laser Precision RkP-335 pyroelectric energy probe and Rk3230

readout unit. The pulsed analog output of the readout unit was also amplified and filtered by a second amplifier/shaper and integrated by a differential gated integrator. Analog signals from the two gated integrators were digitized and stored on floppy disk by a microcomputer which also controlled the wavelength scan. The stored signal and laser intensity data were processed at a later time and plotted to produce the final publication spectra.

Figure Captions

Figure 1. Optical schematic of the Molectron MY-34 pulsed Nd:YAG laser. The oscillator cavity is defined by mirrors M_1 and M_2. SHG and THG are abbreviations for second harmonic generation and third harmonic generation, respectively.

Figure 2. Optical schematic of the Molectron DL-18 dye laser. The letters A through P label the following components: A - beam shutter, B - beam splitter, C- total reflector, D - focusing lens, E - magnetically stirred or flowing dye cell, F - prism beam expander, G - diffraction grating, H - output coupling mirror, J - $\lambda/2$ plate, K - beam expanding telescope, L - post amplifier flowing dye cell, M - right-angle prisim, N - dichroic beam combiner, O - doubling or mixing crystal, P - UV bandpass filter.

Figure 3. Optical schematic of the Molectron DL-200 dye laser. An etalon was not used in the experiments described in this thesis. The polarizer is only used when the dye laser output is being frequency doubled and the grating counter unit is below 28,000.

Figure 4. Schematic of the laser triggering electronics and data collection system used in two-color time-resolved spectroscopy experiments. The operation of this system is described in Section 4.

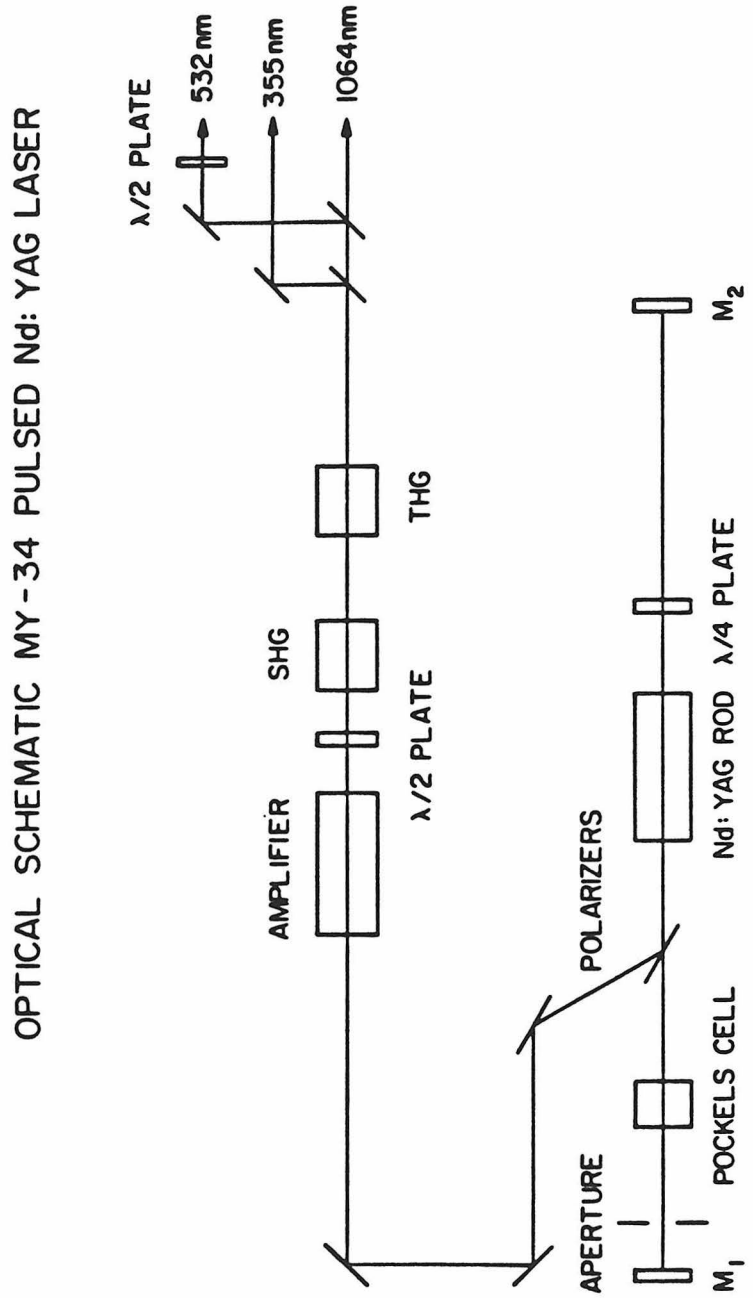
OPTICAL SCHEMATIC MY-34 PULSED Nd: YAG LASER
λ/2 PLATE
532nm
355nm
1064nm
AMPLIFIER
SHG
THG
λ/2 PLATE
POLARIZERS
Nd: YAG ROD
λ/4 PLATE
APERTURE
POCKELS CELL
M1
M2

Figure 1

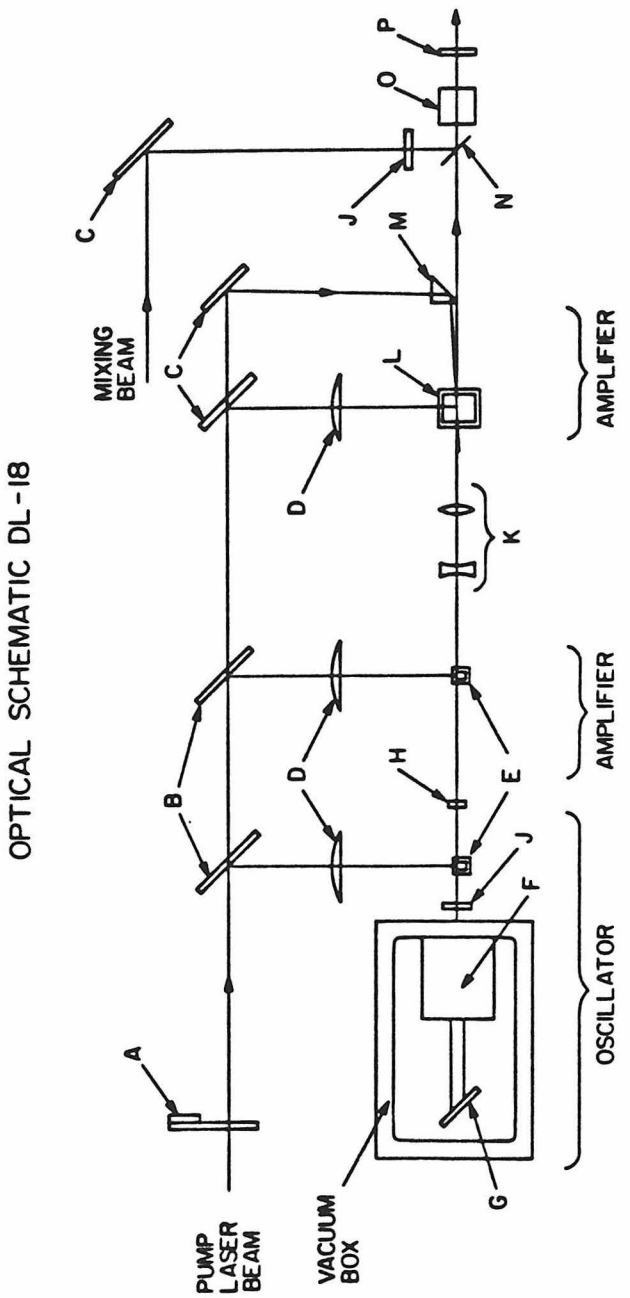
OPTICAL SCHEMATIC DL-18
PUMP LASER BEAM
VACUUM BOX
MIXING BEAM
OSCILLATOR
AMPLIFIER
AMPLIFIER
A
B
C
D
E
F
G
H
J
K
L
M
N
O
P

Figure 2

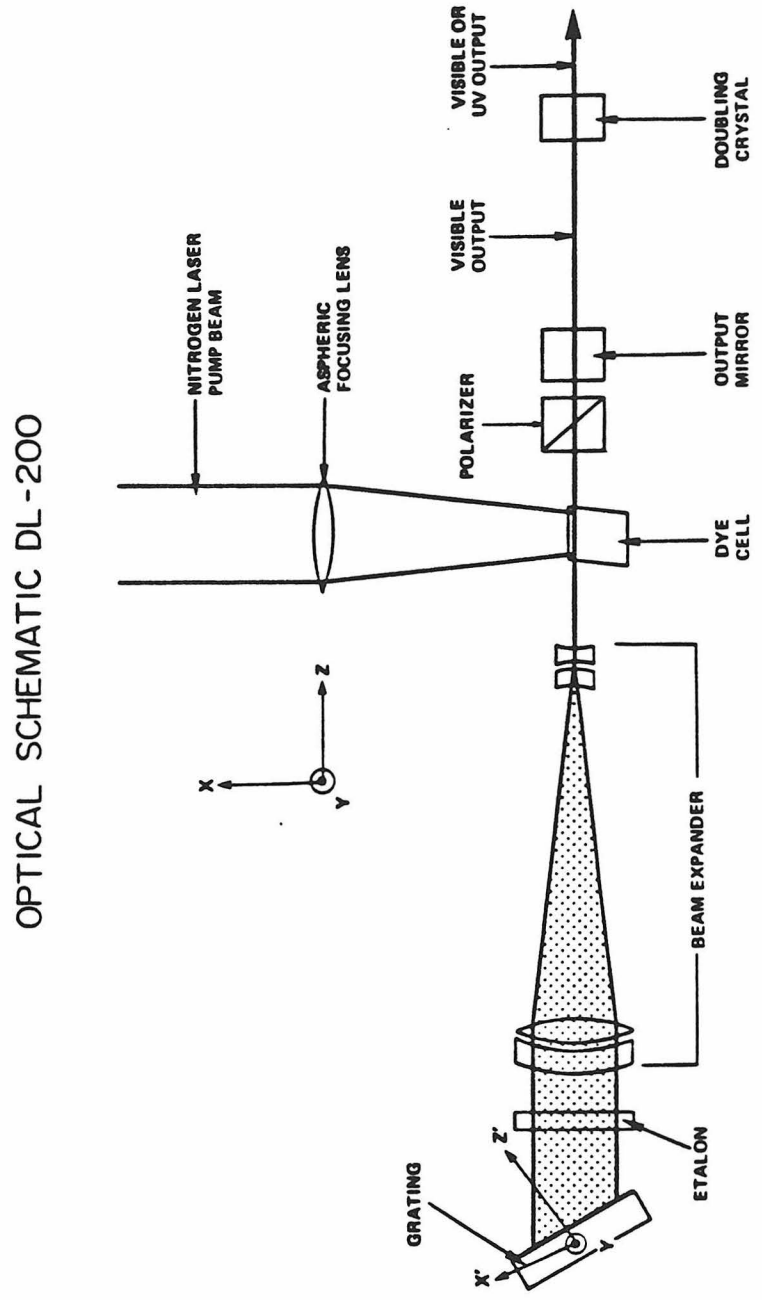
OPTICAL SCHEMATIC DL-200
NITROGEN LASER PUMP BEAM
ASPHERIC FOCUSING LENS
POLARIZER
VISIBLE OUTPUT
VISIBLE OR UV OUTPUT
DOUBLING CRYSTAL
OUTPUT MIRROR
DYE CELL
BEAM EXPANDER
ETALON
GRATING
Z
X
Y
Z'
X'
Y'

Figure 3

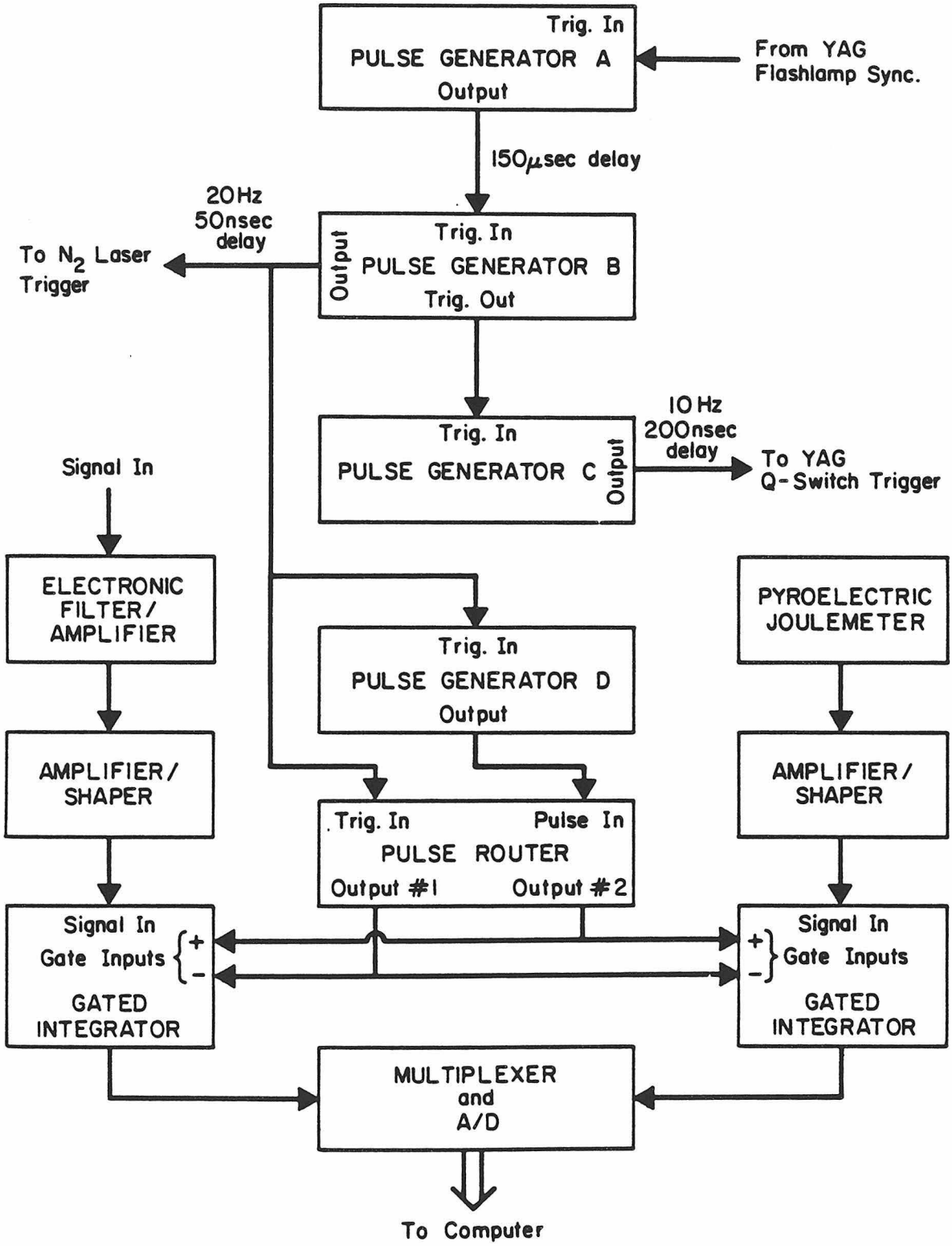
Trig. In
PULSE GENERATOR A
Output
From YAG
Flashlamp Sync.
150μsec delay
20Hz
50nsec
delay
To N_2 Laser
Trigger
Output
Trig. In
PULSE GENERATOR B
Trig. Out
Trig. In
PULSE GENERATOR C
Output
10Hz
200nsec
delay
To YAG
Q-Switch Trigger
Signal In
ELECTRONIC
FILTER/
AMPLIFIER
Trig. In
PULSE GENERATOR D
Output
PYROELECTRIC
JOULEMETER
AMPLIFIER/
SHAPER
Trig. In
Pulse In
PULSE ROUTER
Output #1
Output #2
AMPLIFIER/
SHAPER
Signal In
Gate Inputs
+
-
GATED
INTEGRATOR
Signal In
+
-
Gate Inputs
GATED
INTEGRATOR
MULTIPLEXER
and
A/D
To Computer

Figure 4

APPENDIX B: The Design of Photoacoustic Cells for Pulsed Laser Excitation.

1. Introduction

At the time the experiments described in this thesis were initiated (1977), photoacoustic spectroscopy experiments almost always used CW light sources modulated at audio frequencies. Since that time, a variety of experiments using pulsed laser excitation have been performed,[1] including the experiments described in this thesis. An overview of the important design criteria for optimizing photoacoustic cells for pulsed excitation has not yet appeared in the literature. The photoacoustic cells (PAC's) used in our experiments have evolved through five general design classes as we attempted to improve the sensitivity of our cells. These classes, labeled PAC1 to PAC5, illustrate important aspects of PAC design. A description of each class and its advantages and disadvantages is presented in the following sections.

2. Photoacoustic Cell Design

2.1 PAC 1

Our first photoacoustic cell, PAC1, followed a design used by Reddy and Berry[2] and is similar to the one described by Kreuzer.[3] It consisted of a cylindrical stainless steel chamber 10.2 cm long with an inner diameter of 3.81 cm, which housed a stainless steel cylindrical tube having a 1.27 cm outer diameter, 7.0 cm length and 8.38×10^{-2} cm wall thickness, perforated by about 350 randomly distributed

holes of 0.16 cm diameter. This tube was tightly wrapped with an aluminum-coated mylar film 1.27×10^{-3} cm thick. A potential of 300 volts was applied across the cylindrical concentric capacitor formed by the aluminum coating and the perforated tube. A Canberra model 2001A charge-sensitive preamplifier integrated the signal produced when the photoacoustic pressure wave displaced the mylar diaphragm. The signal consisted of a few successively damped oscillations, each full oscillation lasting about 10 μsec.

The sensitivity for pulsed excitation of PAC1 was compared to another cell which contained a 1" diameter Bruel and Kjaer microphone model MDC 4144. PAC1 was considerably more sensitive to pulsed excitation. The probable reason is that in the cylindrical system we detected a shock wave which struck the entire area of the cylindrical diaphragm simultaneously, rather than a smaller flat area of the planar microphone nonsimultaneously. This produced a shorter, larger amplitude pulse which increased the signal-to-noise ratio.

The sensitivity of PAC1, however, decreased with time due to stretching of the mylar diaphragm. New diaphragms were difficult to install and did not produce reproducible sensitivities.

2.2 PAC2

The irreproducible sensitivity of the cylindrical

microphone forced us to investigate photoacoustic cells containing commercial microphones. Joseph Barrett recommended using a Knowles Electronics model BT1759 miniature electret microphone, based on his experience with photoacoustic cell design.[4-7] This microphone has dimensions of .792 x .559 x .228 cm. A "saltshaker"-like port with a diameter of .476 cm is located on the top. The microphone has a flat responsivity of 10^{-2} volt/Pascal over a frequency range of 50 to 10^4 Hz. An internal FET preamplifier draws a current of 50 μA at 1.3 volts DC.

A photoacoustic cell, PAC2, which incorporated a BT1759 microphone was designed and built. This cell consisted of a small chamber .53 cm long with .24 cm diameter openings at opposite ends. Quartz windows were mounted over the openings using expoxy resin. A BT1759 microphone was mounted over an opening in the side of this chamber. It was located as close as possible to the central axis defined by the window openings. This maximized the amplitude of the pressure wave produced by absorption of the laser pulse.

PAC2 exhibited excellent sensitivity, approximately equal to PAC1. All spectra taken with PAC2, however, contained large amounts of constant background signal due to absorption or scattering of light at the windows. Window absorption heats the gas near the window, which produces a pressure wave. Window scattering causes light to strike the cell walls, which also heats the nearby gas to produce

a pressure wave. In PAC2, the windows were very close to the microphone, causing the window absorption or light scattering pressure waves to arrive at the microphone simultaneously with the pressure wave produced by direct gaseous sample absorption. The constant background was a significant fraction of the total signal so a major modification was required.

2.3 PAC3

PAC3 was designed to minimize window background signals and still retain the sensitivity of PAC2. This was accomplished by moving the windows back away from the microphone. The window absorption and scattering pressure wave still reached the microphone, but not until after the pressure wave from the sample absorption had already been detected. By proper gating of the detection electronics, only the sample absorption pressure wave was detected.

PAC3 consisted of a stainless steel cell with a 3.8 cm long by .56 cm diameter sample chamber. Suprasil 1 windows were mounted at Brewster's angle at each end using Viton o-rings. A BT1759 microphone was mounted over a hole in the cell wall approximately equidistant from both windows. A quartz window was mounted on the side opposite the microphone to allow simultaneous fluorescence measurements.

The window noise was drastically reduced in PAC3 compared

to PAC2. A small residual background signal was still present, however. It was eventually determined that the Brewster angle windows were still contributing scattered light signals. Brewster's angle changes slowly as a function of wavelength and the laser beams are not perfectly polarized. These two effects caused a small amount of light to reflect off the exit window and strike the cell walls. The polished stainless steel surface allowed multiple reflections which caused scattered light to eventually strike the walls near the microphone or the microphone itself. This produced a pressure wave which arrived at the microphone simultaneously with the pressure wave from sample absorption. This effect was small, but still able to overshadow extremely small absorption signals. The sample chamber diameter was also too small. The small diameter required decreasing the 8 mm diameter DL18 dye laser beam to avoid striking the cell walls. This increased the nonlinear absorption effects described in Paper IV.

2.4 PAC4

The PAC4 class of photoacoustic cells had parallel windows oriented perpendicular to the laser beam, and larger diameter chambers. This eliminated the scattering from the Brewster angle windows of PAC3. The larger diameter allowed reduced intensities because tight focusing was no longer

required to keep the beam from striking the cell walls. A BT1759 microphone was mounted as close as possible to the laser beam to maximize the amplitude of the pressure wave. Most of the experiments described in Papers I and IV used the PAC4 design.

PAC4 cells were constructed from brass or stainless steel 3/8 inch Swagelok fittings. A BT1759 microphone was mounted over a hole in the side of a Swagelok tee using epoxy resin. Before mounting, the side of the tee was machined down to allow positioning of the microphone as close as possible to the laser beam. Quartz windows were epoxied onto 3/8 in Swagelok to 1/8 in female pipethread adapters. Short pieces of 3/8 in tubing were used between the tee and pipethread adapters. The overall finished lengths were about 15 cm. The PAC4 cells were inexpensive (<$50.00) and could be constructed from standard fittings in a single afternoon. Their major disadvantage was the difficulty in replacing or cleaning windows. Many samples produce photochemical deposits on the cell windows after irradiation with UV light. The window deposits increase the scattered light background. After extended irradiation, the windows must be removed, cleaned and replaced. Most windows were broken in the process of removing them from the epoxy seals. After replacing the windows, a 24-hour period was required before the cell could be used again. This time period was necessary to allow the epoxy to cure and outgas.

2.5 PAC5

The currently used photoacoustic cell, PAC5, is similar to the PAC4 cells except that 0.5 in stainless steel Swagelok fittings are used. Two pairs of apertures are also mounted inside the cell to decrease scattered light. The two apertures near the windows have diameters of .64 cm. The inner apertures located near the microphone have diameters of .71 cm. This choice of diameters insures that a laser beam passing through both outer apertures will not scatter off the edges of the two larger inner apertures. These apertures essentially eliminate all scattered light which could produce detectable pressure waves that reach the microphone simultaneously with the pressure waves caused by sample absorption. The PAC5 cell was used in the experiments discussed in Papers II and III.

3. Conclusions

In summary, the general criteria which should be considered when designing photoacoustic cells for use with pulsed excitation are: (1) minimize scattered light, (2) locate the windows far enough from the microphone to allow temporal discrimination between sample absorption and window absorption, and (3) mount the microphone as close as possible to the laser beam to increase the amplitude of the detected pressure wave.

The PAC5 cell is currently our state-of-the-art

photoacoustic cell. The sensitivity of this cell could possibly be increased by mounting the microphone inside the cell. In the present configuration, the microphone is mounted over a hole in the cell wall. The hole limits the transmission of the pressure wave to the microphone. Placing the microphone inside the cell would eliminate this problem and also allow the microphone to be closer to the laser beam. If additional pulsed photoacoustic spectroscopy experiments are attempted which require high sensitivity, this new configuration should be tested.

References

1. A partial list of pulsed photoacoustic experiments can be found in Paper IV.
2. M. J. Berry and K. V. Reddy, private communication; K. V. Reddy, PhD Thesis, University of Wisconsin-Madison (1977); K. V. Reddy, Faraday Discuss. Chem. Soc. 67, 188 (1979).
3. L. B. Kreuzer, J. Appl. Phys. 42, 2934 (1971).
4. J. J. Barrett and M. J. Berry, Appl. Phys. Lett. 34, 144 (1979).
5. G. A. West and J. J. Barrett, Opt. Lett. 4, 395 (1979).
6. D. R. Siebert, G. A. West and J. J. Barrett, Appl. Opt. 19, 53 (1980).
7. G. A. West, D. R. Siebert and J. J. Barrett, J. Appl. Phys. 51, 2823 (1980).

APPENDIX C: Wavelength Conversion by Stimulated Raman Scattering.

Wavelength Conversion by Stimulated Raman Scattering

The Molectron Nd:YAG laser, dye laser, and accessories can produce tunable coherent output from about 217 nm to 900 nm by using a variety of dyes, and frequency doubling and mixing in KDP and KPB crystals. The high peak powers available fron Nd:YAG pumped dye lasers and excimer lasers has led to the development of a wide variety of nonlinear optical techniques for converting the output of these lasers to shorter and longer wavelengths. Stimulated Raman scattering (SRS) has gained widespread interest because of its simplicity and broad wavelength range.[1,2]

SRS has been observed in solids, liquids, and gases. It is a nonlinear parametric interaction involving the third-order nonlinear susceptibility X^3. Several review articles have summarized the current understanding of SRS.[3-5] In simple terms, a pump laser pulse at frequency ν_P promotes a molecule from initial state, i, to a virtual state. If the pump pulse is intense, a population inversion can result between the virtual level and a final level, f. In hydrogen, for example, states i and f may correspond to the ground and first vibrational states, respectively. Once a population inversion is produced, stimulated emission occurs at a frequency $\nu_{S1} = \nu_P - (\nu_f - \nu_i) = \nu_P - \nu_R$. For hydrogen, $\nu_R = 4155\ cm^{-1}$. The production of stimulated ν_{S1} output has a flux density threshold. Once this threshold is achieved,

the S1 output increases exponentially with distance from the initial spontaneous Raman output. S1 and the pump beam are in phase and can beat against one another to produce an electronic polarization in the gas at the Raman frequency ν_R. This induced polarization interacts with the pump beam to produce sidebands at $\nu_p \pm \nu_R$. The $\nu_p + \nu_R$ sideband is called first anti-Stokes output and denoted as AS1. (The $\nu_p - \nu_R$ sideband is called first Stokes output and labeled S1.) The process just described is not exactly correct because it implies that there is a time dependence involved in the various processes. Actually, the generation of AS1 is a parametric four-wave mixing process involving simultaneously two ν_p waves and one ν_{S1} wave to produce a ν_{AS1} wave. AS1 can interact with AS0 (the pump) to produce AS2 at frequency $\nu_{AS2} = \nu_p + 2\nu_R$. The process repeats itself again and again to produce a large number of AS lines. Higher order Stokes lines can also be generated parametrically. The end result is that once threshold is reached, a distribution of new frequencies is produced with frequencies $\nu_n = \nu_P + n\nu_R$ with n equal to all integers between approximately -5 and 8, depending on the dispersion of the gas. All Stokes and anti-Stokes beams come out collinear with the pump beam and must be separated with a dispersing prism system. As ν_p is scanned, all Stokes and anti-Stokes lines also scan simultaneously.

H_2 is widely used as a SRS medium because of its very large Raman cross section, widely spaced vibrational levels,

resistance to dielectric breakdown, and low optical dispersion. The low dispersion allows a broad range of Stokes and anti-Stokes lines to be produced. The low order lines have higher outputs. Each successive higher order anti-Stokes line, for example, can be reduced in intensity by 70% of the previous line.[6] Wavelengths as short as 175 nm have been observed, which correspond to the 5AS line of the RGG second harmonic output.[6] The 8AS line of the RGG fundamental has been observed at 194 nm.

In practice, a trade-off is available between conversion efficiency and threshold intensity. Weaker focusing of the pump beam raises the threshold and increases the conversion efficiency. With low power lasers, tight focusing is required to reach threshold. This decreases the conversion efficiency. The H_2 pressure is adjusted to maximize the conversion to the selected Stokes or anti-Stokes line. Optimum conversion occurs between 100 and 300 psi. The Stokes lines generally require the higher pressures.

A SRS cell was constructed in our laboratory to extend the wavelength range accessible to our laser system. Briefly, it consists of three sections of 1.25 in OD x .120 in wall stainless steel tubing in lengths of 15, 30, and 60 cm. Standard Varian 2.25 in high vacuum Conflat flanges are used to join the sections together. A double-sided flange containing a pressure gauge, fill port, and 2000 psi safety relief valve can be inserted between any two sections. 1 in

diameter by .5 in thick Suprasil 1 windows are mounted at each end using two additional flanges. The windows are inserted into the flanges from the inside, allowing the windows to seat against a .125 in wide rim, for maximum pressure handling capability. Viton o-rings are located in this rim to provide a vacuum seal.

The overall length of the cell is variable, depending on which sections are joined together. The highest outputs were obtained by using the maximum cell length of 105 cm and a 50 cm focal length lens for the input pump beam.

Figure 1 shows a typical optical arrangement for SRS. The output of the dye laser is focused into the 105 cm cell with a 50 cm focal length lens. A similar lens recollimates the output beam. A series of four Brewster angle prisms is used for wavelength separation. The first two prisms cause a parallel displacement which is a function of wavelength. An aperture selects the appropriate Stokes or anti-Stokes line. Two additional prisms correct for the change in displacement caused by scanning wavelength. The unwanted beams can be very intense so care is required to avoid stray reflections.

Figure 2 shows the output pulse energies as a function of input pump pulse energy for low order Stokes and anti-Stokes lines. A threshold of $\sim$2 mJ/pulse is observed using the RGG dye output, H_2 pressure of 225 psi, and the optical arrangement just described. After threshold, the 1AS and

2AS line intensities increase linearly with pump pulse energy. Other lines, however, are not linear. For some lines, the output actually decreases with increasing pump energy in certain regions. These curves change as a function of H_2 pressure. By choosing a pump pulse energy where the derivative of the selected line is 0, the SRS process may actually decrease the effect of pulse to pulse energy fluctuations in the pump pulse.

In the wavelength region accessible to the Nd:YAG/dye laser system, 217 to 900 nm, the SRS outputs are lower than the corresponding outputs using various dyes and mixing or doubling. If high pulse energies are not necessary, however, the SRS process is extremely simple to use. One dye like RGG can produce a wide range of wavelengths. Scanning wavelengths is simple, since maintaining the phasematching angle of a nonlinear crystal is not required. For wavelength regions outside the 217 to 900 nm region, SRS is definitely attractive. We were able to easily obtain $\sim$5μJ of output at 192 nm using the 4AS line of doubled RGG. 2.5 mJ at 1061 nm was obtained using the 2S line of the RGG fundamental. Production of shorter wavelengths is possible by changing window materials and using an evacuated beam path after the cell.

The increased wavelength coverage and simplicity of use make the SRS technique an attractive accessory for our laser system. Additional information about SRS technique and theory can be found in References 7-15.

References

1. J. Paisner and S. Hargrove, Energy Technology Review (published by Lawrence Livermore Laboratory), March 1979, p. 1.
2. R. L. Byer, Electro-Optical Systems Design, Feb. 1980, p. 24.
3. N. Bloembergen, Am. J. Phys. 35, 989 (1967).
4. W. Kaiser and M. Maier, Laser Handbook, Vol. II, edit. by F. T. Arecchi and E. O. Schulz-Dubois (North-Holland, Amsterdam, 1972).
5. R. L. Byer and R. L. Herbst, in "Topics in Applied Physics" series, Vol. 16, Nonlinear Infrared Generation, edit. by Y. R. Shen (Springer-Verlag, Berlin, 1977) pp. 81-137.
6. V. Wilke and W. Schmidt, Appl. Phys. 18, 177 (1979).
7. P. Rabinowitz. A. Stein, R. Brickman and A. Kaldov, Opt. Lett. 3, 147 (1978).
8. T. R. Loree, R. C. Sze and D. L. Barker, Appl. Phys. Lett. 31, 37 (1977).
9. V. Wilke and W. Schmidt, Appl. Phys. 16, 151 (1978).
10. T. R. Loree, R. C. Sze, D. L. Barkev and P. B. Scott, IEEE J. Quant. Elect. QE-15, 337 (1979).
11. M. Bierry, R. Frey and F. Pradère, Rev. Sci. Instrum. 48, 733 (1977).
12. R. W. Hellwarth, Phys. Rev. 130, 1850 (1963).
13. Y. R. Shen and N. Bloembergen, Phys. Rev. 137, A1787 (1965).

14. P. Rabinowitz, A. Kaldor, R. Brickman and W. Schmidt, Appl. Opt. 15, 2005 (1976).

15. W. Hartig and W. Schmidt, Appl. Phys. 18, 235 (1979).

Figure Captions

Figure 1. Typical optical arrangement for wavelength conversion by stimulated Raman scattering. The H_2 Raman shifter is filled with between 100 and 300 psi H_2. Right-angle turning prisms are labeled by P1. Two 50 cm focal length lenses labeled L focus the dye laser output into the Raman shifter and recollimate the output beams. Four Suprasil 1 Brewster angle prisms labeled P2 are used to separate out the desired Raman-shifted line.

Figure 2. Output pulse energies as a function of input pump pulse energy for low order Stokes and anti-Stokes lines produced by stimulated Raman scattering in H_2. The 564 nm pump pulse was supplied by the DL18 dye laser using R6G and focused using a 50 cm focal length lens. The H_2 pressure was 225 psi. (A) Stokes lines and pump output. The symbols designate the following output lines: O - 1st Stokes, □ - 2nd Stokes, Δ - 3rd Stokes, ● - pump output. (B) Anti-Stokes lines. The symbols designate the following output lines: O - 1st anti-Stokes, □ - 2nd anti-Stokes, Δ - 3rd anti-Stokes, ■ - 4th anti-Stokes. The pulse energies of the higher order Stokes and anti-Stokes lines were increased by the indicated multiplicative factor before plotting.

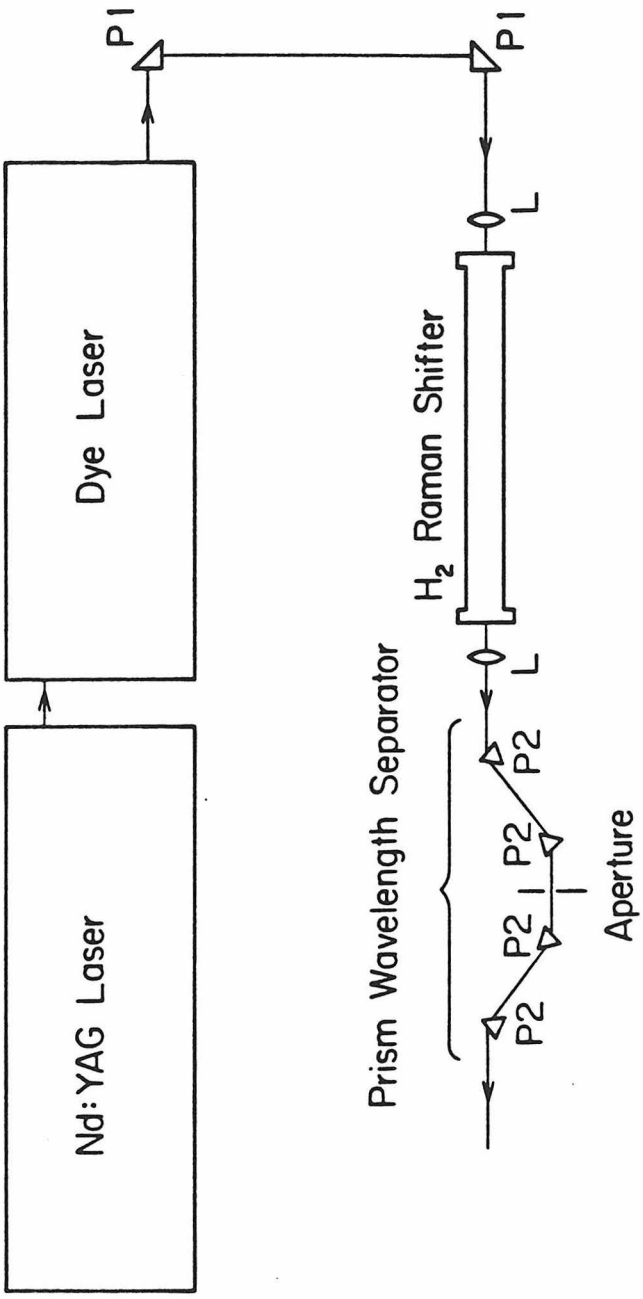
P1
P1
Dye Laser
L
H_2 Raman Shifter
L
Prism Wavelength Separator
P2
P2
P2
P2
Aperture
Nd:YAG Laser

Figure 1

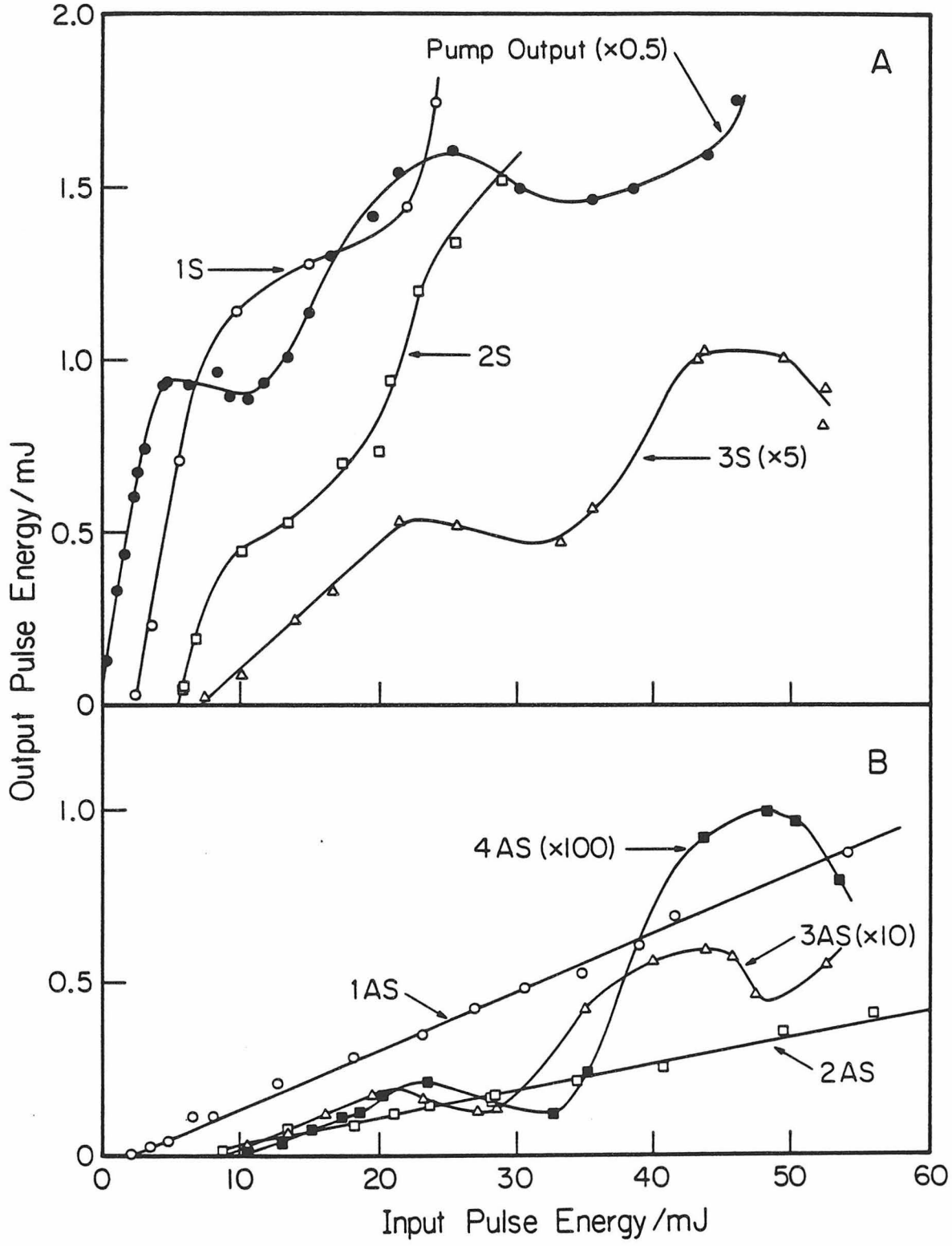
Pump Output (×0.5)
A
1S
2S
3S (×5)
B
4AS (×100)
3AS (×10)
1AS
2AS
Output Pulse Energy / mJ
Input Pulse Energy / mJ
0
0.5
1.0
1.5
2.0
10
20
30
40
50
60

Figure 2

APPENDIX D: Detection of the $^3A_2$ State of CS_2 by Multiphoton Ionization.

Detection of the $^3A_2$ State of CS_2 by Multiphoton Ionization

Ronald Rianda,* David J. Moll and Aron Kuppermann

Arthur Amos Noyes Laboratory of Chemical Physics**
California Institute of Technology, Pasadena, CA 91125, USA

Received

The application of the technique of resonance-enhanced multiphoton ionization (REMPI) spectroscopy to the detection of triplet states via a first photon resonance is examined. It is shown to work well for the $\tilde{a}^3A_2$ state of CS_2. This technique promises to permit the detection of spin-forbidden transitions at high resolution and with great sensitivity.

---

*Work performed in partial fulfillment of the requirements for a PhD in Chemistry at the California Institute of Technology.

**Contribution No. 6082.

The REMPI technique[1-10] has been utilized extensively for the detection of two-photon excitations. However, it has not been employed for the investigation of weak one-photon absorptions, such as singlet-triplet transitions.[10] Such an application could lead to a useful method of studying these kinds of processes, and it is examined in the present paper.

The near-ultraviolet absorption bands of CS_2 extending from 390 to 330 nm have been the subject of extensive experimental and theoretical investigation.[11-18] The vibrational and rotational structure of the bands indicates that the spectrum results from transitions from a linear ground state ($^1\Sigma_g^+$) to a bent excited state of B_2 symmetry.[13] Douglas and Milton[14] and Hougen[15] have studied the pronounced Zeeman effect of the bands and have shown that it can only be understood if the observed B_2 state is a component of a $^3A_2$ state with substantial triplet splitting. Differential cross section measurements performed by Flicker et al.[18] using low-energy, variable-angle electron-impact spectroscopy are also consistent with assignment of the transition as singlet-triplet in nature.

REMPI spectroscopy has proven to be a very sensitive technique for studying two-photon electronic transitions.[1-10] Parker et al.[19] have shown that when the transitions from the two-photon excited state to the continuum are saturated,

which is generally the case at the intensities normally used for such experiments, the weak two-photon process is rate-determining, and the ion current is proportional to the rate of the two-photon resonance excitation. In the present case, the initial one-photon singlet-triplet transition is strongly forbidden ($f < 5 \times 10^{-7}$ in the spectral region studied),[16] and subsequent excitations within the triplet manifold are expected to be many orders of magnitude faster. Therefore, the initial step is the rate-limiting process, and the spectrum of the singlet-triplet transition is generated as the laser wavelength is scanned.

The experimental apparatus used differs somewhat from that reported by other researchers. The laser system consisted of a Molectron DL 200 dye laser pumped by a UV400 nitrogen laser. Output power in the spectral region studied, 375 to 360 nm, varied monotonically from 30 kW to 5 kW using the dye PBD at 20 Hz. The laser beam was focused with a quartz lens (f = 50 mm) into a gas cell containing two parallel plates 0.75 in. square separated by 0.75 in. The charge pulse is detected by a Canberra 2001A charge-sensitive preamplifier with a nominal sensitivity of 10 V/picocoulomb. The preamplifier output and the output from the pyroelectric joulemeter, which monitored the laser-pulse energy, were directed into a dual-channel, gated differential integrator system. A microcomputer system digitized and stored the data and controlled the laser wavelength scan. The sample pressure was 5 torr.

A typical REMPI spectrum of CS_2 is shown in Fig. 1. The spectrum displays the sharp structure characteristic of transitions to the $^3A_2$ state superimposed on a broad, intense doublet. The peaks assigned by Kleman[13] and Douglas and Milton[14] using absorption techniques appear in our spectra with positions agreeing within our wavenumber calibration accuracy of 4 cm^{-1}. Representative results for the Σ and Π bands are summarized in Table I. The band oscillator strengths measured by Barrow and Dixon[16] are also listed to give an indication of the sensitivity of the REMPI technique. We detect vibronic transitions having oscillator strengths as low as 2.7×10^{-8}.

An intense doublet has been observed at 55,002 and 55,197 cm^{-1} by Price and Simpson.[20] Both groups assigned this transition as a π_g orbital to sulfur 4s Rydberg excitation. This transition is forbidden ($^1\Sigma_g^+ \rightarrow {}^1\Pi_g$) for single photon excitation but can acquire intensity through vibronic coupling with either the $\nu_2(\pi_u)$ or $\nu_3(\sigma_u^+)$ vibrational modes. The transition is allowed for two-photon excitations, however. It is likely that the two-photon singlet→singlet transition accounts for the doublet observed in our spectra at about 367.2 and 365.5 nm, corresponding to two-photon transition energies of 54,466 and 54,720 cm^{-1}, respectively. The accuracy of these values is affected by the presence of the superimposed one-photon bands. The differences between the average of our doublets and those obtained by Price and

Simpson[20] and Rabalais et al.[21] are 506 and 370 cm^{-1}, respectively. The latter correlates well with the ν_2 vibrational frequency of 397 cm^{-1} for the ground electronic state.

Several peaks are observed between 368 and 369 nm that, because of their positions and intensities, cannot be assigned to the $\tilde{X}^1\Sigma_g^+ \rightarrow \tilde{a}^3A_2$ excitation. This structure may also result from the two-photon $\tilde{X}^1\Sigma_g^+ \rightarrow \tilde{B}^1{}_g$ transition. The peaks are separated by approximately 36 cm^{-1}, suggesting that they are due to rotational structure arising from a slightly bent configuration in the excited state. Such an explanation has been offered by Price and Simpson[20] for the 40 cm^{-1} spacing between band heads in the 208 nm band.

In summary, we have shown that REMPI spectroscopy is a very sensitive technique for studying spin-forbidden single-photon transitions. The current availability of far more intense pulsed dye lasers promises applicability of this technique to other molecular systems for which the spin-orbit coupling is much weaker than for CS_2. At sufficiently high intensities, however, the nonresonant MPI process will dominate the signal and limit this technique.[22] Below such intensities and under saturation conditions, the different power dependencies of the initially spin-forbidden process vis-a-vis that of any energetically coincident spin-allowed two-photon processes should allow deconvolution of the spectra, yielding both the single-photon spin-forbidden

spectrum as well as the two-photon spin-allowed spectrum. Our measurements indicate that in our experimental arrangement over the pulse energy range 3 to 24 μJ/pulse the 06-Π1 spin-forbidden transition signal varies as laser intensity to the 3/2 power. Such dependence, under saturation conditions, for a first photon resonance multiphoton process has been observed previously[23,24] and attributed to features of the focusing geometry.[23-25] The two-photon spin-allowed transition signal, measured at 366.9 nm where the spin-forbidden transition contribution is assumed to be small (since there is only little sharp structure characteristic of the $\tilde{a}^3A_2$ state at this wavelength), varies approximately as the laser intensity squared. Furthermore, comparison of the resulting intensities of the one-photon spin-forbidden transitions with those of a pulsed ultraviolet laser photoacoustic spectroscopy technique developed recently in our laboratory may furnish information about the dynamics of energy relaxation from these electronically excited states.

Acknowledgments

This research was supported in part by the U. S. Department of Energy Grant No. EX-76-G-03-1305. However, any opinions, findings, conclusions, or recommendations expressed herein are those of the authors and do not necessarily reflect the view of DOE. Partial support was also provided by

the U. S. Department of Energy Contract No. DE-AS03-76SF00767, Project Agreement No. DE-AT03-76ER72004. Report Code: CALT-767P4-181.

TABLE I. Transition wavenumbers (in cm^{-1}) and oscillator strengths for the $\tilde{X}\,^1\Sigma_g^+ - \tilde{a}\,^3A_2$ Σ and Π bands of CS_2.

	Present Work	Kleman[a]	Douglas[b]	$10^7 f_{v'v''}$ Barrow[c]
Σ Bands				
05-02	26,898	26,894.9	26,901.25	0.99
06-02	27,188	27,183.7	27,190.06	2.88
07-02	27,469	27,467.1	27,471.96	4.54
03-00		27,101.8		0.002
04-00		27,402.5		0.007
05-00	27,689	27,698.0	27,703.29	0.029
13-02	26,986	26,981.8	26,990.39	0.27
14-02	27,281	27,278.6	27,285.22	1.01
15-02	27,567	27,564.9		1.98
Π Bands				
06-03	26,790	26788.0		
07-03	27,074	27,068.9		
08-03	27,346	27,342.9		
04-01	27,014	27,013.8		
05-01	27,313	27,309.9	27,314.46	
06-01	27,601	27,599.6		
14-03	26,884	26,882.1	26,886.66	
15.03	27,168	27,166.5		
16-03	27,432	27,430.1		
17-03	27,676	27,675.0		
13-01		27,397.3		
14-01	27,694	27,693.4	27,697.59	

[a] Reference [13].

[b] Reference [14].

[c] Reference [16].

References

1. M. Lambropoulos, S. E. Moody, W. C. Lineberger, and S. J. Smith, Bull. Am. Phys. Soc. 18 (1973) 1514.
2. M. Lambropoulos, S. E. Moody, S. J. Smith, and W. C. Lineberger, Phys. Rev. Lett. 35 (1075) 159.
3. G. Petty, C. Tai, and F. W. Dalby, Phys. Rev. Lett. 34 (1975) 1207.
4. P. M. Johnson, M. R. Berman, and D. Zakheim, J. Chem. Phys. 62 (1975) 2500.
5. P. M. Johnson, J. Chem. Phys. 62 (1975) 4562.
6. P. M. Johnson, J. Chem. Phys. 64 (1976) 4143.
7. P. M. Johnson, J. Chem. Phys. 64 (1976) 4638.
8. D. H. Parker, S. J. Sheng, and M. A. El-Sayed, J. Chem. Phys. 65 (1976) 5534.
9. D. H. Parker and P. Avouris, Chem. Phys. Lett. 53 (1978) 515.
10. R. E. Turner, V. Vaida, C. A. Molini, J. O. Berg, and D. H. Parker, Chem. Phys. 28 (1978) 47. In this work, a triplet state of pyrazine was detected during the course of a REMPI search for the analog of the E_g state observed in benzene by Johnson[7] via a two-photon resonance.
11. L. N. Liebermann, Phys. Rev. 60 (1941) 496.
12. A. E. Douglas, Can. J. Phys. 36 (1958) 147.
13. B. Kleman, Can. J. Phys. 41 (1063) 2034.

14. A. E. Douglas and E. R. V. Milton, J. Chem. Phys. 41 (1964) 357.

15. J. T. Hougen, J. Chem. Phys. 41 (1964) 363.

16. T. Barrow and R. N. Dixon, Mol. Phys. 25 (1973) 137.

17. M.-J. Hubin-Franskin and J. E. Collin, J. Electron Spectrosc. 7 (1975) 139.

18. W. M. Flicker, O. A. Mosher, and A. Kuppermann, J. Chem. Phys. 69 (1978) 3910.

19. D. H. Parker, J. O. Berg, and M. A. El-Sayed, in: Advances in Laser Chemnstry, ed., A. H. Zewai (Springer-Verlag, New York, 1978), pp. 320-335.

20. W. C. Price and D. M. Simpson, Proc. R. Soc. London, Ser. A: 165 (1938) 272.

21. J. W. Rabalais, J. M. McDonald, V. Scheer, and S. P. McGlynn, Chem. Rev. 71 (1971) 73.

22. L. Zandee and R. B. Bernstein, J. Chem. Phys. 71 (1979) 1359.

23. G. Hancock, J. D. Campbell and K. H. Welge, Opt. Commun. 16 (1976) 177.

24. T. P. Cotter and W. Fuss, Opt. Commun. 18 (1976) 31.

25. S. Speiser and J. Jortner, Chem. Phys. Lett 44 (1976) 399.

Figure Caption

Figure 1. Multiphoton ionization spectrum of the single-photon $\tilde{X}^1\Sigma_g^+ \rightarrow \tilde{a}^3A_2$ transition of CS_2 superimposed on the two-photon $\tilde{X}^1\Sigma_g^+ \rightarrow B^1\Pi_g$ transition. The ordinate is corrected for the variation of laser pulse energy with wavelength. The sample pressure was 5 Torr. The band assignments at the top of the figure are for the $\tilde{X}^1\Sigma_g^+ \rightarrow \tilde{a}^3A_2$ transition from Kleman[13] where Σ, Π, Δ,..., correspond to $k' = \ell'' = 0,1,2,3,...$, and the symbol 12-$\Sigma$3 implies $v_1' = 1$, $v_2' = 2$, $v_2'' = 3$, and $v_3' = v_3'' = v_1'' = 0$. k is the symmetric top quantum number and ℓ is the quantum number describing the vibrational angular momentum. Vibrational modes 1, 2, and 3 correspond to the symmetric stretch, bend, and antisymmetric stretch, respectively, with double prime and single prime corresponding to ground and excited electronic states, respectively.

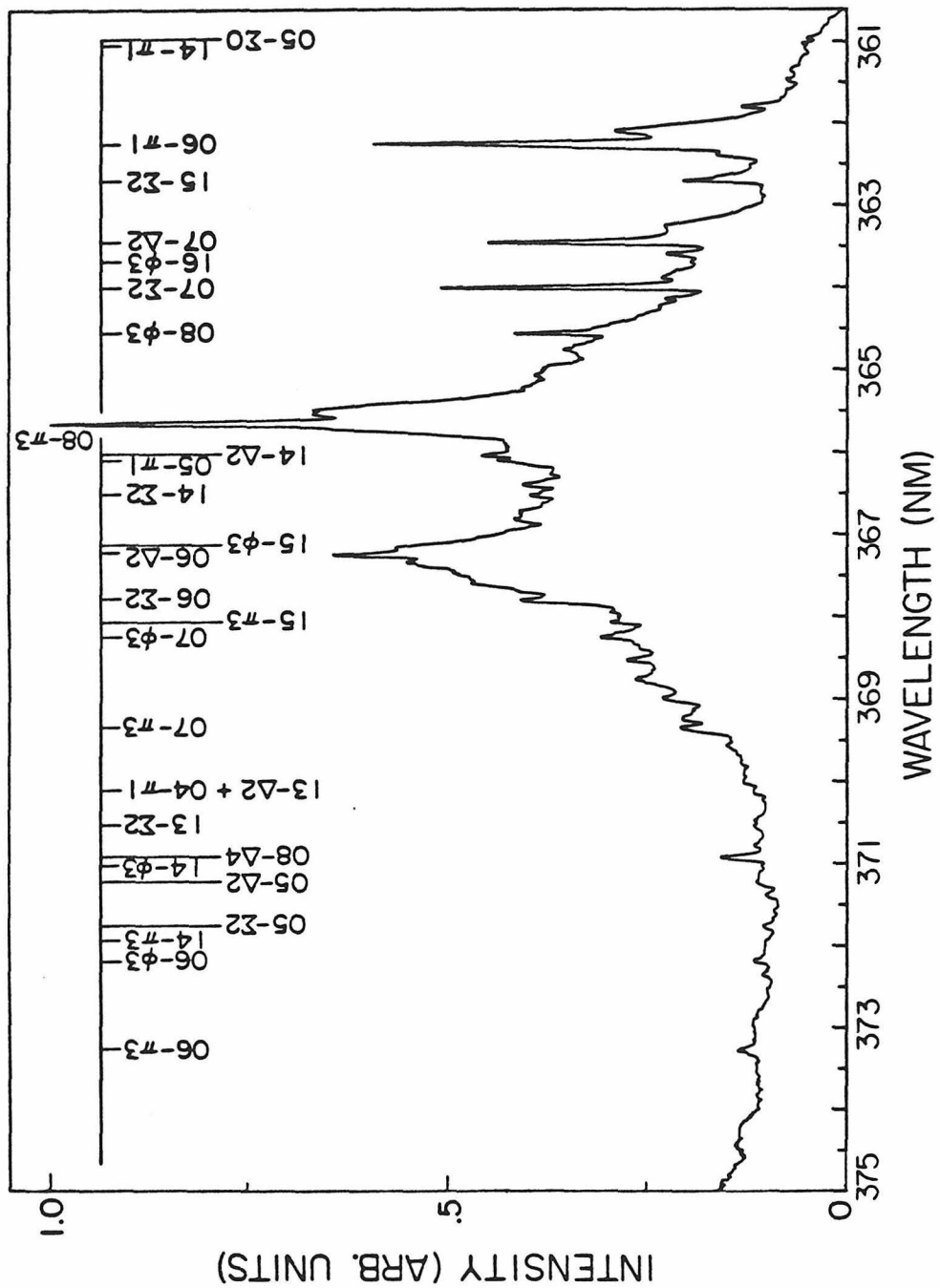
INTENSITY (ARB. UNITS)
1.0
.5
0
WAVELENGTH (NM)
375
373
371
369
367
365
363
361
06-π3
06-φ3
14-π3
05-Σ2
05-Δ2
14-φ3
08-Δ4
13-Σ2
13-Δ2 + 04-π1
07-π3
07-φ3
15-π3
06-Σ2
06-Δ2
15-φ3
14-Σ2
14-Δ2
05-π1
08-π3
08-φ3
07-Σ2
16-φ3
07-Δ2
15-Σ2
06-π1
05-Σ0
14-π1

Figure 1

Proposition I: A Direct Measurement of the Internal Conversion Rate in the S_3 State of Naphthalene Using Picosecond Two-Color Time-Resolved Multiphoton Ionization Spectroscopy.

Abstract: It is proposed that the picosecond two-color time-resolved multiphoton ionization technique be used to investigate internal conversion processes in naphthalene. A direct measurement of the S_3 internal conversion rate in naphthalene-h_8 and -d_8 by this method will provide important information about the dynamics of radiationless processes in this molecule.

Radiationless processes originating in singlet states above the first excited singlet in large molecules are generally very fast.[1] Internal conversion rates for transfer of energy from singlet states S_n for $n > 1$ are typically 10^{10}-10^{13} sec^{-1}. The experimental investigation of the dynamics of these processes is difficult because their rates are significantly faster than the rates of fluorescence ($<10^9$ sec^{-1}). This discrepancy in rates forms the basis for "Kasha's Rule" which states that polyatomic molecules emit only from the lowest electronically excited level of a given multiplicity.[2] Violations of this rule have been observed only in a few selected molecules such as thiophosgene,[3] pyrene,[4] naphthalene[5] and isoquinoline[6] in which emission was observed from S_2.

In this proposition, it is proposed to use picosecond time-resolved two-color multiphoton ionization (MPI) spectroscopy for studying internal conversion processes on the 10^{-12} second timescale. This technique has recently been used to measure isomerization rates in stilbene.[7] The results of Paper III of this thesis demonstrated that the nanosecond version of this technique could measure intersystem crossing rates on the 10^{-9} second timescale in aniline. In that study, a PUMP pulse populated the vibrationless level of S_1. A second pulse, the TRANSFER pulse, ionized molecules in S_1. When the TRANSFER pulse occurred at a later time, $\Delta t > 20$ nsec, no ionization occurred. For values of $\Delta t > 20$ nsec, the initially excited

singlet state has crossed over into a triplet state with 7200 cm^{-1} of vibrational energy. The explanation for the lack of ionization was that the Franck Condon factors for direct ionization from the vibrationally excited triplet raised the vertical ionization potential for that state. This prevented direct ionization. In addition, a fast dissociation process apparently competed with vibrational autoionization, which prevented the occurrence of that ionization mechanism. Similar effects were also observed in benzene.

In both benzene and aniline, the ionization signal decayed exponentially as a function of Δt. The decay time constants for both molecules agreed with previously observed fluorescence decay time constants for those molecules.

The change in Franck Condon factors for ionization, which occurs during intersystem crossing should also occur for internal conversion processes. Therefore, the ionization signal is expected to change during internal conversion just as it does for intersystem crossing. This change should be larger when the TRANSFER pulse excites the molecule to a level just above the adiabatic ionization potential. Under those circumstances, the change in Franck Condon factors may raise the vertical ionization potential above the level excited by the TRANSFER pulse, and therefore decrease the probability of direct ionization.

The time-resolved MPI technique has several advantages over commonly used emission techniques. (1) It should be capable of resolving processes with rates up to 10^{13} sec^{-1} when sub-picosecond laser techniques are used. Fast photomultipliers are limited by electron space charge effects to timescales $>10^{-11}$ sec. Streak cameras can resolve faster events but their sensitivity is lower. (2) It is extremely sensitive. Single electrons are detected easily and electric fields can be used to extract 100% of the electrons from the ionization region. Low solid angle collection efficiencies inherent in fluorescence detection techniques are not present in MPI techniques. (3) The time-resolved MPI technique should be applicable to a large number of molecules. The photoionization process is not limited by symmetry or selection rules. All partial ionization cross sections to a given ionic state are of the same order of magnitude.[10]

Naphthalene is an ideal molecule to study using picosecond two-color time-resolved MPI spectroscopy. It has a low IP (8.15 eV),[8] states S_1, S_2 and S_3 are accessible to current picosecond lasers,[8] and studies of radiationless transitions in that molecule have been reviewed recently.[11]

The dominant nonradiative channel in naphthalene at low excess energy above the S_1 origin (32,020 cm^{-1}) is $S_1 \rightarrow T_1$ intersystem crossing.[11] Stockburger and co-workers have presented evidence for additional intersystem crossing

processes when the excited vibronic level of S_1 is in resonance with T_2 or T_3.[12] Lim and co-workers observed a change in slope of k_{NR} vs. excess energy at the threshold of the S_2 state (35,910 cm^{-1}).[13] They explained this effect by pointing out that direct $S_0 \rightarrow S_1$ optical absorption produces a different vibrational distribution than $S_2 \rightarrow S_1$ internal conversion. Wannier and co-workers[6] observed weak resonance fluorescence from S_2. This emission had an anomalously long lifetime of about 50 nsec. At excess energies of 10,000 cm^{-1} or higher, a rapid decrease of k_{NR} with excess energy was observed by Lim and co-workers.[13] This was explained as being due to the onset of a fast $S_1 \rightarrow S_0$ internal conversion.[14] For excitation in the region of S_3, the lifetime of fluorescence observed from S_1 decreased rapidly with excess energy.[9]

The experimental results indicate that naphthalene has a fast nonradiative process which begins only when it is excited into the region of S_3. The time-resolved MPI technique may be able to measure the actual rate of this process which is probably an internal conversion process.

The proposed MPI experiment is conceptually simple. A picosecond laser pulse at 456 nm (photon energy slightly larger than one-third of the ionization potential) is frequency doubled in KPB and focused into a parallel plate MPI cell. The unconverted 456 nm fundamental would be split off before the cell, pass through an adjustable delay line, and be recombined with the doubled beam before entering the MPI

cell. The cell would be heated to $\sim 35^{o}C$ to increase the naphthalene sample pressure to ~ 0.2 torr.[5] A charge-sensitive preamplifier would integrate the charge produced by ionization.

The frequency doubled pulse would excite S_3. The fundamental pulse would ionize molecules from S_3. If the fundamental pulse is delayed with respect to the doubled pulse, allowing internal conversion to occur, the ionization probability should decrease due to the Franck Condon factor argument given earlier. The lifetime of the S_3 state would be determined by measuring the ionization current as a function of the delay between the frequency doubled pulse and the fundamental pulse.

The 400 to 500 nm wavelength range is not easily accessible by typical picosecond pulse generation techniques. Picosecond pulses at 420 nm have been produced by synchronously pumping a dimethyl POPOP dye laser with a frequency doubled mode-locked ruby laser.[15] The shorter output wavelength of this laser system may decrease the expected change in ionization after internal conversion because molecules would be excited 5700 cm^{-1} above the IP.

The travelling-wave parametric process demonstrated by Seilmeier and Kaiser[16] provides a better alternative. Their technique converts the frequency doubled output of a mode-locked Nd: glass laser to picosecond pulses which are tunable from 2700 to 17,000 cm^{-1}. The wavelength is selected

by angle tuning the two $LiNbO_3$ crystals. The 456 nm fundamental pulse would be obtained by adjusting the crystal angles to produce 10,965 cm^{-1} output and frequency doubling in KDP. These pulses would be amplified in a commercially available Coumarin 450 dye amplifier system[17] pumped by the third harmonic of a Nd:YAG system.

The final pulse energy can be conservatively estimated in the following way. Start with a 10 mJ pulse from a typical mode-locked Nd:glass laser with a 6 picosecond pulsewidth.[18] Conversion efficiencies for each conversion porcess are estimated as: frequency doubling - 10%, parametric process - 1%,[16] frequency doubling - 1%,[15] amplify - 10^6%.[16,18] Using these estimates, the final pulse energy at 456 nm is $\sim$1 mJ. Frequency doubling this pulse with 1% efficiency gives a 10 μJ UV pulse for exciting the S_3 state in naphthalene. The 1 mJ 456 nm pulse would be used to ionize molecules in S_3. The two-color time-resolved MPI experiment on aniline described in Paper III of this thesis used only 0.4 and 13 μJ pulses to excite S_1 and ionize, respectively.

Naphthalene is known to ionize with very high efficiency using two-photon MPI processes which are resonant with S_1.[20] The $S_0 \rightarrow S_3$ transition has a larger absorption coefficient than $S_0 \rightarrow S_1$,[12] which implies that the S_3 resonant MPI process should be even more efficient. Therefore, it seems resonable to assume that the proposed experimental method will provide more than adequate sensitivity.

After an initial measurement of the S_3 internal conversion rate in naphthalene, it would also be interesting to investigate the same process in naphthalene-d_8. Inverse isotope effects for the nonradiative rates ($k_{NR}^H/k_{NR}^D < 1$) have been observed in fluorescence studies for excess energies $\sim$500 cm^{-1} above the S_1 origin.[11] The size of this effect could be measured directly in S_3 internal conversion processes using the MPI technique.

References

1. S. K. Lower and M. A. El-Sayed, Chem. Rev. 65, 199 (1965).
2. M. Kasha, Disc. Faraday Soc. 9, 14 (1950).
3. S. Z. Levine, A. R. Knight and R. P. Steer, Chem. Phys. Lett. 29, 73 (1974); D. Phillips and R. P. Steer, J. Chem. Phys. 67, 4780 (1977).
4. P. A. Geldof, R. P. H. Rettschnick and G. J. Hoytink, Chem. Phys. Lett. 4, 59 (1969); H. Baba, A. Nakajima, M. Aoi and K. Chihara, J. Chem. Phys. 55, 2433 (1971); T. Deinum, C. J. Werkhoven, J. Langelaar, R. P. H. Rettschnick and J. D. W. Van Voorst, Chem. Phys. Lett. 12, 189 (1971).
5. P. Wannier, P. M. Rentzepis and J. Jortner, Chem. Phys. Lett. 10, 193 (1971).
6. P. M. Felker and A. H. Zewail, "Jet Spectroscopy of Isoquinoline", accepted for publication in Chem. Phys. Lett.
7. (a) A. H. Zewail, results of this study will be presented at The Royal Soc. of Chem., Faraday Division, Disc. No. 75 (Intramolecular Kinetics), University of Warwick, England, 18-20 April, 1983. (b) B. I. Greene and R. C. Farrow, results summarized in Laser Focus 19, 24 (1983).
8. D. W. Turner, C. Baker, A. D. Baker and C. R. Brundle, Molecular Photoelectron Spectroscopy (Wiley, London, 1970), p. 321.
9. U. Laor and P. K. Ludwig, J. Chem. Phys. 54, 1054 (1971).
10. J. H. D. Eland, Photoelectron Spectroscopy (Wiley, New York, 1974), p. 58.
11. P. Avouris, W. M. Gelbart and M. A. El-Sayed, Chem. Rev. 77, 793 (1977).

11. M. Stockburger, H. Gattermann and W. Klusmann, J. Chem. Phys. 63, 4519 (1975); J. Chem. Phys. 63, 4530 (1975).

12. J. C. Hsieh, C.-S. Huang and E. C. Lim, J. Chem. Phys. 60, 4345 (1974).

13. J. C. Hsieh and E. C. Lim, J. Chem. Phys. 61, 736 (1974).

14. M. R. Topp and P. M. Rentzepis, Phys. Rev. 3A, 358 (1971).

15. A. Seilmeier and W. Kaiser, Appl. Phys. 23, 113 (1980).

16. Available from Quanta-Ray, Inc. See Laser Focus, Dec. 1982, p. 62.

17. Quantel International markets a mode-locked phosphate glass laser with 6-10 ps. pulsewidth and 5-50 mJ output/ pulse.

18. E. P. Ippen, J. M. Weisenfeld and D. J. Eilenberger, "Sub-Picosecond Optics, Techniques and Applications", presented at Int. Conf. Lasers '79, Orlando, Florida, Dec. 17-21, 1979. Conf. Proc., p. 37.

19. D. E. Cooper, R. P. Frueholz, C. M. Klimcak and J. E. Wessel, J. Phys. Chem. 86, 4892 (1982).

Proposition II: Collisional Relaxation of Rovibrational Levels of Formaldehyde Prepared by Stimulated Emission Pumping.

Abstract: It is proposed to investigate the collision-induced R-R rotational energy redustribution processes in excited vibrational levels of formaldehyde. Specific rovibrational levels will be prepared by stimulated emission pumping. Laser-induced fluorescence will be used to monitor the decay of the initially populated level and the appearance of population in other rotational states.

The inelastic cross section for rotational transitions during energy transfer collisions are of fundamental importance for gas kinetics.[1] Laser isotope separation, gas lasers and interstellar modeling are examples of areas which need accurate cross sections for these processes. Microwave or mirro-wave-infrared double resonance and molecular beam techniques have been used to study rotationally inelastic scattering in noble gas-NH_3 collisions;[2] C_sF collisions with He, CH_4, N_2, N_2O, CF_3Br, etc.;[3] He collisions with N_2, CO and CH_4;[4] and NO collisions with Ar.[5] Many other experimental studies could be listed. However, there remains a large class of molecules which are inaccessible to most experimental techniques. Sophisticated theoretical methods have been applied to molecules in this class.[6-9] Formaldehyde, in particular, has been the subject of several theoretical studies because of its presence in interstellar space and the lack of experimental data on its rotational inelastic cross sections.[7]

In this proposition it is proposed to study rotational relaxation processes in formaldehyde. A stimulated emission pumping (SEP) process[10-14] would prepare formaldehyde molecules in a specific rovibrational state in the ground electronic state. A PROBE pulse would detect the rotational population a short time later (20-500 nsec) through a laser-induced fluorescence (LIF) technique.[11,12] By varying the PROBE wavelength and its delay after the SEP process, the time

dependences of the populations in specific rotational levels could be monitored. The rate of disappearance of the initial level prepared by SEP, the the appearance of population in other levels, would be compared to the results of theoretical studies.[6,7]

The SEP-LIF technique has several advantages which should be pointed out. (1) It is highly selective for populating specific rovibrational levels. (2) A large number of ground electronic state levels are accessible with the SEP process. (3) It allows the use of bulk gas samples. The number of collisions before detection can be controlled by changing the delay between the SEP process and the PROBE pulse. This allows "single-collision" processes to be monitored in bulk gas samples. (4) The temperature can be varied easily.

The $\tilde{A}^1A_2$ and $\tilde{X}^1A_1$ states of formaldehyde have been studied in detail by absorption[15] and emission[13,16,17] spectroscopy. The spectrum of formaldehyde is that of a slightly asymmetric (near-prolate) top, with rotational energy levels labeled by a total angular momentum, J, and its projector, K_a, on the CO symmetry axis such that $J \geq K_a \geq 0$. For $K_a > 0$, each J,K_a level is split by the small asymmetry into even- and odd-parity states. This splitting is labeled by K_c which is a valid quantum number only for the oblate symmetric top limit. The conventional notation for these rotational levels is J_{K_a,K_c}.

The fluorescence bands originating in the $\tilde{A}^1A_1$ state exhibit perpendicularly polarized transitions with selection rules $\Delta K_a = \pm 1$ and $\Delta J = 0, \pm 1$.[17] Transitions are labeled by $N_i^j \; {}^{\Delta K_a}{}_{\Delta J_{K_a'', K_c''}}(J'')$ where N_i^j indicates an electronic transition involving vibrational mode N with j and i quanta in the upper and lower states, respectively, and the double primes designate lower state labels.

The proposed experiment can be broken down into two processes: the preparation of the initial state by SEP, and the detection of molecules in specific rotational levels. The SEP process used to prepare the initial state would be similar to that of Reisner and co-workers.[13] The PUMP pulse, which populates a level of the $\tilde{A}^1A_2$ state, would be supplied by a Nd:YAG laser pumped dye laser. The dye laser would be equipped with an intracavity etalon (output bandwidth $\leqq 0.03$ cm^{-1} FWHM) and frequency doubled in KDP. The DUMP pulse, which stimulates emission down to a rovibrational level of the ground state, would be supplied by a second similar dye laser system pumped by the same Nd:YAG laser. The optics would be arranged so that the DUMP pulse reaches the sample cell $\sim$15 nsec after the DUMP pulse. The PUMP beam is split into two equal intensity beams. One beam would be combined with the DUMP beam and directed into a cell containing $\sim$100 mtorr of formaldehyde and an optical quences gas such as He. The other beam would be directed into a second half of the cell. The difference in

fluorescence signals from both beams would be used to monitor the SEP process.

The population of the initially prepared rovibrational state or other rotational levels of the same vibrational state would be monitored by a LIF technique 20-500 nsec after the SEP process. A second Nd:YAG laser pumped dye laser would excite molecules in the state of interest up to a level in the $\tilde{A}^1A_2$ level. Fluorescence from this level would be proportional to the population of the state of interest. The fluorescence would be dispersed by a high resolution monochrometer to eliminate scattered light and fluorescence from the level of the $\tilde{A}$ state used in the SEP process.

The fluorescence signal from the LIF process is expected to be easily detectable, since Reisner and co-workers[13] estimated that their SEP process in formaldehyde transferred 0.02% of the total thermal population into a specific rovibrational level. Similar LIF techniques have been used in other SEP experiments.[11,12]

The possibilities for states to prepare and probe are endless. One example of an excitation and detection scheme will no be given which could serve as an ideal first experiment. The transitions and their energies are derived from Refs. 13 and 17. The PUMP pulse at ∿354 nm excites the $4_0^1\ ^PQ_{1,3}(4)$ line as in Ref. 13. The DUMP pulses stimulates emission down to the $4_4\ 4_{1,3}$ rovibrational state via the $4_4^1\ ^PQ_{1,3}(4)$ transition at 422 nm. The PROBE pulse would

detect the population of the $4_4\ 4_{1,3}$ level by exciting it by 24,994.6 cm^{-1} to a level which fluoresces at 29,621.5 cm^{-1}. The $3_{1,3}$ and $5_{1,5}$ levels of 4_4 could also be detected by exciting with 25,005.3 cm^{-1} or 24,983.9 cm^{-1} pulses, respectively. The same fluorescence would be observed. By varying the time delay between the SEP pulses and the PROBE pulse, the decrease in the $4_4\ 4_{1,3}$ level population and the increase in the $4_4\ 3_{1,3}$ and $4_4\ 5_{1,5}$ populations could be observed.

Many other wavelengths for PUMP, DUMP and PROBE pulses can be obtained from the spectroscopic transitions listed in Refs. 13 and 17, allowing a large variety of rotational levels to be prepared or detected. Additional transitions can be generated from spectroscopic constants of the various vibrational levels using a program by Birss.[18] This program calculates asymmetric rotor energy levels from spectroscopic constants.

Several types of rotational relaxation could be studied. The experiment-to-measure self-relaxation of formaldehyde is complicated because of the large concentration of $\tilde{A}^1A_2$ states remaining after the SEP process. A better experiment would be to measure relaxation caused by collisions with helium, other rare gases or other molecules. In these experiments, a five-motor sample of formaldehyde and 95-motor sample of the collision partner would be used. Helium is especially attractive because extensive theoretical studies of

He/formaldehyde relaxation have been performed.[6,7] Propensity rules for rotational inelastic collisions have been proposed.[6] These rules are obeyed in the theoretical He/formaldehyde results of Green et al.,[7] but they have not been verified experimentally. A comparison of experimental results for this system with theory should provide a check on the reliability of the approximations used in the calculations.

References

1. J. P.Toennies, Ann. Rev. Phys. Chem. 27, 225 (1976).
2. T. Oka, J. Chem. Phys. 49, 3135 (1968).
3. U. Borkenhagen, H. Malthan and J. Peter Toennies, J. Chem. Phys. 71, 1722 (1979).
4. M. Faubel, K. H. Koh. and J. P. Toennies, J. Chem. Phys. 73, 2506 (1980).
5. P. Anderson, H. Joswig, H. Pauly and R. Schinke, J. Chem. Phys. 77, 2204 (1982).
6. M. H. Alexander, J. Chem. Phys. 76, 3637,5974 (1982).
7. S. Green, B. J. Garrison, W. A. Lester, Jr. and W. M. Miller, Astrophys. J. Supple. Series 37, 321 (1978).
8. R. T. Pack, J. Chem. Phys. 64, 1659 (1975).
9. A. T. Amos and R. J. Crispin, in Theoretical Chemistry, Advances and Perspectives, edit. by Eyring and D. Henderson (Academic, New York, 1976), Vol. 2, pp. 1-66.
10. C. Kittrell, E. Abramson, J. L. Kinsey, S. A. McDonald, D. E. Reisner, R. W. Field and D. H. Katayama, J. Chem. Phys. 75, 2056 (1981).
11. W. D. Lawrence and A. E. W. Knight, J. Chem. Phys. 76, 5637 (1982).
12. W. D. Lawrence and A. E. W. Knight, J. Chem. Phys. 77, 570 (1982).
13. D. E. Reisner, P. H. Vaccaro, C. Kittrell, R. W. Field, J. L. Kinsey and H.-L. Dai, J. Chem. Phys. 77, 573 (1982).

14. D. J. Moll, G. R. Parker, Jr., and A. Kuppermann, "Photoacoustic Detection of Stimulated Emission Pumping in p-Difluorobenzene". To be published (see Paper II of this thesis).

15. V. A. Job, V. Sethuraman and K. K. Innes, J. Molecular Spectrosc. 30, 365 (1969); V. Sethuraman, V. A. Job and K. K. Innes 33, 189 (1970).

16. K. Shibuya, R. A. Harger and E. K. C. Lee, J. Chem. Phys. 69, 751 (1978).

17. J. L. Hardwick and S. M. Till, J. Chem. Phys. 70, 2340 (1979).

18. Referred to in F. W. Birss, R. Y. Dong and D. A. Ramsay, Chem. Phys. Lett. 18, 11 (1973).

Proposition III: An Experimental Investigation of the Mechanism of Plasma Formation during Metal Processing with High Power Ultra-Violet Lasers.

Abstract: It is proposed that the mechanism of plasma formation produced by the interaction of a high power UV laser pulse with the surface of aluminum in vacuum be investigated. Impulse coupling, thermal coupling, total reflectivity, electron production and plasma threshold will be monitored as a function of wavelength and pulse energy. The appearance of two-photon resonant ionization processes should lower the plasma ignition threshold.

The use of lasers by the manufacturing industry has increased tremendously in the past few years. Over 1000 lasers are used daily on U.S. manufacturing lines.[1] A majority of these lasers are used for industrial welding and machining. Solid state and CO_2 lasers are used in most of these applications. Typical output powers of these lasers is around 500 watts CW, but some range as high as 25 kilowatts.[2]

The industrial metalworking applications of high powered lasers has produced a strong interest in understanding the dynamics of the interaction of intense light pulses with metal surfaces. A general picture of the interaction mechanism for CO_2 laser radiation at 10.6 microns is now emerging. At low laser intensities, the thermal energy deposited in the metal surface is determined by the intrinsic absorptivity of the metal.[3] For most metals, the infrared absorptivity is quite low (<5%). At higher intensities ($\sim 10^6$ W/cm^2), the absorptivity changes abruptly due to the presence of plasma effects. In air typical plasma ignition intensities are $\sim 10^9$ W/cm^2. At a rough metal surface, however, the local heating of surface defects causes thermionic emission of electrons. These electrons are accelerated by inverse bremsstahlung absorption of laser radiation.[6] The electrons are cascade multiplied during collisions with metal vapor atoms or air molecules. If the energy gained by the electrons is larger than that lost through collisions, a plasma can be ignited.[5,6]

The metal surface lowers the threshold intensity for plasma ignition in air by a factor of 10^3. In CW operation, the plasma blocks the absorption of laser energy by the metal.[7] For pulsed operation, the plasma is confined to the beam interaction region during the laser pulse. It absorbs the laser energy and reradiates it in the UV or vacuum UV where the metal has a strong absorption. This produces an efficient transfer of energy to the metal surface, even more efficiently than direct infrared absorption.[8,9] As the laser intensity is increased, the energy per unit area deposited into the surface remains essentially constant.[10,11] The plasma pressure is increased by absorption of more energy, expands faster and deposits energy into a larger surface area. This spreading process prevents the actual melting of the metal surface in many cases because the laser energy cannot be localized within the laser spot size.[6]

When the volume surrounding the metal sample is evacuated, the interaction mechanism changes slightly. The air which previously supported the plasma is no longer present. Instead, small metal surface defects are vaporized and ionized.[6,7] This mechanism was verified by Walter et al.[12] who observed emission from ionized and excited metal atoms simultaneously with the increased absorption by the plasma. Several theoretical models of ionization after metal vaporization have been developed.[13,14] The vacuum case is peculiar in that the plasma does not propagate outward significantly

from the focal spot with increasing intensity.[6] This result is not fully understood. Metal surface melting is achieved easily in the vacuum metal vapor plasma case because the energy remains localized within the focal spot. There appears to be no upper limit to the usable laser intensity for applications involving sample surfaces in vacuum.

Only recently have high power UV lasers become available for experiments to determine the mechanism of ultraviolet laser pulse interactions with metal surfaces.[15-18] Duzy and co-workers[16] irradiated an aluminum surface under vacuum with a XeF excimer laser at 353 nm. They monitored the mechanical impulse imparted to the sample by the action of the laser pulse, and observed a low fluence threshold ($\sim$2 J/cm^2) for the appearance of this impulse. Bulk vaporization and ejection of aluminum from the surface is not expected since that requires a fluence of $\geq$40 J/cm^2. The inverse bremsstrahlung absorption is proportional to λ^2. Fluences greater than 100 J/cm^2 would be necessary to produce a plasma by that mechanism. The impulse coupling coefficient was two to four times larger than observed in similar IR experiments. Similar overall effects were observed for KrF laser excitation at 249 nm.[15]

Rosen and co-workers[17] performed similar experiments on aluminum surfaces. They modeled the interaction by including two significant mechanisms for laser-vapor interaction: (1) the high temperatures at the surface could produce vaporized aluminum atoms in excited states which could be

ionized by absorption of one laser photon, and (2) inverse bremsstrahlung increases with the density of the vapor and with the percentage of ionization in the vapor. The experimental results on impulse coupling and plasma ignition threshold were in good agreement with their theoretical model predictions. Increased deposition of energy into the surface was observed above the plasma ignition fluence threshold of 30 J/cm^2.

The model of Rosen et al.[17] did not consider the possibility of two-photon ionization processes in atomic aluminum vapor. The high intensities employed in these experiments ($\geq$60 megawatta/cm^2) and the relatively low ionization potential of aluminum (5.984 eV)[19] make the probability of a two-photon nonresonant ionization process at XeF laser wavelengths very high.

In this proposition, it is proposed to investigate experimentally the role of two-photon ionization processes in the interaction of intense UV laser pulses with metal surfaces. The experiments would involve focusing the output of a tunable high power pulsed UV laser onto a 2024-T3 aluminum surface in vacuum. The wavelength would be scanned through a strong resonance between a low-lying and intermediate level of aluminum atoms while monitoring the following experimental parameters: (1) impulse coupling, (2) thermal coupling, (3) total reflectivity, (4) electron production, and (5) plasma threshold. The laser system and experimental techniques will be described in the following section.

Laser System. The experiments of Duzy et al.[16] used a XeF excimer laser with an output of up to 7 J at 353 nm with ∿1 μsec pulsewidths. Tunable UV lasers are not capable of equaling this performance. However, by using slightly tighter focusing, the same fluence and intensities can be produced. The highest power tunable UV laser in the 353 nm region currently available is a frequency doubled alexandrite laser.[20] The fundamental tuning range of this laser is 700-815 nm. Pulse energies of 3.5 J have been produced. The Q-switched pulsewidth is variable from 30 to 600 nsec. Frequency doubling in KDP crystals of pulses with these characteristics can easily have conversion efficiencies of up to 40%. Therefore, this laser should be capable of producing UV pulses tunable from 350 to 407 nm with a maximum pulse energy of 1.5 J. This is within a factor of 2 of the typical pulse energies used in the fixed wavelength experiments.[16,17] Therefore, the detection techniques employed in other surface interaction experiments should be usable in this experiment.

Aluminum atoms have a strong absorption from the ground state at 394.401 nm[19] which corresponds to the $3s^2 3_p - 3s^2(^1S)4s$ transition array. The oscillator strength f of this transition is 0.115. This is the only transition from the ground state in this wavelength region. Two other hot band absorptions could occur at 395.57 and 396.152 nm. When the laser is in resonance with the transition at 394.401 nm, the rate of production of ions and electrons from vaporized

aluminum should increase by several orders of magnitude. This should increase the impulse and thermal coupling due to plasma formation, and lower the threshold for plasma ignition. The untreated aluminum surface absorptivity ranges from a few percent at IR wavelength to ∿20% at 350 nm,[16] and increases to ∿40% at 249 nm.[15] This increase in absorptivity is gradual compared to the sharp absorption line of aluminum atoms at 394.401 nm. The effects caused by the atomic absorption should be easily distinguishable from the metal surface absorptivity.

Impulse Coupling. The coupling of a mechanical impulse to a metal sample can be produced by (1) expulsion of metal liquid, vapor or fragments from the surface, or (2) pressure on the surface from the creation of a plasma which creates a laser supported detonation wave (LSD).[17,21] The photon momentum transfer is insignificant even at the high intensities of these experiments. As the fluence of the incident pulse is increased, impulse coupling is first detected when vaporization occurs. The impulse may increase further when a plasma is ignited. Impulse coupling would be measured as a function of laser wavelength and intensity using the pendulum method described by Rosen et al.[17] A small aluminum sample is attached to a pendulum of length l of ∿20 cm and effective mass m of ∿5 g. An optical projection system with a magnification ratio M would be used to monitor small deflections X of the pendulum after a laser shot.

The impulse I is given by

$$I = m(X/M)\sqrt{g/1}$$

where g is the acceleration due to gravity.

Thermal Coupling. The efficiency of heat deposition into the sample would be monitored with a chromel-alumel thermocouple mounted in a small hole drilled into the back of the target.[22] The thermal coupling as a function of increasing intensity may first increase, then decrease at the onset of vaporization and increase again at plasma ignition. These effects would be monitored as a function of laser wavelength.

Total Reflectivity. As a plasma is ignited, the inverse Bremsstrahlung process, ionization processes and plasma absorption cause a large decrease in total reflectivity.[23] The total reflectivity is monitored by placing the sample at one focal point of a rotational ellipsoid. The reflected laser light is collected at the other focal point and detected with a fast photodiode. A narrow pass filter centered on the wavelength region of interest would prevent broadband plasma emission from being detected. A second identical photodiode would monitor the temporal characteristics of the laser pulse. By comparing the signals from the two photodiodes, the exact time of plasma formation during the pulse could be monitored as a function of laser wavelength.

Electron Production. The production of electrons and ions, as a function of incident pulse intensity and wavelength,

could be measured easily by applying a bias of a few hundred volts between the metal surface and a nearby electrode, and measuring the current which flows after each laser pulse. A charge sensitive preamplifier would integrate the current pulse as described by Rianda et al.[24] The production of electrons as a function of wavelength should indicate if resonant two-photon ionization of aluminum is occurring at 394.401 nm.

Plasma Threshold. The appearance of a plasma is indirectly detected by the previous four techniques. However, a more direct way of determining the plasma ignition threshold is to observe the broadband emission from the plasma. This emission could be detected photographically or with a fast photodiode. A narrow band rejection filter would be used to exclude scattered light from this incident laser pulse.

The five techniques just mentioned should provide a fairly complete approach to studying the interaction of an intense UV pulse with an aluminum surface. In particular, it is hoped that many of the techniques will reveal enhanced plasma effects when the laser is tuned to 394.401 nm. At that wavelength, ground state aluminum can be ionized efficiently by a two-photon resonant process.

The production of a plasma is important for many laser machining processes. Enhanced thermal coupling and melting of metal can occur when a plasma is present. The plasma pressure also can effectively force molten metal out of the

holes produced in laser drilling or machining processes.[25,26,23] If resonant two-photon ionization occurs, the plasma ignition threshold may appear at lower intensities and fluences, allowing the use of much smaller lasers for a variety of metal-working applications.

References

1. "Industrial Lasers in the U.S.: Vital Statistics", Laser Focus, Sept. 1982, p. 38.
2. S. L. Ream, Laser Focus, Dec. 1982, p. 43.
3. R. G. Root, J. Phys. Colloq. (France), 3rd Int. Symposium on Gas Flow and Chem. Lasers 41(C-9), C9-59-73 (1980).
4. A. I. Barchukov, F. V. Bunkin, V. I. Konov and A. M. Prokhorov, Sov. Phys. JETP Lett. 17, 294 (1973).
5. A. I. Barchukov, F. V. Bunkin, V. I. Konov and A. A. Lyubin, Sov. Phys. JETP 39, 469 (1974).
6. J. A. McKay and J. T. Schriempf, IEEE J. Quant. Elect. QE-17, 2008 (1981).
7. C. T. Walters, R. H. Barnes and R. E. Beverly III, J. Appl. Phys. 49, 2937 (1978).
8. A. N. Pirri, R. G. Root and P. K. S. Wu, AIAA J. 16, 1296 (1978).
9. I. V. Nemchinov, I. A. Polozova, V. V. Svettsov and V. V. Shuvalov, Sov. J. Quant. Electron. 9, 721 (1979).
10. J. A. McKay and J. T. Schriempf, Appl. Phys. Lett. 31, 369 (1977).
11. J. A. McKay, R. D. Bleach, D. J. Nagel, J. T. Schriempf, R. B. Hall, C. R. Pond and S. K. Manlief, J. Appl. Phys. 50, 3231 (1979).
12. W. T. Walter, N. Solimene, K. Park, T. H. Kim and K. Mukherjee, "Optical Properties of Metal Surfaces During Laser Irradiation," Lasers in Metallurgy, AIME-TMS Conf. Series.

13. R. J. Harrach, J. Appl. Phys. 48, 2370 (1977).

14. N. Newstein and N. Solimene, IEEE J. Quant. Elect. QE-17, 2085 (1981).

15. J. A. Woodroffe, J. Hsia and A. Ballantyne, Appl. Phys. Lett. 36, 14 (1980).

16. C. Duzy, J. A. Woodroffe, J. C. Hsia and A. Ballantyne, Appl. Phys. Lett. 37, 542 (1980).

17. D. I. Rosen, J. Mitteldorf, G. Kothandaraman, A. N. Pirri and E. R. Pugh, J. Appl. Phys. 53, 3190 (198).

18. D. I. Rosen, D. E. Hastings and G. M. Weyl, J. Appl. Phys. 53, 5882 (1982).

19. W. L. Wiese, M. W. Smith and B. M. Glennon, Atomic Transition Probabilities, Vol. II, NSRDS-NBS 22, SD Cat. # CB.48:22 (1969).

20. Allied Chemical Electro-Optical Products brochure, "Only Alexandrite Offers All These Features", Box 1021R, Morristown, N.J. 07960.

21. R. D. Dupuis and P. D. Dapkus, Appl. Phys. Lett. 32, 473 (1978).

22. J. A. McKay, J. T. Schriempf, T. L. Cronburg, J. E. Eninger and J.A. Woodroffe, Appl. Phys. Lett. 36, 125 (1980).

23. M. Von Allmen, P. Blaser, K. Affolter and E. Stürmer, IEEE J. Quant. Elect. QE-14, 85 (1978).

24. R. Rianda, D. J. Moll and A. Kuppermann, Chem. Phys. Lett. 73, 469 (1980).

25. J. Fox, Appl. Phys. Lett. 26, 682 (1975).

26. V. Shui, Phys. Fluids 21, 2174 (1978).

Proposition IV: H_2O Vapor Detection in the Chemical Oxygen Iodine Laser by a New Dye Laser Intracavity Absorption Technique.

Abstract: It is proposed to use a new dye laser intracavity absorption technique to monitor the H_2O vapor concentration in the Chemical Oxygen Iodine Laser. A small change in wavelength makes this techique also applicable to ground state O_2 detection.

The work of Derwent and Thrush on energy transfer between O_2 and I_2[1-4] formed the basis for discovery of the chemical generation of a population inversion between the spin-orbit states of atomic iodine.[5] Lasing action was observed using the O_2-I_2 system by McDermott and co-workers.[6] A short time later, this laser was scaled up to produce 100 watts of CW output.[7] This laser has the potential of being scaled up to produce output powers comparable to the current DF military lasers.[8]

The chemical oxygen iodine laser (COIL) operates by mixing excited state $O_2(^1\Delta_g)$ with I_2. The following mechanism is believed to occur.[6]

$$O_2^*(\tilde{a}^1\Delta_g) + O_2^*(\tilde{a}^1\Delta_g) \rightarrow O_2^{**}(\tilde{b}^1\Sigma_g^+) + O_2(\tilde{X}^3\Sigma_g^-) \quad (1)$$

$$O_2^{**}(\tilde{b}^1\Sigma_g^+) + I_2 \rightarrow O(\tilde{X}^3\Sigma_g^-) + 2I(^2P_{3/2}) \quad (2)$$

$$O_2^*(\tilde{a}^1\Delta_g) + I(^2P_{3/2}) \rightarrow O_2(\tilde{X}^3\Sigma_g^-) + I^*(^2P_{1/2}) \quad (3)$$

$$I^*(^2P_{1/2}) \rightarrow I(^2P_{3/2}) + h\nu(\lambda = 1.315\ \mu m) \quad (4)$$

The $O_2^*(a^1\Delta_g)$ can be generated chemically in a variety of ways. One method currently under consideration by TRW Defense and Space Systems Group involves sparging Cl_2 gas through NaOH in liquid H_2O_2.[8] The stoichiometry of the reaction is

$$Cl_2 + 2H_2O_2 + NaOH \rightarrow \frac{3}{2}\,O_2^* + NaOH + H_2O + 2HCl\ . \quad (5)$$

The O_2^* is extracted from the sparger and injected into a laser cavity simultaneously with I_2, which initiates lasing

action. The collisional deactivation of O_2^* is very slow,[9] allowing efficient transfer of O_2^* from the sparger to the laser cavity.

Unfortunately, the H_2O produced in the sparger is an extremely efficient deactivator of O_2^{**}, almost 10^5 times more efficient than O_2.[10,11] H_2O also deactivates O_2^* and I^*, but with a lower efficiency.[11,12] O_2^{**} is necessary to dissociate I_2 (Eq. 2).[13] The deactivation of O_2^{**} should significantly decrease the performance of the COIL. The addition of a cold trap between the sparger and laser cavity reduces the H_2O/O_2 ratio from 2 to $\sim$0.1.[8] High efficiency cold traps may be able to eventually reduce this ratio to 0.0001.[8]

The preliminary experiments needed to scale up this laser require a fast, accurate, real-time technique for measuring the H_2O concentration between the cold trap and laser cavity. It is proposed to use a new technique, photoacoustic detection of intracavity absorption, to measure this H_2O concentration.

Intracavity absorption has been widely used to detect extremely weak absorptions.[14-24] Gas phase absorption coefficients as small as 10^{-8} cm^{-1} [20] and 10^{-9} cm^{-1} [17] have been measured. Using this technique involves placing the sample of interest inside the cavity of a CW dye laser and observing the change in the laser's output wavelengths or power. Two different categories of measurements are possible.

In case (a), the laser mode falls within the absorption linewidth of the sample. In case (b), some or many of the lasing modes fall outside the absorption linewidth. When a sample is inserted into a cavity under case (a) conditions, the resulting increased cavity loss produces a drop in laser power. In case (b), the absorption partially quenches only the modes which fall within the absorption linewidth. The power in these modes is shifted to other modes. The total output power under these conditions is not an accurate indicator of the absorption. Instead, a frequency sensitive detector must be used to monitor the redistribution of output power among the different modes. Measurements made under case (a) conditions have enhancements which are largely the result of the increased effective optical path through the sample.[25] Under case (b) conditions, however, much larger enhancements of up to 10^5 have been observed.[15]

Three techniques have been used to observe the redistribution of output frequencies under case (b) conditions. (1) The spectrum of the laser output is taken using a high resolution spectrometer.[16,21,22] (2) A small amount of identical sample is placed in a fluorescence cell outside the cavity.[15] The laser output produces fluorescence from this cell, which decreases when the sample is placed in the cavity. Since the sample in the fluorescence cell absorbs only the lines which are quenched by the intracavity sample,

the redistribution of output wavelengths away from the quenched lines is monitored. (3) The fluorescence cell of technique (2) is replaced by a hollow cathode discharge lamp containing the same material as the sample. The optogalvanic effect is used to monitor absorption in the hollow cathode lamp.[24]

Techniques (2) and (3) provide fast, accurate and economical methods of monitoring the redistribution of output in multi-mode lasers when a selective absorber is placed in the cavity. These techniques are limited, however, to molecules which fluoresceor atoms which exhibit an optogalvanic effict. The photoacoustic detection technique provides an alternative technique. Since it responds to nonradiative collisional decay pathways, it works well for states of molecules with low quantum yields for fluorescence.

In the proposed H_2O detection scheme for the COIL, the diagnostic duct between the cold trap and cavity would be equipped with two heated windows and placed inside the cavity of a broadband CW dye laser pumped by a mechanically chopped ion laser. The output of the dye laser would be directed into a temperature stabilized photoacoustic cell containing a H_2O vapor sample. The photoacoustic signal would be processed by a lock-in amplifier referenced to the mechanical chopping frequency. In this configuration, the decrease in photoacoustic signal would be proportional to the amount of H_2O in the diagnostics duct.

Several H_2O absorption lines could be used; however, the presence of Cl_2, HCl, O_2, O_2^* and O_2^{**} requires a careful choice to avoid overlapping absorption bands.[26] One possible choice would be the H_2O overtone bands between 715 and 732 nm. One of the strongest H_2O lines in this region is the $303 \rightarrow 404$ (J,K_a,K_c) rotational line of the 301 (v_1,v_2,v_3) vibrational transition at 719-1488 nm.[27] The peak absorption cross section σ_L of this line is relatively insensitive to temperature changes.[27] σ_L can be calculated from the linestrength S of 40.1×10^{-24} $cm^{-1}/(molec./cm^2)$ using the formula

$$\sigma_L = S/\pi\gamma_L \qquad (6)$$

where γ_L is the half-width at half maximum.[27] The total pressure in the diagnostic duct is typically 1 torr.[8] At this pressure, Doppler broadening should contribute almost all of the linewidth. At 298°K the H_2O half-width in this wavelength region due to Doppler broadening[28] is about 0.02 cm^{-1}, yielding a peak absorption cross section of 6.4×10^{-22} cm^2. This linewidth easily allows case (b) intracavity absorption measurements using a broadband dye laser with a simple birefringent tuning element. Using this cross section and assuming a minimum detectable absorption coefficient[17] of 10^{-9} cm^{-1}, the photoacoustic intracavity absorption technique should be able to measure H_2O partial pressures down to 5×10^{-5} torr. This is a factor of 2 better than the lowest expected H_2O partial pressure.

This H_2O absorption line falls near the peak of the gain curve for oxazine 725 laser dye when pumped by a kryton ion laser.[29] The oxygen $X^3\Sigma_g^- \rightarrow b^1\Sigma_g^+$ (0,0) transition also falls on this dye gain curve. By simply changing wavelengths and having both O_2 and H_2O in the photoacoustic cell the O_2 concentration could also be measured. The $O_2\ ^PP_q$ transition at 763.6328 nm[30] has a linestrength of 7.44×10^{-24} $cm^{-1}/(molec./cm^2)$.[31] Repeating the calculation for H_2O for the O_2 case gives a minimum detectable O_2 partial pressure of 2×10^{-4} torr.

The new photoacoustic detection of intracavity absorption technique just described should provide a fast, accurate, real-time method for monitoring the H_2O and O_2 partial pressures in COIL systems. The expected sensitivity for H_2O should easily monitor the minimum projected concentrations when more advanced cold traps are employed. When combined with the existing dimol emission technique for monitoring O_2^* concentrations,[32] the three highest concentration species, H_2O, O_2 and O_2^*, present in the cold trap output can be monitored. This should greatly simplify the scaling up of this promising laser system.

References

1. R. G. Derwent, D. R. Kearns and B. A. Thrush, Chem. Phys. Lett. 6, 115 (1970).
2. R. G. Derwent and B. A. Thrush, Chem. Phys. Lett. 9, 591 (1971).
3. R. G. Derwent and B. A. Thrush, J. Chem. Soc. Faraday Disc. II 68, 720 (1972).
4. R. G. Derwent and B. A. Thrush, Disc. Faraday Soc. 53, 162 (1972).
5. A. T. Pritt, Jr., R. D. Coombe and D. Pilipovich, Appl. Phys. Lett. 31, 745 (1977).
6. W. E. McDermott, N. R. Pchelkin, D. J. Benard and R. R. Bousek, Appl. Phys. Lett. 32, 469 (1978).
7. D. J. Benard, W. E. McDermott, N. R. Pchelkin and R. R. Bousek, Appl. Phys. Lett. 34, 40 (1979).
8. Technical Handout for AE107, a course on High Energy Chemical Lasers taught at Caltech by TRW Defense and Space Systems Group. Fall quarter, 1980/81.
9. K. H. Becker, W. Groth and U. Schurath, Chem. Phys. Lett. 8, 259 (1971).
10. E. A. Ogryzlo and B. A. Thrush, Chem. Phys. Lett. 24, 314 (1974).
11. H. H. Wasserman and R. W. Murray, Singlet Oxygen, Organic Chemistry, A Series of Monographs, Vol. 40 (Academic Press, New York, 1979), pp. 43-48.

12. A. J. Grimley and P. L. Houston, J. Chem. Phys. 69, 2339 (1978).

13. There is some recent but undocumented evidence from Ref. 8 that I_2 may be dissociated by a second mechanism which operates in parallel with reaction (2).

14. N. G. Peterson, M. J. Kurylo, W. Braun, A. M. Bass and R. A. Keller, J. Opt. Soc. of Amer. 61, 746 (1971).

15. T. W. Hansch, A. L. Schawlow and P. E. Toschek, IEEEE J. Quant. Elect. QE-8, 802 (1972).

16. J. P. Reilly and G. C. Pimentel, Appl. Opt. 15, 2372 (1976).

17. V. M. Baev, T. P. Belikova, E. A. Sviridenkov and A. F. Suchkov, Sov. Phys. JETP 47, 21 (1978).

18. V. R. Mironenko and I. Pack, Sov. J. Quant. Elect. 8, 1394 (1978).

19. F. J. Morgan, C. H. Dugan and A. G. Lee, Opt. Commun. 27, 451 (1978).

20. W. T. Hill III, R. A. Abreu, T. W. Hansch and A. L. Schawlow, Opt. Commun. 32, 96 (1980).

21. S. J. Harris and A. M. Weiner, Opt. Lett. 6, 142 (1981).

22. S. J. Harris and A. M. Weiner, J. Chem. Phys. 74, 3673 (1981).

23. Wm. R. Lambert, P. M. Felker and A. H. Zewail, J. Chem. Phys. 74, 4732.

24. E. F. Zalewski, R. A. Keller and C. T. Apel, Appl. Opt. 20, 1584 (1981).

25. H. K. Holt, Phys. Rev. A11, 625 (1975).

26. The I_2 concentration is expected to be low in the diagnostic duct because the I_2 is added in the laser cavity. The near supersonic flows required to sustain high power lasing prevent backflow.[8]

27. T. D. Wilkerson, G. Schwemmer, B. Gentry and L. P. Giver, J. Quant. Spectrosc. Radiat. Transfer 22, 315 (1979).

28. A. Yariv, Quantum Electronics, 2nd edit. (John Wiley, New York, 1975), p. 167.

29. Laser Dye Brochure, Exciton, P.O. Box 3204, Overlook Station, Dayton, OH 45431.

30. H. D. Babcock and L. Herzberg, Astrophysical J. 108, 167 (1948).

31. J. H. Miller, R. W. Boese and L. P. Giver, J. Quant. Spectrosc. Radiat. Transfer 9, 1507 (1969).

32. R. G. Derwent and B. A. Thrush, Trans. Faraday Soc. 67, 2036 (1971).

Proposition V: A Radio-Chemical Tracer Study of the Tungsten Regenerative Cycle in Incandescent Lamps Containing $CBrF_3$.

Abstract: It is proposed that the migration of tungsten in incandescent lamps containing $CBrF_3$ be studied by a tungsten-185 radio-chemical tracer technique. The direction of migration of tungsten-185 depends on whether bromine or fluorine is involved in the regenerative cycle. A direct measurement of this migration should help elucidate the mechanism of regeneration.

The lifetime of conventional gas-filled tungsten incandescent filament lamps has been shown to be inversely proportional to the rate of evaporation of tungsten from the filament.[1] After extended operation, a local "hot spot" develops on the filament. This "hot spot" is located at a position where extra tungsten has evaporated off, leaving behind a smaller cross sectional area with a higher resistance.[2] The increased resistance elevates the temperature of the filament at that point, which increases the rate of evaporation. When the lamp is switched on, a nonequilibrium temperature overshoot occurs at the "hot spot".[3,4] If the overshoot temperature exceeds the melting point of tungsten (3410^{o}C), the filament fuses at the "hot spot" and the lamp is destroyed.

Tungsten atoms or molecules which evaporate from the incandescent filament surface may either transfer to nearby parts of the filament, or escape the high-temperature low-viscosity Langmuir sheath[4] surrounding the filament and diffuse out to the glass envelope where they form a dark metallic film. The accumulation of tungsten on the walls places a limit on the minimum dimensions of the lamp.

The addition of small amounts of halogens to the lamp produces a regenerative cycle which transfers the tungsten back to the filament.[6] In the simplest mechanism, an equilibrium is established between tungsten metal and tungsten halogen compounds.[7,8]

$$W + nX \rightleftharpoons WX_n \quad (1)$$

At low temperatures, the equilibrium favors WX_n, while at high temperatures dissociation occurs to release tungsten metal. Physically, this causes WX_n compounds to form in the cooler envelope regions. WX_n diffuses back into the hot filament region, decomposes and returns the tungsten to the filament.

The halogen cycle continually cleans the envelope walls. This allows the lamp size to be decreased, making it economically feasible to add high pressures of krypton or xenon instead of the usual lighter argon. When quartz envelopes are used, krypton or xenon pressures of up to 10 atmospheres can be used. The high pressures and heavier gases reduce tungsten diffusion away from the filament, allowing operation at higher intensities and up to 100% longer lifetimes.[6]

Typical quartz halogen lamps use iodine, bromine or chlorine halogen cycles. Unfortunately, the tungsten halides formed from these halogens dissociate at temperatures well below the normal filament operating temperature.[9] The tungsten halides which are returning from the walls dissociate in the cooler filament regions, before they are able to reach the central hottest part of the filament. The typical halogen cycle, therefore, eliminates the problem of radial diffusion of tungsten to the envelope walls, but

enhances the axial flow of tungsten from hotter filament areas to cooler areas of the filament. The current quartz halogen lamp technology has greatly increased the brightness and slightly increased the lamp lifetime. The problem of "hot spots", however, still remains as the major cause of lamp burnout.

The axial transport of tungsten can be minimized by using fluorine in the halogen cycle.[10] Tungsten fluoride (WF_6) is stable up to $\sim 3100^{\circ}C$. WF_6, therefore, dissociates only at the hottest filament surfaces. This process replaces the evaporated tungsten preferentially at the thinnest filament areas which are the "hot spots" where filament failure occurs. Schröder was the first to demonstrate this "self-healing" fluorine cycle process.[10,11]

Even with the demonstration of self-healing fluorine lamps, the fluorine cycle has still not appeared in commercial lamps because of several additional problems. First, there is a large temperature gradient along the filament axis. Tungsten near the cool ends of the filament reacts with the fluorine, and gets transported to the hotter center area of the filament. This process is called tail erosion.[6] A second problem arises from the reactivity of fluorine compounds with the quartz envelope. In particular, the following reaction with WF_6 is believed to occur.[6]

$$SiO_2 + WF_6 \rightarrow SiF_4 + WO_2F_2 \qquad (2)$$

The oxyfluorides then dissociate to give tungsten oxides,

$$2WO_2F_2 \rightarrow WOF_4 + WO_3 \qquad (3)$$

which deposit on the envelope. Reaction (2) rapidly consumes the fluorine in the lamp, destroying the regenerative fluorine cycle. Various envelope coatings such as MgF_2 and CaF_2,[12] and glass films based on Al_2O_3-TiO_2-P_2O_5[13] have been tried in attempts to protect the quartz surface. The problems inherent in the fluorine cycle have prevented a widespread commercial application of this technique.

Recently, Hill and Dolenga[14] reported that addition of small amounts of $CBrF_3$ to the fill gas extended the lamp lifetime by a factor of two over lamps containing bromine alone. The normal lamp manufacturing processes which removed trace impurities of oxygen were omitted in their lamps. They claimed that small amounts of oxygen were necessary to form the dominant transfer cycle molecule WO_2F_2. Previous calculations by Neumann[15] had predicted that WO_2F_2 would be the dominant specie at temperatures below 2500°K. Lamps containing 6 atm of krypton and 100 ppm $CBrF_3$ which were operated at a filament temperature of 3250°K exhibited lifetimes of ∿350 hours. Similar lamps which contained CH_2Br_2 had lifetimes which were ∿140 hours. The fluorine did not appear to attack the lamp walls or the cooler part of the filament.

The results of Hill and Dolenga have been criticized strongly by Coaton and Fitzpatrick[6], who suggest that the $CBrF_3$ present may thermally decompose to BrF_3. This compound

is stable up to 2000°K, which produces no free fluorine at the walls or filament tails. They postulate that a fluorine cycle does not occur in these lamps. Instead, the bromine is responsible for the regenerative mechanism which keeps the walls clean.

I propose the use of a radio-chemical tracer study of the $CBrF_3$ lamp to determine whether a completely regenerative fluorine cycle is operating, or if only a radially regenerative bromine cycle is occurring. Using the technique of Bartha and Hangos,[16] a small sample of W-185 radioactive isotope would be added to the center of a tungsten filament. This is accomplished by preparing a solution of ammonium tungstate containing W-185.[17] One drop of solution is placed on the filament and allowed to dry. A hydrogen atmosphere would reduce the tungsten to tungsten metal.

Lamps prepared using the method of Hill and Dolenga[14] containing $CBrF_3$ and the W-185 labeled filament would be burned for a short time. Then the location of the W-185 would be monitored. W-185 decays with a half-life of 75.8 days by emission of a 0.432 MeV beta particle.[18] The W-185 location on the filament or envelope would be detected with a silicon surface-barrier detector[19] placed behind an aperture in a lead plate. By moving the filament slowly across the aperture and detecting the emitted beta particles, the relative concentration of W-185 in different sections of the filament would be determined.

Two different distributions of W-185 could be expected depending on whether a fluorine or bromine cycle is operating. The bromine cycle removes tungsten from the hot central portion of the filament and deposits it on the cooler ends. Since the W-185 would be initially placed in the center, the bromine cycle would slowly move the W-185 out to the ends of the filament. The fluorine cycle, if operating correctly, is a self-healing process which deposits evaporated tungsten back on the central hot part of the filament. Therefore, the W-185 should remain localized in the center of the filament and not appear at the ends if a fluorine cycle is operating.

This radio-chemical tracer technique should be a sensitive and direct probe of tungsten migration in $CBrF_3$ lamps. The ability to differentiate between the bromine or fluorine cycles in these lamps should greatly increase our understanding of this complex chemical behavior.

References

1. E. J. Covington, J. Illum. Eng. Soc. 2, 83 (1973).
2. J. R. Coaton and J. M. Rees, Proc. IEE 124, 763 (1977).
3. D. H. Fax, H. G. Sell and R. Stickler, Illuminating Engineering 66, 187 (1971).
4. F. J. Harvey, J. Illum. Eng. Soc. 3, 295 (1974).
5. I. Langmuir, The Collected Works of Irving Langmuir, Vol. 2 (Pergamon Press, 1960).
6. J. R. Coaton and J. R. Fitzpatrick, IEE Proc. 127, 142 (1980).
7. T. Geszti and I. Gaal, Acta Tech. Acad. Sci. Hung. 78, 479 (1974).
8. S. K. Gupta, J. Electrochem. Soc., Solid State Sci. and Techn. 125, 2064 (1978).
9. A. Rabenau, Angew. Chem. Internat. Edit. 6, 68 (1967).
10. J. Schröder, Philips Tech. Rev. 26, 111 (1965).
11. J. Scrhöder, Philips Tech. Rev. 25, 359 (1964).
12. British Patent 1047302 (1966).
13. R. Rothon and J. M. Rees, Chem. and Industry (1 July 1978), p. 478.
14. J. C. Hill and A. Dolenga, J. Appl. Phys. 48, 3089 (1977).
15. G. M. Neumann, Z. Metallkd. 64, 26 (1973).
16. L. Bartha and I. Hangos, Int. J. Appl. Radiation and Isotopes 24, 605 (1973).

17. Tungsten-185 is commercially available from Atomic Energy of Canada, Ltd. Commercial Products; Amersham Corp.; and New England Nuclear.

18. Handbook of Chemistry and Physics, 57th edition (CRC Press, Ohio, 1976), p. B-322.

19. Silicon surface barrier detectors are available from Ortec Inc., 100 Midland Rd., Oak Ridge, TN 37830. The features and operation of these detectors are described in their catalogs.